Air Force Institute of Technology

AFIT Scholar

9-2007

Raman Fiber Lasers and Amplifiers based on Multimode Fibers and their Applications to Beam Cleanup

Nathan B. Terry

Follow this and additional works at: https://scholar.afit.edu/etd

Part of the Plasma and Beam Physics Commons

RAMAN FIBER LASERS AND AMPLIFIERS BASED ON MULTIMODE GRADED-INDEX FIBERS AND THEIR APPLICATION TO BEAM CLEANUP

DISSERTATION

Nathan B. Terry, Captain, USAF

AFIT/ DS/ENP/07-02

DEPARTMENT OF THE AIR FORCE
AIR UNIVERSITY

AIR FORCE INSTITUTE OF TECHNOLOGY

Wright-Patterson Air Force Base, Ohio

APPROVED FOR PUBLIC RELEASE

The views expressed in this dissertation are those of the author and do not reflect the official policy or position of the United States Air Force, Department of Defense, or the United States Government.

AFIT/DS/ENP/07-02

RAMAN FIBER LASERS AND AMPLIFIERS BASED ON MULTIMODE GRADED-

INDEX FIBERS AND THEIR APPLICATION TO BEAM CLEANUP

DISSERTATION

Presented to the Faculty

Graduate School of Engineering and Management

Air Force Institute of Technology

Air University

Air Education and Training Command

in Partial Fulfillment of the Requirements for the

Degree of Doctor of Philosophy

Nathan B. Terry, BS, MS

Captain, USAF

June 2007

APPROVED FOR PUBLIC RELEASE; DISTRIBUTION UNLIMITED

AFIT/DS/ENP/07-02

RAMAN FIBER LASERS AND AMPLIFIERS BASED ON MULTIMODE GRADED-

INDEX FIBERS AND THEIR APPLICATION TO BEAM CLEANUP

Nathan B. Terry, BS, MS
Captain, USAF

Approved:
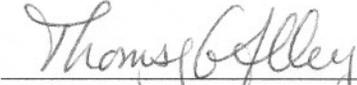
_____   _____
Thomas G. Alley (Chairman)   15 June '07
                                           Date
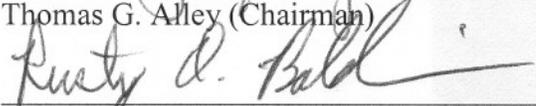
_____   _____
Rusty O. Baldwin (Dean's Representative)   18 Jun '07
                                           Date

_____   _____
Matthew E. Goda (Member)   2 JUL 07
                                           Date

_____   _____
Robert L. Hengehold (Member)   2 Jul 07
   Date

_____   _____
Timothy H. Russell (Member)   2 JUL 07
                                           Date

Accepted:

_____   _____
M. U. Thomas, PhD   9 Jul 07
Dean, Graduate School of   Date
Engineering and Management

Abstract

A numerical model is used to describe the interaction of the transverse pump modes and the transverse Stokes modes of a multimode fiber. This model explains why beam cleanup is confined to graded-index fibers and has not been observed in step-index fibers. According to this model the beam quality of the Stokes output of a Raman fiber amplifier (RFA) based on a multimode graded-index fiber is a function of the beam quality of the input seed beam and the beam quality of the input pump beam.

An experimental examination of an RFA based on a graded-index fiber showed that given a pump beam with poor beam quality, the beam quality of the output Stokes beam was similar to the beam quality of the input Stokes seed. This was true for a seeding geometry where the seed beam co-propagated with respect to the pump beam and for a seeding geometry where the seed beam counter-propagated with respect to the pump beam. The Stokes output of the backwards-seeded geometry was primarily confined to the first Stokes order. On the other hand, due to four wave mixing, the Stokes output of the forward-seeded geometry contained a cascade of multiple Stokes orders.

Several configurations of a Raman fiber laser (RFL) based on a multimode graded-index fiber were also examined. The maximum Stokes power produced by any of the tested RFL configurations was 7 W with a slope efficiency of 60%. However, as the power of the output Stokes beam increased the beam quality of the output Stokes beam decreased. Furthermore, the reflectivity of the output coupler also affected the beam quality of the Stokes output. RFL configurations which used a high reflectivity fiber Bragg grating (FBG) as the output coupler produced Stokes beams with worse beam

quality than RFL configurations which used a low reflectivity FBG as the output coupler. RFL configurations that employed dichroic mirrors instead of FBGs were examined and shown to be potentially useful for RFLs based on very large diameter graded-index fibers.

Finally, two continuous-wave pump beams were combined to generate a single Stokes beam using the process of stimulated Raman scattering (SRS). Two SRS beam combination techniques were examined. The first technique used an RFA as the SRS beam combiner and operated with an optical conversion efficiency of 10%. The second technique used an RFL as the SRS fiber beam combiner. This second technique produced an output Stokes beam with 5.5 W of power which was 296% brighter than the pump beam used generate it. The optical conversion efficiency of the RFL beam combiner was 56%.

Table of Contents

List of Figures

xiv

List of Tables

List of Acronyms

ABL—Airborne Laser
ALL—Airborne Laser Laboratory
BSRS—Backward Stimulated Raman Scattering
COIL—Chemical Oxygen-Iodine Laser
CW—Continuous Wave
DCF—Double Clad Fiber
DCFL—Double Clad Fiber Laser
DoD—Department of Defense
EYDFA—Er-Yr Co-Doped Fiber Amplifier
FBC—Fiber Beam Combiner
FBG—Fiber Bragg Grating
FWM—Four Wave Mixing
FWHM—Full Width Half Maximum
FSRS—Forward Stimulated Raman Scattering
HR—Highly Reflective
IR—Infrared
LIMO— Lissotschenko Mikrooptik
MMFBG—Fiber Bragg Grating written to Multimode fiber
MOPA—Master Oscillator Power Amplifier
OSA—Optical Spectrum Analyzer
PBS—Polarizing Beamsplitter
RA—Raman Amplifier
RFA—Raman Fiber Amplifier
RFL—Raman Fiber Laser
SBS—Stimulated Brillioun Scattering
SHG—Second Harmonic Generation
SFG—Sum Frequency Generation
SRS—Stimulated Raman Scattering
UV—Ultraviolet

List of Symbols

Roman Symbols

a	radius of fiber core
$A_{p,s}$	amplitude of pump and Stokes waves
$A_{p,s}^m$	amplitude of pump and Stokes waves of the mth fiber mode
A_{eff}	effective area of the fiber
$B(\theta,\varphi)$	angular distribution of scattered photons
B	brightness
$\vec{B}$	magnetic induction
c	speed of light
$c.c.$	complex conjugate
C_1	1st coefficient used to calculate the variance of a field
C_2	2nd coefficient used to calculate the variance of a field
D	constant of proportionality for Raman scattering
$\vec{D}$	electric displacement
$\hat{e}$	unit vector
$\vec{E}_{p,s}$	electric field ; subscripts denote pump and Stokes respectively
$\vec{F}$	force
g	Raman gain per unit area
g_R	Raman gain coefficient
$g(z)$	effective gain of each mode per unit length per unit power
G	Raman gain per unit length
$\vec{H}$	magnetic field
$\hbar$	Plank's constant
$I_{p,s}$	intensity of pump, Stokes respectively
j	integer
$\vec{J}_f$	free current density
$\vec{k}$	wave vector
k_B	Boltzmann's constant
k_T	transverse propagation constant
L	fiber length
L_{eff}	effective length of a fiber
m	effective mass
$m_{p,s}$	average number of photons per mode; subscripts denote pump and Stokes modes
M	total number of available Stokes modes
M	number of modes supported by a fiber
M^2	beam quality factor
$n_{1,2}$	index of refraction of the fiber core and cladding respectively
N	number density of molecules
N_n	principal mode number
NA	numerical aperture
p_j	fraction of pump power launched into the jth mode of the fiber
P_p	power
P_s	probability of scattering into a Stokes mode per unit time

$\vec{P}$	induced polarization
P_{th}	pump threshold
P_0	pump power
q	displacement
Q	number of modes in the fiber
r	radius
R	reflectivity
R	normalized radius
T	temperature
$u(r)$	radial component of a fiber mode
$\hat{u}$	unit vector
V	fiber V parameter
V	volume of radiating region
$w(z)$	beam radius
w_0	radius of beam waist
$\langle x \rangle$	center coordinate of a fiber mode
y	probability of scattering
z_0	location of beam waist

Greek Symbols

α	polarization of a molecule
α_0	equilibrium polarization
$\alpha_{p,s}$	attenuation of pump and Stokes beams
β	z component of propagation constant
$\beta_{f,b}$	propagation constant for forward and backward waves respectively
β_{lm}	propagation constant of the LP_{lm} mode
γ_c	decay term
γ_p	damping term
Δ	relative index difference in a fiber
$\Delta\vec{k}$	momentum mismatch between fiber modes
$\Delta\omega$	linewidth
ε_0	electric permeability of vacuum
λ	wavelength
Λ	grating period
μ_0	magnetic permeability of free space
θ_r	ray angle
θ	radial angle
ρ_f	free charge density
σ	scattering cross section
σ_x^2	variance
$\phi_{p,s}$	phase of pump, Stokes
φ	azimuthal angle
$\chi^{(n)}$	n^{th} order susceptibility
$\chi_{SRS}^{(3)}$	nonlinear susceptibility term responsible for SRS

$\chi_{FWM}^{(3)}$ nonlinear susceptibility term responsible for FWM

ψ_n n^{th} transverse mode of the fiber

$\psi(r, \phi, z)$ spatial component of electric field

ω_0 mode field radius

$\omega_{p,s}$ frequency of pump and Stokes beams

ω_v resonance frequency

$\psi_{p,s}^{m}$ electric field of the mth pump and Stokes modes

Ω Stokes shift

List of Publications

Peer Reviewed Journals

N. B. Terry, K. T. Engel, T. G. Alley, and T. H. Russell, "Use of a Continuous Wave Raman Fiber Laser in Graded-Index Multimode Fiber for SRS beam Combination", *Opt Express*, **15**, 602-7, 2007.

Conferences and Conference Proceedings

N. B. Terry, K. Engel, T. G. Alley, T. H. Russell, and W. B. Roh, "Forward and Backward Seeded Continuous-Wave Raman Fiber Amplifiers Based on Multimode Fibers", in *Photonics West*, 2007. San Jose, California.

N. B. Terry, B. Flusche, K. Engel, T. G. Alley, T. H. Russell, and W. B. Roh, "Beam Cleanup and Beam Combination in Raman Fiber Amplifiers and Lasers based on Multimode Fibers*",* in *Directed Energy Symposium,* 2006. Los Angeles, California.

N. B. Terry, T. G. Alley, and W. B. Roh. "Brightness Conversion Using a Raman Fiber Laser Based on a Multimode Fiber," in *Proc Advanced Solid State Photonics*, 2006. Incline Village, Nevada.

N. B. Terry, T. G. Alley, and W. B. Roh. "Singlemode Operation of Multimode Fiber Raman Laser," in *Solid State and Diode Laser Technology Review*, 2005. Los Angeles, California.

In Progress

"Beam Cleanup and Delaying FWM-Generated Stokes Cascades in Continuous-Wave Seeded Raman Fiber Amplifiers based on Multimode Fibers"

"SRS Beam Cleanup in Graded-Index versus Step-Index Fibers"

RAMAN FIBER LASERS AND AMPLIFIERS BASED ON MULITMODE GRADED-INDEX FIBERS AND THEIR APPLICATION TO BEAM CLEANUP

1. Introduction

1.1. Purpose

The world's first laser was demonstrated by Maiman in 1960. Since that time, lasers have been developed for a wide variety of military applications, including communications systems, laser radar, targeting, and perhaps most dramatically, laser weapons. In order for a laser to be useful, it must satisfy a number of requirements. Perhaps the most obvious requirement is power. Laser weapons require very high power laser systems; other applications such as communications can use low power laser systems. Wavelength is another defining characteristic of a laser system. The size of a system is also an extremely important consideration for aerospace applications which integrate the laser system into a relatively small platform. Lastly, while a system may produce a large amount of power, the ability of the system to focus this energy on a target is limited by its beam quality.

In summary, a laser system with military utility will produce the right amount of power, at the right wavelength, on the right platform, and with good beam quality. Raman fiber devices based on graded-index fibers have the potential to fulfill these requirements. The original experiments described in this document show that Raman fiber devices based on graded-index fibers can produce moderate output powers; this innovative research also explores the conditions under which Raman fiber devices based on multimode fibers produce Stokes beams with reasonable beam quality.

1

1.2. Motivation

One of the first military applications of laser technology was shown on 13 May 1972 when four U.S. F-4D aircraft successfully attacked the Thahn Hoa Bridge in North Vietnam using laser-guided bombs [1]. A direct demonstration of laser weapons followed on 13 November 1973 when a 100 kW CO_2 laser disabled the control system of a 12-foot long radio controlled drone, knocking it out of the air. The next day, the CO_2 laser locked onto another drone's fuel tank for 1.2 seconds, ignited the interior fuel vapors and crashed the vehicle [2].

In 1975, a laser was placed aboard a KC-135A, dubbed the Airborne Laser Laboratory (ALL). Eight years later, the ALL successfully shot down five Sidewinder air-to-air missiles and an aerial drone [2]. Interest in developing laser systems is not confined to the Air Force. On 6 June 2000, the Army's Tactical High Energy Laser/Advanced Technology Demonstrator used a chemical laser to detonate the high-explosive warhead of a Katusha rocket at the White Sands Missile Range in New Mexico [3]. That this was a joint project with Israel underscores the fact that the United States is not the only nation interested in military laser systems. The Navy is also interested in developing solid state lasers, as well as free electron lasers for use on ships [4].

Like its sister services, the Air Force is interested moving laser systems from the laboratory to the battlefield. Perhaps the prime example of this is the Airborne Laser (ABL). The ABL, designed as a defense against ballistic missiles, consists of a megawatt class chemical oxygen-iodine laser (COIL). In the COIL system, chlorine gas is combined with a fine spray of hydrogen peroxide which has been mixed with sodium, lithium and potassium [5]. The resulting chemical reaction produces excited oxygen

2

molecules. Excited oxygen molecules transfer energy to iodine atoms which are in turn excited. The iodine atoms then produce laser energy at the 1315 nm wavelength.

The ABL with its chemical laser is not the only possible aerial platform for directed energy systems. The Air Force is also interested in employing laser systems on the C-130 [6]. By thus employing laser weapons, the Air Force would gain the ability to launch high precision strikes against very specific targets. For example, laser weapons make it possible to disable the tires or the engine of a truck without damaging the rest of the vehicle.

Wavelength is a very important characteristic of a laser because different wavelengths are needed to fulfill different missions. For example, the atmospheric transmission of a laser beam is highly dependant on its wavelength; some wavelengths are selectively absorbed by the various constituent molecules of the atmosphere [7]. Other wavelengths, such as the output from a CO_2 (10.6 μm), are highly absorbed by water, making lasers that operate at these wavelengths useful as medical tools capable of removing diseased tissue [8]. It turns out that laser wavelengths above 1400 nm are heavily absorbed by the cornea and lens of the human eye. When these wavelengths are incident on the eye, absorption in the cornea and the lens attenuates the laser intensity which is focused onto the retina. This increases the damage threshold of the retina by a factor of 50 over non-eyesafe wavelengths [9]. Wavelengths which reach the retina with reduced intensity are sometimes termed "eyesafe".

Using a laser that operates at an eyesafe wavelength mitigates the risk of collateral damage associated with that laser system. The potential for collateral damage is significant. For example, the ABL could pose an eye hazard for a distance of some

3

28,000 kilometers [6]. The problem of stray reflections becomes even more complicated when lasers are mounted on high velocity, low-flying aerial platforms. Rapid changes in the angle of the incident beam relative to the target are inherent in such geometries. The U.S. military as well as foreign militaries have expressed interest in eyesafe laser wavelengths because lasers operating at these wavelengths minimize the risk of collateral eye damage to military or civilian personnel [10,11].

The Air Force is also interested in creating mid-range infrared (IR) lasers which can be mounted on an aircraft and used to disable the IR tracking systems of inbound missiles. Due to the relatively small size of fighter aircraft and unmanned aerial vehicles, compact and lightweight laser systems are very useful. Whereas conventional laser systems require large and bulky cooling systems, the large surface to volume ratio of fiber lasers allows extensive air cooling, reducing the need for more complex and bulky cooling systems. Furthermore, it has recently been demonstrated that a kW class fiber laser can have a wall plug efficiency of 30%, which is significantly better than the demonstrated efficiency of other industrial lasers [12]. Increasing the wall plug efficiency reduces the power requirements and thus the logistical footprint of the laser system. Efficient cooling and high wall plug efficiency make fiber lasers one of the most promising laser systems for small tactical aerial platforms [13].

Many lasers are useful only insofar as they produce output beams with good beam quality. A laser beam with excellent beam quality will be comprised only of a single transverse mode which is nearly perfectly Gaussian. Such a high quality beam is generally the preferred output of a laser system because of its increased ability to concentrate laser energy on a target.

The Raman fiber laser (RFL), which has become increasingly popular due to its compactness, ruggedness and flexibility, has the potential to be very attractive for DoD applications. The RFL is based on stimulated Raman scattering (SRS), a nonlinear optical process whereby photons from a pump beam are converted into lower energy photons of a Stokes beam. In general, an RFL consists of a fiber gain medium with an input coupler fiber Bragg grating (FBG) on the front end and an output coupler FBG on the back end of the fiber cavity. FBGs can be written directly to the ends of the RFL with an ultraviolet (UV) laser [14] or written to separate pieces of fiber and then spliced onto the ends of the RFL.

RFLs have two main advantages. The first advantage of RFLs is that they can generate a wide range of novel laser wavelengths. For example, altering the wavelength of the pump laser of an RFL alters the wavelength of the output Stokes beam. Carefully tailoring the gain medium provides even more wavelength flexibility. Another method of wavelength selection employs a series of nested fiber cavities to cascade the Stokes output to the desired wavelength. Clearly, RFLs are one promising way to generate the right wavelength on the right platform.

The second advantage of RFLs is that they can produce laser output with good beam quality. Traditionally, RFLs have produced singlemode output through the use of fibers with singlemode cores. Unfortunately, RFLs have historically produced only modest output powers; RFLs based on singlemode fibers have produced continuous-wave (CW) output powers of up to 13 W [15]. While lasers based on singlemode fibers produce singlemode output, it is difficult to efficiently couple multimode pump light into

5

a fiber with a singlemode core. This limits the efficiency and ultimately the output power of RFLs based on singlemode fibers.

The pump laser of choice for RFLs has typically been the double clad fiber laser (DCFL). A DCFL utilizes a double clad fiber (DCF) in the laser cavity instead of using a more traditional singlemode fiber. A diagram of a DCF is shown in Figure 1. The core of a DCF is surrounded by two layers of cladding material. The first layer known as the inner cladding confines laser radiation to the fiber core. The second cladding layer, also known as the outer cladding, confines pump radiation to the inner cladding. The outermost layer of the DCF is a buffer added to provide mechanical strength to the fiber.
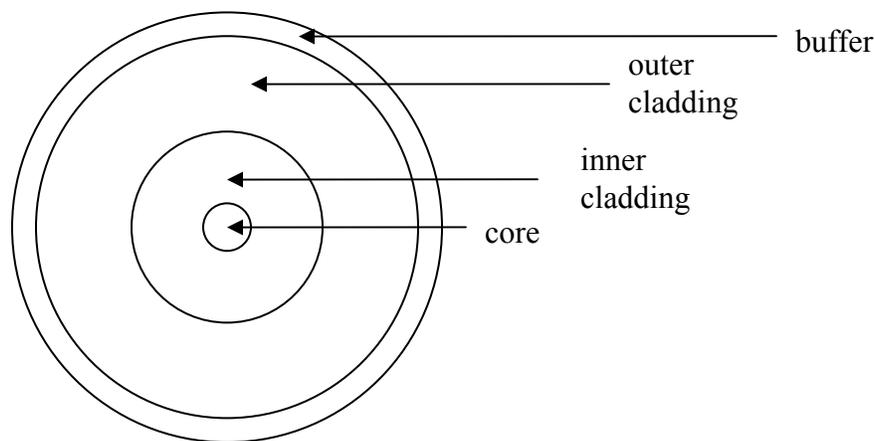
Figure 1. Cross section of a notional DCF.

While the multimode inner cladding of a DCFL is pumped with a multimode diode pump laser, the core of the DCFL is typically singlemode. The singlemode output of the DCFL can be used as a singlemode pump for an RFL. The typical DCFL can be considered to be an intermediary pump laser which converts a multimode pump beam into a singlemode pump beam. Unfortunately, using such an intermediary reduces the overall efficiency of the RFL system.

6

One way to increase the efficiency of RFLs is to base them on a multimode fiber instead of using a singlemode fiber. Larger gain fibers enable more efficient pump coupling. Higher efficiency leads to higher output powers. This document examines RFLs based on multimode graded-index fibers.

Fortunately, an RFL based on a multimode fiber can produce near-singlemode output through the beam cleanup properties of SRS [16]. Beam cleanup occurs when the most Gaussian-like components of the Stokes beam grow faster than the less Gaussian-like components of the Stokes beam. Through the process of beam cleanup, a multimode pump beam is converted into a near-singlemode Stokes beam. As will be shown in this document, the SRS beam cleanup process requires the use of a graded-index fiber; beam cleanup does not occur in step-index fibers. Through SRS beam cleanup in a graded-index fiber it is possible for an RFL to create the right wavelength on the right platform with good beam quality.

It should be noted that experimental observations of unseeded SRS have demonstrated dramatic improvement in the beam quality of the output Stokes beam relative to the beam quality of the input pump beam [17,18,19,20,21]. This has led at least one author to suggest the output beam of a Raman fiber amplifier (RFA) will be nearly diffraction-limited regardless of the beam quality of the input seed source [22]. This document examines the beam quality of the Stokes output of an RFA based on a graded-index fiber and shows that the beam quality of the output Stokes beam depends on the beam quality of the input Stokes seed. The original research presented in this document shows that an RFA based on a multimode graded-index fiber can have relatively high optical-to-optical efficiency (25%) with 9 dB of gain.

7

The telecommunications industry is very interested in developing fiber amplifiers which can boost a transmitted signal and thereby improve the signal-to-noise ratio. While much of the research in optical communications has focused on fiber amplifiers doped with Erbium, Ytterbium or other materials, there has been significant interest in the development of the RFA. Like RFLs, RFAs have traditionally been based on singlemode fibers. RFAs offer two main advantages over their doped fiber counterparts.

First, the RFA provides wavelength flexibility because significant gain occurs at a wavelength which is shifted from the pump wavelength. The magnitude of the change in wavelength is determined by the Stokes shift of the material. By carefully choosing and/or tailoring the Stokes shift of the gain medium, it is possible to use RFAs to amplify input beams at almost any wavelength, provided an appropriate pump source is available. For this same reason, the communications industry has been interested in the development of the RFL as a means to generate novel pump wavelengths.

The second advantage of the RFA is its very wide gain bandwidth. The bandwidth of SRS is about 30 nm in a fused silica fiber which is pumped at 1450 nm [23]. However, if an RFA is pumped with two lasers of different wavelengths, the gain bandwidth the two respective Stokes shifts can overlap, potentially doubling the overall gain bandwidth of the RFA. Using multiple pump lasers can make the gain bandwidth of an RFA very broad [24]. A broad gain bandwidth means that a single RFA can be used to pump multiple signals in a wavelength multiplexing scheme. By contrast, the Erbium-doped fiber amplifier only has a typical gain bandwidth of 30 nm.

Another option for power scaling the Stokes output of RFLs and RFAs is beam combination, a process in which multiple pump beams are used to generate a single

Stokes beam. While SRS beam combination has been demonstrated in bulk media, its development in fibers has been limited by the difficulty of reaching the SRS threshold [25]. This document describes two methods of SRS fiber beam combination which effectively lowered the SRS threshold and allowed the SRS fiber beam combination of two continuous-wave (CW) pump beams. The first of these beam combination methods used a Stokes seed to lower the effective SRS threshold, while the second beam combination method used an RFL to lower the effective Stokes threshold.

1.3. Overview

The research described in this dissertation focused on developing Raman fiber devices based on 50 μm graded-index fibers. RFLs and RFAs were constructed and characterized in terms of the power, the beam quality and the spectral properties of the output Stokes beam. The efficiency of these devices was characterized by examining the output Stokes power as a function of the coupled pump power. The spectrum of the output Stokes beam was examined to determine if the Raman fiber device produced any higher Stokes orders. The original research presented in this document showed that the onset of a Stokes cascade generated by an RFA using a backward stimulated Raman scattering (BSRS) geometry was delayed relative to the onset of the Stokes cascade generated by an RFA using a forward stimulated Raman scattering (FSRS) geometry.

Both RFLs and RFAs based on graded-index fibers were examined in terms of the beam quality of the generated Stokes output. The beam quality of the Stokes output of an RFL was shown to be a function of the output Stokes power of the RFL as well as a function of the reflectivity of the FBGs used to construct the RFL. Higher Stokes powers as well as higher reflectivity of the output coupler corresponded to worse beam quality of

9

the Stokes beam. In the case of an RFA, the beam quality of the output Stokes beam was a function of the beam quality of the input seed beam.

A computer model was developed to explain the beam quality of the Stokes output generated by unseeded SRS. Unseeded SRS beam cleanup was examined by determining the fiber mode with largest Raman gain given a large number of random mode configurations of the input pump beam. The gain of the Stokes modes of a notional graded-index fiber and the gain of the Stokes modes of a notional step-index fiber were examined. In the graded-index fiber, the lower-order transverse Stokes modes exhibited greater gain than the higher-order transverse Stokes modes. This was not true of the step-index fiber, which explains why beam cleanup is confined to graded-index fibers.

The beam quality of the Stokes output of an RFA based on a graded-index fiber was also theoretically examined. This was done by numerically solving the coupled differential equations describing the interaction of the various pump and Stokes modes of the fiber. The modal distribution of the output Stokes beam was calculated for different configurations of the input pump beam and input seed beam. The modal distribution of the input and the output were compared in terms of the beam quality factor, M^2, for a large number of different launching conditions. This numerical model demonstrated that the beam quality of both the input pump beam and the input seed beam determined the beam quality of the Stokes output of an RFA based on a graded-index multimode fiber.

This research also examined two methods for the SRS beam combination of two independent CW laser beams. Two pump beams were first polarized and then overlapped using a common polarizing beamsplitter (PBS). These two overlapped beams were then combined to generate a single Stokes beam via SRS in an RFA. In a separate, but related

10

experiment, these overlapped pump beams were combined to generate a single Stokes beam via SRS in an RFL. In the case of the RFA beam combiner, both the FSRS geometry and the BSRS geometry were considered. The RFL beam combiner proved to be highly efficient; this demonstrated that using an RFL is a practical method of SRS beam combination.

1.4. Document Highlights and Organization

This document presents original research, the highlights of which include:

1. The SRS beam combination of two independent CW laser beams using an RFL based on a 50 μm multimode graded-index fiber.

2. The experimental development and characterization of an RFA based on a 50 μm multimode graded-index fiber.

3. The modeling of unseeded SRS beam cleanup in a 50 μm multimode graded-index fiber.

4. The absence of beam cleanup in a step-index fiber is explained.

5. The modeling of the beam quality of the Stokes output of an RFA based on a 50 μm multimode graded-index fiber.

6. The optimization and characterization of moderate power RFLs based on a 50 μm graded-index fiber.

7. The SRS beam combination of two independent CW pump beams using an RFA based on a 50 μm graded-index fiber.

8. The demonstration of beam cleanup in a 50 μm multimode graded-index fiber pumped by a CW laser.

11

9. The examination of an RFL based on a multimode graded-index fiber which used a dichroic mirror as an output coupler.

Chapter 2 of this document presents the background material useful for understanding the operation of Raman fiber devices based on multimode graded-index fibers. Chapter 3 describes the fiber modes associated with multimode fibers. This serves to introduce the numerical models of beam cleanup presented in Chapter 4. One model examines beam cleanup in both graded-index and step-index fibers. A model of the beam quality of the output of an RFA based on a graded-index fiber is also considered. Chapter 5 describes experiments which examined the performance of an RFA based on a graded-index fiber in terms of the beam quality, the gain and the spectral content of the output. Both the BSRS and the FSRS geometries of an RFA are considered. Chapter 6 examines the utility of using an RFA as a method for the SRS fiber beam combination of two independent CW pump beams.

Chapter 7 examines the performance of RFLs based on graded-index fibers. This chapter discusses the performance of an RFL based on a graded-index fiber. The power and the beam quality of the output Stokes beams are examined. An RFL is shown to be a practical device for SRS fiber beam combination. Chapter 8 discusses the performance of an RFL based on a graded-index fiber which uses dichroic mirrors in place of FBGs.

Chapter 9 summarizes the conclusions of this research and details the technical contributions of this work. Chapter 9 also provides suggestions for future research, including the direct diode pumping of Raman fiber devices based on graded-index fibers. The use of novel fiber materials and novel FBG configurations is also considered, as are cascaded RFLs based on multimode graded-index fibers.

12

2. Theoretical Background

2.1. Nonlinear Optics

In conceptual terms, nonlinear optics can be understood by examining the effect of an electromagnetic wave on an optical medium consisting of positively charged nuclei surrounded by a collection of negative electric charges. In a conductor many of these negative charges are free to roam through the material. In an insulator the negative charges are more tightly bound to their parent nuclei. The presence of a sufficient electric field displaces these bound charges, creating an electric dipole. An oscillating electric field induces oscillating dipoles which serve as the source of a generated electromagnetic wave. Resulting electric fields which constructively interfere with one another are said to be phase-matched.

The behavior of electromagnetic waves in matter is more precisely described by Maxwell's equations, which can be expressed in differential form in MKS units as

$$\nabla \bullet \vec{D} = \rho_f \tag{1}$$

$$\nabla \bullet \vec{B} = 0 \tag{2}$$

$$\nabla \times \vec{E} = -\frac{\partial \vec{B}}{\partial t} \tag{3}$$

$$\nabla \times \vec{H} = \vec{J}_f + \frac{\partial \vec{D}}{\partial t} \tag{4}$$

In the above equations, $\vec{D}$ represents the electric displacement field, $\vec{E}$ represents the electric field, $\vec{B}$ represents the magnetic induction, $\vec{H}$ represents the magnetic field, $\vec{J}_f$ represents the free current density and ρ_f represents the free charge density [26]. In a non-magnetic medium ($\mu = \mu_0$), the magnetic induction is related to the magnetic field

13

according to $\vec{B} = \mu_0 \vec{H}$, where μ_0 is the magnetic permeability of free space. The electric

displacement field can be expressed in terms of the electric field and the induced

polarization $\vec{P}$ according to

$$\vec{D} = \varepsilon_0 \vec{E} + \vec{P} \qquad (5)$$

where ε_0 is the electric permittivity of free space.

These equations can be used to derive the wave equation by first taking the curl of

both sides of Eq. (3). The left hand side of the resulting equation can be simplified using

the following identity

$$\nabla \times (\nabla \times \vec{E}) = \nabla(\nabla \cdot \vec{E}) - \nabla^2 \vec{E} \qquad (6)$$

and assuming the free charge density to be zero. The right hand side of the resulting

equation can be simplified by recalling the relationship between the magnetic induction

and the magnetic field in free space and invoking Eq. (4). The free current density is

assumed to zero. Using equation (5) and noting that although the divergence of the

electric field is not identically zero, it is nearly so [27], the wave equation for a dielectric

medium then takes the following form

$$\nabla^2 \vec{E} - \mu_0 \varepsilon_0 \frac{\partial^2 \vec{E}}{\partial t^2} = \mu_0 \frac{\partial \vec{P}^2}{\partial t^2} \qquad (7)$$

The electric field can also be used in conjunction with the susceptibility tensors

$\chi^{(n)}$ to define the induced polarization as follows

$$\vec{P} = \varepsilon_0 (\chi^{(1)} \cdot \vec{E} + \chi^{(2)} : \vec{E}\vec{E} + \chi^{(3)} : \vec{E}\vec{E}\vec{E} + ...) \qquad (8)$$

The order of each susceptibility tensor is denoted by the superscript n. The first order

susceptibility tensor $\chi^{(1)}$ is associated with several of the linear properties of a material,

including the index of refraction and absorption. The second order non-linear

14

susceptibility tensor $\chi^{(2)}$ is associated with the Pockels effect, second harmonic generation, parametric mixing and parametric amplification. The third order nonlinear susceptibility tensor $\chi^{(3)}$ is connected to many other optical phenomena, including SRS, stimulated Brillioun scattering (SBS), and four wave mixing (FWM).

2.2. Raman Process

2.2.1. Raman Scattering

The quantum-electrodynamic explanation of Raman scattering is diagrammed in Figure 2. A pump photon of frequency ω_p is annihilated and a molecule makes a transition from a real ground state $|g\rangle$ to a virtual excited state $|h\rangle$. The virtual excited state $|h\rangle$ is actually a superposition of the possible eigenstates of the molecule. A Stokes photon with a frequency ω_s is created and the molecule transitions from the virtual excited state $|h\rangle$ to a real vibrationally excited state $|f\rangle$. The energy of the vibtrationally excited state is associated with an optical phonon.

An equivalent explanation states that a Stokes photon is created and the molecule transitions from the ground state $|g\rangle$ to a virtual excited state $|h\rangle$. The pump photon is annihilated and the molecule transitions from the virtual excited state $|h\rangle$ to the vibrationally excited state $|f\rangle$. In either case, due to the indeterminate energy of the virtual excited state, the uncertainty principal dictates that the Raman scattering process proceeds near-instantaneously.

These various transitions can be used to describe the non-linear susceptibility associated with SRS according to [28]

15

$$\chi^{(3)}(-\omega_s;\omega_p,-\omega_p,\omega_s) = \frac{Ne^4}{6\hbar^3\varepsilon_0(\Omega_{fg}+i\Gamma_{fg}-\omega p+\omega s)}$$

$$\sum_{bd}\left[\frac{\vec{e}_p^*\cdot\vec{r}_{gb}\vec{e}_s\cdot\vec{r}_{bf}\vec{e}_s^*\cdot\vec{r}_{fd}\vec{e}_p\cdot\vec{r}_{dg}}{(\Omega_{bg}-\omega_p)(\Omega_{dg}-\omega_p)}+\frac{\vec{e}_s\cdot\vec{r}_{gb}\vec{e}_p^*\cdot\vec{r}_{bf}\vec{e}_s^*\vec{r}_{fd}\vec{e}_p\cdot\vec{r}_{dg}}{(\Omega_{bg}+\omega_s)(\Omega_{dg}-\omega_{p)}}+\frac{\vec{e}_p^*\cdot\vec{r}_{gb}\vec{e}_s\cdot\vec{r}_{bf}\vec{e}_p\cdot\vec{r}_{fd}\vec{e}_s^*\cdot\vec{r}_{dg}}{(\Omega_{bg}-\omega_p)(\Omega_{dg}+\omega_s)}+\frac{\vec{e}_s\cdot\vec{r}_{gb}\vec{e}_p^*\cdot\vec{r}_{bf}\vec{e}_p\cdot\vec{r}_{fd}\vec{e}_s^*\cdot\vec{r}_{dg}}{(\Omega_{bg}+\omega_s)(\Omega_{dg}+\omega_s)}\right] \quad (9)$$

where N is the number density of molecules, $\rho_0(a)$ is the density matrix of the state labeled a, $\vec{e}\cdot\vec{r}$ represents the dipole moment operator and where the damping factor is represented by Γ. The subscripts b,d,f,g represent the states of the molecule.

The Stokes photon has a frequency defined by

$$\omega_s = \omega_p - \Omega \quad (10)$$

where Ω is the vibrational frequency of the material.
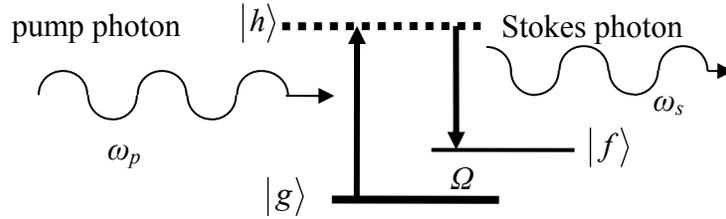
Figure 2. Energy diagram showing the generation of a Stokes photon.

The creation of an anti-Stokes photon is depicted in Figure 3. In this case, the vibrationally excited state $|f\rangle$ is populated by molecules which are vibrationally excited relative to the ground state $|g\rangle$. An incident pump photon is annihilated and the molecule transitions from the vibrationally excited state $|f\rangle$ to the virtual excited state $|h\rangle$. An anti-Stokes photon is created and the molecule undergoes a radiative transition to the ground state $|g\rangle$. Again, an equivalent explanation associates the creation of the anti-

16

Stokes photon with the transition from of the molecule from the real excited state $|f\rangle$ to the virtual excited state $|h\rangle$ while associating the annihilation of the pump photon with the transition from the virtual excited state $|h\rangle$ to the real ground state $|g\rangle$. The frequency of the anti-Stokes photon is given by

$$\omega_{as} = \omega_p + \Omega \qquad (11)$$

If the system is in thermal equilibrium, the population of $|f\rangle$ is smaller than the population of $|g\rangle$ by the Boltzmann factor of $\exp(-\hbar\Omega/k_B T)$. As a result the intensity of anti-Stokes lines are typically orders of magnitude smaller than the intensity of the associated Stokes lines.
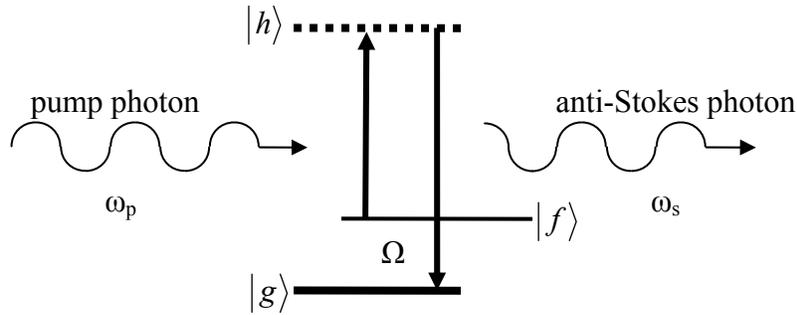
Figure 3. Energy diagram showing the generation of an anti-Stokes photon.

Experimental observations of Raman scattering were first made by Raman and Krishnan in 1928 [29,30]. To produce the strong illumination necessary to observe the Raman effect, sunlight was focused onto samples of 60 different liquids and several gases via a telescope. All of the samples tested showed some degree of Raman scattering. The downshifted frequencies are called the Stokes component; upshifted frequencies are called the anti-Stokes component.

Boyd explained the relationship between stimulated Raman scattering and spontaneous Raman scattering by considering the average number of photons in a given radiation mode, a quantity known as the photon occupation number [31]. The radiation modes are the pump and Stokes modes of an ideal rectangular cavity. Using these photon occupation numbers, the probability of a pump mode scattering into a given Stokes mode per unit time is postulated as

$$P_s = Dm_p(m_s + 1) \tag{12}$$

where m_p is the average number of photons in each pump mode and m_s is the average number of photons in each Stokes mode. D is a constant of proportionality. The first term on the right hand side of Eq. (12) represents the contribution of stimulated Raman scattering, while the second term represents the contribution of spontaneous Raman scattering. P_s in Eq. (12) can be considered as the time rate of change of the average number of photons in a single Stokes mode. Therefore,

$$\frac{dm_s}{dt} = Dm_p(m_s + 1) \tag{13}$$

After a change of variables using the relationship $dz/dt=c/n$, this expression takes the form

$$\frac{dm_s}{dz} = \frac{n}{c}Dm_p(m_s + 1) \tag{14}$$

In the regime of spontaneous scattering where $m_s \ll 1$, the solution to Eq. (14) is

$$m_s(z) = m_s(0) + \frac{n}{c}Dm_p z \tag{15}$$

where $m_s(0)$ is the number of Stokes photons at $z=0$. In the regime of stimulated scattering when $m_s \gg 1$, the solution to Eq. (14) becomes

18

$$m_s(z) = m_s(0)e^{Gz} \qquad (16)$$

where the Raman gain coefficient is defined by

$$G = \frac{nDm_p}{c} \qquad (17)$$

The value of the proportionality constant D can be determined by first recognizing that the generation of a single Stokes photon requires the annihilation of a pump photon. A pump photon however, can generate a Stokes photon in any available Stokes mode of the cavity. The change in the number of pump photons in the system is therefore equal to the total number of Stokes photons generated in all of the Stokes modes of the system. The number of Stokes modes available to the cavity is given by [31]

$$M = \frac{V\omega_s^2 \Delta\omega n^3}{\pi^2 c^3} \qquad (18)$$

where V is the volume of the ideal cavity, ω_s is the angular frequency of a given mode and $\Delta\omega$ is the linewidth of the scattered radiation. The index of refraction in this cavity is denoted by n.

The scattering of pump photons into the various Stokes modes of the cavity isn't necessarily uniform, but can have angular dependence $b(\theta,\varphi)$, where θ and φ denote the radial angle and azimuthal angle of the radiation. By considering the non-uniform scattering of a pump mode into the various Stokes modes of the cavity, the depletion of this pump mode is given by

$$\frac{dm_p}{dz} = -\frac{n}{c}Dm_p Mb(\theta,\varphi) \qquad (19)$$

The depletion rate of pump photons can also be expressed in terms of the scattering cross section of the medium, σ, according to

19

$$\frac{dm_p}{dz} = -N\sigma m_p \qquad (20)$$

where N is the number density of molecules in the gain medium. By comparing Eq. (19) and Eq. (20), it is easy to see that the proportionality constant D can be expressed as

$$D = \frac{N\sigma c}{nMb(\theta,\varphi)} \qquad (21)$$

Using this expression for the proportionality constant, along with Eq. (18), the Raman gain coefficient defined in Eq. (17) can be expressed as

$$G = \frac{N\pi^2 c^3 m_p}{V\omega_s^2 b(\theta,\varphi)n^3}\left(\frac{\partial\sigma}{\partial\omega}\right)_0 \qquad (22)$$

where the gain cross section has been expressed in terms of its center value and linewidth according to $\sigma = \left(\dfrac{\partial\sigma}{\partial\omega}\right)_0 \Delta\omega$.

Initially, Stokes photons are generated via spontaneous Raman scattering, which in forward SRS has been shown to be equivalent to injecting one Stokes photon per transverse and longitudinal mode into the fiber at z=0 [32]. Given sufficient intensity, these photons begin to further stimulate the Raman process, giving rise to SRS.

Classically, SRS can be ascribed to the polarizability of a medium by considering how an electric field acts on the molecules in the Raman gain medium [31,33]. Consider the combined electric fields of the pump wave and the Stokes wave of the fiber

$$\begin{aligned}\vec{E} &= A_p(z)\exp(i\vec{k}_p\cdot\hat{z} - i\omega_p t)\hat{e}_p \\ &+ A_s(z)\exp(i\vec{k}_s\cdot\hat{z} - i\omega_s t)\hat{e}_s + c.c.\end{aligned} \qquad (23)$$

where $A(z)$, $\vec{k}$, ω, $\hat{e}$ respectively represent the amplitude, wave vector, frequency and the polarization unit vector of the electric field. The pump and Stokes components are

20

denoted by the subscripts *p* and *s* respectively. While not particularly important to deriving the polarizability of the medium, the *z*-dependence of the amplitude of the electric field will become important in describing the interaction of the pump and Stokes beams in Chapter 4 and will be explicitly stated in the remainder of the derivation. In order to avoid cumbersome notation however, the *z*-dependence of other variables will not be explicitly stated in the remainder of the derivation.

The force exerted by an electric field can be determined by considering the energy required to establish an oscillating dipole, which is given by $W = \frac{1}{2}\alpha\langle \bar{E}^2 \rangle$, where the brackets denote the time average [31]. The force can be expressed as $\bar{F} = \frac{dW}{dq}$, which means that the electric field exerts a force on a degree of freedom of the molecule is equal to

$$\bar{F} = \frac{1}{2}\left(\frac{d\alpha}{dq}\right)_0 \left\langle \left|\bar{E}(t)\right|^2 \right\rangle \hat{u} \qquad (24)$$

where $\hat{u}$ is a unit vector and α is the polarizability of the molecule. The quantity q denotes the displacement of the atoms in the molecule from their equilibrium separation distance, $q_0(\Omega)$, where Ω is the difference between the pump and Stokes frequencies. The force exerted on the molecule is related to its displacement by

$$\left(\frac{d^2q}{dt^2} + 2\gamma_p\frac{dq}{dt} + \omega_v^2 q\right)\hat{u} = \frac{\bar{F}(t)}{m} \qquad (25)$$

where γ_p is a damping term, ω_v is the resonance frequency of the molecule and *m* is the effective mass of the molecule. The resulting displacement of the molecule is given by

$$q = q_0(\Omega)\exp[i(\bar{k}_p - \bar{k}_s)\cdot\hat{z} - \Omega t] + c.c. \qquad (26)$$

The magnitude of the displacement can be shown to be [31]

$$q_0(\Omega) = \frac{(d\alpha/dq)_0 A_p(z) A_s{}^*(z)}{m(\omega_v^2 - \Omega^2 - 2i\Omega\gamma_p)} \qquad (27)$$

In this case, the magnitude of the induced polarization is given by

$$\vec{P} = N\left[\alpha_0 + \left(\frac{d\alpha}{dq}\right)_0 q\right]\vec{E} \qquad (28)$$

where N is the number density of molecules in the medium. The symbol α_0 denotes the polarizability of the molecule when the atoms of the molecule are at their equilibrium separation distance. Substituting Eqs. (26) and (27) into Eq. (28) and keeping only the nonlinear term oscillating at ω_s, the amplitude of Stokes polarization can be defined as

$$\left|\vec{P}^{NL}\right| = \frac{N(\partial\alpha/\partial q)_0^2 |A_p|^2 A_s \exp[i(\vec{k}_s \cdot \hat{z})]}{m(\omega_v^2 - \Omega^2 + 2i\Omega\gamma_p)} \qquad (29)$$

By defining the Raman susceptibility as

$$\chi_{SRS}^{(3)}(\omega_p, -\omega_p, \omega_s) \equiv \frac{1}{6m}\frac{N(\partial\alpha/\partial q)_0^2}{[\omega_v^2 - (\omega_p - \omega_s)^2 + 2i(\omega_p - \omega_s)\gamma_p]} \qquad (30)$$

the amplitude of the nonlinear component of the polarization can be expressed as

$$\vec{P}^{NL} = 6\chi_{SRS}^{(3)}(\omega_p, -\omega_p, \omega_s)|A_p|^2 A_s \exp[i(\vec{k}_s \cdot \hat{z})] \qquad (31)$$

The growth of the amplitude of the Stokes wave in a fiber can be derived from the wave Eq. (7). The right hand side of the equation can be expressed in terms of the induced polarization given by Eq. (8) and is simplified by recalling that in an isotropic medium, $\chi^{(2)}=0$. The left hand side of the wave equation is simplified by invoking the slowly varying envelope approximation. Using the form of the electric field given by Eq.

22

(23) and by grouping terms which oscillate at like frequencies, the growth in the amplitude of the pump and Stokes waves can be shown to be governed by

$$\frac{n_{p,s}\omega_{p,s}}{c}\left(A_{p,s}^{*}\frac{\partial A_{p,s}}{\partial z}+A_{p,s}\frac{\partial A_{p,s}^{*}}{\partial z}\right)=6\varepsilon_{0}\mu_{0}\omega_{p,s}^{2}\times$$
$$\left|A_{s,p}\right|^{2}\left|A_{p,s}\right|^{2}\text{Im}[\chi_{SRS}^{(3)}(\omega_{s,p},-\omega_{s,p},\omega_{p,s})] \qquad (32)$$
$$-\left|A_{p,s}\right|^{2}\varepsilon_{0}\mu_{0}\omega_{p,s}^{2}\text{Im}[\chi^{(1)}(\omega_{p,s})]$$

It is useful to consider the relationship between intensity and the field amplitude

$$I_{p,s}=2\varepsilon_{0}cn\left|A_{s,p}\right|^{2} \qquad (33)$$

It should also be noted that [34]

$$\text{Im}[\chi_{SRS}^{(3)}(\omega_{p},-\omega_{p},\omega_{s})]=-\text{Im}[\chi_{SRS}^{(3)}(\omega_{s},-\omega_{s},\omega_{p})] \qquad (34)$$

Furthermore, by considering the relationship between the 1st order susceptibility and absorption (denoted by α_s) and also recalling the relationship between the 3rd order susceptibility and the Raman gain coefficient [34]

$$\alpha_{p,s}=\frac{\omega_{p,s}}{n_{p,s}c}\text{Im}[\chi^{(1)}(\omega_{p,s})] \qquad (35)$$

$$g_{R}=\frac{-3\omega_{s}}{\varepsilon_{0}c^{2}n_{s}n_{p}}\text{Im}[\chi_{SRS}^{(3)}(\omega_{p},-\omega_{p},\omega_{s})] \qquad (36)$$

the interaction of the pump beam and the Stokes beam is given by

$$\frac{dI_{s}}{dz}=g_{R}I_{p}I_{s}-\alpha_{s}I_{s} \qquad (37)$$

and

$$\frac{dI_{p}}{dz}=-\frac{\omega_{p}}{\omega_{s}}g_{R}I_{p}I_{s}-\alpha_{p}I_{p} \qquad (38)$$

In this equation, I_s is the intensity of the Stokes wave and I_p is the intensity of the pump beam. The Raman gain coefficient is denoted by g_R. In the simple case when the pump is assumed to be undepleted by the growth of the Stokes component (i.e., when the pump is only depleted by attenuation), the power in the Stokes component is given by

$$I_s(L) = I_s(0)\exp[g_R I_s(0)L_{eff} - \alpha_s L] \qquad (39)$$

where the effective length of the fiber is defined as

$$L_{eff} = \frac{1 - \exp[-\alpha_p L]}{\alpha_p} \qquad (40)$$

where α_p is the absorption coefficient of the pump.

2.2.2. Raman Gain

As discussed in the previous section, Raman scattering shifts light from the input pump wavelength to the output Stokes wavelength. One measure of the strength of this scattering process is the Raman gain coefficient, g_R. The relationship between G and g_R can be understood by considering that G gives the Raman gain per unit length. On the other hand, g_R is given in terms of the Raman gain per unit length per unit power.

In many materials, the Raman gain is significant only for a limited number of discrete bands. One example is the Raman gain spectrum of sulfur, which is shown in Figure 4. On the other hand, in an amorphous solid such as fused silica, discrete bands broaden and overlap to form the Raman gain spectrum shown in Figure 5. The Raman gain spectrum of every material is unique, making Raman spectroscopy possible.

$\chi^{(3)}$, and hence the Raman gain of a material are dependent on ω_p and ω_s. This can be seen by examining Figure 4 and Figure 5 which show that the Raman gain has a strong dependence on the Stokes shift and is properly denoted as $g_R(\Omega)$ [35,36]. To

24

understand the consequence of the functional form of $g_R(\Omega)$, consider a pump beam incident on fused silica. Spontaneous Raman scattering produces photons across a broad range of Stokes wavelengths. Through SRS, these photons are amplified across the entire bandwidth of the Raman gain spectrum. The Stokes wave grows fastest however, at the wavelength with the maximum gain. In pure fused silica, the maximum gain and hence the maximum Stokes production occurs when input pump is shifted by 12.6 THz.
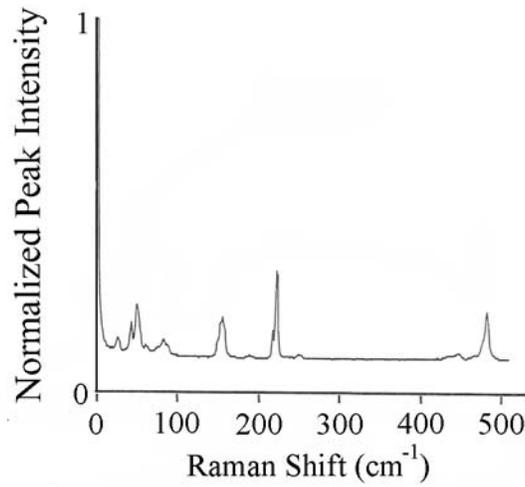
Figure 4. The Raman spectrum of sulfur, normalized to the peak intensity of the input probe beam [33].

The Raman gain of a fiber can also be affected by doping. For example the addition of the dopant GeO_2 changes the relative index difference, Δ, between the index of refraction of the core and the index of refraction of the cladding of the fiber. This difference can be tailored by altering the level of doping in the fiber. In a step-index fiber, the Raman gain coefficient is linearly proportional to the relative index difference induced by the doping according to [37]

$$g_R(12.9THz) \approx 2.75\times10^{-14} + 2.16\times10^{-14}|\Delta| \text{ m/W} \quad (41)$$

25

The relative index difference is typically less than 1%. It should be noted that Eq. (41) has been shown to be valid for graded-index fibers with an arbitrary index profile in which Δ is not uniform across the core of the fiber.
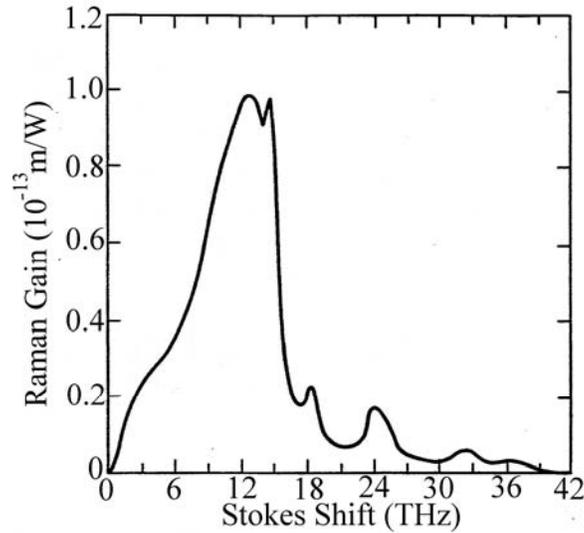
Figure 5. Raman gain of fused silica as a function of the frequency shift [34].

The Raman gain coefficient changes as new chemical bonds are formed by the introduction of the dopant. Vitreous SiO_2 consists of a collection SiO_4 tetrahedrons. The oxygen atom in a corner of one tetrahedron sometimes serves as the corner of an adjacent tetrahedron, an arrangement known as corner-sharing. The silicon atom at the center of two adjacent tetrahedrons along with the oxygen atom in the shared corner forms a bond which is denoted by Si-O-Si. The 440 cm^{-1} Stokes shift of fused silica is formed by the motion of the oxygen atom of this bond [38,39].

Doping with GeO_2 introduces GeO_4 tetrahedra into the vitreous fiber core. GeO_4 tetrahedrons share corners with other GeO_4 tetrahedrons or with adjacent SiO_4 tetrahedrons, resulting in Ge-O-Ge bonds and Si-O-Ge bonds respectively. Vibrations in the former produce a Stokes shift of 416 cm^{-1}, while stretching vibrations in the latter produce a relatively broad Stokes band ranging from 978-1010 cm^{-1} [38]. At low levels

26

of GeO$_2$ doping, Si-O-Ge bonds are much more common than Ge-O-Ge bonds. As the vibrational modes of Si-O-Si, Ge-O-Ge and Si-O-Ge are coupled, the addition of GeO$_2$ dopant alters the form of the Raman gain spectrum by decreasing the strength of certain peaks (particularly those at 485 cm^{-1} and 600 cm^{-1}) and by causing the growth of additional peaks at 675 cm^{-1} and 1000 cm^{-1} [38,39].

2.2.3. Stimulated Raman Threshold

When the overall gain of the fiber exceeds the propagation losses of the fiber , the Stokes beam can initially grow exponentially at the wavelength associated with the peak Raman gain. The threshold condition of an oscillator is when the product of the cavity gain and the cavity losses is unity, i.e.,

$$1 = \exp[2gP_pL_{eff}]R_1R_2\exp[-2\alpha_sL] \qquad (42)$$

In this equation, the first term on the right hand side represents the Raman gain. R_1 and R_2 correspond to the reflectance at each end of the laser cavity. The exponential term corresponds to the round trip cavity absorption losses where α_s is the absorption loss per unit length of the fiber at the Stokes wavelength and L is the length of the fiber. P_p is the input pump power an g is the Raman gain per unit area. The effective area of the fiber is expressed in terms of the mode field radius, ω_0 as

$$A_{eff} = \pi\omega_0^2 \qquad (43)$$

The radius of a multimode beam depends on the exact modes which make up that beam. However, calculating the mode field radius of the fundamental mode provides a lower bound on the radius of a multimode beam. The mode field radius of the fundamental mode of a graded-index fiber can be approximated by [40]

27

$$\omega_0 \approx a\left(\sqrt{\frac{2}{V}} + \frac{0.37}{V^{1.5}} + \frac{26.9}{V^6}\right) \qquad (44)$$

where a is the physical radius of the fiber core and V is the fiber V parameter or V-number, which is defined as

$$V = ak_0NA \qquad (45)$$

where k_0 is the wave number of the pump beam and NA is the numerical aperture of the fiber. Calculating the pump threshold necessary to produce a Stokes beam in an singlemode oscillator through SRS is straightforward by using Eqs. (42)-(45). Calculating the SRS threshold in a multimode fiber is more complicated due to the challenge of precisely defining the radius of the beam.

For a single-pass configuration, the threshold condition of the forward Stokes beam is given by Smith to be the pump power above which stimulated effects must be considered [32]. A good approximation of the threshold pump power can be obtained by invoking the undepleted pump approximation, integrating the resulting solution to Eqs. (37) and (38) over the entire Raman gain bandwidth and assuming the gain curve to be Lorentzian in shape. The single-pass SRS threshold is then given by [32]

$$P_{th} = \frac{16A_{eff}}{g_R L_{eff}} \qquad (46)$$

The threshold condition for the backward Stokes beam is calculated the same way, except that the sign of the left hand side of Eq. (38) is reversed. The resulting pump threshold for the backward Stokes beam is similar to the threshold of the forward Stokes beam given in Eq. (46), except that the factor of 16 becomes a factor of 20 [32].

Smith also showed that in the FSRS geometry, spontaneous Raman scattering can be considered to be a seed consisting of a single fictitious photon per longitudinal and

transverse mode which is injected into the front end of the fiber [32]. In the BSRS geometry, spontaneous Raman scattering can be considered to be a backwards propagating seed consisting of a single photon per mode injected into the fiber at the location where the accumulated attenuation losses equals the Raman gain [32].

These calculations assume that the Stokes wave and the pump wave are in step, which occurs when the fiber maintains the polarization of the wave. It has been shown for SBS that gain occurs only insofar as the polarization of the Stokes component is the same as the polarization of the pump component [41]. When the polarization of the pump component is completely orthogonal to the polarization of the Stokes component, the SBS gain is zero. Similar arguments can be made for polarization with regard to SRS [36].

2.3. Four Wave Mixing

Like SRS and SBS, FWM is a parametric nonlinear $\chi^{(3)}$ process in which three photons interact to form a photon at a fourth frequency, according to

$$\omega_1 + \omega_2 - \omega_3 = \omega_4 \qquad (47)$$

FWM affects the SRS process when the photon generated at ω_4 falls within the Raman gain bandwidth. In this case, FWM essentially creates a seed at ω_4, a seed which is subsequently amplified by the SRS process.

FWM can be described in terms of nonlinear polarization using the same approach that was used to derive Eq. (31). In the case when $\omega_1 = \omega_2$, the terms oscillating at $2\omega_1 - \omega_3$ are collected; the resulting nonlinear polarization term takes the form [31]

$$\vec{P}^{NL} = 3\chi_{FWM}^{(3)}(\omega_1, \omega_1, -\omega_3) A_1 A_2 A_3^* \times$$
$$\exp[(2\vec{k}_1 - \vec{k}_3) \cdot \hat{z}] \qquad (48)$$

where

$$\chi_{FWM}^{(3)}(\omega_1, \omega_1, -\omega_3) \equiv \frac{1}{3m} \frac{N(\partial \alpha / \partial q)_0^2}{[\omega_v^2 - (\omega_1 - \omega_3)^2 + 2i(\omega_1 - \omega_4)\gamma_p]} \quad (49)$$

Unlike SRS and SBS, which are self-phase-matched processes, FWM is associated with the following generalized phase-matching condition

$$\vec{k}_1 + \vec{k}_2 - \vec{k}_3 = \vec{k}_4 \quad (50)$$

This phase-matching condition is very important in understanding the difference between the spectrum of a forward propagating Stokes beam and the spectrum of a backward propagating Stokes beam generated by an RFA. The phase-matching condition of Eq. (50) can be satisfied for the forward geometry, but not for the backward geometry. This difference is explained and its consequences are discussed in Chapter 5.

3. Transverse Modes of an Optical Fiber

3.1. Introduction

One of the main reasons to study RFLs and RFAs based on multimode fibers is that in a graded-index fiber, a multimode pump beam can be used to create a Stokes beam with good beam quality. This phenomenon, known as beam cleanup, occurs when the LP_{01} Stokes mode of a fiber experiences greater Raman gain than other transverse Stokes modes of the fiber. The magnitude of the Raman gain depends on the product of the intensity of the pump and Stokes beams. Knowing the mathematical form of the modes of a multimode fiber is critical to calculating the intensity of these two beams.

This chapter begins with a derivation of the mathematical form of the modes of a step-index fiber. Similar derivations can be found in the literature [42,43]. After developing a mathematical description of the modes of a step-index fiber, this chapter concludes with a description of the modes of a graded-index fiber.

3.2. Transverse Modes of a Step-Index Fiber

This derivation begins by assuming the fiber is linear and isotropic. The wave equation for a given mode of the fiber is then given by

$$\nabla^2 \vec{E} - \frac{n^2}{c^2} \frac{\partial^2 \vec{E}}{\partial t^2} = 0 \tag{51}$$

Assuming that the electric field has the general form $\vec{E} = \psi(r,\phi,z)\exp(-i\omega t)\hat{e}$, where ψ is the spatial component of the mode being considered. The wave equation gives rise to the Helmholtz equation

$$(\nabla^2 + k^2)\psi(r,\varphi,z) = 0 \tag{52}$$

In cylindrical coordinates, the Helmholtz equation can be expressed as

31

$$\frac{\partial^2 \psi(r,\varphi,z)}{\partial r^2} + \frac{1}{r}\frac{\partial \psi(r,\varphi,z)}{\partial r}\frac{\partial^2 \psi(r,\varphi,z)}{\partial \varphi^2}$$

$$+ \frac{\partial^2 \psi(r,\varphi,z)}{\partial z^2} + n^2 k_0^2 \psi(r,\varphi,z) = 0 \tag{53}$$

where k_0 is the wave number and n is the index of refraction. By assuming solutions will take the form of traveling waves which are propagating in the z direction, the spatial component of the electric field becomes.

$$\psi(r,\varphi,z) = u(r)e^{-il\varphi}e^{i\beta z}, \text{ where } l=0,\pm1,\pm2,\ldots \tag{54}$$

where l is an index labeling the various solutions; this index must be an integer in order for the modes of the fiber to be periodic over φ. The z component of the propagation constant is denoted by β. The first term on the right hand side of Eq. (54), $u(r)$, represents the radial component of the field; the middle term represents the azimuthal component, while the last term represents the longitudinal component of the field. Substituting Eq. (54) into the Eq. (53) provides an equation for the radial component of the field, namely

$$\frac{d^2 u(r)}{dr^2} + \frac{1}{r}\frac{\partial u(r)}{\partial r} + (n^2 k_0^2 - \beta^2 - \frac{l^2}{r^2})u(r) = 0 \tag{55}$$

While this equation is valid both for the core of the fiber and the cladding of the fiber, the index of refraction in these two regions is different. It is useful to define k_T, the transverse propagation constant for the fiber core, as

$$k_T^2 \equiv n_1^2 k_0^2 - \beta^2 \tag{56}$$

where n_1 is the index of the core. It is also useful to define a decay parameter, γ_c, which is related to the index of refraction for the cladding, n_2, according to

$$\gamma_c^2 \equiv \beta^2 - n_2^2 k_0^2 \tag{57}$$

32

Implicit in these two definitions is the fact that

$$a^2 k_T^2 + a^2 \gamma_c^{\;2} = V^2 \qquad (58)$$

where a is the radius of the fiber, V is the V-number of the fiber.

Taking Eq. (55) and multiplying both sides by r^2 gives an equation for the radial component of the mode field in the fiber

$$r^2 \frac{d^2 u(r)}{dr^2} + r \frac{du(r)}{dr} + [r^2 (n^2 k_0^2 - \beta^2) - l^2] u(r) = 0 \qquad (59)$$

Eq. (59) is known as Bessel's equation. The two classes of solutions of Bessel's equation which are applicable to fibers are Bessel functions of the first kind (denoted $J_l(r)$) and modified Bessel functions of the second kind (denoted as $N_l(r)$). The second class of solutions is also known as Weber's functions or Neumann's functions. Both classes of solutions are of order l.

In the cladding region, which is assumed to be infinite, the solutions to Bessel's equation are the modified Bessel functions of the 2nd kind of order l. Bessel functions of the first kind are ruled out as they do not monotonically decrease as r→∞. This means that for an infinite cladding region $r>a$, (where a is the radius of the fiber)

$$u_l(r) \propto N_l(\gamma_c r) \qquad (60)$$

In the core region, the first class of solutions to Bessel's equation are appropriate since the Bessel functions of the first kind are bounded at $r=0$, unlike the Neumann functions which approach ∞ as r→0. This means that for $r<a$

$$u_l(r) \propto J_l(k_T r) \qquad (61)$$

Eq. (61) expresses the radial component of the electromagnetic field in the core of the fiber in terms of the transverse propagation constant. The value of k_T, can be

determined by considering the boundary conditions of the fiber. The simplified approach presented here, known as the weakly-guiding approximation, assumes that the index of the cladding and the core are similar. The assumption of a weakly-guiding fiber ($n_1 \approx n_2$) means that $u(r)$ and its derivative are continuous at $r=a$ such that

$$\frac{(k_T a)J_l'(k_T a)}{J_l(k_T a)} = \frac{(\gamma_c a)N_l'(\gamma_c a)}{N_l(\gamma_c a)} \tag{62}$$

Using the identities

$$J_l'(x) = \pm x J_{l \mp 1}(x) \mp \frac{l J_l(x)}{x} \tag{63}$$

and

$$N_l'(x) = -N_{l \mp 1}(x) \mp l \frac{N_l(x)}{x} \tag{64}$$

and by noting that $J_{-l}(x) = (-1)^l J_l(x)$, Eq. (62) can be expressed as

$$k_T a \frac{J_{l-1}(k_T a)}{J_l(k_T a)} = \pm \gamma_c a \frac{N_{l-1}(\gamma_c a)}{N_l(\gamma_c a)} \tag{65}$$

Eq. (65) can be solved graphically as shown in Figure 6. The multiple intersection points represent the transverse propagation constants of each of the various modes of the fiber. The index m is used to distinguish the various transverse propagation constants corresponding to each azimuthal index l, i.e., k_{lm}. The first intersection point is denoted by k_{01}, the second is k_{02}, etc. These fiber modes are generally described by the LP_{lm} notation, which is used because these modes are linearly polarized. The radial and azimuthal components of the resulting mode fields of the fiber core are a linear combination of the modes defined by Eq. (54) and are given by [42,44]

34

$$\psi_{lm} = \frac{J_l(k_{lm}R)}{J_l(k_{lm}a)}\cos(l\phi) \qquad (66)$$

where $R = r/a$
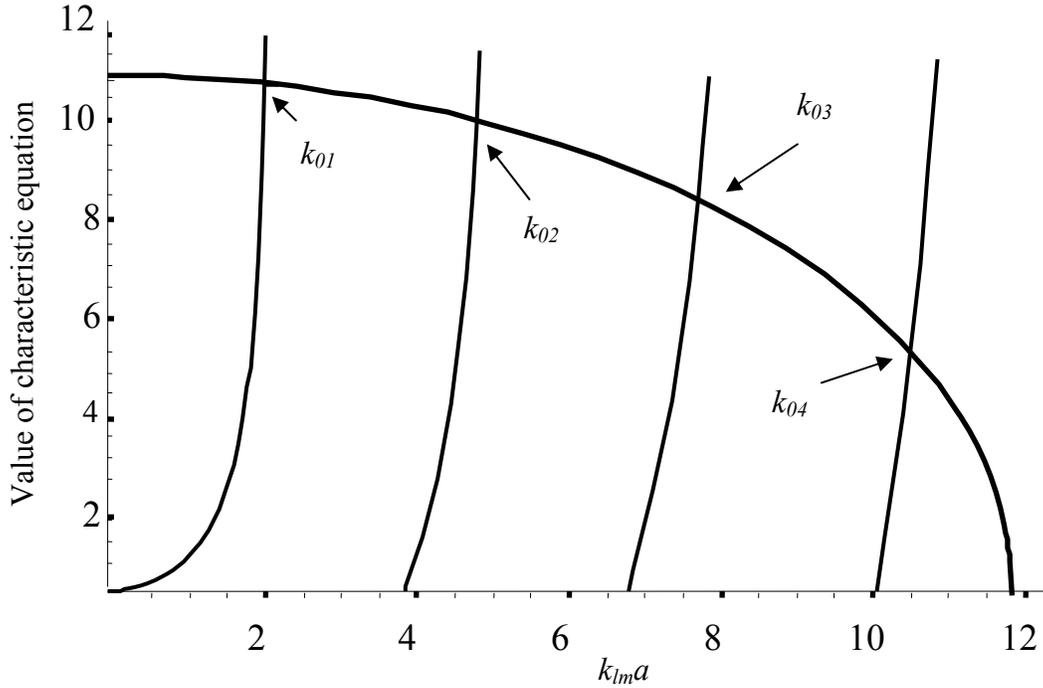
Figure 6. Graphical solutions to the general form of Eq. (65).

The number of modes supported by a fiber is related to the *V*-number. A step-index fiber can support $M \approx \frac{V^2}{2}$ modes. The minimum value of *V* for which a mode can propagate is known as the cutoff value of *V* and is determined by finding the first roots of the radial distribution function $J_{l-1}(k_{lm}a)$. For example, the first root of $J_{-1}(k_{01}a)$ is 0 and the first root of $J_0(k_{11}a)$ is 2.405, meaning that for *V*<2.405, only a single transverse, known as the fundamental or LP_{01} mode is supported by the fiber. In other words, the fiber is singlemode.

35

3.3. Transverse Modes of a Graded-Index Fiber

Having developed a mathematical description of the modes of a step-index fiber in the previous section, this section provides a description of the modes of a graded-index fiber. In a graded-index fiber, the index of refraction is not uniform across the core of the fiber. Instead, the index is highest in the center of the fiber and gradually decreases as a function of radius. Therefore, in the core of a graded-index fiber, Eq. (55) becomes

$$\frac{d^2u(r)}{dr^2} + \frac{1}{r}u(r) + (n^2(r)k_0^2 - \beta^2 - \frac{l^2}{r^2})u(r) = 0 \qquad (67)$$

The exact solution of this equation depends on the exact form of the radial profile of the index of refraction of the fiber core, $n_1(r)$. For simplicity, the index profile can approximated to be infinitely parabolic according to [44]

$$n_1^2(R) = n_1^2(1 - 2\Delta R^2) \qquad (68)$$

where $R=r/a$ and

$$\Delta = \frac{n_1^2 - n_2^2}{2n_1^2} \qquad (69)$$

It should be noted that an infinite parabolic profile is physically unrealizable because as R approaches ∞, $n^2(r)$ approaches $-\infty$. However, in the region of the fiber core, the index profile given by Eq. (68) is reasonable when used in conjunction with the weakly-guiding approximation, $\Delta \ll 1$. Given the index profile of Eq. (68), the modes of the graded-index fiber take the form [44]

$$\psi_{lm} = \cos(l\phi)R^l L_{m-1}^{(l)}(VR^2)\exp(-\frac{1}{2}VR^2) \qquad (70)$$

where $L_{m-1}^{(l)}$ are the associated Laguerre polynomials. Figure 7 depicts the intensity distribution of several of the lower-order transverse modes of a graded-index fiber. The

number of modes in a graded-index fiber can be approximated as $\frac{V^2}{4}$, which is only

about half the number of modes supported by an equivalent step-index fiber.
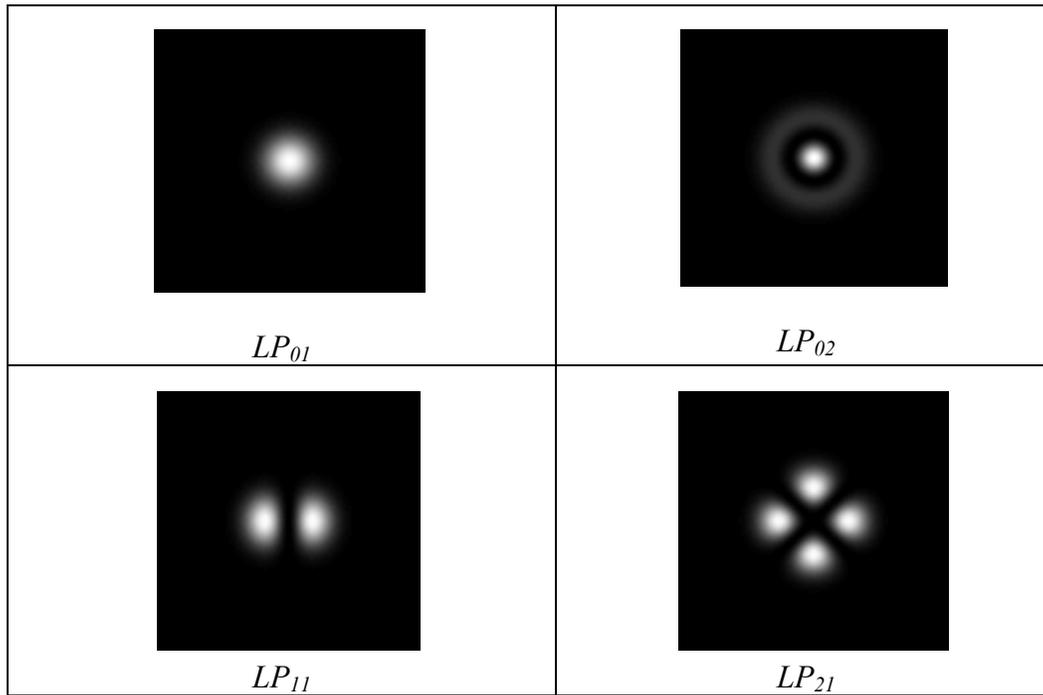
Figure 7. Intensity profiles of four transverse modes of a graded-index fiber.

4. Model of SRS Beam Cleanup in Multimode Fibers

4.1. Introduction to Beam Cleanup

Good beam quality is an important characteristic of many laser systems. A singlemode beam is the natural output of a fiber laser based on a singlemode fiber. A fiber laser based on a multimode fiber, on the other hand, will produce multimode output unless specific steps are taken to improve the beam quality of the output beam.

Singlemode output from a multimode fiber can be achieved using a variety of techniques. One of the most common methods is to bend the fiber so as to induce losses in higher-order transverse fiber modes [45,46,47,48,49]. Another method achieves diffraction-limited output by using an external resonator cavity as a mode selector [47,50]. Similarly, singlemode output from a fiber laser can also be achieved through the addition of an intracavity spatial mode filter comprised of a short section of singlemode fiber [48]. Good beam quality can also be produced using nonlinear scattering processes such as SRS and SBS.

SRS beam cleanup has been experimentally demonstrated for bulk media [25, 51,52,53,54]. Van Heuvel created a numerical model of SRS beam cleanup in bulk media which explained the process in terms of the balance between amplification and diffraction [55]. SRS beam cleanup, as well as SBS beam cleanup, have been demonstrated for multimode graded-index fibers [17,18,19,20,21]. However, SRS beam cleanup has not been observed in step-index fibers [57].

Chiang created a simple model of SRS beam cleanup in multimode fibers, but this effort was limited in a number of ways. First, Chiang based his model on the intensity profiles of the modes of a step-index fiber [21]. This is problematic because beam

38

cleanup does not occur in step-index fibers. Chiang further simplified his analysis by only considering the intensity patterns of the fiber modes rather than the mode fields. Chiang also confined his model to considering the undepleted pump regime. Finally, Chiang only considered beam cleanup for a single, carefully chosen launching condition of the pump beam.

After describing the work of Chiang, this chapter develops a model of SRS beam cleanup based on the overlap of the pump field modes and the Stokes field modes of a multimode fiber given a variety of input pump mode distributions. This chapter presents a table of some of the normalized overlap integrals of a notional graded-index fiber. For comparison, this model also presents the normalized overlap integrals of a notional step-index fiber. These tables provide a clear conceptual picture of beam cleanup.

These tables of overlap integrals consider the overlap of the intensity pattern of the pump modes and the intensity pattern of the Stokes modes. This chapter also presents a more robust model of beam cleanup which considers the nuanced interaction of the fields of the pump modes with the fields of the Stokes modes. This part of the model examines unseeded SRS beam cleanup for a variety of a launching conditions.

This model shows that mode competition in a graded-index fiber tends to favor the lower-order transverse Stokes modes of the fiber at the expense of the higher-order transverse Stokes modes of the fiber. This explains why beam cleanup occurs in a graded-index fiber. On the other hand, in a step-index fiber, mode competition does not tend to favor the lower-order transverse Stokes modes. This explains why SRS beam cleanup has not been reported for step-index fibers.

39

After presenting a model of unseeded SRS beam cleanup, this chapter develops a model which describes the beam quality of the Stokes output of an RFA based on a graded-index fiber. This model is based on the coupled differential equations which define the relationship between the power in the pump modes and the power in the Stokes modes of the fiber. The solutions of these equations were calculated using a Runge-Kutta method. The beam quality of the input beams and the output beams of the RFA are presented in terms of the beam quality factor, M^2.

This model examined 1800 random input pump and seed configurations. The results of these simulations show that the beam quality of the output Stokes beam depended on the beam quality of the input seed beam and the beam quality of the input pump beam. The beam quality of the output Stokes beam was shown to be better than the beam quality of the input seed beam in the case of a pump beam with good beam quality. In the case of a pump beam with poor beam quality, the beam quality of the output Stokes beam was similar to the beam quality of the input seed beam. In other words, according to this model, the beam quality of the input of the RFA determined the beam quality of the output of the RFA. Chapter 5 describes experiments that validate several of the predictions of this model.

4.2. Observations of SRS Beam Cleanup in Multimode Fibers

Chiang demonstrated SRS beam cleanup in a graded-index fiber in 1992 [21]. In his experiment, a pulsed dye laser at 585 nm was launched into a graded-index fiber with a core size of 50 μm (NA=0.2). Chiang noted that the when the launching conditions of the pump beam were optimized, the generated Stokes beam propagated in the LP_{01} mode. In the case of a 30 m long fiber the Stokes beam could be made to propagate in different

lower-order modes by adjusting the angle and position of the input end of the fiber. The LP_{01}, LP_{11}, LP_{21}, LP_{02}, LP_{31}, LP_{12} and the LP_{41} modes were observed individually. Several of these modes were also observed simultaneously, sometimes resulting in a ring pattern. In a 1 km long fiber, Chiang similarly observed several lower-order transverse Stokes modes which appeared when the input fiber was aligned to provide the proper launch conditions. The second Stokes order was only observed to propagate in the LP_{01} mode.

In 1997, Islam and Sakuda also reported beam cleanup in a multimode graded-index fiber [56]. A frequency doubled, mode locked and *Q*-switched Nd:YAG laser with a wavelength of 532 nm was coupled into a 90 m long fiber with a core diameter of 42 μm (*NA*=0.2). It was noted that while the pump beam was multimode, the Stokes beam appeared to propagate in the fundamental mode of the fiber.

In 2002, Russell *et al.* performed an SRS beam cleanup experiment using a 300 m long 50 μm graded-index fiber [17]. In this experiment, diagrammed in Figure 8, the 300 m long multimode fiber was pumped with a *Q*-switched Nd:YAG laser at 532 nm. It was observed that while the pump beam had poor beam quality (M^2=20.7), the Stokes beam had a dramatically improved beam quality (M^2=2.4).

It should be noted that when Sharma *et al.* studied a 50 m long step-index fiber with a core diameter of 7.9 μm, beam cleanup was only observed when the fiber was bent [57]. Bending the fiber introduced significant losses to the higher-order transverse Stokes modes of the fiber, but not to the LP_{01} mode of the fiber. Good beam quality in the Stokes output beam was achieved by spatially filtering the Stokes beam. In other words, SRS beam cleanup was not observed in the step-index fiber.

41
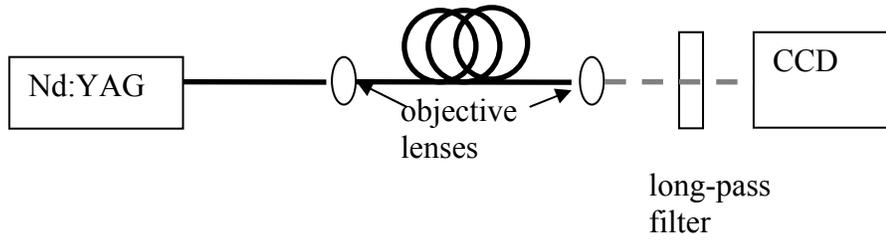
Figure 8. Setup for demonstrating unseeded beam cleanup in a graded-index fiber [17].

4.3. Theory of Beam Cleanup

4.3.1. Background

Beam cleanup can be explained in terms of mode competition between the various transverse Stokes modes of a graded-index fiber; beam cleanup occurs when the LP_{01} mode experiences preferential gain relative to the other transverse modes of the fiber. Beam cleanup produces a Stokes beam which has much better beam quality than the input pump beam used to generate it.

In a multimode fiber, a multimode pump beam is coupled into many different modes of the fiber which in turn stimulates many different Stokes modes. Pump power launched into the LP_{01} pump mode of the fiber will generate Stokes power in the LP_{01} Stokes mode of the fiber. To a lesser degree, Stokes power will also be generated in other neighboring Stokes modes. The same is true of pump power launched into any other pump mode of the fiber. Power in every pump mode will generate power in the corresponding Stokes mode of the fiber as well as in neighboring Stokes modes of the fiber. The following section develops a quantitative description of the interaction of the various modes of the fiber.

4.3.2. Overlap Integral

The competition between modes can be quantified using the concept of the overlap integral [18,19,21,58,59,60]. The overlap integral can be derived using the coupled differential equations which describe the interaction of the pump and Stokes waves during the SRS process. This relationship is given by Eqs. (37) and (38). In order to convert these equations to into a form relating the power in the pump modes to the power in the Stokes modes, Eqs. (37) and (38) are integrated over the cross-sectional area of the fiber. In terms of power, the coupled differential equations then take the following form

$$
\frac{\partial P_p(z)}{\partial z} = -g(z)\frac{\omega_p}{\omega_s}P_p(z)P_s(z) - \alpha_p P_p(z)
$$

$$
\frac{\partial P_p(z)}{\partial z} = g(z)P_p(z)P_s(z) - \alpha_s P_s(z)
$$

(71)

where P is the power in the beams and where the subscripts p and s denote the pump and Stokes beams respectively. The effective gain of each mode is given as

$$
g(z) = g_R \frac{\int I_p(x,y,z)I_s(x,y,z)dxdy}{P_p(z)P_s(z)}
$$

(72)

The irradiance $I_{p,s}$ is related to the electric field according to

$$
I_{p,s}(x,y,z,t) = 2\varepsilon_0 cn\left\langle \left|\bar{E}_{p,s}(x,y,z,t)\right|^2 \right\rangle
$$

(73)

where the angle brackets are used to indicate time average. The electric field in a multimode fiber can be considered to be a superposition of the modes of the fiber according to

$$
\bar{E}_{p,s}(x,y,z,t) = \sum_m A_{p,s}^m \psi_{p,s}^m [\cos(\bar{k}_{p,s}^m \cdot \hat{z} - \omega_{p,s}t + \phi_{p,s}^m)\hat{e}] \quad (74)
$$

43

In this case, $A_{p,s}^m$, $\psi_{p,s}^m$, $\bar{k}_{p,s}^m$, $\phi_{p,s}^m$ represent the field amplitude, the mode field

distribution, the propagation constant and the phase of the mth mode of the fiber. The

subscript p and s denote the pump and Stokes contributions. By incorporating Eq. (73)

and Eq. (74) into Eq. (72), the Raman gain coefficient is given by

$$g(z) = g_R (\varepsilon_0 c n)^2 \frac{\sum\limits_{n'} A_{n'}^s \sum\limits_{n''} A_{n''}^s \sum\limits_{n'''} A_{n'''}^p \sum\limits_{n''''} A_{n''''}^p \gamma_{n'n''n'''n''''}}{P_s(z)P_p(z)} \qquad (75)$$

where

$$\gamma_{n'n''n'''n''''} = \int \psi_{n'}^{s,p} \psi_{n''}^{s,p} \psi_{n'''}^{p,s} \psi_{n''''}^{p,s} \cos(\Delta\bar{k}_{n'n''}^{s,p} \cdot \hat{z} + \Delta\phi_{n'n''}^{s,p}) \cos(\Delta k_{n'''n''''}^{p,s} z + \Delta\phi_{n'''n''''}^{p,s}) dx dy$$

$$(76)$$

and

$$\Delta\bar{k}_{n,n'}^{p,s} \equiv \bar{k}_n^{p,s} - \bar{k}_{n'}^{p,s}$$
$$\Delta\phi_{n,n'}^{p,s} \equiv \phi_n^{p,s} - \phi_{n'}^{p,s} \qquad (77)$$

The time average included in Eq. (73) accounts for the elimination of the time dependant

terms.

The concept of the overlap between the pump and the Stokes modes of a fiber has

been considered by previous authors [18,59,60]. Stolen introduced the overlap integral as

a method of computing the Raman gain in fibers in connection with RFLs [60]. Dianov

et al. used the overlap integral to analyze an RFA based on a singlemode fiber [59].

Russell *et al.* applied the concept of the overlap integral to analyzing unseeded SBS beam

cleanup [18].

Chiang applied the overlap integral to the concept of mode competition in order to

explain SRS beam cleanup, albeit in a simplified way [21]. Chiang considered the case

of weak mode coupling by assuming that the gain of each Stokes mode was independent

44

of the gain of every other Stokes mode. Chiang simplified the overlap integral expressed in Eq. (76) by only considering the intensity patterns of the fiber modes using the following expression

$$\gamma_{n'n'''} = \frac{\int\limits_{-\infty-\infty}^{+\infty+\infty} \psi_{n'}^2 \psi_{n'''}^2 dxdy}{\int\limits_{-\infty-\infty}^{+\infty+\infty} \psi_{n'}^2 dxdy \int\limits_{-\infty-\infty}^{+\infty+\infty} \psi_{n'''}^2 dxdy} \qquad (78)$$

In this equation, $\psi_{n'}$ and $\psi_{n'''}$ are the mode fields of the overlapping intensity patterns of the n' Stokes mode and n''' pump modes respectively. Chiang further simplified his analysis by invoking the non-depleted pump approximation and expressing the gain of each individual mode of the fiber as

$$g_i = g_R(\Omega) P_p L_{eff} \sum_j p_j \gamma_{n'n'''} \qquad (79)$$

where P_p is the total pump power and p_j is the fraction of the pump power launched into the jth mode of the fiber. By using a carefully chosen input pump beam configuration, Chiang showed that the gain of the LP_{01} Stokes mode exceeded the gain of all of the other Stokes modes of a notional step-index fiber.

While Chiang's model was insightful, there are several ways it can be improved. First, it only used the modes of a step-index fiber to explain the behavior of a graded-index fiber. Second, Eq. (78) only considers the intensity patterns of the modes and not the more nuanced interactions of the mode fields. Lastly, it is important to consider the gain of the various modes of a fiber for a variety of input pump distributions rather than only examining a single special configuration of the input pump beam.

4.3.3. Model of Beam Cleanup

The model of SRS beam cleanup developed for this dissertation addresses beam cleanup by converting the expression for the overall Raman gain given by Eq. (75) into an expression of the gain of each individual fiber mode. This can be done by carefully considering the terms of Eq. (75) and grouping them appropriately. In order to simplify the notation, the following convention will be used, where the indices n' and n'' correspond to the Stokes modes and the indices n''' and n'''' correspond to the pump modes

$$A_{n'}^s A_{n''}^s A_{n'''}^p A_{n''''}^p \gamma_{n'n''n'''n''''} \equiv g_{n'n''n'''n''''} \tag{80}$$

The model developed in this chapter will ultimately be applied to a notional fiber with 20 transverse modes. Eq. (75) therefore contains a total of 20^4 terms. Although all 20^4 of these terms will be used to model SRS beam cleanup, justifying Eq. (82) can be done by considering a fiber with only two transverse modes. This reduces the number of terms to be considered to 16 (i.e., 2^4). These 16 terms can be fully expressed and grouped as follows. Fortunately, the following method of grouping is fully generalizable to a notional fiber with 20 transverse modes.

In the simplified case of a fiber with two modes, the total gain of both modes can be expressed as

$$
\begin{aligned}
g(z) \propto (&g_{1111} + g_{1112} + g_{1121} + g_{1122} + g_{1211} + g_{1212} \\
&+ g_{1221} + g_{1222} + g_{2111} + g_{2112} + g_{2121} + g_{2122} \\
&+ g_{2211} + g_{2212} + g_{2221} + g_{2222})
\end{aligned}
\tag{81}
$$

For clarity, the terms in the above expression are rearranged in the following manner

$$g(z) \propto$$
$$g_{1111}(z) + g_{1112}(z) + g_{1121}(z) + g_{1122}(z) +$$
$$g_{2211}(z) + g_{2212}(z) + g_{2221}(z) + g_{2222}(z) + \qquad (82)$$
$$g_{1211}(z) + g_{1212}(z) + g_{1221}(z) + g_{1222}(z) +$$
$$g_{2111}(z) + g_{2112}(z) + g_{2121}(z) + g_{2122}(z)$$

In this equation, the 1st row of terms describes the growth of the 1st Stokes mode and only the 1st Stokes mode. The only Stokes elements represented in this 1st row are those of the 1st Stokes mode; these "11" terms involve the overlap of the 1st Stokes mode with itself. As there are no components of the 2nd Stokes mode in the 1st row of terms of Eq. (82), this 1st row is clearly attributable to the growth of the 1st Stokes mode and not to the growth of the 2nd Stokes mode. By the same reasoning, the 2nd row of terms in Eq. (82) is only attributable to the growth of the 2nd Stokes mode because the Stokes elements of the 2nd row of terms in Eq. (82) involve the overlap of the 2nd Stokes mode with itself. The remaining two rows in Eq. (82) include Stokes cross terms which describe the interaction of the 1st Stokes mode with the 2nd Stokes mode.

There are several options for dealing with the 3rd and 4th rows. One option is to consider that the gain of one mode has no direct effect on the gain of neighboring modes. In this regime, the 3rd and 4th rows are simply ignored. This approximation has the disadvantage that it underestimates the Raman gain. Calculating the Stokes output of an RFA using Eq. (82) and ignoring the 3rd and 4th rows underestimates the total output Stokes power produced by the RFA.

Another alternative is to retain the terms in question and allow the gain of one mode to directly affect the gain of neighboring modes. The simplest way to account for this is to assume that the gain of the 1st Stokes mode affects the gain of the 2nd Stokes

47

mode as much as the gain of the 2nd Stokes mode affects the gain of the 1st Stokes mode. Thus, as an approximation, the terms of the 1st and 3rd rows of Eq. (82) were used to calculate the gain of the 1st Stokes mode. Likewise, the terms of the 2nd and 4th rows of terms in Eq. (82) were used to calculate the gain of the 2nd Stokes mode. Since it turns out that the array is symmetric with regards to an interchange of the indices n' and n'', the 3rd and 4th rows are equivalent to one another. It is should also be noted that the array is symmetric with regards to an interchange of the indices n''' and n''''. Furthermore, symmetry arguments can be used to show that a number of these gain terms are equal to zero.

By assuming that the gain of each Stokes mode can be calculated individually and by using the aforementioned grouping of terms, the gain of each Stokes mode is given by

$$g_{n'}(z) = g_R (\varepsilon_0 c n)^2 \frac{A_{n'}^s \sum_{n''} A_{n''}^s \sum_{n'''} A_{n'''}^p \sum_{n''''} A_{n''''}^p \gamma_{n'n''n'''n''''}}{P_s(z)P_p(z)} \quad (83)$$

Essentially, the gain of the 1st Stokes mode is approximated to affect the gain of the 2nd Stokes mode as much as the gain of the 2nd Stokes mode affects the gain of the 1st Stokes mode.

By simply calculating which Stokes mode has the highest gain, unseeded SRS fiber beam cleanup can be modeled; this is done in Section 4.5.3. On the other hand, by combining Eq. (83) with the coupled power equations given in Eq. (71), the evolution of a seed in an RFA can be described. In order to be physically meaningful however, a model of the beam quality of an RFA requires some way to transform the modal power distributions into a measurable quantity such as beam quality. A method for converting the modal distribution into beam quality is described in the following section.

4.4. Beam Quality of Higher-Order Transverse Modes

One of the most commonly used characterizations of beam quality is the beam quality factor known as M^2, which compares the spot size and divergence of a multimode beam to the spot size and divergence of an ideal Gaussian beam. The beam cleanup experiments described in Chapters 5-8 report the beam quality of the measured beam in terms of M^2. The simulations of an RFA described in Section 4.5.3 also characterize beams in terms of M^2.

Yoda *et al*. derived a method of determining the beam quality of the transverse modes of a step-index fiber [61]. Using their method, Yoda *et al*. calculated the beam quality of various individual LP_{lm} modes, as well as the beam quality of a linear combination of two LP_{lm} modes, in terms of M^2. This section outlines the method used by Yoda *et al*. to determine the M^2 value of a given mode distribution in a step-index fiber.

To begin, this method considers the transverse profile of the electric field at the end facets of the fiber. Using the notation of Yoda *et al*., which defines the beam center using the 1st moment method, the center coordinate $\langle x \rangle$ and the variance $\sigma_x^2(x)$ of the normalized intensity distribution are defined by

$$
\langle x \rangle(z) = \langle x \rangle(z_0) - i \frac{\lambda}{4\pi}(z - z_0) \times
$$
$$
\iint [E(x,y,z_0)\frac{\partial E(x,y,z_0)}{\partial x} - c.c]dxdy
$$
$$
\sigma_z^2(z_0) = \sigma_x^2(z_0) - i\frac{\lambda}{2\pi}C_1(z - z_0)
$$
$$
+ \frac{\lambda^2}{(2\pi)^2}C_2(z - z_0)^2
$$

(84)

where the coefficients C_1 and C_2 are expressed as

$$C_1 = \iint (x - \langle x \rangle (z_0))[E(x,y,z_0)\frac{\partial E(x,y,z_0)}{\partial x} - c.c.]dxdy$$

$$C_2 = \iint \left| \frac{\partial E(x,y,z_0)}{\partial x} \right|^2 dxdy \qquad\qquad (85)$$

$$+ \frac{1}{4}\left\{ \iint [E(x,y,z_0)\frac{\partial E^*(x,y,z_0)}{\partial x}dxdy - c.c. \right\}$$

where z_0 is the location of the fiber facet.

By comparing the center and the variance as given in Eqs. (84) and (85) with the center and variance of a Gaussian beam, Yoda *et al*. showed that the beam quality is of a beam emerging from a step-index fiber is given by [61]

$$M_x^2 = \sqrt{4C_2\sigma_x^2(z_0) + C_1^2} \qquad\qquad (86)$$

Calculating the beam quality of the modes of a graded-index fiber is fairly straightforward using this equation. In the case of pure LP_{lm} modes, the transverse profile of the electric field is given by Eq. (70). The beam quality (in terms of M^2) of several individual LP_{lm} modes of a graded-index fiber is shown in Table 1. Asymmetric modes have two different values of M^2, one for the x axis and one for the y axis. The beam quality of a beam containing multiple fiber modes can be determined by considering the electric field of the beam to be a simple superposition of modes according to Eq. (74).

When considering the beam quality of a superposition of modes, the relative phase of each mode at the facet of the fiber is important. Yoda *et al*. evaluated the effect of phase on the M^2 of a step-index fiber for two cases. The first case was a combination of the LP_{01} mode with the LP_{11} mode. Given an equal weighting of the two modes, Yoda *et al*. showed that when the modes were in phase, the beam quality of the superposition of modes was approximately $M^2=1.3$; when the two modes had a relative phase difference of $\pi/2$, the beam quality was $M^2=2.1$. Yoda *et al*. also examined a combination of the LP_{01}

50

mode with the LP_{02} mode and again found that when the two modes were in phase, the value of M^2 was lower than when the modes were not in phase [61].

Table 1. Beam quality of the transverse modes of a notional graded-index fiber.

Mode	M^2
LP_{01}	1.0
LP_{02}	3.0
LP_{03}	5.0
LP_{11}	1.0,3.0
LP_{12}	2.0,6.0
LP_{13}	3.0,9.0
LP_{21}	3.0
LP_{22}	5.0
LP_{23}	7.0
LP_{31}	4.0,8.0
LP_{32}	4.0,6.0
LP_{41}	5.0
LP_{42}	7.0
LP_{51}	5.0,6.0

Assuming all of the fiber modes have the same relative phase at the fiber facet simplifies calculations involving M^2. Calculations made using this assumption yield the optimum beam quality of the beam at that fiber facet. While this approximation is obviously somewhat non-physical, it is useful because it simplifies calculations of M^2. Fortunately, it is still possible to compare the beam quality of the input and the output mode distributions given this approximation. By assuming that all modes have the same relative phase at the input and output facet of the fiber, this model compares the optimum input beam quality to the optimum possible beam quality of the output.

4.5. Results and Discussion

4.5.1. Overview

This section describes the results of numerical simulations based the model described in Section 4.3 and Section 4.4. The results of these simulations fall into two

categories. The first category describes unseeded SRS beam cleanup. The second category considers the beam quality of the Stokes output of an RFA.

Unseeded SRS beam cleanup was modeled by considering the overlap integrals of a graded-index fiber and a step-index fiber. The overlap of the LP_{01} Stokes mode with the LP_{01} pump mode in a graded-index fiber was shown to be greater than the overlap of any other pair of pump and Stokes modes. Given the uniform seeding associated with spontaneous Raman scattering in a long fiber, the LP_{01} Stokes mode will be the dominant component of the output Stokes beam of a graded-index fiber. In other words, the model predicts that the beam quality of the output Stokes beam will be better than the beam quality of the pump beam used to generate it. An analysis of the gain of the Stokes modes of a step-index fiber showed that the gain of the higher-order transverse Stokes modes was equal to or greater gain than the gain of the lower-order transverse Stokes modes. This explains why beam cleanup does not occur in a step-index fiber.

While a simple examination of the overlap integrals is insightful, it ignores the fact that the Raman gain of any given fiber mode depends on the modal distribution of the pump beam. Chiang used the overlap integrals in conjunction with a single, well-chosen pump configuration to demonstrate that the LP_{01} Stokes mode had greater gain than any other Stokes mode.

The more comprehensive approach of this section considered the relative gain of the various Stokes modes of a fiber for a large number of random pump launching conditions. This approach showed that for random configurations of the pump beam, the lower-order transverse Stokes modes of a graded-index fiber tended to have a higher average gain than the higher-order transverse Stokes modes of a graded-index fiber. This

52

is not the case in step-index fibers, which explains why beam cleanup has only been observed in graded-index fibers and not in step-index fibers.

In a graded-index fiber, an unseeded pump beam can generate a Stokes beam with beam quality which is dramatically improved relative to the beam quality of the pump beam used to generate it. Rice predicted a similarly dramatic improvement in the beam quality of a seed beam as it is amplified by an RFA based on a multimode graded-index fiber [22]. The remainder of this section describes a numerical model which analyzes the beam quality of the Stokes output of an RFA based on a graded-index fiber.

The beam quality of the Stokes output was modeled by calculating the gain of each individual mode according to Eq. (83). The gain of each mode is a critical element in the coupled differential Eqs. (71) which describe the interaction of the power in the pump modes of the fiber and the power in the Stokes modes of the fiber. The initial modal distribution of Stokes seed was compared with the final distribution of Stokes modes. These simulations showed that the beam quality of the input pump and Stokes beams determined the beam quality of the output beam. In the case of a poor quality pump beam, the beam quality of the amplified seed was similar to the beam quality of the input seed beam. In the case of relatively good quality input pump beam, the beam quality of the amplified seed was better than the beam quality of the input seed beam.

4.5.2. Modeling of Unseeded SRS Beam Cleanup

4.5.2.1. Overlap Integrals

In the case of unseeded SRS, the Stokes beam resulted from the amplification of Stokes photons generated by spontaneous Raman scattering. As discussed in Chapter 2, forward spontaneous Raman scattering in a long fiber ($\alpha_p L \gg 1$) can be viewed as seeding

by one fictitious photon per transverse mode of the fiber at z=0 [32]. The Stokes output was assumed to be generated as part of a single longitudinal Stokes mode. This model of unseeded SRS beam cleanup considered the Stokes seed to be uniformly distributed between the transverse modes of the fiber. Since all transverse modes began with equal power, the mode with the largest gain dominated the Stokes output. The goal of these simulations of unseeded SRS beam cleanup was to determine the Stokes mode with the greatest gain.

As described in Section 4.3, the gain of a given Stokes mode is related to the overlap of that Stokes mode with the other modes of the fiber. In the case of a graded-index fiber, the overlap of the various pure pump modes and pure Stokes modes (i.e. the overlap of the intensity patterns) was calculated via Eq. (78); the mode fields, ψ, used in these calculations were defined by Eq. (70). The values of this simplified overlap integral, normalized to the value of the LP_{01}-LP_{01} overlap, are presented in Table 2.

A graphical depiction of the overlap integrals is presented in Figure 9, which simply plots the values of the normalized overlap integrals tabulated in Table 2. This figure clearly shows that the overlap of the LP_{01} Stokes mode with the LP_{01} pump mode is greater than the overlap of any other combination of pure pump and pure Stokes modes. Furthermore, the overlap of the intensity patterns becomes progressively smaller for higher-order transverse modes. According to this simple description, mode competition in a graded-index fiber will favor the LP_{01} Stokes mode.

The overlap integrals of the notional graded-index fiber are very different from the overlap integrals of a notional step-index fiber. The overlap integrals of a step-index fiber were calculated using Eq. (78) and normalized to the overlap of the LP_{01} Stokes

54

mode with the LP_{01} pump mode; the mode fields for the step-index fiber were defined by Eq. (66). These overlap integrals, presented in Table 3, clearly show that several transverse Stokes modes have higher overlap with their respective pump modes than does the LP_{01} Stokes mode with the LP_{01} pump mode. Unlike the case of a graded-index fiber, the overlap integrals of the mode intensities tended to be greater for higher-order transverse Stokes modes than for the lower-order transverse Stokes modes, although this trend is not monotonic. It should be noted that in general, the overlap integrals of the step-index fiber were about an order of magnitude smaller than the overlap integrals of the graded-index fiber.

Table 2. Overlap integrals for the pure pump modes and the pure Stokes modes of a notional graded-index fiber. All overlap integrals are normalized to the value of the LP_{01}-LP_{01} overlap. Self-overlap is highlighted in bold font. The largest value of the overlap integral is noted in blue.

		Pump Modes						
		LP_{01}	LP_{11}	LP_{21}	LP_{02}	LP_{31}	LP_{12}	LP_{41}
Stokes Modes	LP_{01}	**1.0000**	0.5120	0.2622	0.5003	0.1162	0.3781	0.0687
	LP_{11}	0.4880	**0.7496**	.3838	0.2562	0.2620	0.3754	0.1677
	LP_{21}	0.2381	0.3658	**0.5618**	0.2557	.3197	0.1922	0.2455
	LP_{02}	0.5003	0.2441	0.2437	**0.4494**	0.2495	0.2619	0.2243
	LP_{31}	0.1162	0.2380	0.3046	0.2495	**0.4679**	0.1933	0.2795
	LP_{12}	0.3721	0.3754	0.1832	0.2379	0.1813	**0.4675**	0.1920
	LP_{41}	0.0567	0.1451	0.2230	0.2123	0.2664	0.1976	**0.4092**

A graphical depiction of the normalized overlap integrals of a step-index fiber is presented in Figure 10. Chiang calculated similar results for the value of the overlap integrals of a step-index fiber [21]. In doing so, Chiang ignored the wavelength dependence of the V-number in his calculations, which accounts for the symmetry of his reported results. Generally, mode competition in a step-index fiber does not favor the LP_{01} Stokes mode. This explains why beam cleanup has not been reported for step-index fibers [57].
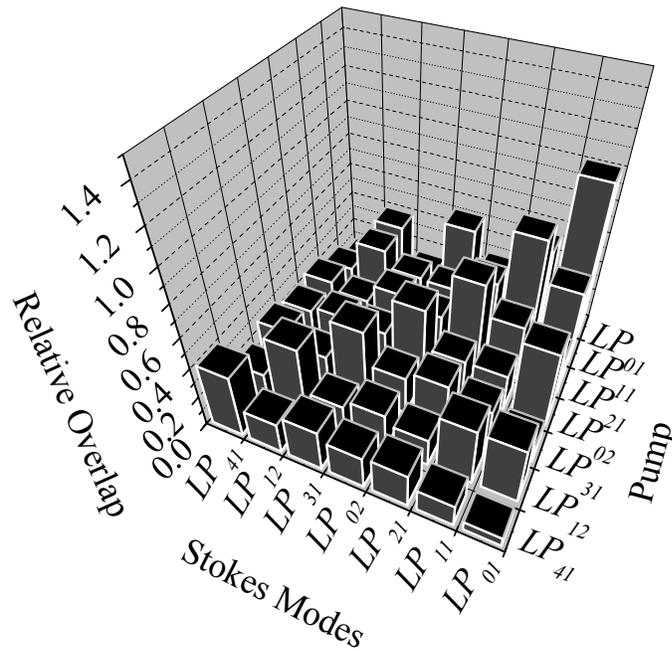
Figure 9. Graphical representation of the normalized overlap integrals of a notional graded-index fiber; these results are also presented in Table 2. Note that the greatest overlap occurs between the LP_{01} pump mode and the LP_{01} Stokes mode.

Table 3. Overlap integrals for the pure pump modes and the pure Stokes modes of a notional step-index fiber. All overlap integrals are normalized to the value of the LP_{01}-LP_{01} overlap. Self-overlap is highlighted in bold font. The largest value of the overlap integral is noted in blue.

		Pump Modes						
		LP_{01}	LP_{11}	LP_{21}	LP_{02}	LP_{31}	LP_{12}	LP_{41}
Stokes Modes	LP_{01}	**1.0000**	0.6683	0.5130	0.8209	0.3749	0.7538	0.7717
	LP_{11}	0.6664	**1.0606**	0.6772	0.4217	0.5659	0.7391	0.5442
	LP_{21}	0.5094	0.6744	**1.1095**	0.4106	0.6784	0.3952	0.6677
	LP_{02}	0.8215	0.4208	0.4096	**1.1986**	0.4044	0.6778	0.6495
	LP_{31}	0.3715	0.5624	0.6770	0.4053	**0.9981**	0.3489	0.3710
	LP_{12}	0.7540	0.7394	0.3946	0.6737	0.3470	**1.2491**	0.7450
	LP_{41}	0.7709	0.5444	0.6681	0.6460	0.3704	0.7445	**1.4467**

This section presented the overlap integrals associated with intensity patterns of

several pump modes and Stokes modes in both a graded-index fiber and a step-index

fiber. While this model provides good insight into the beam cleanup process, it only

56

considers the overlap of the modal intensity patterns rather than considering the more nuanced interactions of the mode fields. In the next section, the Stokes mode with the highest gain will be calculated for a large number of random launching configurations of the pump beam.
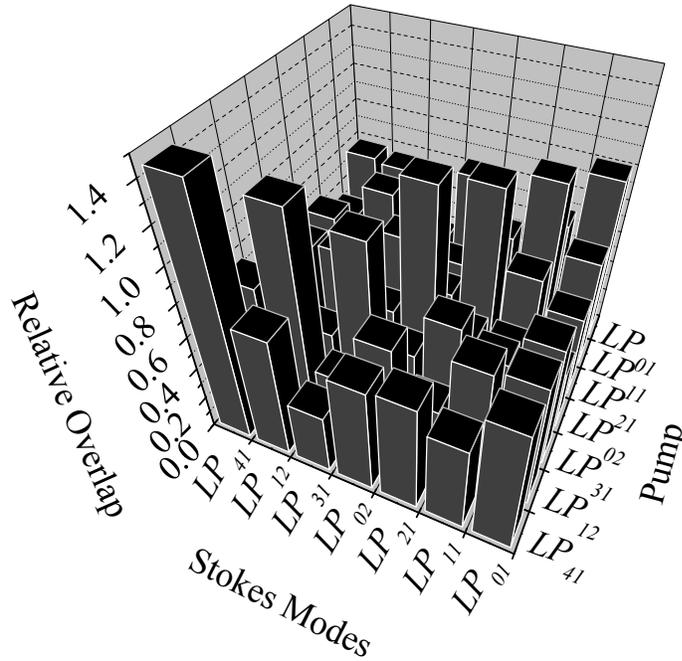
Figure 10. Graphical representation of the normalized overlap integrals of a notional step-index fiber; these results are also presented in Table 3. Note that the greatest overlap does not occur between the LP_{01} pump mode and the LP_{01} Stokes mode.

4.5.2.2. Modeling Unseeded SRS Beam Cleanup

The analysis of unseeded SRS beam cleanup presented here calculates the gain of various Stokes modes of a notional fiber given a wide range of pump launching conditions. The gain of each fiber mode, given by Eq. (83), was calculated at $z=0$ for a series of 50,000 random pump beam configurations. In this simulation, the pump wavelength was 1064 nm. The notional fiber had a core diameter of 50 μm (NA=0.2) with V=30. As was discussed in Chapter 3, such a graded-index fiber actually contains

about 225 modes. To limit the computation time of the numerical simulations however, the notional fiber used in this analysis contained only 20 transverse modes.

The power of each pump mode and the phase of each pump and Stokes mode were initialized using a random number generator. The amplitude of each Stokes mode was taken to be equal in order to approximate seeding via spontaneous Raman scattering. It should be noted that the LP_{lm} modes of the fiber can have two possible orientations if the index l is odd. The letter T will be used to denote the transpose orientation of these modes, i.e. $LP_{lmT.}$

The results of this simulation are given in Figure 11, which shows the percentage of pump mode configurations which resulted in a given Stokes mode having the greatest gain. From this figure, it is clear that given random launching conditions of the pump beam, the LP_{01} Stokes mode tended to experience greater gain than any other Stokes modes of the fiber. This dominance of the LP_{01} mode was by no means universal; the LP_{01} mode had the highest gain for only about 25% of the random pump launching conditions. Given other sets of pump launching conditions, other Stokes modes had the highest gain. This is consistent with Chiang's observation that the generated Stokes modes of the fiber could be tailored by careful aligning the pump beam.

A similar description of SRS beam cleanup is given by Figure 12, which gives the relative gain of each Stokes mode averaged over each of the 50,000 random pump launching configurations. Again it is clear that the LP_{01} mode had the greatest gain and was therefore the dominant component of the Stokes output. Progressively higher-order transverse modes of the fiber tended to have a progressively lower average gain.

58
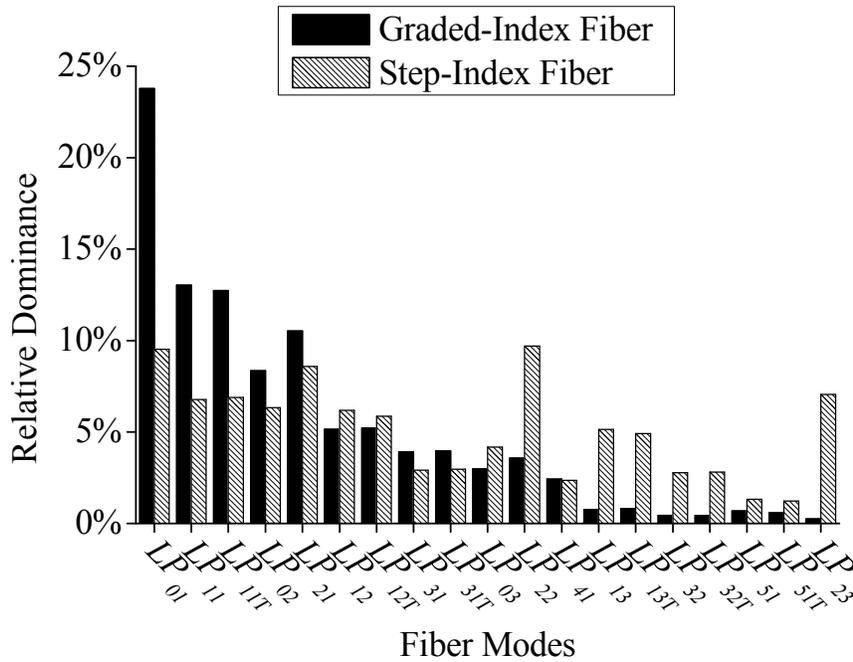
Figure 11. Probability that a given Stokes mode will have the greatest Raman gain of any Stokes mode in a multimode fiber.

Having examined beam cleanup in a graded-index fiber, this section will now address the relative gain of the Stokes modes of a step-index fiber. The notional step-index fiber had 20 transverse modes and a core diameter of 50 μm (NA=0.2). The pump wavelength was 1064 nm. The amplitude of each pump mode was defined by a random number generator. The phase of each pump and Stokes mode was also defined using a random number generator. The transverse Stokes mode field of the fiber is given by Eq. (66).

This simulation used Eq. (83) to calculate the gain of each of the various Stokes modes of a step-index fiber for 50,000 sets of random pump launching conditions. The results of this simulation are given in Figure 11, which shows the percentage of pump configurations for which a given mode had the greatest gain. From this figure, it is clear

that given random launching conditions of the pump beam, the LP_{01} Stokes mode had the greatest gain for less than 10% of the pump launching conditions examined. The LP_{22} mode was dominant almost 10% of the time; the LP_{21} mode is dominant for almost, but not quite, the same percentage of the pump launching configurations examined. Furthermore, there was not a trend of higher-order transverse modes having lower gains than the lower-order transverse modes.

A similar description of step-index fibers is given by Figure 12, which shows the relative gain of each Stokes mode averaged over the 50,000 random pump launching configurations. According to Figure 11 and Figure 12, no single individual mode will dominate the Stokes output of a step-index fiber.

4.5.2.3. Conclusions

In summary, this section described a model which explained why unseeded SRS beam cleanup occurs in graded-index fibers, but not in step-index fibers. This model evaluated the overlap integrals of both kinds of fiber. These overlap integrals were used to determine the Raman gain of the various Stokes modes of the fiber. It was shown that in a graded-index fiber, the gain of the LP_{01} Stokes mode was dominant for a range of launching conditions. This simulation also showed that in a step-index fiber, the gain of the LP_{01} Stokes mode was roughly equal to or slightly less than the gain of several other transverse Stokes modes of the fiber.

Furthermore, this model is consistent with observations that beam cleanup does not occur in step-index fibers [57]. This is a significant improvement over the beam cleanup explanation offered by Chiang, who considered beam cleanup in a graded-index

60

fiber by using the overlap integrals of a step-index fiber in conjunction with a single, carefully chosen launching condition of the pump beam.

4.5.3. Modeling Beam Quality in a Raman Fiber Amplifier

While the previous section analyzed unseeded SRS beam cleanup in a graded-index fiber and a step-index fiber, this section considers a model of the beam quality of the Stokes output of an RFA based on a graded-index fiber. In an RFA the modal distribution of the input Stokes seed was non-uniform; different Stokes modes contained different amounts of seed power. While it is still true that the LP_{01} mode generally had better overlap with the input pump beam than other Stokes modes, the LP_{01} mode was not necessarily the dominant component of the Stokes output. This was because the gain of each Stokes mode described by Eq. (83) contained both overlap terms and power terms. A Stokes mode with a poor overlap with the pump beam was sometimes seeded with large amounts of power and therefore had a larger gain than a Stokes mode with good overlap with the pump beam but low seed power.

The interaction of the power in the pump beam and the power in the Stokes beam is governed by Eq. (71). In the case of a multimode fiber, these two coupled differential equations become a set of $2Q$ coupled differential equations, where Q is the number of modes in the fiber. Solutions to these equations are complicated by the fact that the Raman gain of each and every mode is related to the power in every other mode according to Eq. (83). This problem is extremely complicated for the case of a 50 μm graded-index fiber which contains hundreds of fiber modes. To simplify this problem, the model described in this section considered a 5200 m long notional graded-index fiber which contained only 20 transverse modes.

61
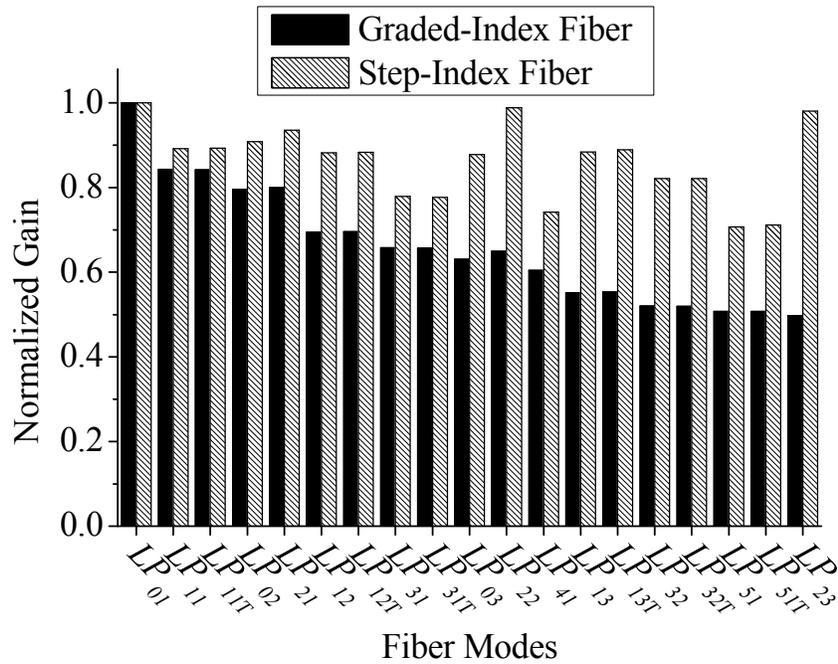
Figure 12. Average relative gain of various Stokes modes in a multimode fiber.

Since the evolution of the input seed depended on the modal power distribution of

the pump and the Stokes beams, a large number of random distributions of the both

coupled pump beam and the input seed beam were examined. For each set of random

launching conditions, the power in the pump and Stokes beams were determined by

solving Eq. (71) using a Runge-Kutta solver. The gain, g(z), at each point in the fiber

was calculated using Eq. (83).

The beam quality (M^2) of each input and each output configuration was calculated

using Eq. (86). These beam quality calculations assumed that all the fiber modes were in

phase at the input facet and at the output facet of the fiber. This approximation was

acceptable in the limit of a long fiber because in a long fiber, imperfections would

eventually cause the initial phase information to be lost as the beams traversed the fiber.

This approximation is consistent with the experimental setup described in Chapters 5 and 6, which only examined RFAs based on long fibers.

Beam quality calculations made using this simplification consistently yielded the minimum possible values of M^2. By assuming all the modes of the fiber were in phase, the calculated M^2 values of both the input beam and the output beam were, on average, equally underestimated. As section compared the beam quality of the input beam with the beam quality of the output beam, this approximation was valid.

The performance of the RFA was numerically evaluated for 1800 random input pump and input seed configurations. The coupled pump power was defined to be 3.5 W and the input seed power was 330 mW, values which were selected to match the pump and seed values for the experimental investigation of the RFA considered in Section 5.4. The relative amplitude of each pump and each Stokes mode was selected using a random number generator. The beam quality of the amplified seed versus the beam quality of the input seed for each of these random launching configurations is shown in Figure 13. Each point on the graph represents one random launching configuration, while each color on the graph represents a specific range of beam quality of the pump beam.

Figure 13 shows that the better the beam quality of the input pump beam, the better the beam quality of the amplified seed. In the case of a pump beam with relatively poor quality, the beam quality of the amplified seed was very similar to the beam quality of the input seed. In the case of a pump beam with good beam quality, the beam quality of the amplified seed was generally improved relative to the beam quality of the input seed.

This analysis assumed that all the modes of the fiber were in phase at the input and output fiber facets. If the modes were not in phase, the beam quality of both the input and output beams would decrease (M^2 would increase) along both the seed M^2 axis and the amplified seed M^2 axis. While this would result in a spreading of the points, the points would still tend to remain below the dotted line.
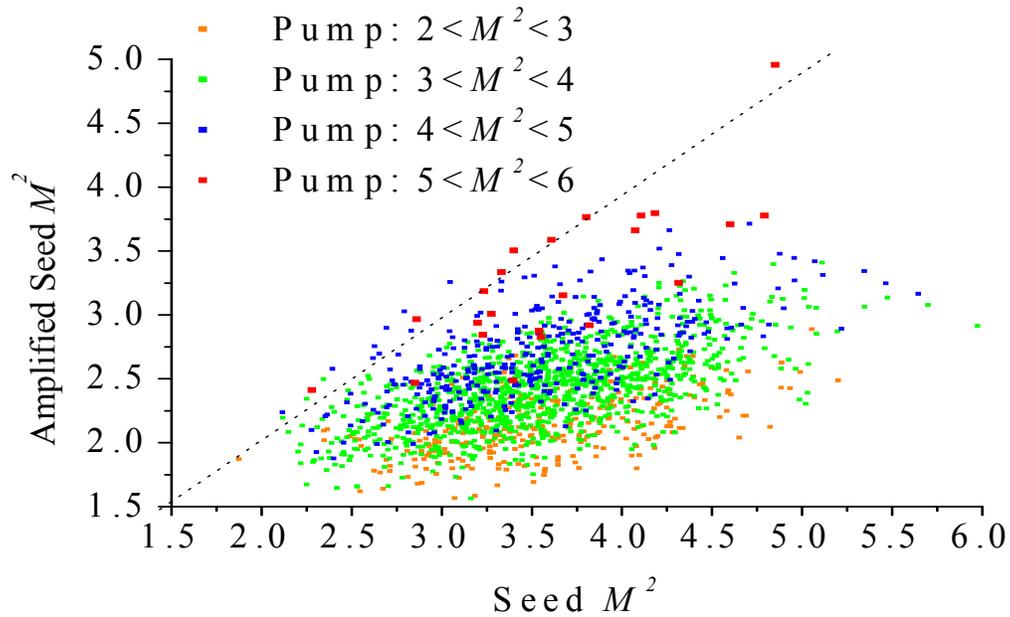
Figure 13. Beam quality of the amplified seed versus the beam quality of the input seed. Each dot represents the beam quality of a random pump/seed configuration. Each color represents a different range of beam quality values of the pump beam. Points below the dotted line exhibited beam cleanup of the amplified seed relative to the input seed.

It should be that noted two significantly different pump configurations can share a similar M^2 value. As shown by Table 1, the LP_{03} mode, the LP_{22} mode and the LP_{41} mode share the same beam quality parameter ($M^2=5.0$). However, as can be seen by Figure 12, these modes do not have the same average Raman gain. Therefore, a seed containing an equal weighting of say the LP_{01} Stokes and the LP_{03} Stokes mode would have the same beam quality as a seed containing an equal weighting of say, the LP_{01}

Stokes mode and the LP_{22} Stokes mode. Both configurations would have the same beam quality as a seed containing equal weighting of the LP_{01} mode and the LP_{41} mode. The beam quality factor would be M^2=3.0 in all three cases.

While the exact growth depends on the exact modal composition of the input pump beam, examining Figure 12 shows that each of these mode configurations will experience different amounts of Raman gain. Even though each of these configurations begins with the same initial beam quality, the evolution of the various components of the input seed will be different. This explains how two input configurations with the same value of M^2 value can evolve into output configurations with different values of M^2.

Chapter 5 examines the beam quality of the amplified seed for the case of an RFA based on a graded-index fiber. A summary of these measurements, shown in Figure 14, shows that the beam quality of the input seed beam was roughly the same as the beam quality of the output Stokes beam. In these measurements, the beam quality of the pump beam ranged from M^2=4.5-6.5. This data is consistent with predictions of the model presented in this chapter for the pump configurations corresponding to a relatively low quality input pump beam.

4.6. Chapter Summary

This chapter presented a model which described SRS beam cleanup in a multimode fiber. It was demonstrated that the LP_{01} Stokes mode of a graded-index fiber tended to have higher gain than other Stokes modes of the fiber. This was different from the case of a step-index fiber where the gain of the LP_{01} Stokes mode was not significantly greater than the gain of many of the other Stokes modes of the fiber. This

explains why dramatic beam cleanup has been observed for unseeded SRS in graded-index fibers and not in step-index fibers.

A model for describing the beam quality of the Stokes output of an RFA based on a graded-index fiber was also developed in this chapter. This model described the evolution of a random input seed beam configuration as it interacted with a random input pump beam configuration. It was shown that the beam quality of the output Stokes beam depended on the beam quality of the input pump beam and on the beam quality of the input seed beam. In other words, the beam quality of the input into the RFA determined the beam quality of the output of the RFA. This is a sharp contrast to the rather dramatic SRS beam cleanup reported for the case of unseeded SRS in a graded-index fiber. The predictions of the model of the beam quality of the Stokes output of an RFA were validated by the experiments described in Chapter 5.
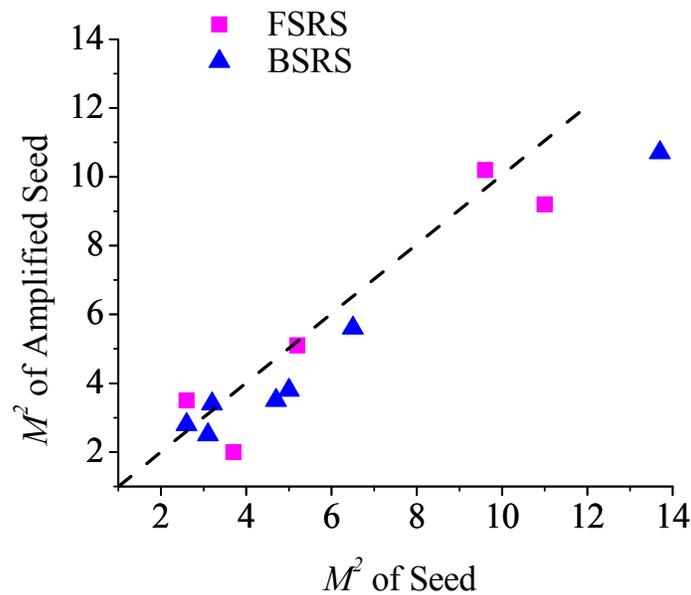
Figure 14. Experimental measurements of the beam quality of the input seed versus the beam quality of the amplified seed. The dotted line shows the point where the beam quality of the seed and the amplified seed were the same.

5. Raman Fiber Amplifier based on a Graded-Index Fiber

5.1. Motivation

RFAs have been extensively studied, particularly for applications involving the amplification of telecommunications signals. Conventional RFAs use singlemode gain fibers, allowing them to amplify a singlemode signal beam while still maintaining its diffraction-limited beam quality. One drawback of using a single clad, singlemode gain fiber is that efficient pump coupling can only be achieved by using a singlemode pump beam. Efficiently pumping a singlemode gain fiber is only possible if there is some way to convert the multimode pump beam into a singlemode pump beam. Such an intermediary mode converter however, reduces the overall efficiency of the RFA. On the other hand, a multimode gain fiber can be directly pumped with a multimode beam eliminating the necessity of a mode converter and improving the overall efficiency of the device. Using a multimode gain fiber therefore provides one avenue for the power scaling of RFAs.

Due to the beam cleanup property of SRS, which was described in Chapter 4, a graded-index multimode fiber can produce a Stokes beam with good beam quality. SRS beam cleanup has been demonstrated in bulk media [51,52,53,54]. SRS beam cleanup in graded-index multimode fibers has generally been confined to demonstrations involving unseeded Stokes beams [17,20,21,56,]. These experiments demonstrated dramatic improvements in the beam quality of the output Stokes beam relative to the input pump beam used to generate it.

One important extension of these previous experiments is the development of an RFA based on a multimode graded-index fiber. Rice predicted that an RFA with a

67

multimode core would not only preserve the quality of the seed beam, but improve it [22]. Morgan developed an RFA based on a multimode fiber using the BSRS geometry [110]. His work showed that in the BSRS geometry, the beam cleanup of the amplifier was much less dramatic than the unseeded SRS beam cleanup discussed in Chapter 4. Morgan's work also showed that there is a difference in the number of Stokes orders produced by the unseeded FSRS geometry and the number of Stokes orders produced by the BSRS geometry. This difference was attributed to FWM. Morgan's work however, did not demonstrate an RFA based on a multimode fiber using the FSRS geometry, nor did his work examine how the amplified seed was affected by the beam quality and power of the input seed beam.

This chapter begins with a review of experiments which have investigated Raman amplifiers (RAs) in bulk media, as well as a review of RFAs based on singlemode fibers. After reviewing these experiments and after reviewing the work of Morgan, the remainder of this chapter describes innovative experiments which have been conducted in order to test the beam quality of the Stokes output of an RFA given two seeding regimes. The first regime used a low-order transverse mode Stokes seed beam, while the second regime used a near-singlemode Stokes seed beam. The former regime tested the ability of an RFA based on a graded-index fiber to improve the beam quality of a multimode seed beam, while the latter regime demonstrated the ability of the RFA to maintain the beam quality of a near-singlemode seed beam. This extends the work of Morgan by showing that in both seeding regimes the beam quality of the seed determined the beam quality of the amplified seed.

This chapter also describes experiments which compared and contrasted the performance of the FSRS geometry of an RFA to the performance of the BSRS geometry of an RFA. Both geometries were characterized in terms of the beam quality, the spectral content as well as the power of the amplified seed. This chapter demonstrates that the spectral output of the BSRS geometry of the RFA was superior to the spectral output of the FSRS geometry of the RFA. At the power levels tested, the output of the BSRS geometry was confined to a single Stokes wavelength, while the output of the FSRS geometry contained a cascade of multiple Stokes wavelengths. The difference between the Stokes spectra generated by the two geometries can be explained in terms of the phase-matching condition of FWM. A quantitative analysis of the Stokes thresholds of the various Stokes orders confirmed that FWM contributed to the Stokes cascade only for the FSRS geometry of the RFA.

5.2. Background

5.2.1. Demonstrations of Raman Amplifiers based on Bulk Media

Komine *et al.* demonstrated SRS beam cleanup using a H_2 Raman Amplifier (RA) pumped with a pulsed XeCl master oscillator power amplifier (MOPA) [51]. While both the pump beam and the injected Stokes beam were aberrated, a comparison of the Strehl ratio of the seed with the Strehl ratio of the amplified seed showed that the amplified seed was cleaned up relative to the pump beam. Goldhar *et al.* also examined a RA in terms of its ability to amplify a low quality (not diffraction-limited) seed beam [52]. In their experiments, a pulsed KrF laser was split into two channels. One channel was used to pump a Raman oscillator, which served as a seed. The other channel was used to pump an RA. The beam quality of the seed beam was 2 ½ times diffraction-limited. The beam

quality of the amplified seed was the same as the beam quality of the seed beam. In other words, the RA described in these two experiments maintained or improved the beam quality of the amplified seed relative to the input seed.

Hanna *et al*. performed a similar experiment in 1985 [53]. In their work, the output of a pulsed XeCl laser was split into two channels. One channel pumped an H_2 Raman oscillator; an aperture inside the oscillator ensured that the output Stokes beam was diffraction-limited. This diffraction-limited Stokes output beam was used as a seed for an H_2 RA which was pumped by the other channel of the XeCl laser. An examination of the waist size and divergence of the amplified seed beam showed that the Stokes output was diffraction-limited. This demonstrated that an RA based on a bulk medium could maintain the beam quality of a diffraction-limited Stokes seed beam.

Reintjes *et al*. also demonstrated an RA which used H_2 as the gain medium [54]. They split the output from a XeCl laser into two channels, which were used to pump both the seed (a Raman oscillator) as well as the RA. In their experiments, an abberator was used to distort the pump beam. However, both the seed and the amplified seed were diffraction-limited. In other words, Reintjes *et al*. showed that even if the RA was pumped with an aberrated pump beam, the beam quality of the seed was maintained.

In summary, previous experiments with gas RAs examined the beam quality of the output of an RA. These experiments demonstrated that the beam quality of the amplified seed was the same as or better than the beam quality of the input seed. This was shown to be the case even for aberrated pump beams.

5.2.2. Demonstrations of Raman Fiber Amplifiers

Lin and Stolen created the first RFA in 1976 [62]. A pulsed dye pump laser was used to amplify a signal which was generated by another pulsed dye laser. The signal was tunable over the range of 540-560 nm. Using a BSRS geometry, the signal was coupled into a 1 m long gain fiber which had a 3.8 μm core. This RFA amplified a small signal by a factor of 45. Gain at higher signal powers was significantly lower due to pump depletion. Lin and Stolen also observed that the gain was reduced when the seed was tuned away from the peak of the Raman gain curve.

Ikdea created an RFA which operated in an FSRS configuration in 1981 [63]. The gain fiber consisted of 1.3 km length of 4.8 μm Ge-doped silica fiber. The pump was a LiNbO$_3$ Q-switched optical parametric oscillator. The seed was generated by a CW Nd:YAG laser. Ikdea examined the effects of polarization on the gain and noted that when the pump polarization was parallel to the seed polarization, the gain was 40% higher than when the polarization of the pump and the seed were orthogonal.

Nakzawa *et al*. studied an RFA based on a singlemode fiber using both an FSRS geometry and a BSRS geometry in 1985 [64]. Their seed source was an RFL which was wavelength tuned between 1.3 μm and 1.6 μm. The pump laser was a polarized Q-switched YAG at 1.34 μm. The gain fiber was a 1 meter long polarization maintaining fiber. In the FSRS configuration, the amplified seed contained two Stokes orders. In the BSRS configuration, only the first Stokes order was observed; higher Stokes orders were absent. Gain as high as 25 dB was reported for the BSRS configuration.

Vilhelmsson compared forward and backward-propagating Stokes beams which were generated using a pulsed, polarized pump beam [65]. Using an 11 μm singlemode

71

fiber with lengths ranging from 15 to 100 m, he observed that the unseeded SRS process generated two Stokes orders in the forward direction, but only a single Stokes order in the backward direction. This asymmetry between the spectral content of the forward Stokes beam and the backwards Stokes beam was similar to the difference noted by Nakazawa *et al*. In both cases, the forward geometry produced multiple Stokes orders, while the backward geometry produced only a single Stokes order. As discussed in Section 5.4.3, the difference between the output spectra of the two geometries can be attributed to FWM.

Previous investigations of RFAs have generally relied on singlemode fibers. While singlemode fibers provide inherently singlemode output, they possess only a limited ability to gather light. Multimode fibers on the other hand, possess a greater ability to gather light. Codemard blended the advantages of singlemode and multimode fibers by creating an RFA based on a DCF with a singlemode core and a multimode inner cladding [66]. The gain fiber had a 9 μm core and a 21.6 μm inner cladding; the output was singlemode. Two lengths of fiber were examined: 400 m and 1100 m. A pulsed MOPA pump at 1547 nm was used to amplify a signal at 1663 nm. An optical conversion efficiency of 36% was reported.

In general, previous studies of RFAs employed pulsed pump beams. One exception was the work of Koepf *et al*., which used a CW pump beam to amplify a signal generated by an LED [67]. As in most previous experiments, singlemode output was achieved by using a gain fiber with a singlemode core.

It is possible to create an RFA based on a multimode fiber and to pump this device with a CW laser. This was demonstrated by Morgan, who developed a RFA based

on graded-index fiber [110]. In his experiment, Morgan coupled an Nd:YAG pump laser into a graded-index fiber with a 50 μm core; long fiber lengths of 5.2 km and 2.5 km were examined. The seed, created using the RFL described in Section 7.2, was coupled into the back end of the RFA. Morgan only considered an RFA configured in the BSRS geometry—the FSRS geometry of the RFA was not examined. Morgan noted that the beam quality of the amplified seed was not as good as the beam quality of a Stokes beam generated by unseeded SRS.

Morgan also considered the spectrum of unseeded Stokes beams generated using the BSRS and the FSRS geometries. He noted that the forward Stokes beam contained a greater number of Stokes orders than the backwards Stokes beam. This difference was attributed to FWM, the phase-matching condition of which can only be satisfied in the forward direction and not in the backward direction.

The experiments described in the rest of this chapter extend the work of Morgan in two ways. First, this original research compares the performance of the BSRS geometry of the RFA to the performance of the FSRS geometry of the RFA in terms of the power, the beam quality and the spectral content of the output Stokes beam. In the FSRS geometry, the beam quality of the seed was roughly maintained by the amplifier. Likewise, in the BSRS geometry of the RFA, the beam quality of the amplified seed was similar to the beam quality of the input seed.

5.3. Amplification of a Low-order Transverse Mode Seed

5.3.1. Introduction

The model presented in Chapter 4 examined the performance of an RFA based on a long graded-index fiber. According to this model, the beam quality of the amplified

seed depended on the beam quality of the input seed beam and the beam quality of the input pump beam. This section validated some of the predictions of the model presented in Chapter 4 by experimentally examining the performance of an RFA based on graded-index fiber with a 62.5 μm core. In these experiments a seed beam with a relatively poor beam quality was used. Two geometries of the RFA were examined: the FSRS geometry and the BSRS geometry. The beam quality of the input pump beam, the beam quality of the input seed beam and the beam quality of the output Stokes beam were characterized for both geometries. Several different launching conditions of the seed beam were examined; this demonstrated that the beam quality of the output Stokes beam was a function of the beam quality of the input seed beam. The gain of the RFA was also characterized and shown to be a function of the launching conditions of the input seed.

5.3.2. Experimental Setup

The setup for studying the RFA using a low-order transverse mode seed launched into the RFA in the BSRS geometry is depicted in Figure 15. The seed was generated by an RFL based on graded-index fiber. The RFL, pumped by an Nd:YAG laser, consisted of a 300 m long Ge-doped fused silica fiber with a 50 μm graded-index core (NA=0.2). A single FBG was spliced onto each end of the RFL. The singlemode reflectivity of each FBG was measured by the manufacturer (Avensys) to be 99.9% at the Stokes wavelength (1117 nm). The output power of the RFL seed averaged ~800 mW; the beam quality of the seed was M^2=3.6±0.1 as it emerged from the RFL. An edge filter separated the seed beam from the residual pump beam. A more detailed description of RFLs based on multimode graded-index fibers is presented in Chapter 7 of this document.

74
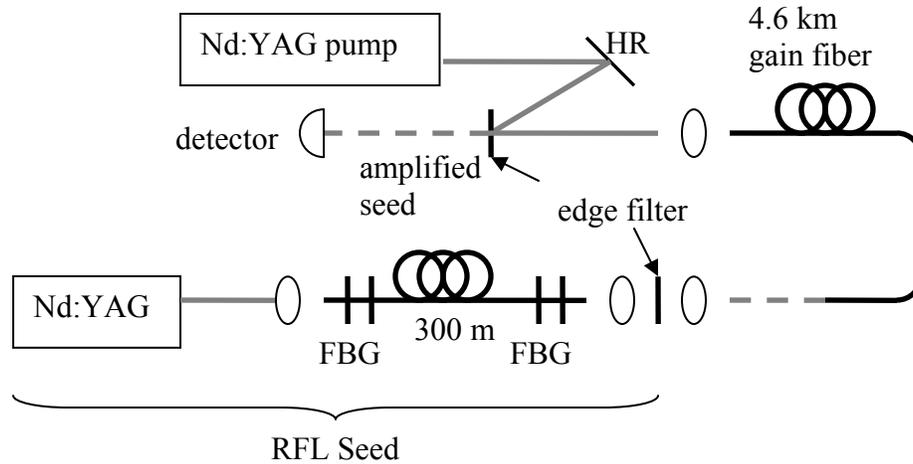
Figure 15. Experimental setup for characterizing the performance of the BSRS geometry of an RFA based on a graded-index fiber. An RFL provided the seed.

The RFA was pumped by a Nd:YAG pump laser at 1064 nm which was launched into the front end of the gain fiber; in the BSRS geometry the seed beam was launched into the back end of the gain fiber. The beam quality of the coupled pump beam was M^2=6.5±0.1. The RFA gain fiber was a 4.6 km long Ge-doped fused silica fiber with a 62.5 μm graded-index core (NA=0.28). An edge filter on the front end of the gain fiber separated the counter-propagating seed beam from the pump beam, allowing the amplified seed to be characterized with respect to its beam quality and power for various launching conditions of the seed.

The setup of the FSRS geometry of the RFA is depicted in Figure 16. In this configuration, the RFL seed laser and the pump laser were both launched into the front end of the gain fiber. An edge filter on the back end of the gain fiber separated the amplified seed from the residual pump beam. An edge filter was also used immediately after the RFL to separate the seed beam from the residual RFL pump beam. The edge filter on the front end of the gain fiber reflected the pump beam into the gain fiber, while at the same time transmitting the input Stokes beam.

75
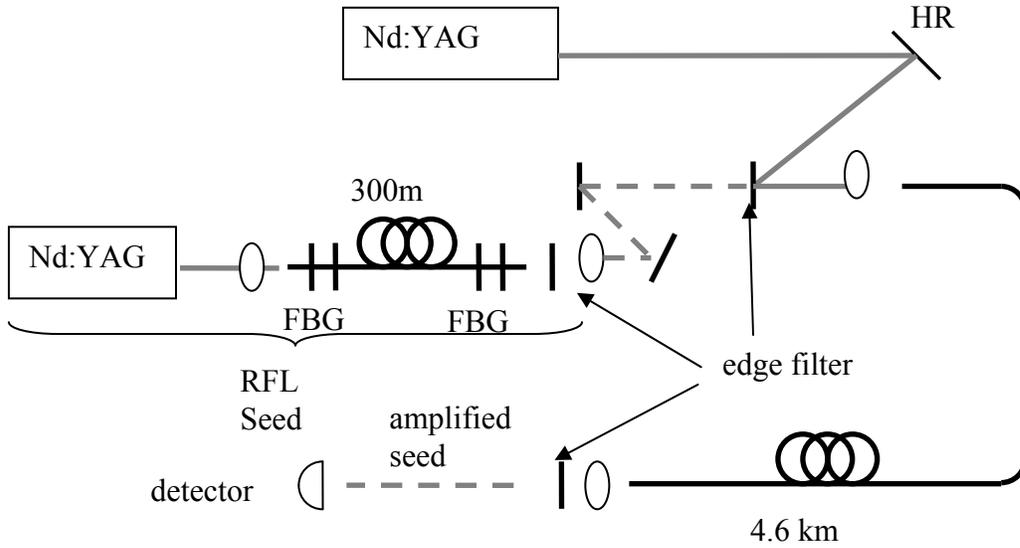
Figure 16. Experimental setup for characterizing the performance of the FSRS geometry
of an RFA based on a graded-index fiber. An RFL provided the seed.

5.3.3. Results & Discussion

5.3.3.1. Beam Quality

The beam quality of the beam was determined by measuring the diameter of the

beam as it traversed the focus of a lens and comparing the resulting profile to the profile

produced by a perfect Gaussian according to [68]

$$w(z) = w_0 \sqrt{1 + \left(\frac{M^2 \lambda (z - z_0)}{\pi w_0^2} \right)^2} \qquad (87)$$

where $w(z)$ is the radius of the beam, z_0 is the measured location of the beam waist and w_0

is the measured radius of the beam waist. Images of the beam were obtained with an

Alpha NIR camera; the beam diameter was determined using the second-moment

method.

In this experiment, the beam quality of the amplified seed was examined as a

function of coupled pump power for 3 distinct launching conditions of the seed beam.

76

The results of this experiment are shown in Figure 17. These measurements indicate that for the BSRS geometry of the RFA, there was a small incremental improvement in the beam quality of the amplified seed as the coupled pump power increased. The most pronounced improvement in beam quality occurred in the case where the coupled seed beam had the worst beam quality.

Since the output of the BSRS geometry exhibited no dramatic changes in the beam quality of the amplified seed as the coupled pump power increased, the beam quality of the amplified seed in the FSRS geometry was only characterized at the maximum available coupled pump power. The beam quality of the amplified seed at the maximum available coupled pump power was compared to the beam quality of the unamplified seed beam as it exited the gain fiber (i.e., the beam quality of the Stokes beam given zero input seed power). This pair of beam quality measurements was taken for three different seed coupling geometries in both the BSRS geometry and the FSRS geometry; the results are detailed in Table 4. The beam quality of the pump beam as it exited the RFA was similar for all three sets of measurements (M^2=6.5±0.1).

Table 4 compares the beam quality of the seed and the amplified seed of both the FSRS and the BSRS geometries and shows that for most of these seeding conditions, the beam quality of the amplified seed was mildly improved relative to the beam quality of the input seed. In one case, the amplified seed produced by the FSRS geometry appeared to be mildly degraded relative to the beam quality of the seed. These measurements demonstrated that the beam quality of the input seed was an important factor in determining the beam quality of the amplified seed. These experimental observations are

consistent with the theoretical results described in Chapter 4. The experimental results are also consistent with the performance of the bulk RAs described in Section 5.1.
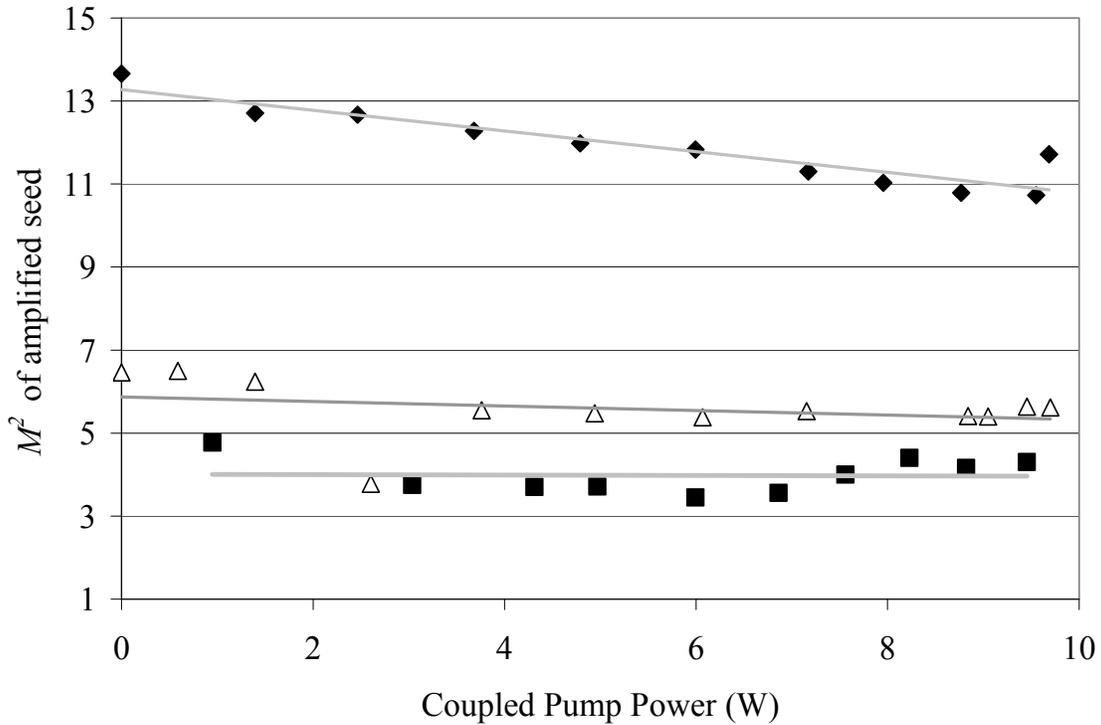
Figure 17. Beam quality of the amplified seed as a function of the coupled pump power for three different seed launching conditions. Each shape represents a different seed launching condition (diamonds, squares and triangles).

The beam quality of the amplified seed for the BSRS geometry was also measured as a function of the input seed power. The coupled seed power was varied using a graded filter wheel which was inserted between the seed RFL and the gain fiber; the filter wheel was gradually rotated to reduce the power of the RFL seed which was coupled into the RFA gain fiber. A plot of the beam quality of the amplified seed versus the throughput seed power is shown in Figure 18. In the absence of a seed, the pump beam generated a Stokes beam with $M^2=1.4$; the resulting Stokes power was on the order of milliwatts. Immediately after a seed beam was introduced, even a seed beam with low

power, the beam quality of the output Stokes beam was immediately degraded by the presence of the poor quality input seed beam.

Table 4. Beam quality measurements of the seed and the amplified seed for both the BSRS and the FSRS configurations of an RFA based on a 62.5 μm diameter graded-index fiber.

BSRS geometry of RFA		FSRS geometry of RFA	
Seed M^2	Amplified Seed M^2	Seed M^2	Amplified Seed M^2
13.7±0.1	10.7±0.6	11.0±0.8	9.2±0.6
6.5±0.2	5.6±0.1	9.6±0.3	10.2±0.9
5.0±0.2	3.8±0.1	5.2±0.2	5.1±0.3
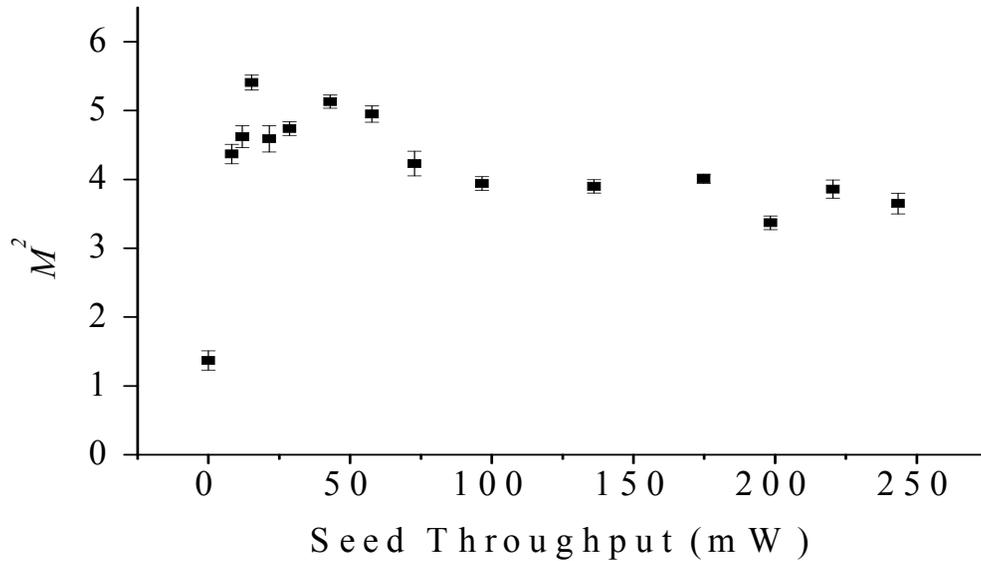
Figure 18. Beam quality of the amplified seed versus the throughput power of the seed beam.

An explanation of these results was presented in Chapter 4. Before reviewing this explanation, it is useful to reemphasize the terminology used to describe the gain of the various modes of the fiber. The gain of each mode, given by Eq. (83), can be divided into two essential parts. The first part is the overlap of a given Stokes mode with the various pump modes of the fiber, $\gamma_{n'n''n'''n''''}$. This term is defined by the overlap integral of Eq. (76). The second part of the gain described by Eq. (83) concerns the power

79

distribution of the pump modes and the seed modes given by the product $A_{n'}A_{n''}A_{n'''}A_{n''''}$.
To understand the experimental results shown in Figure 18, it is important to consider that the power distribution and the overlap integral both affect the gain of a given Stokes mode and that they do so independently. In other words, it is the product of the overlap and the modal distribution that determines the gain of a given Stokes mode.

In this experiment, the pump beam generated an unseeded Stokes beam with good beam quality. The lower-order transverse Stokes modes of the fiber had better overlap with the pump beam than the higher-order transverse Stokes modes of the fiber. Spontaneous Raman scattering provided a uniform internal seed for each Stokes mode and so the Stokes modes with the greatest overlap with the pump beam, namely the lower-order transverse Stokes modes, dominated the Stokes output. As soon as an input Stokes seed was introduced, the seeding Stokes power was no longer uniformly distributed between the transverse Stokes modes of the fiber.

The overlap integrals were not affected by altering the distribution of the seed power, so it was still true that the lower-order transverse Stokes modes of the fiber had better overlap with the pump beam than did the higher-order transverse Stokes modes of the fiber. However, poor launching conditions excited higher-order transverse Stokes modes of the fiber, meaning that Stokes modes with poor overlap with the pump beam but higher initial power competed with Stokes modes with better overlap with the pump beam but lower initial power. In the case of very poor launching conditions, the resulting mode competition did not favor the lower-order transverse Stokes modes. Instead, the higher-order transverse Stokes modes remained the dominant component of the Stokes output. As shown in Figure 14, the beam quality of the amplified seed was very similar

80

to the beam quality of the input seed. As a result, the beam quality of the Stokes beam produced by the RFA was much less dramatic than the beam quality of the Stokes beam produced by unseeded SRS which was described in Chapter 4.

The mode competition in a poorly seeded RFA also affected the total Stokes power of the amplified seed. Power launched into higher-order transverse Stokes modes of the fiber experienced less gain than power which was launched into the lower-order transverse Stokes modes of the fiber. Optimized seed launching conditions produced greater output Stokes power than did poor seed launching conditions. This was demonstrated experimentally as described in the next section.

5.3.3.2. Output Stokes Power

The Stokes power generated by an RFA in the BSRS geometry was characterized as a function of the coupled pump power for two different seed launching conditions. The results of these two measurements are shown in Figure 19. The two launching conditions correspond to the best and worst seed coupling conditions used in the previous section. In the case of optimal coupling of the input seed beam, the input seed power was attenuated using a filter wheel. This ensured that the same amount of power was launched into the gain fiber for the case of poor seed coupling and for the case of optimal seed coupling.

The only difference between the two launching conditions was the modal distribution of the seed power. Even though the coupled seed powers and the coupled pump powers were similar for these two configurations, the output Stokes powers produced by these two configurations were very different. This is because the seed power that was coupled into lower-order transverse Stokes modes experienced more gain

81

than the seed power that was coupled into higher-order transverse Stokes modes. In short, better coupling meant better overlap, which translated into higher overall gain.
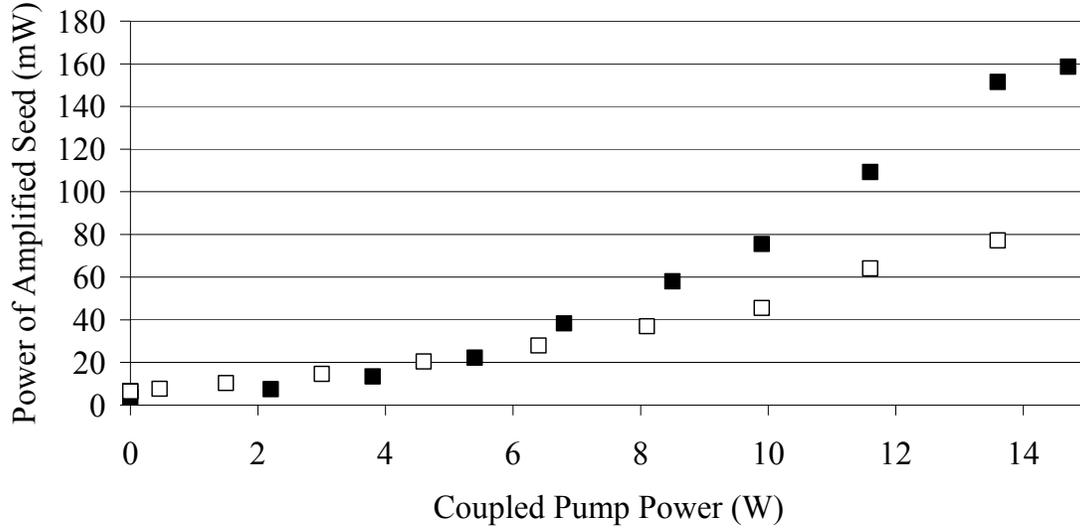
Figure 19. Power in the amplified seed as a function of pump power for two different fiber alignments. Optimum alignment is depicted with filled squares; poor alignment is depicted with hollow squares.

5.3.3.3. Brightness

The combination of the power and the beam quality of a beam can be expressed in terms of a quantity known as brightness. Brightness can be defined as

$$B = \frac{P}{(M^2)^2 \lambda} \, , \tag{88}$$

where P is the power, M^2 is a measure of the beam quality and λ is the wavelength. The BSRS geometry of the RFA described in Section 5.3 produced a ~1 W Stokes beam (1116 nm) with M^2=3.8. This was not as bright as the 10 W, M^2=6.5 pump beam (1064 nm) used to produce it. In the case of the FSRS geometry, the ~ 1 W Stokes beam with M^2=5.1 was also dimmer than the pump beam used to produce it. In short, an RFA based

www.manaraa.com

on a 62.5 μm fiber was not a favorable brightness converter when it was used to amplify a poor quality seed beam.

5.3.4. Summary

These results showed that an RFA based on a multimode graded-index fiber in either a BSRS or an FSRS geometry roughly maintained the beam quality of a seed beam rather than dramatically improving it. This experimentally demonstrated that the beam quality of the input seed determined, at least in part, the beam quality of the Stokes output of an RFA. These results are consistent with the beam quality model presented in Chapter 4 of this document, which predicted that the beam quality of the amplified seed was a function of the beam quality of the input seed.

5.4. Amplification of a Near-Singlemode seed

5.4.1. Motivation

Rice predicted that if a singlemode Stokes signal was launched into an RFA with a graded-index multimode core, the process of SRS and its associated beam cleanup property would maintain the Stokes signal in the LP_{01} mode of the fiber [22]. The model described in Chapter 4 also predicted that a Stokes seed launched only into a single transverse Stokes mode of the fiber would emerge as an amplified seed composed of only a single transverse Stokes mode. As perfectly singlemode propagation of the Stokes seed was not realized experimentally, Rice's prediction was examined by characterizing the performance of an RFA which was instead seeded with a near-singlemode Stokes beam.

The experimental characterization of both the FSRS geometry and the BSRS geometry of an RFA are described in this section. For both geometries, the amplified Stokes seed was compared to the input Stokes seed in terms of its power and its beam

quality. The spectrum of the output generated by these two geometries was also examined.

In terms of its spectral output, the BSRS geometry exhibited superior wavelength confinement relative to the FSRS geometry. Due to FWM enhancement of the Raman gain, the FSRS geometry generated a Stokes beam which consisted of a cascade of multiple Stokes orders. In the BSRS geometry, the phase-matching condition of FWM was not satisfied which delayed the onset of the Stokes cascade relative to the FSRS geometry.

5.4.2. Experimental Setup

The setup for examining the BSRS geometry is shown in Figure 20. In this setup, the gain fiber was a 5.2 km long 50 μm graded-index fiber (NA=0.2) which had been angle polished at both ends to prevent Fresnel reflections. The seed, depicted in Figure 21, was generated using an 8.8 km long 62.5 μm graded-index fiber which was pumped with a CW Nd:YAG laser. A diffraction grating ensured that only the 1st Stokes order of the seed was launched into the gain fiber of the RFA. The beam quality of the output seed beam emerging from the RFL was characterized by M^2=1.4±0.1. The coupling of the seed into the gain fiber was optimized by adjusting the alignment of the input seed relative to the gain fiber in order to minimize the measured M^2 value of the seed as it exited the gain fiber. Because of fiber mismatch however, a value of M^2=1.4±0.1 was not maintained. In the best case, the beam quality of the unamplified seed beam was worse (M^2=2.6±0.1) as it exited the RFA.

The FSRS geometry of the RFA, depicted in Figure 22, also used the seed generated using the setup shown in Figure 21. Again, the seed was coupled into the RFA

gain fiber so as to minimize the measured M^2 value of the seed beam as it exited the gain

fiber.   Great care was taken to ensure that the launching conditions of the pump beam

were the similar for both the FSRS and the BSRS geometries of the RFA.
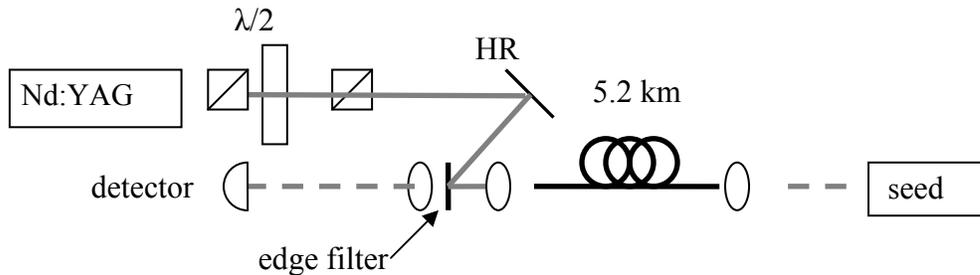
Figure 20. Schematic of the BSRS geometry of the RFA used to amplify a near-
singlemode seed. The setup of the seed is depicted in Figure 21.
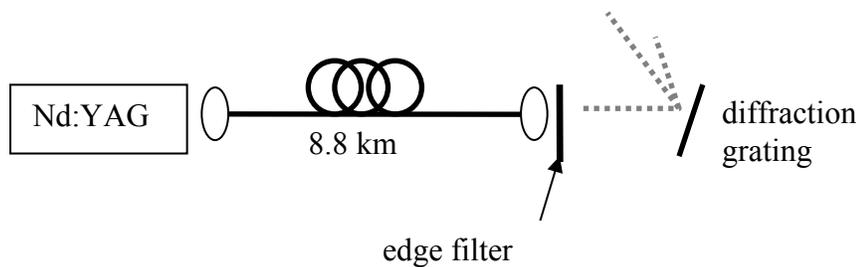
Figure 21. Configuration used to create a near-singlemode seed.

5.4.3. Results and Discussion

5.4.3.1. Spectral Measurements

One of the main differences between the FSRS geometry of the RFA and the

BSRS geometry of the RFA was the number of Stokes components contained in the

output Stokes beam. Due to FWM, the FSRS geometry contained a cascade of Stokes

wavelengths. Since the phase-matching condition of FWM cannot be satisfied for the

BSRS geometry, the Stokes output was primarily contained in the 1st Stokes order. The

Stokes cascade generated using the unseeded FSRS geometry contained the five Stokes

orders shown in Figure 23. Given 3.5 W of coupled pump power, the peak of the 1st

Stokes order was about 3 times higher than the peak of the 2nd Stokes order and about 6.5

times higher than the peak of the 3rd Stokes order.
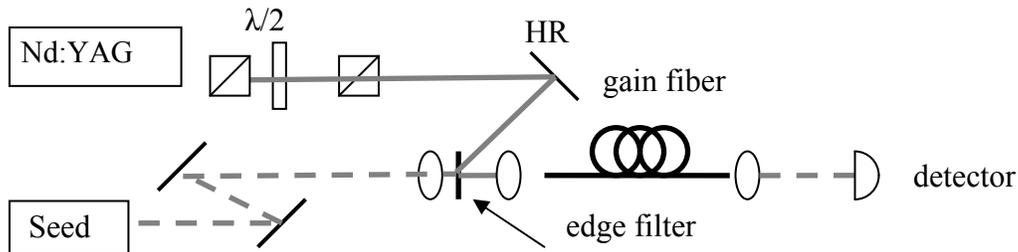
Figure 22. Schematic of the FSRS geometry of the RFA used to amplify a near-singlemode seed. The setup of the seed is depicted in Figure 21.
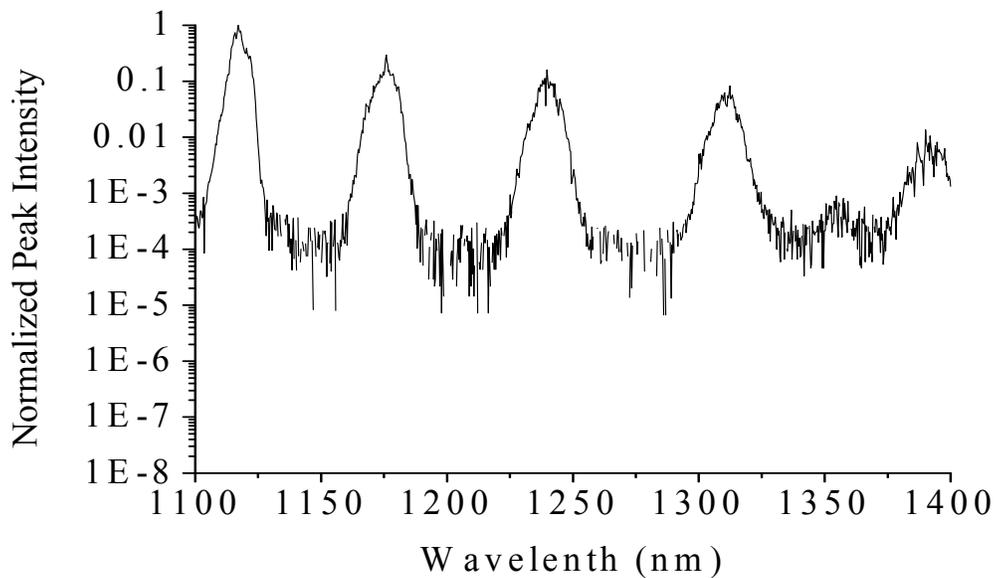
Figure 23. Spectral characterization of the Stokes output of an unseeded FSRS geometry.

The Stokes cascade generated by the seeded FSRS geometry of the RFA is shown

in Figure 24. In this case, the 1st Stokes order had a peak intensity that was about 20

times higher than the 2nd Stokes order and about 64 times higher than the 3rd Stokes

order. An estimate of the power in each Stokes order, made by doing a simple numerical

integration of the area under each intensity curve, is presented in Table 5. The 1st Stokes

order was amplified by a factor of almost 7.2. The 2nd Stokes order was amplified by a

factor of 3 relative to the unseeded case, even though the injected seed contained no 2nd

Stokes order. The power in the 3rd Stokes order was amplified by a factor of

approximately 4.
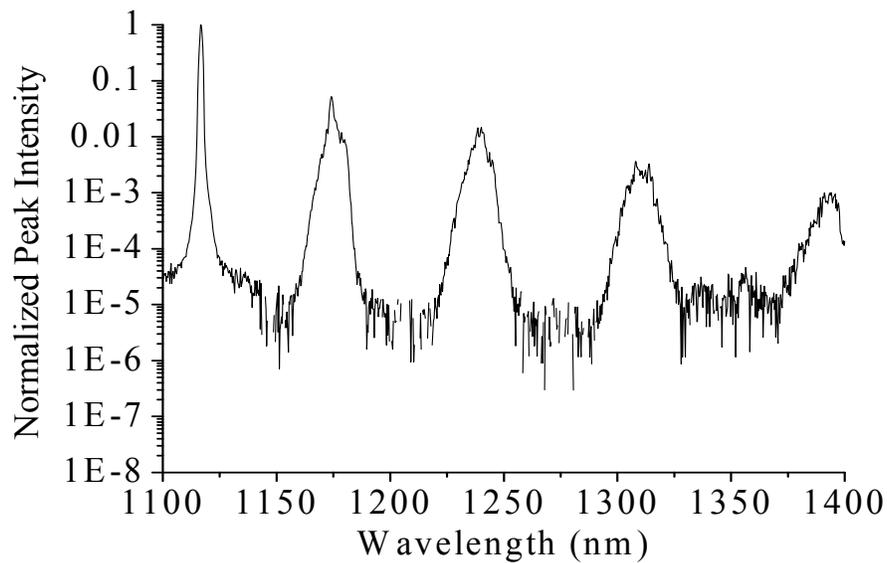
Figure 24. Spectral characterization of the Stokes output of an RFA using the seeded
FSRS geometry.

Having described the Stokes cascades generated by the unseeded FSRS geometry

and the FSRS geometry of the RFA, this section now turns to describing the spectra

produced by the BSRS geometry. The spectrum produced by the unseeded BSRS

geometry is shown in Figure 25, while the spectrum produced by the seeded BSRS

geometry of the RFA is shown in Figure 26. The relative power in each Stokes order,

shown in Table 6, was determined by doing a simple integration of the area underneath

the intensity curves. In the unseeded BSRS geometry, the power of the 2nd Stokes order

was 16 times less than the power of the 1st Stokes order.

87

Table 5. Power generated in various Stokes orders by the FSRS geometry of unseeded SRS and the FSRS geometry of the RFA.

Stokes Order	FSRS		
	Unseeded	Seed	Amplified Seed
1st	68 mW	103 mW	750 mW
2nd	29 mW	--	95 mW
3rd	12 mW	--	47 mW
4th	4 mW	--	8 mW
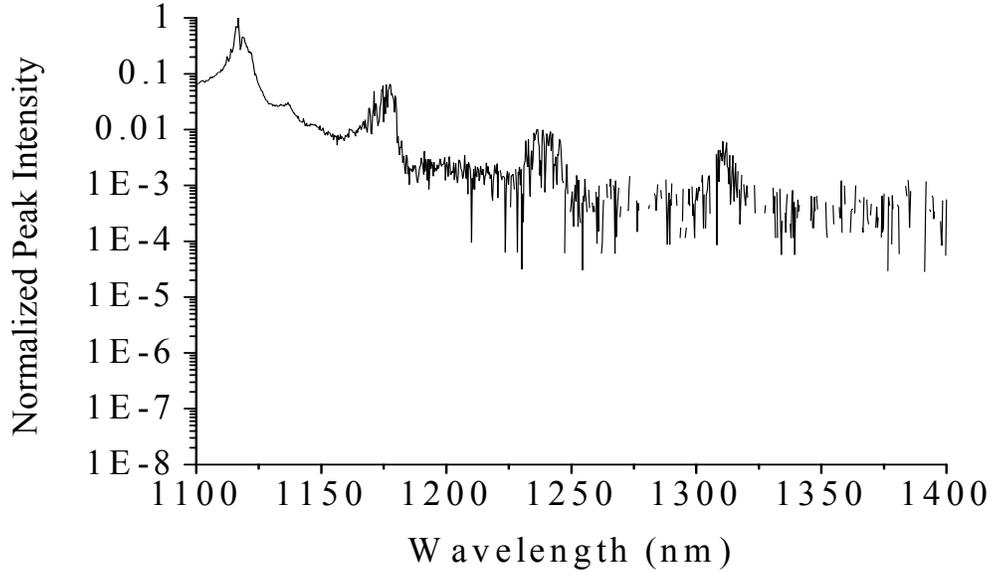
Figure 25. Spectral characterization of the Stokes output of an unseeded BSRS geometry.

The power in the 2nd Stokes order generated by the seeded RFA in the BSRS geometry was about 0.2 mW, which was well under 0.1% of the total generated Stokes power. The peak intensity of the 2nd Stokes order of the amplified seed was about 4.5 orders of magnitude less than the peak intensity of the 1st Stokes order. Clearly the BSRS geometry of the seeded RFA provided better spectral confinement of the output Stokes beam than the FSRS geometry of the RFA. This is attributable to FWM.
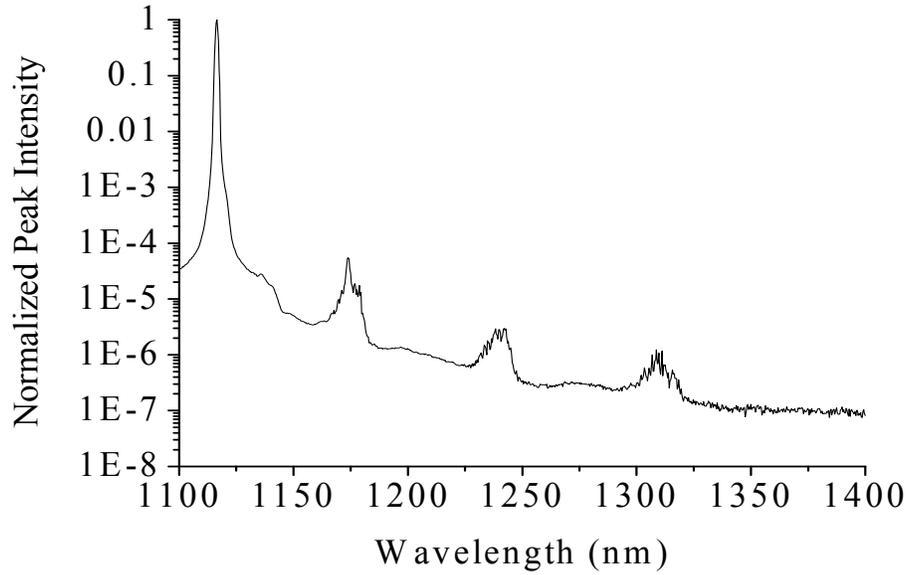
Figure 26. Spectral characterization of the Stokes output of the BSRS geometry of the RFA.

Table 6. Power generated in various Stokes orders by the BSRS geometry of unseeded SRS and the BSRS geometry of the RFA.

Stokes Order	BSRS		
	Unseeded	Seed	Amplified Seed
1st	<5 mW	103 mW	~300 mW
2nd	<0.3 mW	--	~0.08 mW
3rd	<0.04 mW	--	~0.1 mW
4th	<0.01 mW	--	~0.03 mW

FWM is the reason for the difference between the spectral output of the FSRS geometry and the spectral output of the BSRS geometry. Unlike SRS, which is generally considered a self-phase matched process, FWM must satisfy the phase-matching condition given by Eq. (50). Consider the case where FWM combines 2 photons at 1116 nm with a photon at 1064 nm to generate a new photon at 1172 nm. The phase-matching condition of Eq. (50) can be satisfied in a collinear geometry in which the photons at 1116 nm co-propagate with the photon at 1064 nm, as shown by wave vectors in Figure 27(a).

89
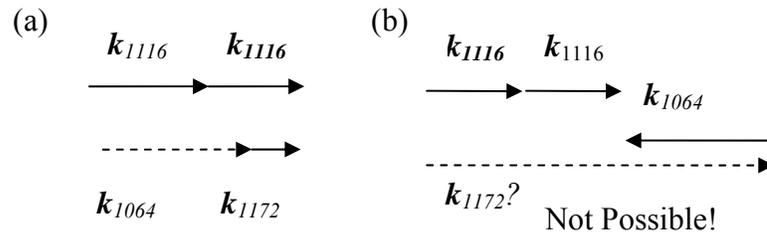
Figure 27. The phase-matching condition of FWM can only be satisfied in the FSRS geometry (a) and not in the BSRS geometry (b) because conservation of energy dictates that $\mathbf{k}_{1172}$ must have a smaller magnitude than $\mathbf{k}_{1116}$.

However, as shown in Figure 27(b), the phase-matching condition cannot be satisfied in a geometry in which the photons at 1116 nm counter-propagate with the photon at 1064 nm. In order to satisfy the phase-matching condition for the BSRS geometry, the magnitude of the wave vector of the 1172 nm photon must be larger than the wave vector of the 1116 nm photon. This is not possible however, since the wave vector is inversely proportional to the wavelength. The magnitude of the wave vector of the 1172 nm photon must be smaller than the magnitude of the wave vector of the 1116 nm photons.

The phase-matching condition for the FWM generation of 1172 nm photons will not be satisfied in the BSRS geometry. Thus, the BSRS geometry will delay the onset of a cascade of Stokes wavelengths by preventing seeding via FWM. This means that the BSRS geometry of the RFA provides better spectral confinement of the amplified seed than does the FSRS geometry.

The FSRS geometry of the RFA clearly generated a significant amount of power in the higher Stokes orders (17%). The Stokes beam generated by the BSRS geometry of the RFA did not contain significant amounts of power in the higher Stokes orders (<0.1%), a clear indication that power was not being efficiently transferred from the lower Stokes orders to the higher Stokes orders. In other words, at the pump powers

90

tested, the Stokes threshold for the higher Stokes orders was not reached in the BSRS geometry.

Evidence of FWM in the FSRS geometry manifested itself during an examination of the Stokes thresholds of several Stokes orders using the experimental setup diagrammed in Figure 28. In this setup a CW Nd:YAG pump laser was coupled into a 5200 m long graded-index fiber with a 50 μm core. An edge filter was used to separate the residual pump beam from the Stokes beam.

The Stokes spectra produced by the FSRS geometry of the RFA at 300 mW, 360 mW, 400 mW and 500 mW of input pump power are shown in Figure 29 through Figure 32 respectively. Comparing Figure 29 with Figure 30 shows that the observed threshold for the 1st Stokes order was between 300 mW and 360 mW of input pump power. Comparing the spectra of Figure 30 and Figure 31 shows that the observed thresholds for the 2nd and 3rd Stokes orders were between 360 and 400 mW of pump power. As demonstrated by the Stokes cascade shown in Figure 32, the observed threshold of the 5th Stokes order was less than 500 mW of pump power.
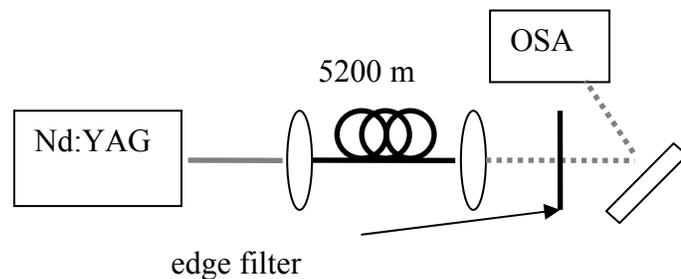
Figure 28. Setup for measuring the FSRS Stokes thresholds associated with a CW, single-pass pumping geometry.

91

These observed threshold values for the sequential Stokes orders cannot be explained by a sequential application of the single-pass SRS threshold condition given by Eq. (46).   Using Eq. (46), the threshold for the 2nd Stokes order corresponds to hundreds of milliwatts of Stokes power in the first Stokes order. The total unseeded Stokes power observed in this experiment was only a few milliwatts; clearly the conventional SRS threshold for the 2nd Stokes order was never reached. Higher Stokes orders were likewise observed to have much lower thresholds than were predicted by Eq. (46).

These low thresholds can be explained by FWM which essentially provided a seed for the higher Stokes orders. The seeded Stokes orders were then amplified by the SRS process. The FWM generated seed lowered the effective threshold of SRS and allowed a forward Stokes cascade at relatively low pump powers. Similar results were obtained by Russell and Roh, who concluded that FWM reduced the threshold of SBS
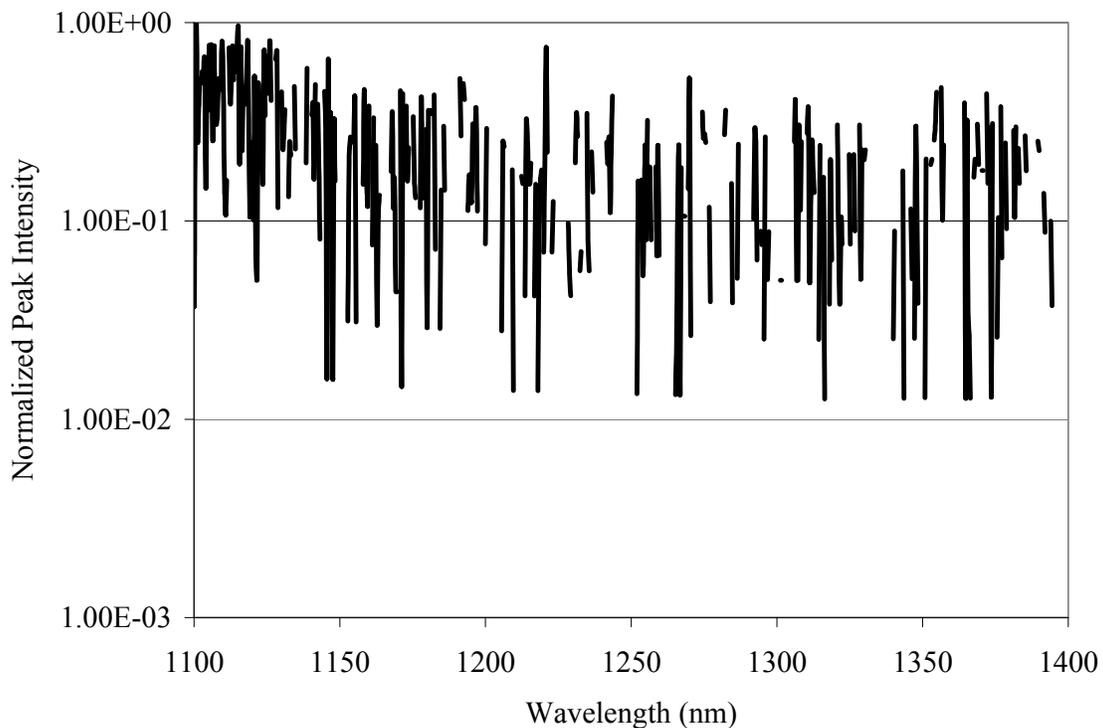
Figure 29. Unseeded Stokes spectra produced by 300 mW of pump power.
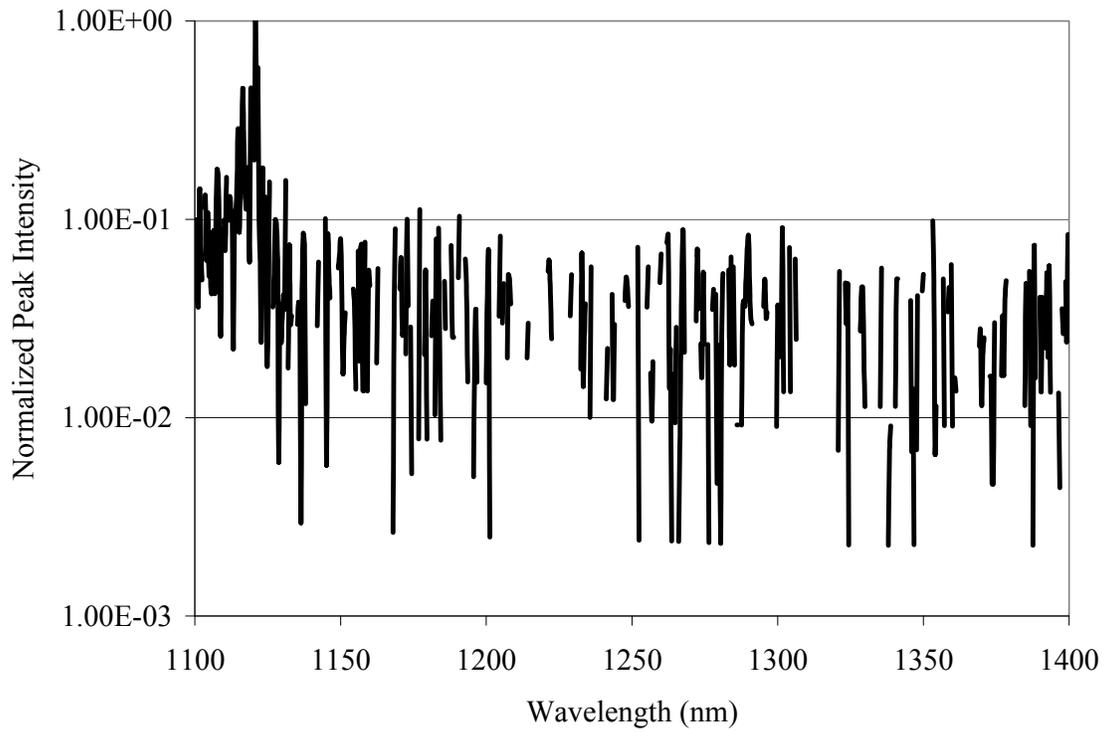
Figure 30. Unseeded Stokes spectra produced by 360 mW of pump power.
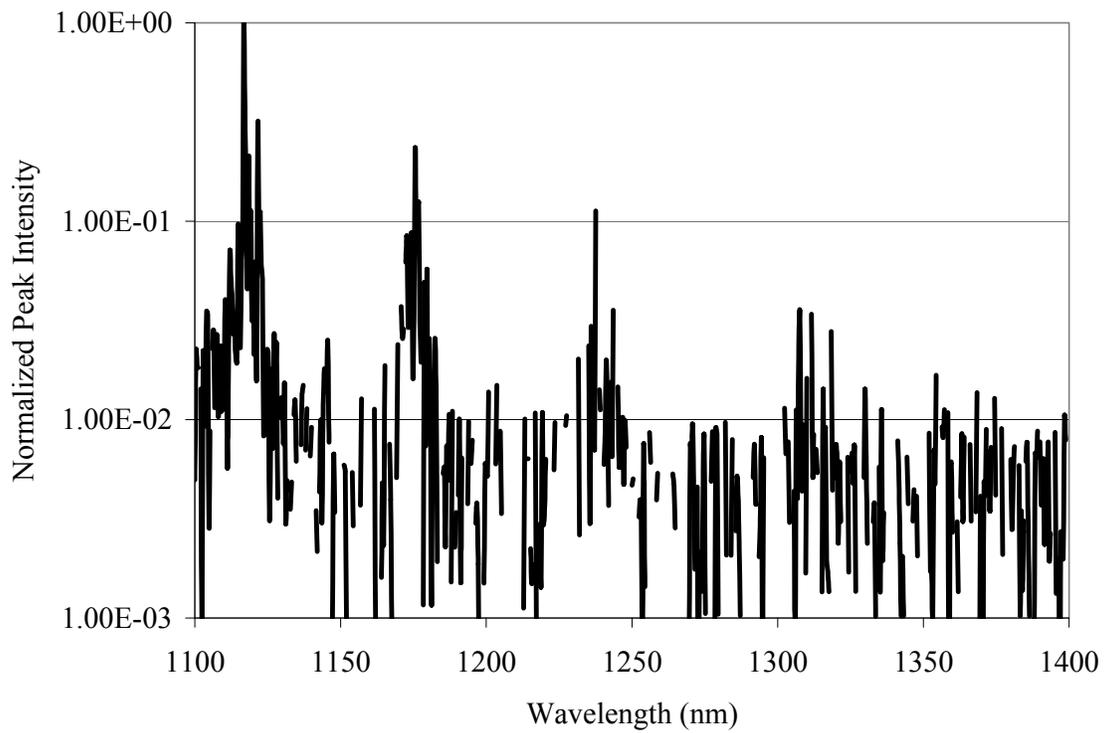
Figure 31. Unseeded Stokes spectra produced by 400 mW of pump power.
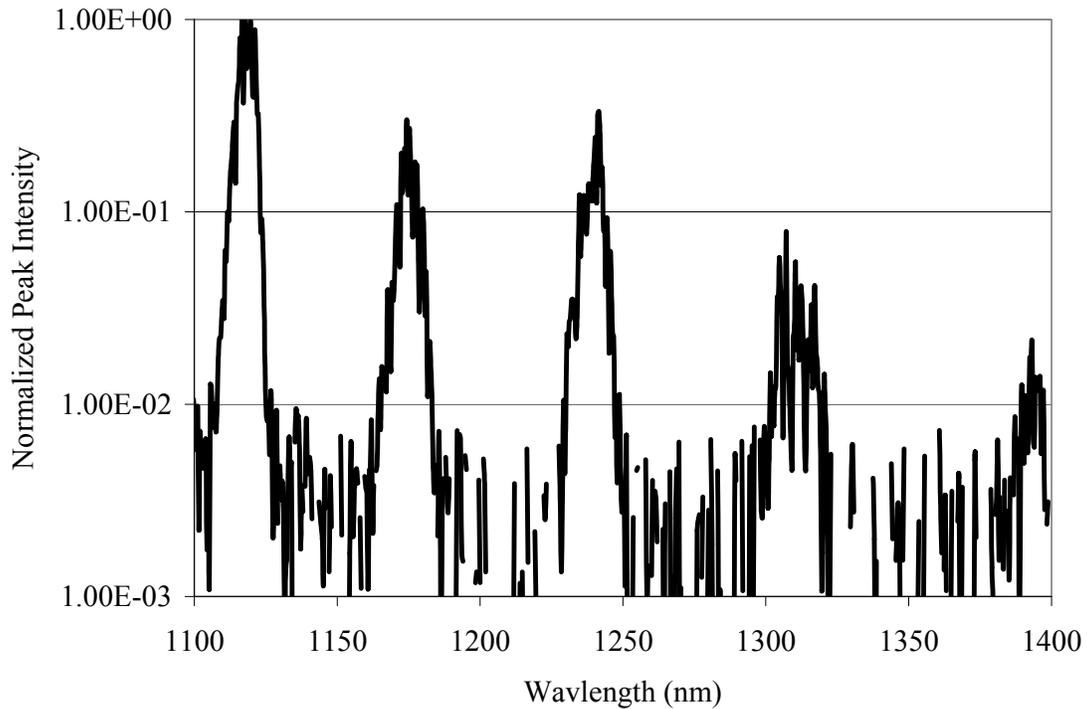
Figure 32. Unseeded Stokes spectra produced by 500 mW of pump power.

[69]. On the other hand, the necessary phase-matching condition for FWM cannot be satisfied in the BSRS geometry and hence the onset of the Stokes cascade was delayed.

In summary, there was clearly a difference between the number of Stokes orders produced using the FSRS and the BSRS geometries of the RFA. This is similar to the observations of Nakazawa *et al*. that two Stokes orders were generated by the FSRS geometry of an RFA and that only one Stokes order was generated by the BSRS geometry of an RFA [64]. Vilhelmsson made similar observations [65]. This difference arose because the phase-matching condition of SRS can only be satisfied in the FSRS geometry.

In the FSRS geometry, the Stokes output contained a Stokes cascade consisting of multiple Stokes orders, with about 17% of the Stokes power residing in higher Stokes

94

orders. In the BSRS geometry, FWM could not be phase-matched. This delayed the onset of the Stokes cascade and as a result, 99.9% of the power was confined to the 1st Stokes order. Even in the BSRS geometry, the power of the 1st Stokes order will eventually become high enough to reach the SRS threshold given by Eq. (46) for the 2nd Stokes order. Once the threshold for the 2nd Stokes order is reached, the 2nd Stokes order will generate 3rd order Stokes photons, via FWM eventually resulting in a cascade of Stokes wavelengths. However, using the BSRS geometry delays the onset of this Stokes cascade relative the onset of the Stokes cascade in the FSRS geometry.

5.4.3.3. Beam Quality Measurements Given Near-Singlemode Seed

This section describes the measured beam quality of an RFA given a near-singlemode input seed. The beam quality of the seed and the amplified seed at 3.5 W of coupled pump power was measured for both the FSRS and the BSRS geometries. A summary of these measurements is provided in Figure 14. The best cases of beam cleanup are shown in Table 7.

Table 7. Best case beam quality measurements of the seed and the amplified seed for both the BSRS and the FSRS geometries of an RFA given optimal launching conditions of a near-singlemode seed beam.

	BSRS geometry of RFA		FSRS geometry of RFA	
Pump	Launched Seed M^2	Amplified Seed M^2	Launched Seed M^2	Amplified Seed M^2
4.5±0.2	3.2±0.2	2.5±0.1	3.7±0.1	2.0±0.1

The results shown in Figure 14 indicate that the beam quality of the amplified seed was similar to the beam quality of the input seed. Simulations based on the model developed in Chapter 4 showed that in the case of a poor quality pump beam, the beam quality of the amplified seed was similar to the beam quality of the input seed. Furthermore, the model of Chapter 4 predicted that a pump beam with good beam quality

95

would produced an amplified seed beam with much better beam quality than that of the input seed beam. Unfortunately, this prediction could not be tested due to the lack of a high power pump beam at 1064 nm with good beam quality.

5.4.3.4. Power Measurements

Besides analyzing the beam quality and spectral content of the Stokes output, the output Stokes power generated by the RFA given optimal seed launching conditions was also examined. The Stokes power was measured as a function of the coupled pump power; the results of this measurement are shown in Figure 33, which provides a comparison of the Stokes powers produced by the FSRS and the BSRS configurations of an RFA as well as the powers generated by unseeded SRS in both geometries. The difference in the measured powers between the two geometries is not understood in this case.

The combination of the beam quality and output power of the amplified seed can be characterized in terms of brightness according to Eq. (88). When the RFA was seeded with a near-singlemode seed, the RFA in an FSRS geometry was a brightness converter which produced a Stokes beam which was up to 30% brighter than the pump beam used to amplify it. In the best case of the BSRS geometry, the output Stokes beam was only 20% as bright as the pump beam which was used to amplify it.

5.5. Chapter Summary

This chapter examined the performance of an RFA based on a 50 μm graded-index fiber. It was experimentally demonstrated that the RFA maintained the beam quality of the seed as it was amplified. This was a sharp contrast to the unseeded SRS

96

beam cleanup addressed in Chapter 4 where the beam quality of the Stokes beam was
dramatically improved relative to the beam quality of the pump beam used to generate it.
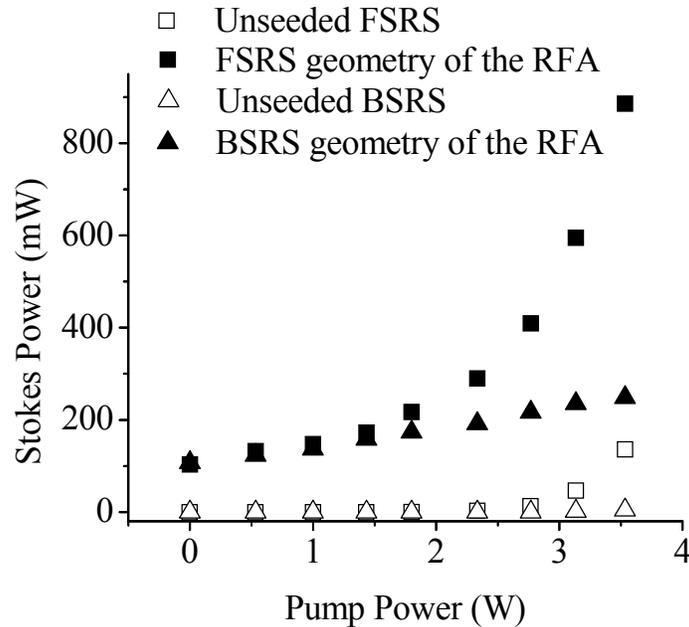
Figure 33. Stokes power as a function of coupled pump power for the FSRS geometry
(squares) and the BSRS geometry (triangles). The output of unseeded SRS (unfilled
figures) and the RFA (filled figures) are shown.

The spectral content of the Stokes beam produced by the RFA was also examined.

The FSRS geometry of the RFA generated a Stokes cascade in which 17% of the Stokes

power resided in the higher Stokes orders. In the BSRS geometry, the Stokes output was

primarily confined to the 1st Stokes order at coupled pump powers of up to 3.5 W; less

than 0.1% of the Stokes power was contained in higher Stokes orders. The difference

between the spectrum produced by the FSRS geometry of the RFA and the spectrum

produced by the BSRS geometry of the RFA was explained in terms of FWM. As the

phase-matching condition of FWM cannot be satisfied in the BSRS geometry, the onset

www.manaraa.com

of a Stokes cascade in the BSRS geometry of the RFA was delayed relative to the FSRS geometry of the RFA.

The Stokes powers generated by the FSRS and the BSRS geometries were also contrasted. Given 3.5 W of coupled pump power, the FSRS geometry of the RFA produced almost 900 W of Stokes power. This corresponded to an optical conversion efficiency of 25%. The BSRS geometry, on the other hand, produced about 300 mW of Stokes power, which corresponded to an optical efficiency of less than 10%. It was also shown that in the FSRS geometry, the RFA functioned as a brightness converter which produced a Stokes beam which was 30% brighter than the pump beam used to generate it.

6. SRS Beam Combination in Multimode Graded-Index Fibers using a Raman Fiber Amplifier

6.1. Introduction

Many authors have investigated ways to efficiently combine semiconductor lasers, fiber lasers and/or solid state lasers to produce a single bright, high power output beam [70]. Coherent beam combination combines beams of the same wavelength and involves some mechanism for controlling the phases of the various beams. Wavelength (or spectral) beam combination utilizes a diffractive optic to combine beams of different wavelengths into a spectrally broad single beam. Beam combination via nonlinear optical processes such as SRS and SBS is another approach that is not easily classified in either of these two categories. The difficultly of achieving the SRS threshold has limited the development of SRS fiber beam combination. Flusche *et al*. overcame this problem by using a pulsed pump laser in conjunction with a fiber beam combiner [20]. By contrast, the work described in this chapter demonstrated that an RFA in either the FSRS geometry or the BSRS geometry can be used for the SRS fiber beam combination of two CW pump beams.

This chapter begins by briefly reviewing previous efforts at nonlinear beam combination in bulk media and in fibers. Next, this chapter describes the experimental setup of a CW SRS fiber beam combiner, with a particular emphasis on the differences between the FSRS and the BSRS geometries of the RFA. The results of these experiments showed that the power and the beam quality of the Stokes output of the RFA beam combiner were similar for both geometries. It is demonstrated however, that the Stokes beam produced by the BSRS geometry of the RFA was more spectrally confined than the Stokes beam produced by the FSRS geometry.

In summary, this chapter demonstrates the feasibility of using an RFA to combine two temporally incoherent CW pump sources to create a single Stokes shifted output beam. While this SRS beam combination technique was only demonstrated for 1064 nm pump sources, it is generally applicable to a large spectrum of other wavelengths, including the more eyesafe region around 1500 nm.

6.2. Background

This section reviews three categories of nonlinear beam combination. First, this section reviews SBS beam combination in fibers because it is complimentary to SRS beam combination. While the latter can be used to combine broadband pump sources, the former can be used to combine narrowband pump sources. Second, this section will review SRS beam combination in bulk media (i.e. H_2 gas). Finally, this section reviews SRS fiber beam combination of pulsed pump lasers [20].

SBS has been used for beam combination in bulk media [71,72]. SBS beam combination has also been demonstrated for SBS in multimode fibers [17,73,74,75,]. Rodgers *et al*. demonstrated both coherent and incoherent SBS beam combination [75]. Coherent beam combination was demonstrated by splitting a single 150 mW diode laser into two channels which were both coupled into a 4.4 km silica fiber with a 9.5 μm core (*NA*=0.12). The fiber supported multiple modes (*V*≈4.4). Incoherent beam combination was demonstrated using a separate 150 mW laser for each channel. In both cases, the Stokes output was shown to be a Gaussian-like beam. Russell *et al*. demonstrated SBS beam combination and beam cleanup in a 4.4 km long 50 μm graded-index fiber [17].

SRS beam combination is another type of nonlinear beam combination which is complimentary to SBS beam combination. The latter provides a higher nonlinear gain

100

coefficient, but places spectral restrictions on the available pump beams due to its narrow gain bandwidth. SRS on the other hand, has a relatively large gain bandwidth (~3 THz at 1 μm wavelength in silica fibers) which allows broadband lasers to be used as pump sources for SRS beam combination. SRS, as well as SBS, has the ability to produce a Stokes beam with far better beam quality than the pump beam. This process, known as beam cleanup, was described in Chapter 4.

Chang *et al*. demonstrated Raman beam cleanup and beam combination in an H_2 RA in 1985 [76]. The pump beam used in their experiment was a frequency-doubled CW dye laser. Part of the pump beam was aberrated and sent to an array of 24 adjustable mirrors segments. Each mirror segment was aligned to focus a part of the diverging pump beam into the RA, essentially pumping the amplifier with 24 separate pump beams. The other part of the pump beam was coupled into a Raman oscillator which created a near-diffraction-limited Raman seed. When the multiple pump beams and the seed beam were launched into the amplifier, the amplified Stokes output was near-diffraction-limited.

Basov demonstrated the SRS beam combination of 50 individual beams in 1984 [77]. In his experiment, the output from an Nd MOPA was separated into 50 individual pump beams which were coupled into an RA which consisted of a 0.5 m H_2 cell nestled inside of a square light-guide. Basov noted that the generation of the 2nd Stokes order was suppressed by reducing the pressure of the gas. (Decreasing the pressure of the gas decreased the Raman gain.) Smith *et al.* also the studied the SRS beam combination of two pump lasers (353 nm) using high pressure H_2 gas [78]. The pump beams were

focused into a Raman gain cell at shallow angles. The diffraction-limited Stokes output contained two Stokes orders.

While SRS beam combination has been demonstrated in bulk media, SRS beam combination in fibers remains largely undeveloped, partly because it is difficult to achieve a low Stokes threshold. Flusche *et al.* demonstrated SRS fiber combination using temporally coherent pulsed pump laser beams [20]. The setup of their experiment is depicted in Figure 34. The pump was an Nd:YAG *Q*-switched laser (1.064 μm). Several beamsplitters divided the pump into four separate channels of equal energy. Each of the channels was coupled into one of the four input fibers of a fiber beam combiner (FBC). The core diameter of each input fiber was 100 μm (*NA*=0.19); the single output fiber of the beam combiner had a core diameter of 105 μm (*NA*=0.49); a significant amount of energy was lost due to this fiber mismatch.

The output from the FBC was coupled into one of two different graded-index gain fibers. The first gain fiber had a core of 100 μm (*NA*=0.29). The second gain fiber was a 2.5 km long 200 μm fiber (*NA*=0.275). The beam quality of the pump beam and the resulting Stokes beam were measured in terms of M^2. In the case of the 100 μm fiber, the beam quality of the transmitted pump beam was measured to be M^2=26.1, while the beam quality of the associated Stokes beam was measured to be M^2=2.6. In the case of the 200 μm fiber, the beam quality was measured to be M^2=42.1 and M^2=2.8 for the pump beam and the Stokes beam respectively.

Besides analyzing the beam quality of the Stokes output, Flusche *et al*. also characterized the spectrum of the Stokes beam using an optical spectrum analyzer (OSA). The output Stokes beam contained of a cascade of multiple Stokes orders. Flusche *et al*.

demonstrated that the higher Stokes orders were highly attenuated by the fiber. Essentially the Stokes cascade transformed the energy of the pump beam into higher Stokes orders which were absorbed by the fiber. As a result, the efficiency of the beam combiner was severely limited.
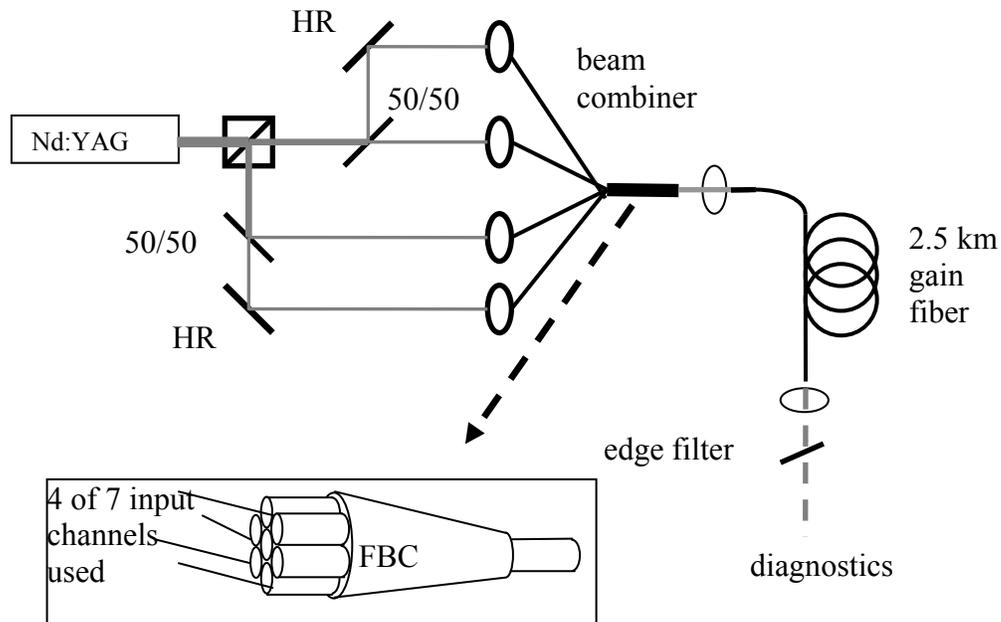
Figure 34. Schematic for SRS beam combination using a fiber beam combiner [20].

While the work by Flusche *et al*. demonstrated the feasibility of SRS fiber beam combination, there were several limitations to their study. First, Flusche *et al*. employed a pump laser which was split into four temporally coherent channels. Furthermore, the work of Flusche *et al*. was limited to studying unseeded SRS, which is why they used the high pump energies produced by a pulsed pump laser. Finally, significant amounts of power were produced in higher Stokes orders, a definite disadvantage considering that the goal was to produce a beam with a narrow-band spectral output.

6.3. Experimental Setup

Having reviewed previous studies of nonlinear beam combination, this section now turns to a description of SRS fiber beam combination. The beam combiner, an RFA based on a multimode graded-index fiber, combined two CW pump beams and generated a single Stokes beam. Both the FSRS and the BSRS geometries of the RFA were examined.

The setup of the FSRS geometry of the RFA is shown in Figure 35. In this setup, two separate unpolarized Nd:YAG pump lasers (1064 nm) were polarized in orthogonal directions using two separate PBSs. Each polarized pump beam (channel) then traversed a λ/2 wave plate before being overlapped into a single beam by passing each channel through a common PBS. Rotating the respective wave plates changed the amount of pump power which was launched into the gain fiber; rotating the wave plates did not alter the launching conditions of either pump beam. The overlapped pump beams were launched into 5.2 km long fiber with a 50 μm graded-index core (*NA*=0.20). The coupling efficiency of both channels was approximately 75%.

In the FSRS geometry, the seed was launched into the same end of the 5200 m long gain fiber as the two pump beams. A near-singlemode seed beam at 1117 nm with M^2=1.4 was generated by using a third Nd:YAG laser (1064 nm) to pump an 8.8 km long fiber with a 62.5 μm graded-index core (*NA*=0.28). The configuration used to generate the seed is diagrammed in the lower left corner of Figure 35. A diffraction grating ensured that only the 1st order Stokes component of the seed was launched into the gain fiber. An edge filter prevented the residual pump beam from damaging the diffraction

www.manaraa.com

grating. The BSRS configuration, shown in Figure 36, was identical, except that the seed

beam was counter propagating relative to the two pump beams.
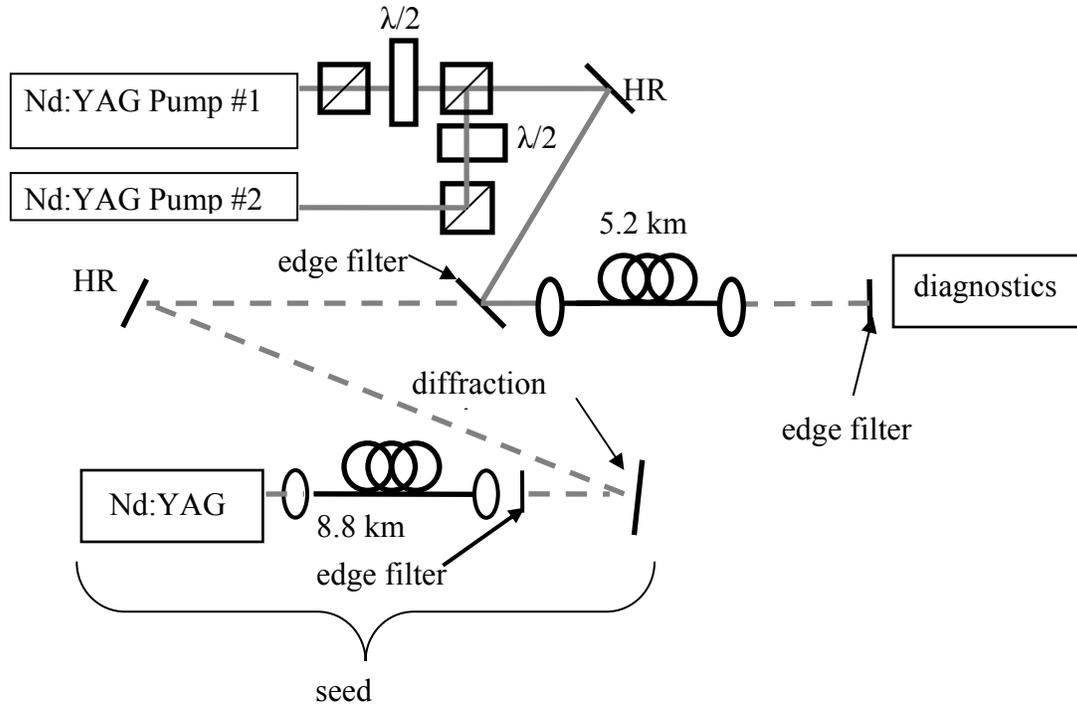
Figure 35. Setup of an SRS beam combiner using the FSRS geometry of the RFA.

6.4. Results and Discussion

The power in the amplified seed was measured as a function of the pump power

coupled into the gain fiber. Initially, the RFA was pumped with only a single pump

channel. Once the coupled pump power in channel #1 reached 5.3 W, additional pump

power was added via pump channel #2. The output Stokes power versus the coupled

pump power is shown in Figure 37. In the graph shown in Figure 38, the coupled pump

power was first added via pump channel #2; additional pump power was then added via

pump channel #1. Both Figure 37 and Figure 38 show that the power of the amplified

seed had a smooth transition between single-channel and double-channel pumping. The

generated Stokes powers were essentially independent of which channel was used for the initial pumping.
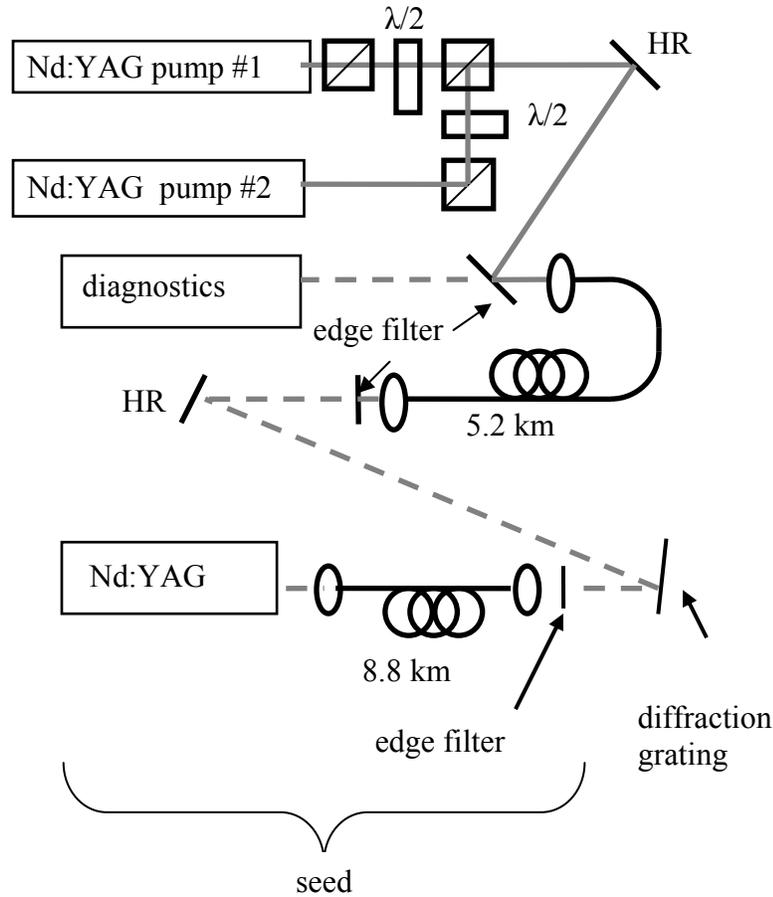
Figure 36. Setup of an SRS beam combiner using the BSRS geometry of the RFA.

The power of the amplified seed is governed by the coupling between Eq. (37) and Eq. (38). By invoking the non-depleted pump approximation, the relationship between the output Stokes power and the coupled pump power is approximated by [79],

$$P_s(L) = P_s(0)\exp(gP_pL_{eff} - \alpha_s L) \qquad (89)$$

where $P_s(0)$ is the seed power, g is the Raman gain coefficient per unit area (g_R/A_{eff}), P_p is the coupled pump power, α_s is the attenuation of the Stokes beam at the Stokes wavelength, L is the length of the fiber and L_{eff} is the effective length of the fiber.   The

fits shown in Figure 37 and Figure 38 plot the Stokes power as given by Eq. (89) assuming a Raman gain per unit area of $g=1.1 \times 10^{-4}$ $W^{-1}m^{-1}$ for the BSRS geometry and $g=1.0 \times 10^{-4}$ $W^{-1}m^{-1}$ for the FSRS geometry. Given a peak Raman gain coefficient of $g_R = 1.0 \times 10^{-13}$ mW^{-1} (the Raman gain of fused silica as given by Stolen [79]), the calculated effective area of the Stokes beam in the fiber was 9.1×10^{-10} m^2 and 1.0×10^{-9} m^2 for the BSRS geometry and the FSRS geometry respectively. In both the BSRS geometry and the FSRS geometry, the effective area was less than the upper bound set by the size of the fiber core (7.9×10^{-9} m^2), but greater than the effective area of the fundamental mode (4.9×10^{-10} m^2) calculated using Eq. (44).
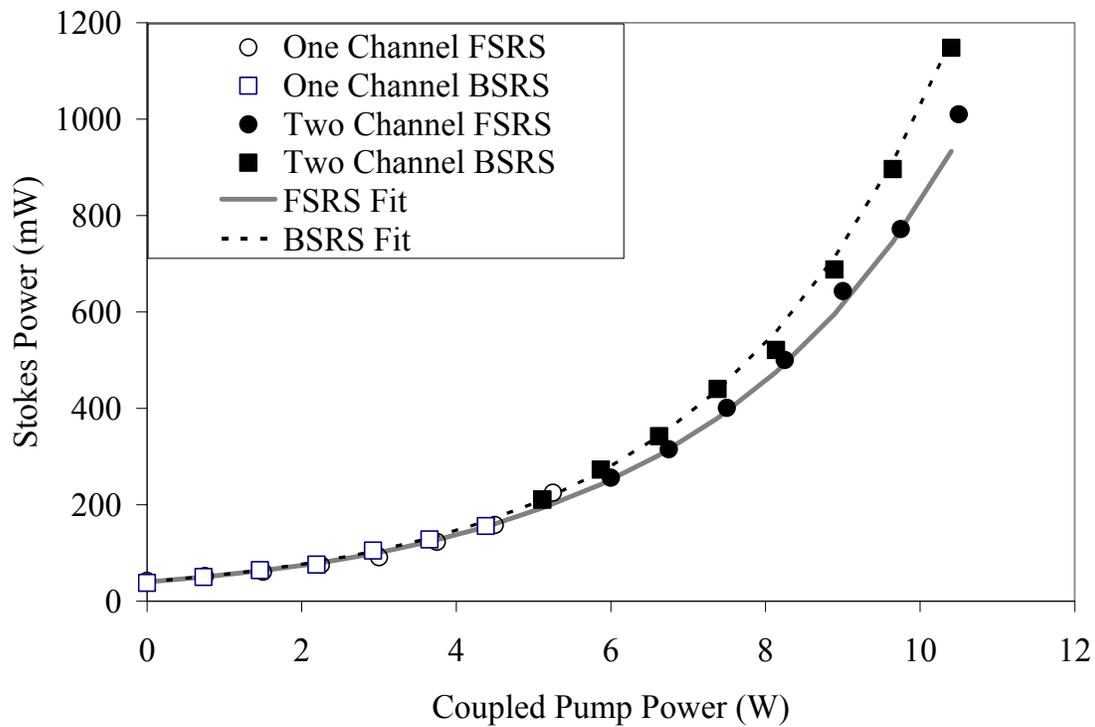
Figure 37. Power in the amplified seed versus the coupled pump power with only pump channel #1 (open circles and squares) and with pump channels #1 and #2 together (closed circles and squares). The power given by the non-depleted pump approximation is also shown (black dashed and solid grey lines).
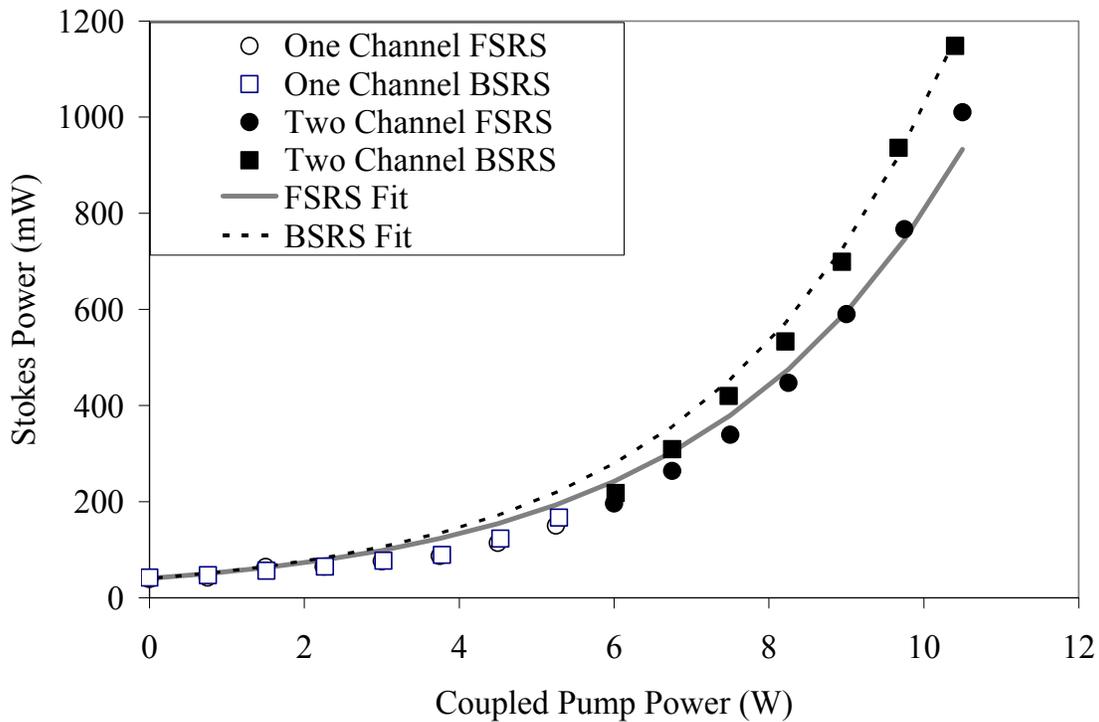
Figure 38. Power in the amplified seed versus coupled pump power with only pump channel #2 (open circles and squares) and with pump channels #2 and #1 together (closed circles and squares). The power given by the non-depleted pump approximation is also shown (black dashed and solid grey lines).

The small difference in the performance of the FSRS geometry and the BSRS geometry is attributed to minor alignment differences between the two configurations. These alignment differences corresponded to different overlaps between the pump and Stokes modes of the fiber, which translated into small differences in the overall Raman gain. A comparison of Figure 37 and Figure 38 shows that the performance of the beam combiner was slightly better when pump #1 was used as channel #1. While both pump lasers launched approximately the same amount of power into the gain fiber, pump #1 had slightly better overlap with the Stokes modes of the fiber. It should also be noted that when the input seed was turned off, there was no significant unseeded Stokes generation (<1mW) in either the FSRS or the BSRS configurations. This indicated that the single-

108

pass Stokes threshold defined by Eq. (46) had not been reached in either geometry of the RFA beam combiner.

Beam quality measurements of the Stokes beam produced by both the FSRS and the BSRS configurations are shown in Table 8. Beam quality in the form of M^2 was characterized by measuring the diameter of the beam at about 20 different locations as it traversed the focus of a lens with a 300 mm focal length. The diameter of the beam at each location was determined using the average of 100 images obtained using an Alpha NIR InGaAs camera. Neutral density filters prevented saturation of the camera. A least-squared fit was determined the value of M^2.

Table 8. The beam quality of the seed beam exiting the gain fiber and the beam quality of the amplified seed when pumped by each individual pump channel and both pump channels together. The beam quality of each pump beam as it exited the fiber is also shown.

	FSRS	BSRS
Seed	3.0±0.1	3.0±0.1
Amp. Seed (Pump #1)	2.5±0.1	2.3±0.1
Amp. Seed (Pump #2)	2.5±0.1	2.4±0.1
Amp. Seed (Pump #1 & #2)	2.3±0.1	2.3±0.1
Pump #1	5.0±0.3	
Pump #2	6.3±0.3	
Pump #1 & #2	5.8±0.3	

In both the FSRS and the BSRS geometries, the amplified seed had slightly better beam quality than the unamplified seed beam. The beam quality of the Stokes beams generated by all three pump configurations was similar. There was no significant difference between the beam quality of the amplified seed produced by the FSRS geometry and the beam quality of the amplified seed produced by the BSRS geometry of the RFA beam combiner. According to Eq. (88), which uses the combination of power and beam quality to describe the brightness of a beam, both the FSRS geometry and the

109

BSRS geometry of the RFA beam combiner produced a Stokes beam with similar brightness. However, the generated Stokes beams were only about 2/3 as bright as the overlapped pump beams used to generate them. In other words, the RFA beam combiner was not a favorable brightness converter in either geometry.

The spectra of the amplified seed produced by the FSRS and the BSRS geometries of the RFA beam combiner are shown in Figure 39 and Figure 40 respectively. For the FSRS geometry at 10.5 W of coupled pump power, the 2nd Stokes order (at approximately 1170 nm) was present along with the 1st Stokes order, but with a peak intensity of <10^{-4} times that of the 1st Stokes order. There was no detectable 2nd Stokes order generated by the BSRS configuration at approximately 10.5 W of coupled pump power. With the pump power available, it was not possible to investigate if the Stokes cascade appeared at higher powers, although this is presumably the case.

6.5. Chapter Summary

The experiments described in this chapter demonstrated that an RFA can be used as a method of SRS fiber beam combination. The high pump power threshold previously reported for unseeded SRS fiber beam combination was avoided by launching a low power seed into the gain fiber. Both the FSRS geometry and the BSRS geometry of the RFA beam combiner were examined. The gain of both geometries was 15 dB at 10.5 W of coupled pump power. The optical efficiency of the RFA beam combiner was approximately 10% for both geometries. It was shown that while both geometries maintained the beam quality of the input seed, the RFA beam combiner was not a brightness converter.

110
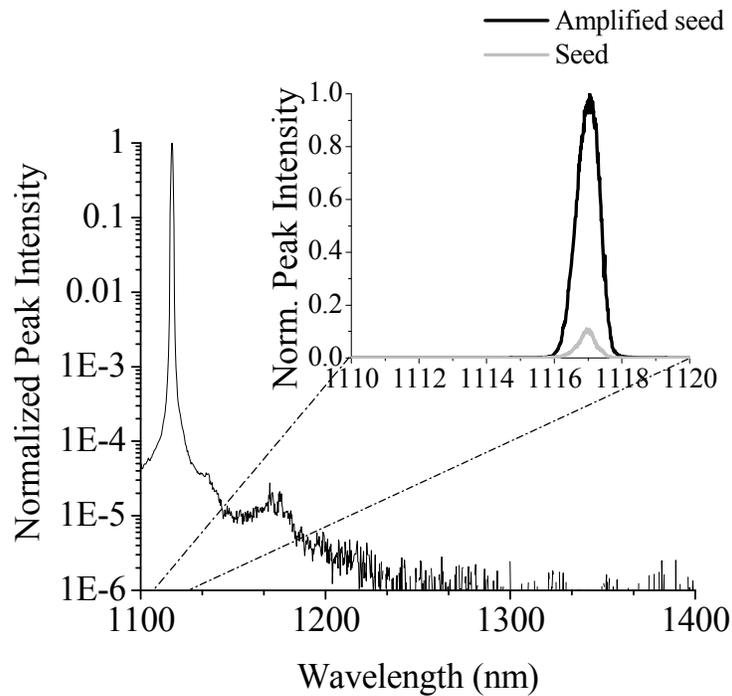
Figure 39. Spectra of the output of the FSRS geometry of the RFA beam combiner. Inset uses a linear y axis scale; otherwise the y axis uses a logarithmic scale.
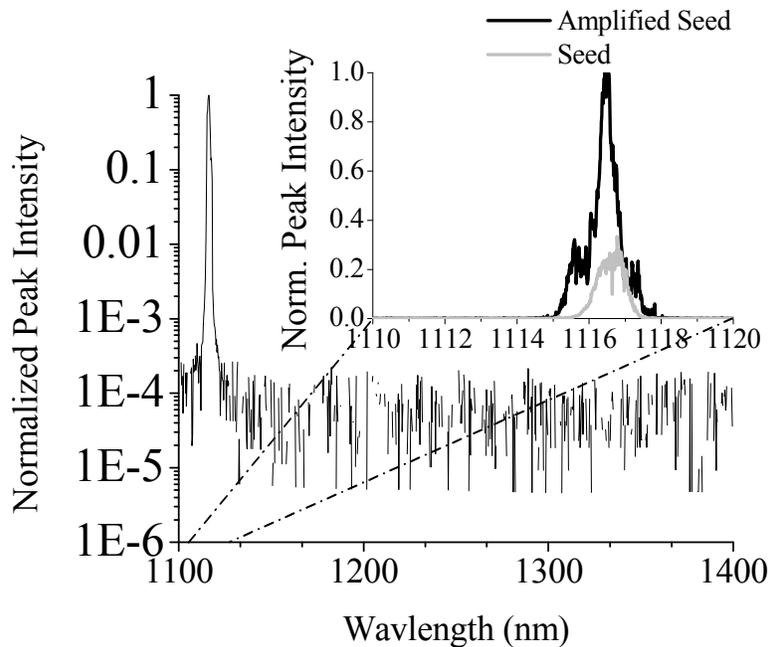
Figure 40. Spectra of the output of the BSRS geometry of the RFA beam combiner. Inset uses a linear y axis scale; otherwise, the y axis uses a logarithmic scale

111

7. Raman Fiber Lasers based on Graded-Index Fibers

7.1. Introduction

RFLs have long been recognized for their ability to generate laser radiation at novel wavelengths. Due to the flexibility of the SRS process, different pump lasers can be combined with various fiber materials to generate a wide selection of laser wavelengths. In general, RFLs have been based on fibers with singlemode cores. This allows singlemode operation, but often requires the use of some sort of singlemode pump beam. This limits the amount of coupled power available for conventional RFLs and restricts the output of these devices to moderate powers.

Recently, an RFL based on a multimode fiber was demonstrated by Baek and Roh [16]. The output Stokes beam was near-singlemode (M^2=1.67). However, the slope efficiency and output power were limited to 7% and 800 mW respectively. Clearly power scaling is needed to make this technology useful in comparison with RFLs which use fibers with singlemode cores. This chapter reports original research which demonstrated the power scaling of RFLs based on multimode fibers.

The first section of this chapter explores FBG technology, with a particular emphasis on FBGs written to multimode fibers (MMFBGs). This section describes the multimode properties of MMFBGs, properties which significantly affect the performance of RFLs based on multimode fibers. The reflectivity of each mode of an MMFBG is associated with a specific wavelength; each of these wavelengths has its own reflectivity coefficient. The first section of this chapter theoretically and experimentally documents the multimode nature of the MMFBGs used to construct the RFLs discussed in the rest of the chapter.

The next section of this chapter details original research demonstrating that RFLs based on a multimode graded-index fiber can produce 7 W of output Stokes power and can operate with slope efficiencies approaching 60%. This is a significant advance relative to the power and efficiency demonstrated by Baek and Roh [16]. However, high output Stokes power comes at the price of degraded beam quality. Higher powers resulted in spectral broadening and gain saturation, which introduced additional wavelength components in the Stokes output. Due to the multimode nature of MMFBGs, these additional 1st order Stokes wavelengths corresponded to higher-order transverse Stokes modes which degraded the beam quality of the Stokes beam.

The research described in this chapter also showed that an RFL based on a graded-index multimode fiber is an effective mechanism for SRS fiber beam combination. This enabled two CW pump beams to be combined to generate a single output Stokes beam. Beam combination was possible due to the low Stokes threshold inherent in an RFL. The performance of the RFL beam combiner was characterized in terms of the spectral content, the beam quality and the power of the output Stokes beam.

7.2. Fiber Bragg Gratings

7.2.1. Introduction

While early RFLs employed dichroic mirrors at each end of the cavity, modern RFLs employ FBGs at each end of the fiber cavity. This makes it possible to fabricate highly reflective elements with linewidths of several nanometers directly onto the singlemode core of an RFL [80]. FBGs have also been created in multimode fibers. One of the main properties of MMFBGs is that different fiber modes are reflected at different wavelengths. Physical changes in the fiber (such as bending) can alter the transverse

modal structure of propagating signal. This allows MMFBGs to be used for sensing applications.

The modal response of the MMFBG also affects the performance of RFLs based on multimode graded-index fibers. Increasing the output power of the RFL leads to spectral broadening and wavelength splitting. An MMFBG translates these new wavelengths into additional transverse modes in the Stokes beam, degrading the beam quality of the Stokes output and partially offsetting the SRS beam cleanup effect.

This section begins by describing the multimode nature of an MMFBG. After briefly outlining the processes used to fabricate FBGs, this section will describe two methods of characterizing of FBGs. These methods are used to characterize the MMFBGs incorporated into the RFLs described in Section 7.3 and Section 7.4.

7.2.2. Background

The first FBG was created by Hill *et al*. in 1978 [81]. A germanium doped silica fiber with a 2.5 μm core was illuminated by an argon ion laser operating at 488 nm. The forward propagating beam and the backward propagating Fresnel reflection combined to form an interference pattern inside the fiber. In the alternating high and low intensity regions of the interference pattern, the index of refraction was altered due to photorefraction. The photosensitivity of a fiber stems from Ge related defects and can be altered by increasing the concentration of dopants in the fiber [82].

In 1989, Meltz *et al*. developed a method to control the spectral responsivity of the grating [83]. In their experiment, a dye laser operating at 486-500 nm was frequency-doubled, split into two equal intensity halves and then recombined to form an interference pattern. The basic geometry of this setup for creating gratings is shown in Figure 41.

The transmission and reflection characteristics of the grating can be tailored by adjusting the angle θ.
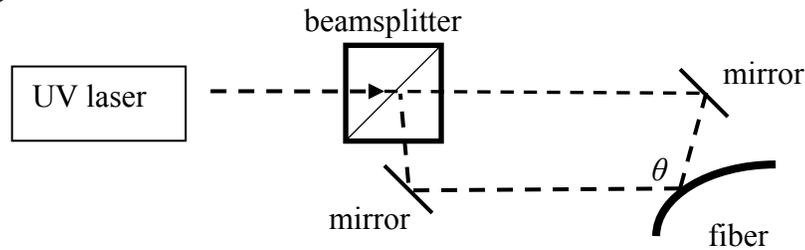
Figure 41. Diagram of an early setup for writing FBGs.

A more commonly used technique for writing FBGs employs a phase mask instead of using a beamsplitter [82]. A common setup for writing FBGs with a phase mask is shown in Figure 42. The phase mask consists of a series of grooves in a UV transmitting mask plate. A cylindrical lens focuses the UV light through the phase mask and onto the fiber, increasing the power density in one dimension without affecting the length of the grating. When the UV light is incident on the phase mask at normal incidence, three diffraction orders are produced: the 0th order and the $\pm 1^{st}$ orders. Two mirrors bring together the $+1^{st}$ and the -1st orders, creating a sinusoidal interference pattern on the fiber. The presence of the 0th order would degrade the interference pattern; a block is inserted to prevent this. Adjusting the mirrors allows the properties of the grating to be modified.

Using a phase mask provides several advantages. First, a phase mask has no moving parts. This lack of moving parts makes the phase mask technique a highly repeatable process suitable for the mass production of FBGs. Furthermore, the lack of moving parts the makes setup extremely stable and allows long inscription times. Lastly, a phase mask setup is insensitive to the translation of the UV beam along the fiber length, allowing long-length FBGs to be written using a scanning technique.

115
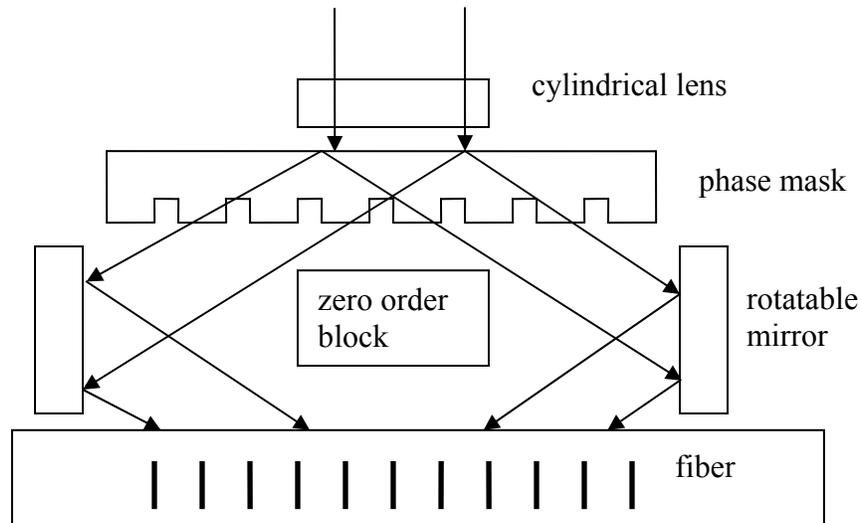
Figure 42. Diagram of a setup for writing FBGs using a phase mask [82].

In 1993, Lemaire *et al*. successfully introduced the technique of hydrogen loading

fibers [84]. Hydrogen loading diffuses H_2 molecules into the fiber at low temperature.

Diffused hydrogen reacts with oxygen to form hydroxyl (OH), which then interacts with

Ge to create GeH. Hydrogen loading allows large index changes to be created in almost

any fused silica fiber.

7.2.3. Characterization of FBGs

Two primary configurations are used to determine the spectral response of an

FBG: measuring the transmissivity and measuring the reflectivity. Measuring the

reflectivity spectrum of the FBG is perhaps the most commonly used method of

characterization. A schematic of this technique is shown in Figure 43. In this setup, a

source is directed to the FBG through a 2x2 fiber coupler; the source can either be a

broadband source or a tunable laser. By incorporating index-matching fluid, light is only

reflected off of the FBG. The power coupled back into the OSA is a direct measurement

of the power reflected by the FBG as function of wavelength.

116
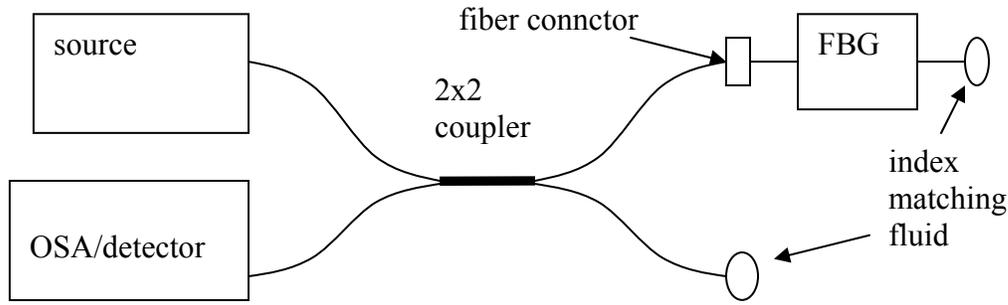
Figure 43. Setup for directly measuring the reflectivity spectrum of an FBG.

Using this method, the reflectivity of the grating is related to the Fresnel reflection of the fiber according to [85]

$$R(\lambda) = \frac{P_1(\lambda)}{P_2(\lambda)} \times \left(\frac{n-1}{n+1}\right)^2 \qquad (90)$$

The power reflected by the FBG as a function of wavelength is denoted by $P_1(\lambda)$. When the FBG is disconnected from the setup, the newly exposed fiber end allows the Fresnel reflection as a function of wavelength to be measured. This measurement, denoted by $P_2(\lambda)$, serves as a reference which can be used to determine the reflectivity spectrum of the grating. Eq. (90) simply states that the ratio between the power reflected by the FBG and the power in the Fresnel reflection is equal to the ratio of the reflectivity of the FBG to the reflectivity of the Fresnel surface.

Measurements of the transmissivity spectrum of an FBG can be made using the relatively straightforward setup shown in Figure 44. The FBG can be illuminated by either a broadband source or a tunable laser. When using a broadband source, the transmission spectrum is characterized using an OSA. When using a tunable laser as the source, a power meter is used to measure the power transmitted by the FBG as a function of wavelength [85]. The FBG can be connected to the source/OSA/power meter using fiber connectors or by splicing the FBG directly to the input/output fibers.

117
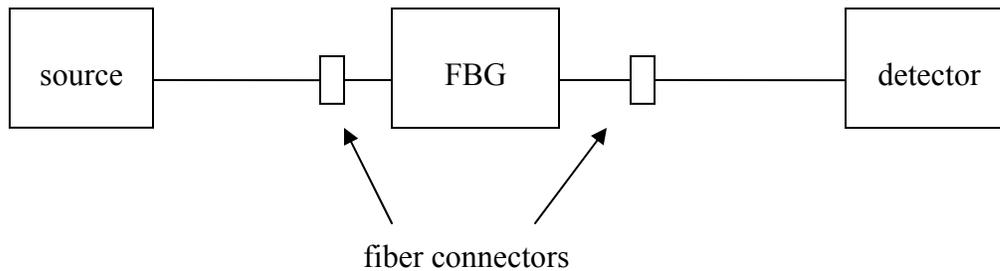
Figure 44. Setup for measuring the transmission spectrum of an FBG.

7.2.4. Fiber Bragg Gratings Written to Multimode Fibers

7.2.4.1. Theoretical Description of MMFBGs

MMFBGs are inherently multimode devices. Conceptually, this can be understood by considering the modes of a multimode step-index fiber in terms of ray optics. Each mode of the fiber can be considered to be a ray propagating through the fiber at a unique angle, θ_r. Bragg's law states that reflection occurs when the period of the grating is related to this angle by

$$2\Lambda \sin \theta_r = j\lambda \tag{91}$$

where Λ is the period of the grating, λ is wavelength and j is an integer. Since the grating period is fixed, each wavelength is reflected a unique angle. As different modes can be considered to be traveling at different angles, they will be reflected at different wavelengths.

The multimode properties of an MMFBG can also be explained in terms of the propagation constants of the various modes of the fiber. The phase-matching condition of an MMFBG is given by

$$\beta_f - \beta_b = \frac{2\pi}{\Lambda} \tag{92}$$

118

where β_f represents the propagation constant of the forward propagating mode and β_b represents the propagation constant of the backward propagating mode. In the case when a mode is reflected back onto itself, i.e., when $-\beta_f = \beta_b$, the phase-matching condition simplifies to

$$\beta = \frac{\pi}{\Lambda} \qquad (93)$$

Rather than considering the phase-matching condition for each of these modes individually, the concept of a principal mode can be applied [85]. A principal mode is a collection of modes which share approximately the same propagation constant. The principal modes of the fiber are labeled by the principal mode number, N_n. The 1st principal mode, $N_n = 0$, is the collection of modes with the highest propagation constant. The 2nd principal mode, $N_n = 1$, denotes the modes with the 2nd highest propagation constant, etc. Table 9 lists several principal modes of a notional graded-index fiber with their associated effective index of refraction and the LP_{lm} modes which they are associated with. The propagation constant of a given LP_{lm} fiber mode is given by [44]

$$\beta_{lm} = \frac{V}{a(2\Delta)^{1/2}} \left[1 - \frac{4\Delta}{V}(2m + l - 1) \right]^{1/2} \qquad (94)$$

By recalling the definition of V given by Eq. (45) and by recalling the relationship between NA and Δ given by Eq. (69), the propagation constant as a function of wavelength can be approximated by [85]

$$\beta(\lambda) \approx \frac{2\pi}{\lambda} n_1 \left[1 - (N_n + 1)\frac{NA\lambda}{\pi a n_1} \right]^{1/2} \qquad (95)$$

where n_1 is the index of the fiber core and a is the radius of the fiber core. The principal mode number is defined as $N_n = 2m + l - 2$. When Eq. (95) is substituted into Eq. (92) or Eq.

119

(93), it becomes clear that different principal modes are reflected at different wavelengths. For example, the LP_{01} mode is reflected on to itself at the wavelength λ_{01}. The LP_{11} mode is reflected onto itself at the wavelength λ_{11}. However, the reflection of the LP_{01} mode onto the LP_{11} mode (and vice versa) occurs at the average wavelength of

$$\frac{\lambda_{01} + \lambda_{02}}{2} [85].$$

Table 9. Table listing the calculated index of refraction of the first 8 principal modes of a notional 50 μm graded-index fiber.

N_n	n_{eff}	modes	N_n	n_{eff}	modes
0	1.4991	LP_{01}	4	1.4955	$LP_{03}, LP_{22}, LP_{41}$
1	1.4982	LP_{11}	5	1.4946	$LP_{13}, LP_{32}, LP_{51}$
2	1.4973	LP_{02}, LP_{21}	6	1.4937	$LP_{04}, LP_{23}, LP_{42}, LP_{61}$
3	1.4964	LP_{12}, LP_{31}	7	1.4928	$LP_{33}, LP_{52}, LP_{71}$

7.2.4.2 Previous Experimental Demonstrations

Several authors have studied the modal response of MMFBGs [85,86,87,88]. These studies confirm that the reflectivity spectrum of an MMFBG is highly dependent on the modal content of the signal incident on the grating. Mizunami *et al*. examined how a signal consisting of lower-order transverse modes of the fiber was reflected by an MMFBG and contrasted this to the reflectivity of signal consisting of higher-order transverse modes of the fiber [88]. Figure 45 shows the reflectivity spectra of the MMFBG given lower-order mode excitation and given higher-order mode excitation.

Yu *et al*. studied MMFBGs illuminated with a singlemode source and showed the reflectivity response was highly dependant on the launching conditions of the singlemode source into the grating [85]. They launched light from a tunable laser into an MMFBG via a singlemode fiber and noted that altering the launching conditions of the singlemode source altered the response spectrum of the MMFBG.

Figure 46 shows the spectrum measured by Yu *et al*. for the case of optimal coupling of the singlemode fiber into the MMFBG. This figure clearly shows that each wavelength has a different reflectivity coefficient. Furthermore, each wavelength corresponds to a different principal mode of the fiber. Given optimized launching conditions, the peak reflectivity was observed at approximately 1525 nm. The rightmost peak corresponded to the lowest-order principal transverse mode of the fiber, while the leftmost peak corresponded to the highest-order transverse principal modes of the fiber where were reflected by the grating.
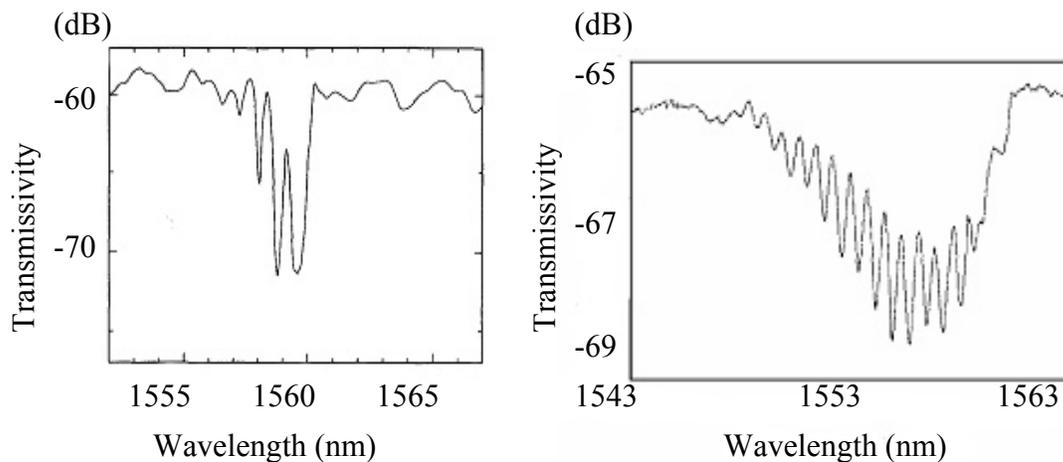
Figure 45. Transmissivity spectrum for a MMFBG given lower-order mode excitation (left) and given higher-order mode excitation (right) [88].

Introducing a lateral offset between the center of the singlemode fiber and the center of the MMFBG coupled the signal into the higher-order transverse modes of the fiber. As a result, the reflectivity spectrum of the MMFBG was altered. The reflectivity spectrum resulting from the offset launching conditions is shown in Figure 47. The higher-order transverse modes of this fiber were resonant with the MMFBG at shorter wavelengths than were the lower-order transverse modes of the fiber. For the offset launching conditions, the principal mode corresponding to a reflected wavelength of 1515

nm had the greatest reflectivity. No significant power was reflected in the principal mode corresponding to 1525 nm. The principal mode associated with 1520 nm had a reflectivity of about 10% for both the optimized launching condition and the offset launching condition. By contrast, the peak at ~1522 nm had a reflectivity of 30% for the optimized launching condition and a reflectivity of between 5% and 10% for the offset launching condition. This clearly shows that different modes of the fiber are reflected by the MMFBG at different wavelengths.
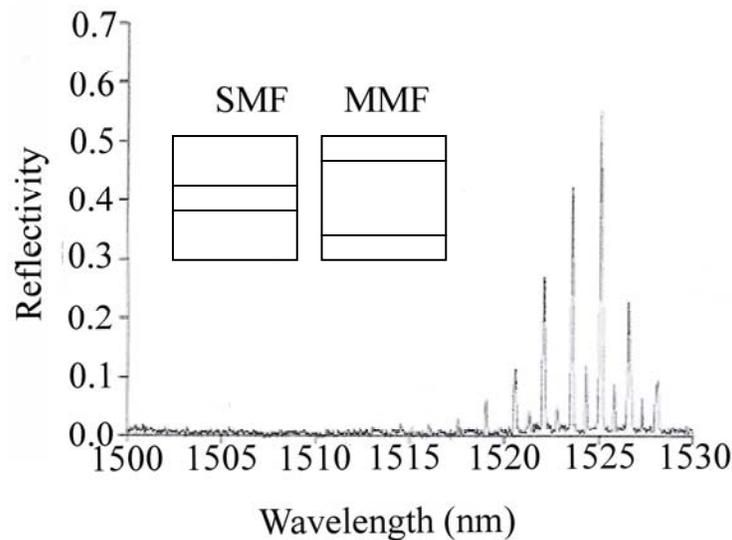
Figure 46. Transmission spectrum of an MMFBG when the singlemode input fiber was centered on the MMFBG [85].

The multimode character of MMFBGs has also been demonstrated in experiments which used MMFBGs to construct wavelength tunable lasers. Introducing microbends to the fiber changes the mode structure of the propagating field and hence the observed reflectivity spectrum of the grating. Su and Lu capitalized on this to create a fiber laser with variable wavelength output [89]. A 3-tooth deformer introduced microbends into a segment of multimode fiber immediately preceding the MMFBG. Different modes of the

cavity were resonant with the grating at different wavelengths. This allowed the laser output to be tuned to one of 31 discrete wavelengths. Yu *et al.* used a similar technique by incorporating an MMFBG into a laser cavity. By adjusting the alignment of the pump laser relative to the MMFBG, Yu *et al.* altered the transverse mode content of the light incident on the MMFBG which allowed the resonant output wavelength to be selected [90].
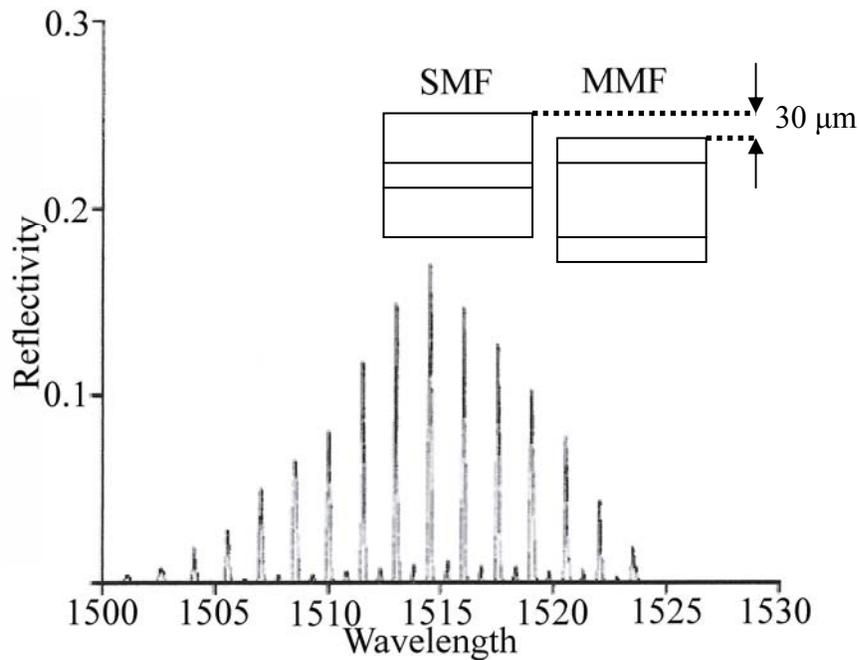
Figure 47. Transmission spectrum of an MMFBG when the singlemode input was laterally offset from the MMFBG [85].

It should also be noted that the reflectivity spectrum of an MMFBG can have a polarization dependence. This provides another avenue for the creation of wavelength selectable fiber lasers [91,92]. By incorporating a polarizer into the laser cavity, the loss experienced by various modes was altered to prevent (or allow) lasing to occur at different wavelengths. It was also shown that properly adjusting the polarization allowed multiple wavelengths to be produced simultaneously.

123

These experiments confirm that MMFBGs do not reflect light in the same way as would a narrowband FBG written to a singlemode fiber. Furthermore, the MMFBG does not reflect light as would some sort of broadband dichroic mirror. Instead, MMFBGs reflect different transverse modes of the fiber at different wavelengths and with different reflectivities.

While MMFBGs have often been used as a mechanism for wavelength selection, they also have demonstrated applicability to RFLs. It was shown by Baek and Roh that MMFBGs can be used as part of an RFL based on a multimode fiber [16]. At the low powers demonstrated in their experiments, the multimode nature of gratings and its effect on the beam quality of the Stokes beam did not become apparent. The work described in this dissertation shows that at high Stokes powers the multimode nature of the MMFBG affects the beam quality of the Stokes output of an RFL based on a multimode fiber. The following section describes the reflectivity spectra of the MMFBGs used to construct the RFLs described in this document.

7.2.5. Experimental Setup and Results

Three different sets of measurements were used to characterize the MMFBGs used in this dissertation effort. The manufacturer of the gratings (Avensys) characterized the spectral response of the MMFBGs to a singlemode source. In this characterization, the setup of which is diagrammed in Figure 44, a piece of singlemode fiber was attached to each end of the MMFBG. One piece of singlemode fiber connected the MMFBG to the fiber source while the other piece of singlemode fiber connected the MMFBG to the OSA. The reflectivity spectrum reported by Avensys, shown in Figure 48, exhibits a broad reflectivity peak centered at 1116.5 nm, with a FWHM of 1.52 nm and a ~99%

reflectivity. The adjacent left peak corresponds to a higher order principal mode. The reflectivity of this higher-order principal mode was ~10 dB or 90% according to Avensys.

The reflectivity response of this same grating was characterized using the setup depicted in Figure 43. A short piece of singlemode fiber was inserted between the broadband source and the 2x2 connector. The spectral response of the grating, depicted in Figure 49, shows that the first principal mode of the fiber was reflected at 1116.5 nm; additional principal modes were reflected at wavelengths separated by several tenths of a nanometer.

The transmissivity response of the MMFBG to a multimode source was also measured using the setup depicted in Figure 44. In this case, the output of the broadband source was coupled into a short piece of 50 μm graded-index fiber. The response spectrum of the grating is shown in Figure 50. The results are similar to those obtained by Mizunami et *al*. [88].

The essential difference between the reflectivity spectrum shown in Figure 49 and the transmissivity spectrum shown in Figure 50 is the modal composition of the input source. The spectral response shown in Figure 49 was generated when the broadband source was coupled into a short piece of singlemode fiber. The spectral response shown in Figure 50 was generated when the broadband source was coupled into a short piece of multimode fiber. The same broadband source was used for both characterizations.

Several other MMFBGs were used in the RFL experiments described in Section 7.3 and Section 7.4 of this document. The reflectivity response of each of these gratings

www.manaraa.com

was characterized using the setup depicted in Figure 43. In each case, a singlemode piece of fiber connected the broadband source to the 2x2 coupler.
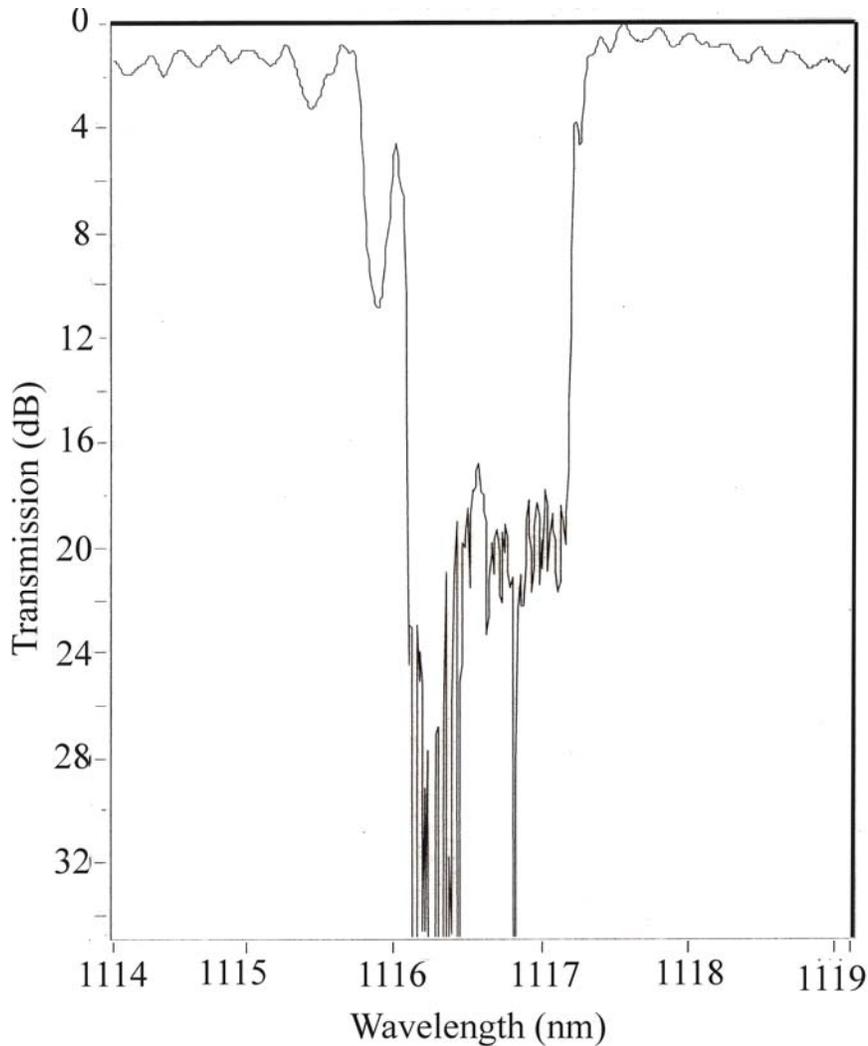
Figure 48. The transmission spectrum of an MMFBG as measured by Avensys. Note the logarithmic scale on the y axis.

The reflectivity response of additional gratings is shown in Figure 51 through Figure 54. Avensys reported the singlemode reflectivity of these MMFBGs to be R=90%, R=80%, R=60%, and R=30% respectively. The rest of the document refers to these gratings by the singlemode reflectivity reported by the manufacturer.

This section reviewed the properties of MMFBGs from a theoretical standpoint; these multimode properties were also demonstrated experimentally. The experimental evidence presented here includes studies by previous authors who documented the multimode properties of MMFBGs. More importantly, the work in this section experimentally characterized the MMFBGs used to construct the RFLs described in Section 7.3 and Section 7.4. This analysis showed that the MMFBG with a singlemode reflectivity of R=99% exhibited a highly multimode reflectivity response to an input signal. It was clearly demonstrated that an MMFBG reflects each principal mode of the fiber at a different wavelength.
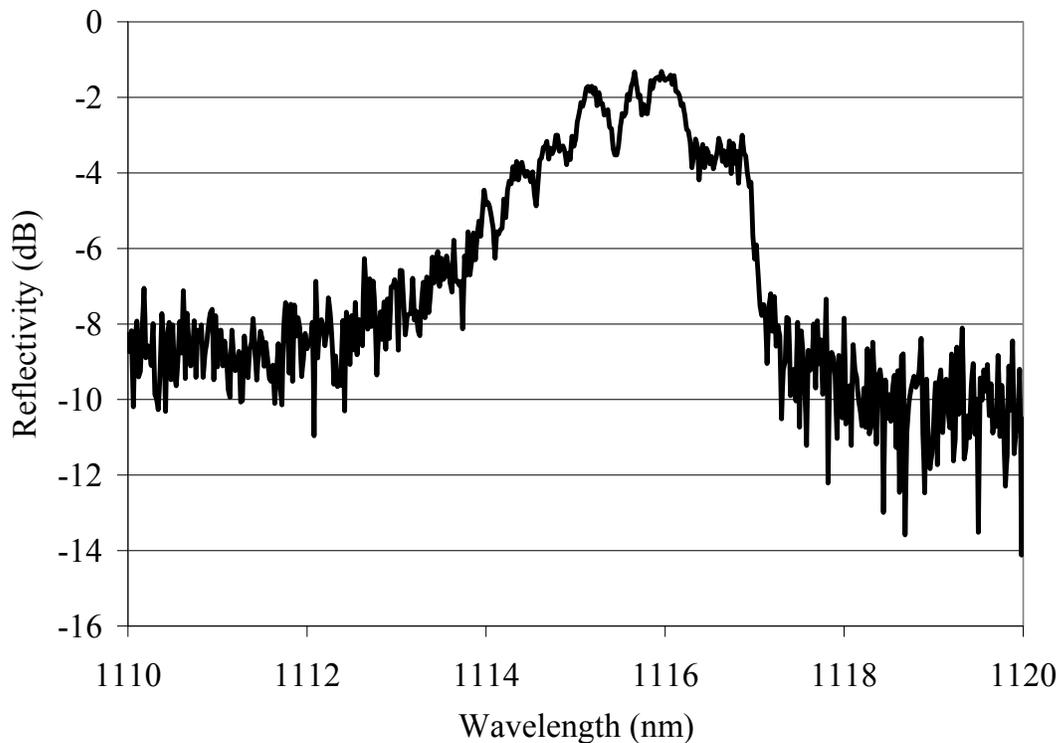
Figure 49. Lower-order mode reflectivity of a grating reported by the manufacturer to have a singlemode reflectivity of R=99%; the source was coupled to a singlemode fiber.
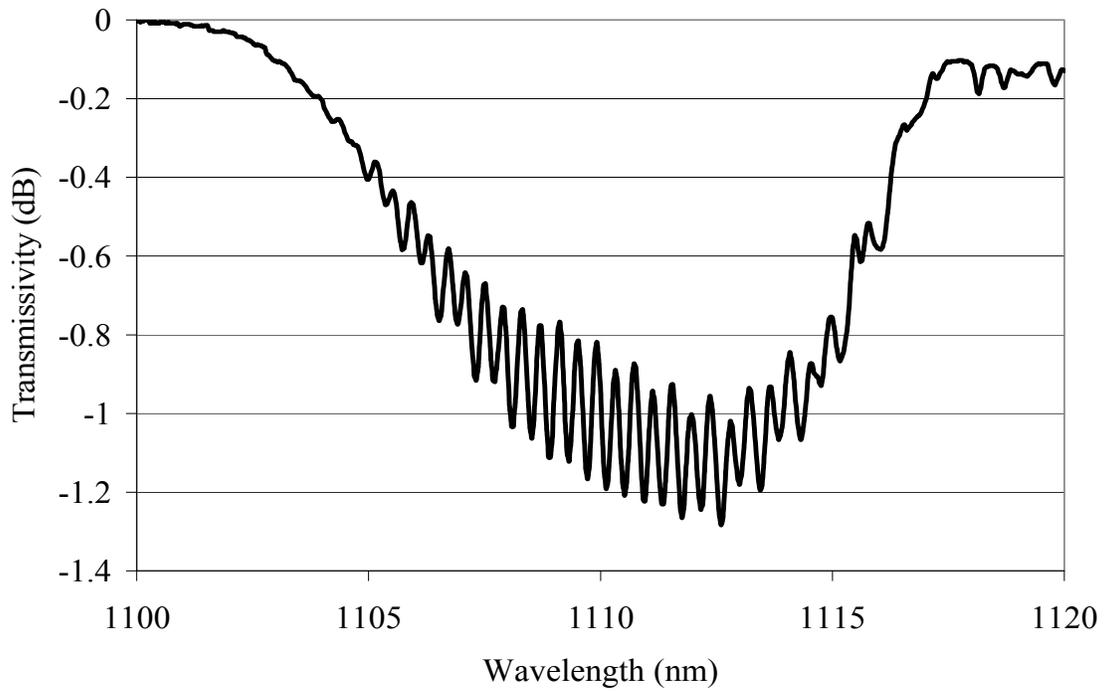
Figure 50. Transmissivity spectrum of an MMFBG reported by Avensys to have a singlemode reflectivity of *R*=99%. The source was coupled to a multimode fiber.
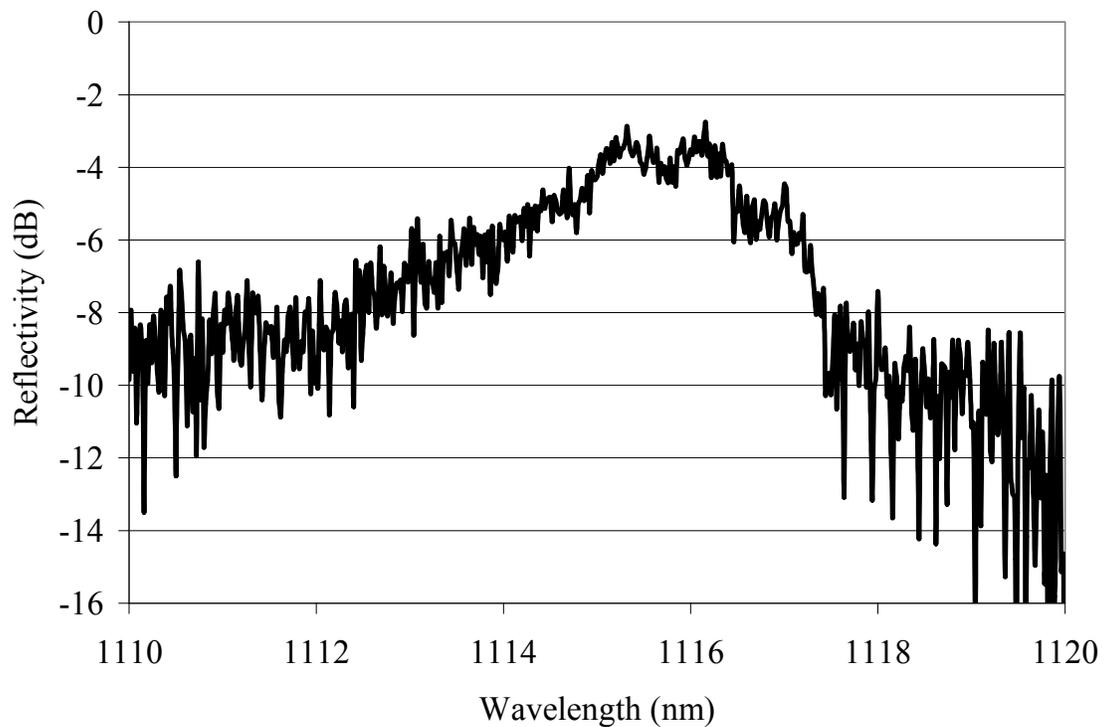
Figure 51. Lower-order mode reflectivity of an MMFBG reported by the manufacturer to have a singlemode reflectivity of *R*=90%.

128
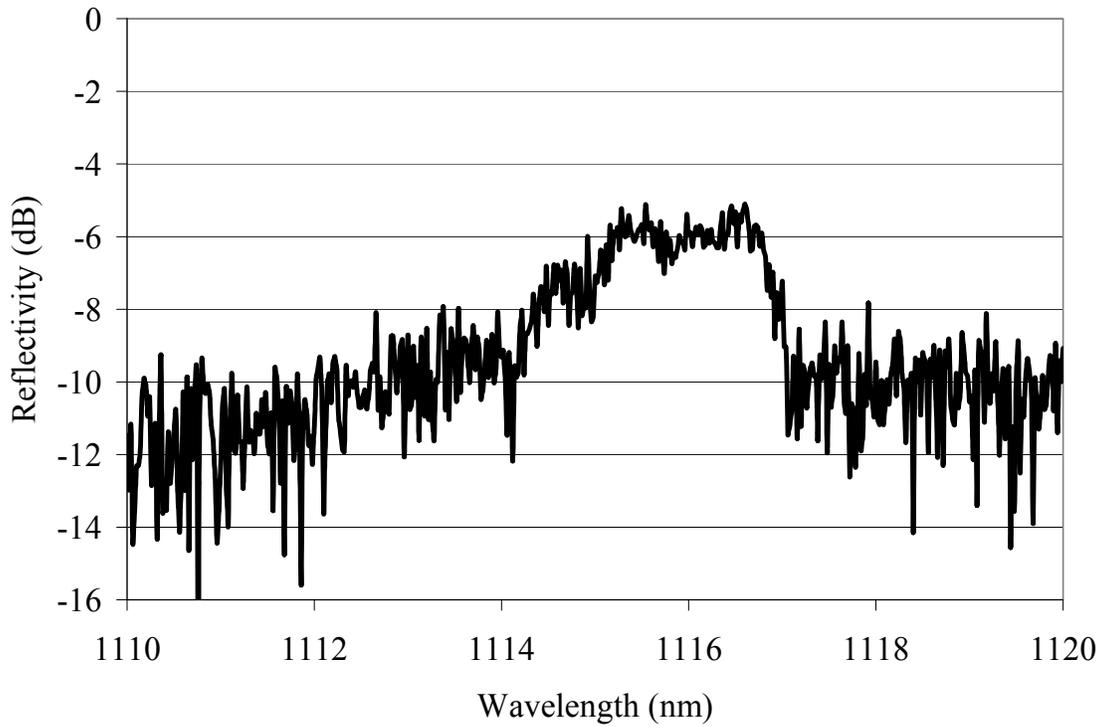
Figure 52. Lower-order mode reflectivity of an MMFBG reported by the manufacturer to have a singlemode reflectivity of R=80%.
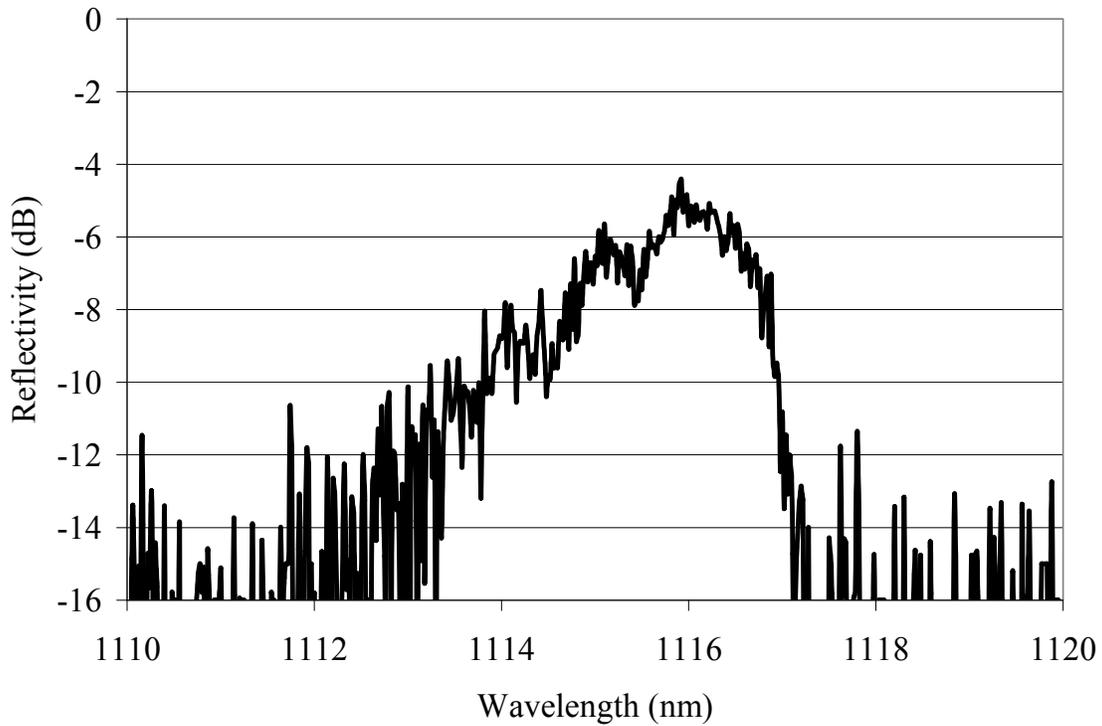
Figure 53. Lower-order mode reflectivity of an MMFBG reported by the manufacturer to have a singlemode reflectivity of R=60%.
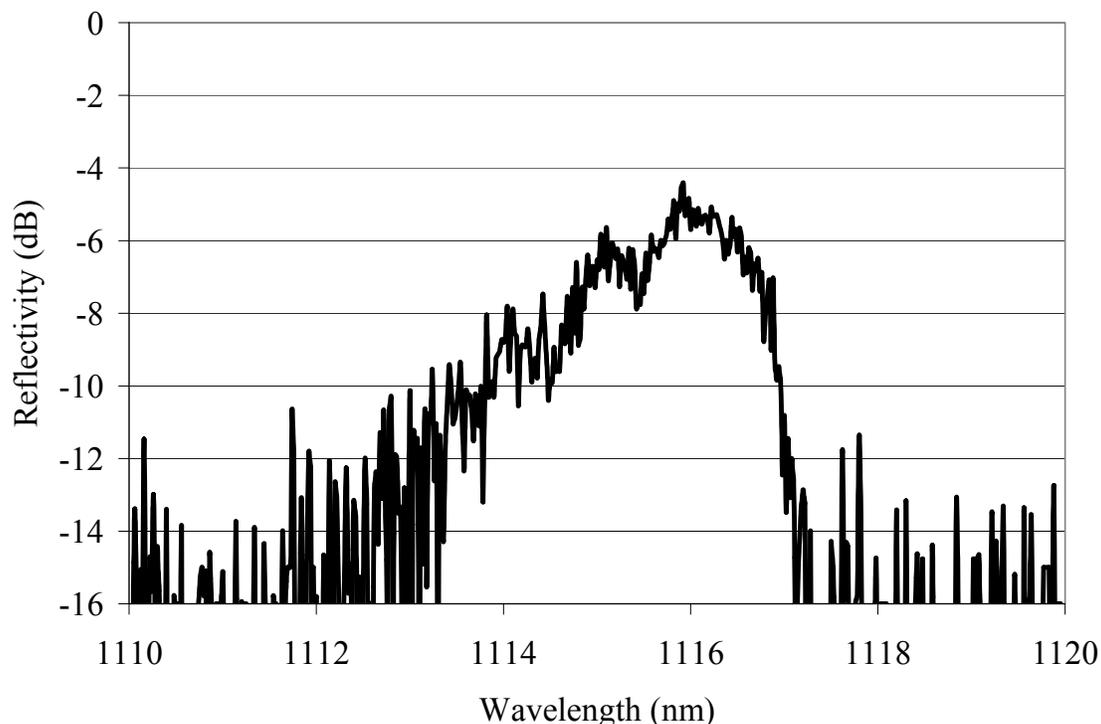
Figure 54. Lower-order mode reflectivity of an MMFBG reported by the manufacturer to have a singlemode reflectivity of *R*=30%.

As shown in the next two sections of this chapter, the multimode response of the MMFBG can offset the beam cleanup effect and degrade the beam quality of the Stokes output of an RFL based on a multimode fiber. Unfortunately, the broadband source used in the experiments described in this section only allowed low resolution measurements of these MMFBGs. The high resolution measurements of an MMFBG made by Yu *et al*. used a tunable laser instead of a broadband source [85]. While the low resolution measurements described in this section allowed a qualitative analysis of the MMFBGs and an explanation of their effects on the beam quality of the Stokes output of an RFL, these low resolution measurements cannot be used for a more comprehensive quantitative analysis. The high resolution measurements of Yu *et al*. were possible by using a high resolution tunable laser, a source which was not available to characterize the MMFBGs

used to construct the RFLs described in this document. It is also possible that using a sufficiently bright broadband source or a proper choice of the spectrum analyzer might also allow the MMBGs to be properly characterized.

7.3. Raman Fiber Lasers

7.3.1. Introduction

RFLs offer several advantages over their more traditional laser counterparts. As a fiber laser, the RFL is a lightweight, robust and compact device suitable for many aerospace applications. Moreover, the RFL offers much greater wavelength flexibility than more traditional fiber lasers. The wavelength flexibility of the RFL primarily stems from the SRS process, which downshifts the frequency of the input pump beam by the vibrational frequency of the gain medium. The wavelength of this resulting Stokes beam can be tailored by carefully choosing the input pump wavelength. Similarly, the resulting Stokes wavelength can also be tailored by carefully selecting or creating a gain medium with an appropriate Stokes shift. Current research in RFLs investigates RFLs based on novel materials, including chalcogenide glasses [93], and photonic crystal fibers [94]. Additional wavelength flexibility has also been demonstrated through prism tuning and by using multiple nested FBG cavities.

RFLs have typically been based on singlemode fibers. However, it is difficult to efficiently couple light into an RFL based on a singlemode fiber. Using a singlemode fiber makes traditional RFLs relatively inefficient devices which produce relatively low powers. One avenue for power scaling RFLs is to base them on multimode fibers with the expectation that larger fibers will allow higher pump coupling efficiencies.

Baek and Roh demonstrated an RFL based on a multimode graded-index fiber which had limited efficiency and output power, but near-singlemode beam quality [16]. This section describes an RFL based on a multimode graded-index fiber which produced 7 W of output Stokes power. This RFL had an optical-to-optical conversion efficiency of almost 50%. This is much greater than the conversion efficiency previously demonstrated for RFLs based on singlemode fibers [107,108].

This chapter shows that higher power and efficiency come at a price; it turns out that the beam quality of the output Stokes beam decreased as the Stokes power increased. Higher Stokes powers resulted in spectral broadening and peak splitting, which due to the MMFBG used in the RFL, degraded the beam quality of the Stokes output.

7.3.2. Early Raman Fiber Lasers

A Raman oscillator based on a liquid-core fiber was reported by Ippen in 1970 [95]. The fiber had a liquid carbon disulfide (CS_2) core surrounded by a 12 μm glass waveguide. The pump was a pulsed argon ion laser (514.5 nm). A prism separated the Stokes beam from the residual pump beam. 700 mW of Stokes power with a slope efficiency of 40% was reported. The Stokes threshold was 3.2 W.

Stolen *et al.* constructed the first all glass RFL two years later [96]. Their design, depicted in Figure 55, consisted of a glass fiber with a 4 μm core pumped by a pulsed Nd:YAG laser at 532 nm. Oscillation in a 1.9 m long fiber occurred at 500 W of pump power. As in Ippen's experiment, a prism was used to separate the Stokes beam from the pump beam.

A CW RFL was reported by Hill *et al.* in 1976 [97]. In this demonstration, three different fiber configurations were tested: 20 m and 60 m long fibers with a core

diameter of 2.4 μm and a 100 m long fiber with a core diameter of 4 μm. Each

configuration was pumped by an argon-ion laser at 488 nm. The Stokes threshold for

each of these setups was approximately 2.5 W.
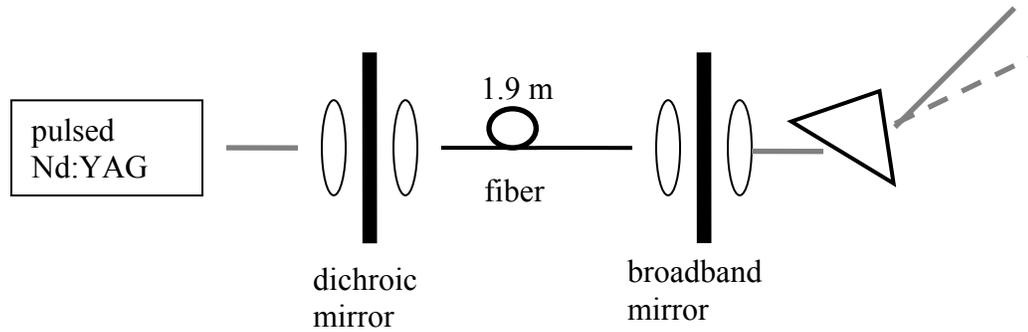
Figure 55. Schematic of the first all-glass RFL [96].

7.3.3. Peak Splitting in Raman Fiber Lasers

Peak splitting has been observed in RFLs based on singlemode fibers [98,99,100].

Babin *et al*. explained peak splitting by noting that the output Stokes power of an RFL

can be maximized by optimizing the transmissivity of the output coupler FBG [98].

When the reflectivity spectrum of the FBG was symmetric around the center Stokes

wavelength and the reflectivity was sufficiently high, the output Stokes power was

maximized at two different wavelengths and peak splitting occurred. This can be

understood by considering the center wavelength region to be gain saturated.

Babin *et al*. further noted that for RFL configurations which used gratings with

low reflectivity, the gain was not saturated and optimum transmission occurred at only a

single wavelength—no peak splitting was observed. Babin *et al*. also showed that by

temperature tuning the FBG, the spectrum of the grating could be shifted [99]. These

temperature-induced shifts of the grating spectrum created asymmetry of the output

Stokes spectrum with one peak being more intense than the other peak. Altering the

133

temperature shifted the region of gain saturation and thus adjusted the splitting of the Stokes peaks.

In an RFL which uses an MMFBG, peak splitting introduces additional transverse modes into the Stokes output, degrading the beam quality of the Stokes beam. Peak splitting was more pronounced in RFLs with high reflectivity MMFBG output couplers. This is consistent with observations that RFL configurations which used low reflectivity output coupler MMFBGs had better beam quality than RFL configurations which used high reflectivity output couplers. These observations are detailed in Section 7.4 and Section 7.5.

Babin *et al.* also reported that the width of the Stokes spectrum was a linear function of the output Stokes power of the RFL, a phenomenon known as spectral broadening [100]. In an RFL based on an MMFBG, power scaling introduced additional wavelengths through spectral broadening. These additional wavelengths added additional transverse modes to the Stokes output and degraded the beam quality of the Stokes beam.

7.3.4. Wavelength Flexibility using Raman Fiber Lasers

There are many ways to tailor the output wavelength of an RFL. The Stokes wavelength can be adjusted by altering the pump wavelength. The Stokes wavelength can also be adjusted by selecting a Raman gain medium which has a Stokes shift with a different magnitude. For example, fused silica has a Stokes shift of 440 cm^{-1}, while phosphosilicate fiber offers a Stokes shift of 1330 cm^{-1}. Given a 1064 nm pump laser, these two Stokes shifts correspond to a Stokes output of 1116 nm and 1239 nm respectively. Several other wavelength selection methods have also been demonstrated

for Raman lasers: the use of prism tuning, the use of non-linear crystals and the use of multiple cavity cascades.

Prism tuning of RFLs was demonstrated in 1977 using the CW RFL diagramed in Figure 56 [101]. Wavelength tuning in this configuration was primarily a result of the broad Raman gain spectrum of fused silica which created Stokes photons at a wide range of wavelengths. This range of Stokes wavelengths was spatially separated by the two internal cavity prisms. Only the single narrowband Stokes wavelength incident on mirror 2 was resonant with the cavity. This wavelength was tuned by simply adjusting the prisms. The pump and the Stokes wavelengths were separated using a diffraction grating. Jain *et al*. created an RFL which was tunable over a 5 nm range using a 100 m long 3.3 μm step-index silica fiber [101]. This tunable laser had a threshold of 1 W and a slope efficiency of 9%.
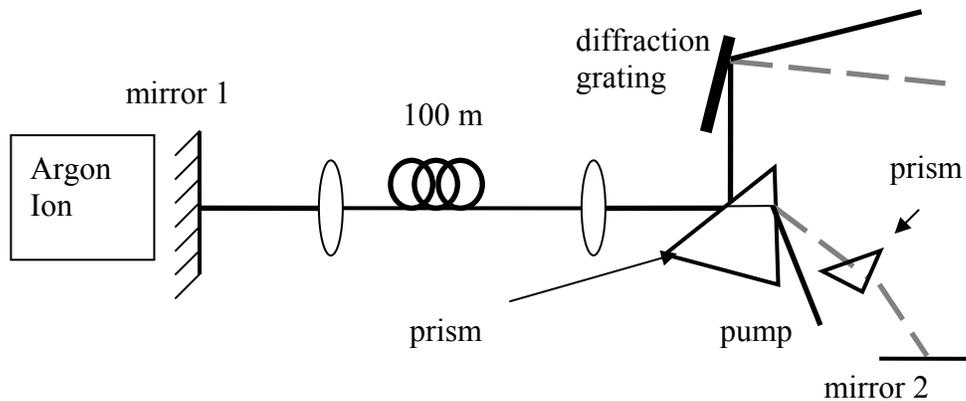
Figure 56. Schematic of the wavelength tunable RFL created by Jain *et al*. [101].

More recently, Ilev *et al*. reported using a prism-tuned configuration to produce a *Q*-switched RFL with a wavelength which ranged from 0.54 μm to 1.01 μm [102]. The pump power level of this setup was extremely high (near the damage threshold of the fiber). This extremely high pump power created a Stokes cascade containing 21 Stokes

orders. It should be noted that while this experiment used a multimode fiber, the beam quality of the output was not examined.

The output wavelength of a Raman laser can also be tailored by combining multiple types of non-linear optical processes. Amman introduced such a laser in 1979 [103]. The gain medium of this laser was $LiIO_3$, a crystal which possesses a significant second-order as well as a significant third-order nonlinear susceptibility; both SRS and second-harmonic generation (SHG) are possible in this crystal. Amman capitalized on this and created a pulsed Raman laser which operated at one of five specific wavelengths ranging from 565-655 nm.

One wavelength resulted from frequency-doubling the pump photons. Two additional wavelengths were created by frequency-doubling the first and the second Stokes orders. Two more wavelengths were obtained through sum-frequency generation (SFG) which combined either a first-order Stokes photon or a second-order Stokes photon with an SHG photon. Phase-matching determined which of these five processes dominated; the phase-matching condition was satisfied by angle-tuning the $LiIO_3$ crystal. Recent work has shown that the output wavelengths can be further tailored by choosing one crystal for the Raman gain medium while using a different crystal as the SHG/SFG medium [104]. The crystal could also be phase matched using both angle- and temperature-tuning. While this technique is not readily applicable to fiber lasers, this example is useful because it illustrates the general flexibility of Raman lasers.

Another method of tailoring the output wavelength of an RFL, a device known as a cascaded RFL, was reported in 1994 [105]. A cascaded RFL utilizes a nested set of fiber cavities to produce laser output corresponding to a higher order Stokes shift. A

diagram of this setup is shown in Figure 57.   In this configuration, the innermost pair of

FBGs creates a cavity which generates laser output at the 1st order Stokes wavelength.

The 2nd inner-most set of gratings are an oscillator cavity which is pumped by the 1st

order Stokes output from the 1st inner-most pair of gratings. The resulting 2nd order

Stokes output can be converted to the 3rd order Stokes wavelength via the next outer-most

set of gratings, and so on.

In 1994, a cascaded CW RFL was pumped with a 1060 nm Nd:YAG laser to

produce 300 mW of 3rd order Stokes output at 1239 nm [105]. Sim *et al*. reported the

creation of a two-stage RFL with a maximum Stokes output of 13.2 W at 1539 nm [106].

In this case, a 450 m length of singlemode P-doped fiber was used.   The slope efficiency

was 37.4%.
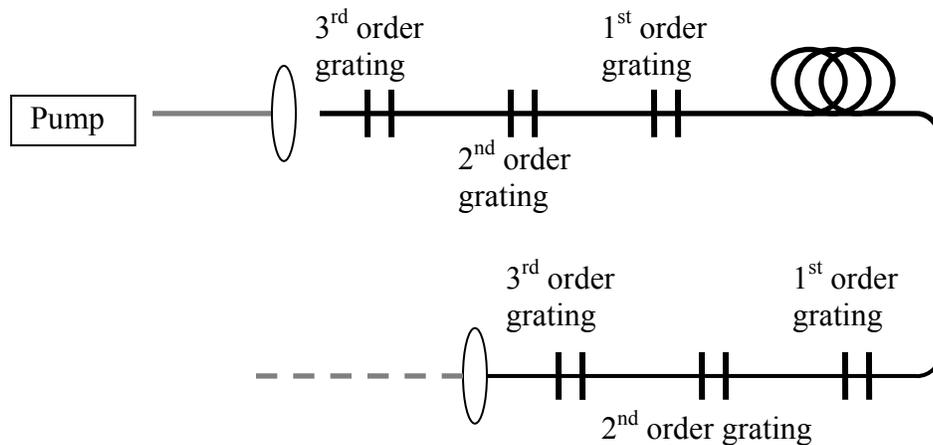
Figure 57. Diagram of a cascaded RFL.

7.3.5. Raman Fiber Lasers and Double Clad Fibers

The RFLs discussed in the previous section generally employed fibers with

singlemode cores, typically necessitating the use of a singlemode pump. RFLs are low

power devices partly due to the difficulty inherent in efficiently coupling significant

www.manaraa.com

pump power into a singlemode fiber core. This difficulty can be partially mitigated by incorporating a DCFL into the pumping scheme. The general architecture of a DCFL was outlined in Chapter 1. Commercially available RFLs are commonly pumped by DCFLs [105]. However, this pumping scheme often limits the efficiency of RFLs. For example, Karpov *et al.* reported an RFL with a slope efficiency of 48% relative to the DCFL [107]. Relative to the laser diode array used to pump the DCFL however, the RFL only had a slope efficiency of 34%; the total optical-to-optical conversion efficiency (diode light to RFL light) was only 23%.

Codemard *et al*. developed an RFL based on a DCF with a singlemode core, which was pumped by a MOPA based on a Er-Yb co-doped fiber amplifier (EYDFA) at 1552 nm [108]. On the front end of the RFL was an input coupler consisting of an FBG with a reflectivity of R=80% at the Stokes wavelength. The output coupler was the Fresnel reflection off of the back end of the DCF. The core of the DCF was 9 μm and the inner cladding was 21.6 μm, with an *NA* of 0.14 and 0.22 respectively. The inner cladding and the core were composed of germanosilicate fiber. This singlemode fiber ensured that the output was truly singlemode.

Codemard *et al*. reported a total output power of 10.2 W, with a slope efficiency of 47.6% in the forward direction and 84% when losses from the backward direction were considered. While the RFL had a slope efficiency of 84% and an optical conversion efficiency of ~50% (relative to the coupled pump power), the slope efficiency of the EYDFA was only 21%. The overall optical-to-optical efficiency of this RFL was on the order of 10%, which was less than half of the overall optical-to-optical efficiency of the RFL reported by Karpov *et al*. [107]. It is clear from these two examples that using an

138

RFL with a singlemode core results in RFLs with low overall optical-to-optical efficiency.

7.3.6. RFL based on a Multimode Fiber

In 2004, Baek and Roh reported the creation of a RFL based on a multimode graded-index fiber which produced near-singlemode Stokes output [16]. The fiber cavity was composed of a 40 m long multimode graded-index fiber with a 50 μm core. At each end of the cavity was an MMFBG with a reported singlemode reflectivity of R=99%. Each MMFBG was written directly to the fiber cavity. With this configuration, 800 mW of Stokes power with M^2=1.66 was produced. The slope efficiency was reported to be about 7%, with an optical-to-optical efficiency of around 6%. While this RFL produced near-singlemode output, its efficiency and output power were obviously limited.

7.4. Power Scaling Raman Fiber Lasers based on Graded-Index Fibers

7.4.1. Introduction

The work described in this section demonstrated that an RFL based on a multimode fiber can produce up to 7 W of output power with a slope efficiency of 60% and an optical-to-optical conversion efficiency (coupled pump power to output Stokes power) of 51%. This RFL produced significantly higher powers and greater efficiencies than the initial RFL demonstration of Baek and Roh. This increased performance came at a price, however. Higher output powers generally corresponded to lower beam quality of the Stokes beam. Furthermore, this work demonstrated that using a high reflectivity MMFBG as the RFL output coupler degraded the beam quality of the output Stokes beam.

139

7.4.2. Experimental Setup

The setup of the RFL is shown in Figure 58. The gain fiber was a 300 m long germanosilicate silica graded-index fiber with a 50 μm core (*NA*=0.2) and a 125 μm cladding. An MMFBG was fusion spliced to each end of the RFL cavity fiber using an Ericsson FSU 995 FA fusion splicer. A list of the splicing parameters used in these splices, known as the splice recipe, is provided in Appendix A.
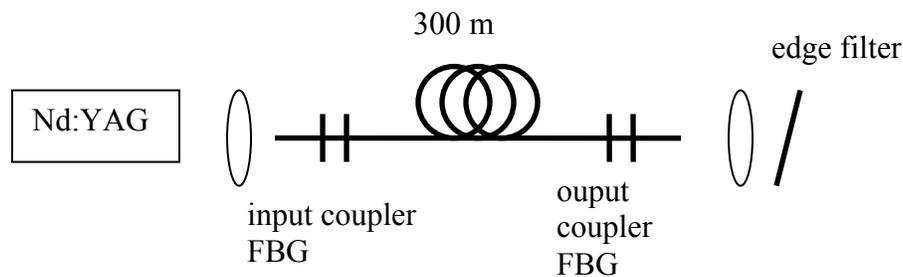
Figure 58. Experimental setup of an RFL based on a multimode graded-index fiber.

The RFL was pumped with a CW Nd:YAG laser (15 W @ 1064 nm), which was launched into the RFL using a microscope objective. The output from the RFL was collimated using a separate microscope objective. The beam quality of the pump beam was approximately M^2=3.7 as it exited the fiber (i.e., below the RFL threshold). A long wave pass edge filter at 1064 nm separated the Stokes beam from the residual pump beam.

The performance of four RFL configurations was tested. Each configuration was defined by the MMFBG used as the output coupler; the RFL configurations were identical in other respects. The characterization of these MMFGBs was presented in Section 7.2.

The launching conditions of the pump laser were optimized by adjusting the angle and position of the input fiber of the RFL. This adjustment was done in two steps. The

140

first step aligned the fiber to maximize the transmitted pump power. The second step aligned the fiber so as to maximize the output Stokes power. The beam quality (M^2) was determined by characterizing the diameter of the output beam as it traveled though a lens with a 300 mm focal length and comparing the results to the profile of a Gaussian beam.

7.4.3. Results and Discussion

The output Stokes power as a function of the coupled pump power was measured for each of the RFL configurations. These measurements are shown in Figure 59. The efficiency, the threshold and the beam quality of the Stokes beam produced by each configuration is listed in Table 10. The highest Stokes power was produced by the RFL configuration which used the output coupler MMFBGs with a singlemode reflectivity of R=99%; RFL configurations which used output couplers with lower singlemode reflectivity produced lower output Stokes powers. The slope efficiency of these configurations also followed this trend, with the exception of the RFL configuration which used an output coupler MMFBG with a singlemode reflectivity of R=90%. This table also shows that RFL configurations which used output coupler MMFBGs with high singlemode reflectivity produced Stokes beams with poorer beam quality than RFL configurations which used output coupler MMFBGs with low singlemode reflectivity. It should also be noted that none of these RFL configurations was a brightness converter of the pump beam.

The work of this section also compared the effectiveness of the single-pass pumping geometry of an RFL with the effectiveness of a double-pass pumping geometry. An RFL configuration which used an output coupler with a singlemode reflectivity of R=80% served as the baseline. After the RFL was aligned in the single-pass pumping

geometry, the reflective edge filter was aligned so that the retro-reflection of the residual

pump beam was coupled back into the RFL.
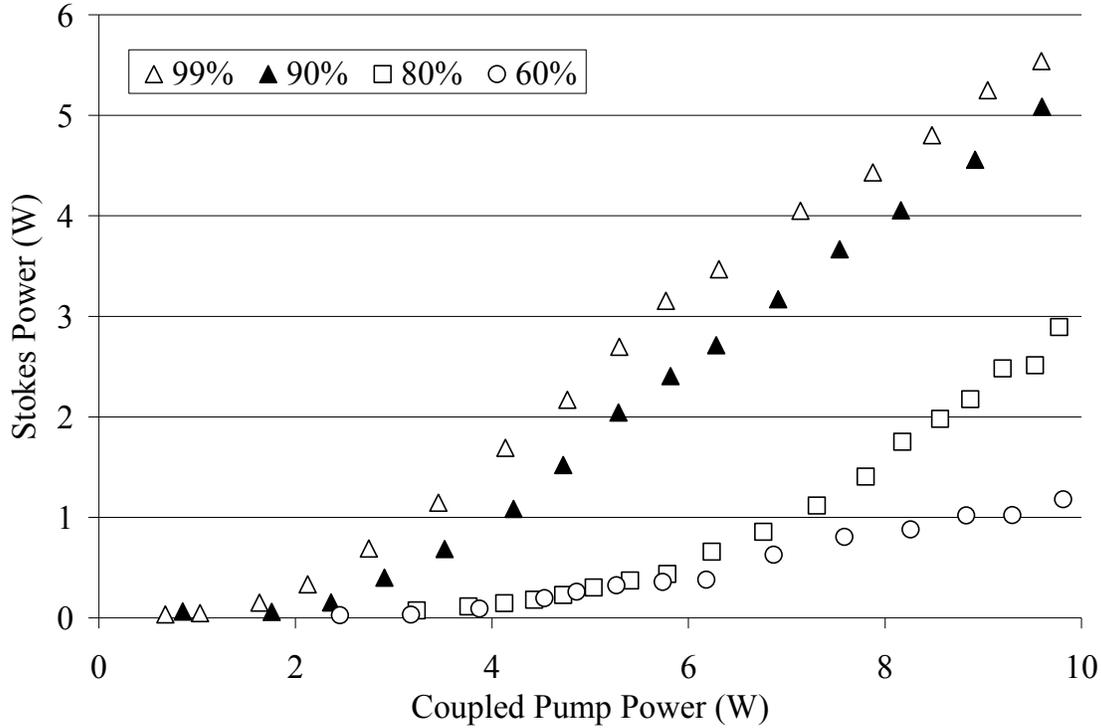
Figure 59. Output Stokes power as a function of coupled pump power for various RFL configurations.

Table 10. Comparison of the performance of various RFL configurations.

Singlemode Output Coupler Reflectivity	Pump	99%	90%	80%	60%
Maximum Power (W)	10	5.5±0.1	5.1±0.1	2.9±0.1	1.2±0.1
Slope Efficiency	NA	59%	66%	53%	22%
Optical-to-Optical Efficiency	NA	40%	37%	21%	8.5%
Threshold (W)	NA	0.7	2.3	~4.5	~4.5
Beam Quality (M^2)	3.8	3.6	3.1	2.5	1.9
Brightness Enhancement	NA	-40%	-30%	-40%	-50%

A comparison of the performance of the double-pass pumping geometry with the

performance of the single-pass pumping geometry is presented in Figure 60. The slope

efficiency of the single-pass pumping geometry and the double-pass pumping geometry

142

were 52% and 73% respectively. The Stokes thresholds were 5.5 W and 2.0 W

respectively. It should be noted that the input pump alignment of the single-pass

pumping geometry was the same as the input pump alignment of the double-pass

pumping geometry. This allowed a valid comparison of the two pumping configurations.
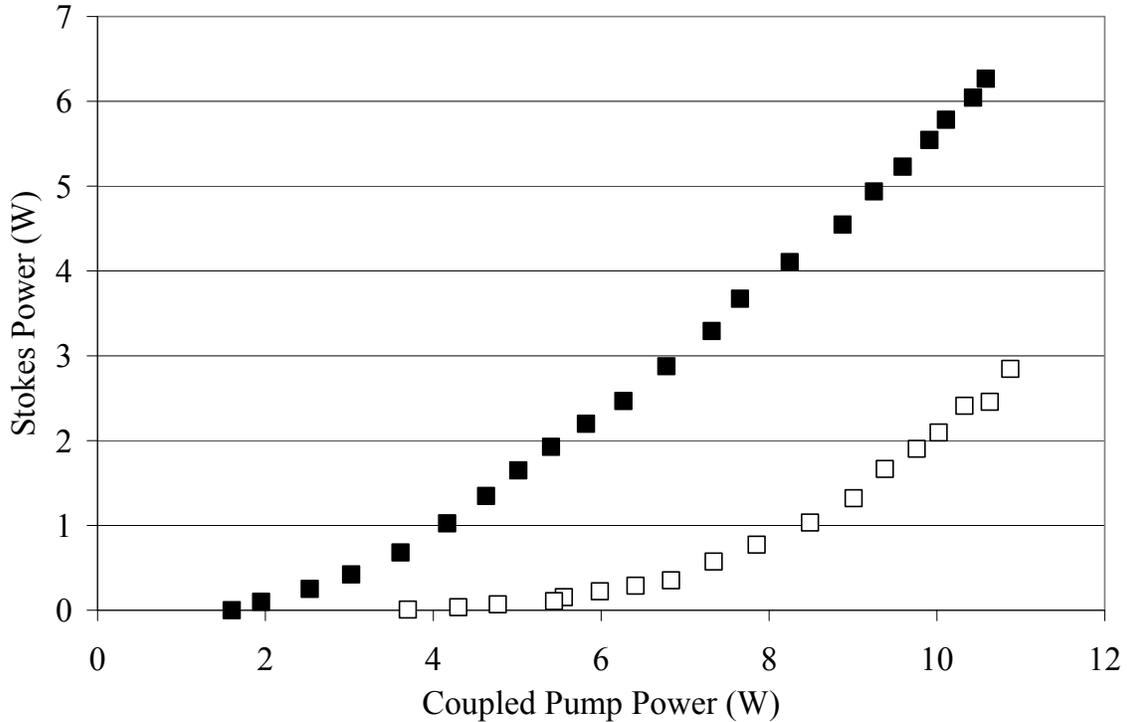
Figure 60. The performance of an RFL configuration using a double-pass pumping
geometry and the performance of an RFL configuration using a single-pass pumping
geometry. The MMFBG output coupler had a singlemode reflectivity of *R*=80% for both
pumping geometries.

At this point, it is worth noting the RFL configuration which produced the

greatest output Stokes power. Using an output coupler with a singlemode reflectivity of

R=99%, this configuration converted 14 W of coupled pump power into 7 W of output

Stokes power. The performance of this configuration is shown in Figure 61. This

configuration had a slope efficiency of 67% and a Stokes threshold of 3.5 W. This

particular configuration was different from other RFL configurations discussed in this

143

section in that it was pumped using a different pump laser configuration, i.e., the

Nd:YAG had M^2=6.6. This performance information is included simply to show that an

RFL based on a multimode graded-index fiber can produce at least 7 W of Stokes power.
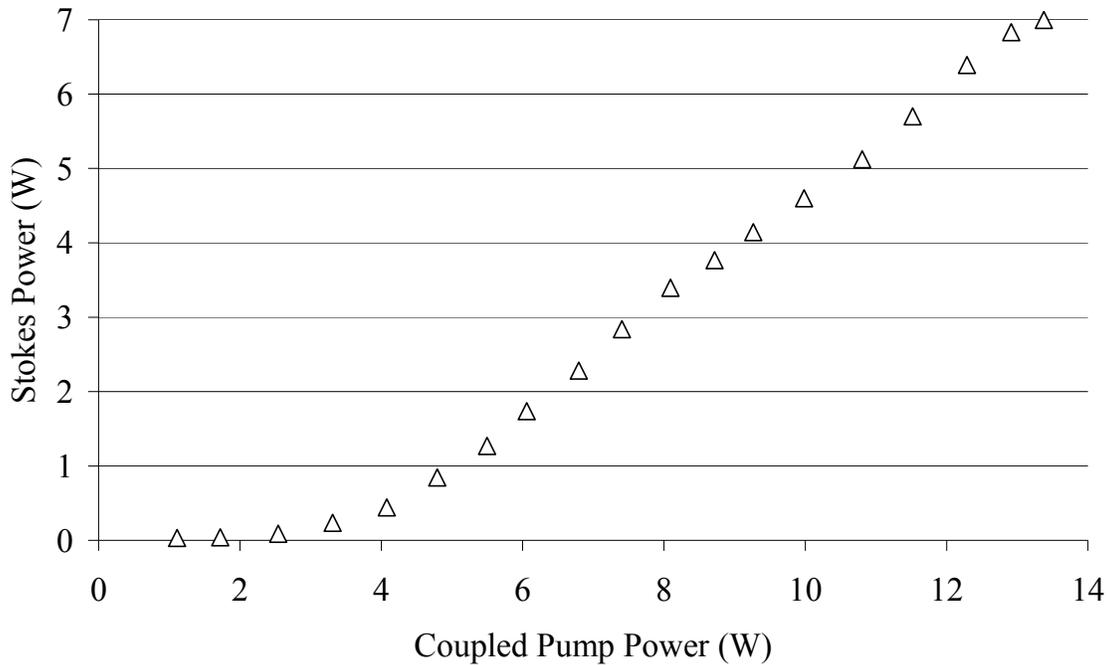
Figure 61. Stokes power versus the coupled pump power for the RFL configuration that produced the greatest Stokes power of all the configurations examined in the course of this research.

Unfortunately, higher power Stokes beams generally had worse beam quality than

lower power Stokes beams. Two experiments explored the relationship between the

beam quality and the Stokes power of the output of an RFL based on a multimode fiber.

The first experiment examined the beam quality of the Stokes beam as a function of the

Stokes power produced by the RFL. The RFL configuration tested in this experiment

used an output coupler MMFBG with a singlemode reflectivity of R=99%. In this

experiment, the beam quality of the Stokes output was measured at a number of output

144

Stokes powers. The Stokes power was increased by increasing the pump power coupled into the RFL; the pump power was controlled by adjusting the current of the pump laser.

The results of this experiment, shown in Figure 62, demonstrated that the beam quality of the Stokes beam was generally degraded as the power in the output Stokes beam increased. In analyzing this data, it is possible to attribute the decreased beam quality of the Stokes beam to decreases in the beam quality of the pump beam induced by altering the current of the pump laser. However, the same relationship of increased Stokes power and decreased beam quality was observed in the performance of the RFL beam combiner discussed in Section 7.5. Since the pump power in the RFL beam combiner was varied by rotating wave plates, the degradation of beam quality cannot be attributed to changes in the beam quality of the input pump beam.

A second experiment investigated the effect of the MMFBG on the beam quality of the output of an RFL based on a multimode graded-index fiber by examining the spectrum of the Stokes output. Since different Stokes modes of the fiber are reflected by an MMFBG at different wavelengths, the effect of the MMFBG on the output manifested itself in the spectrum of the Stokes output. The Stokes spectrum of the output of the RFL configuration which used an output coupler with a singlemode reflectivity of R=99% was characterized at different coupled pump powers using an OSA.

The results are depicted in Figure 63 through Figure 67 which show the output spectra as a function of total output Stokes power. At 30 mW of Stokes power, which was just above the Stokes threshold, only a single, relatively narrow Stokes peak was present. As the Stokes power increased to 500 mW, the width of the spectral peak broadened. As the Stokes power continued to rise, an additional lower wavelength

145

asymmetric shoulder appeared; by 1500 mW of Stokes power, this shoulder evolved into a completely separate peak. This peak was still present at 1900 mW of Stokes power.
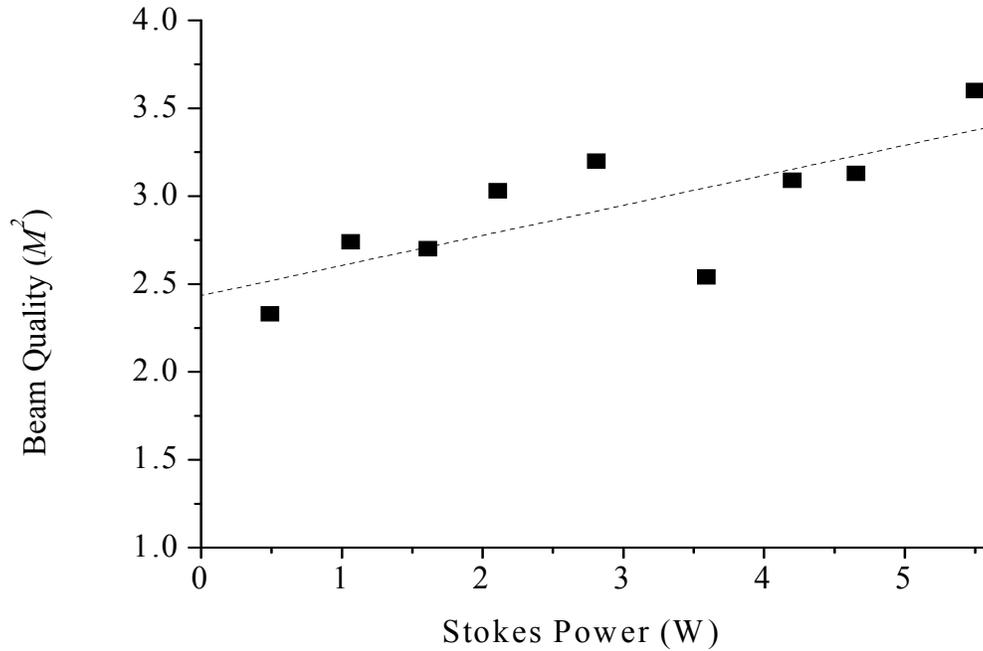
Figure 62. The beam quality of the Stokes output of an RFL as a function of the output Stokes power of the RFL.

This series of spectral images showed that a lower-wavelength peak manifested itself at higher Stokes powers. This lower-wavelength peak corresponded to one of the principal modes listed in Table 9 and contained multiple transverse Stokes modes of the fiber. These additional transverse Stokes modes decreased the beam quality of the Stokes beam and offset the SRS beam cleanup effect. While it should be noted that there was some variability in the output spectra, the results shown in Figure 63 through Figure 67 were typical of the observed spectra.

In summary, there are two definitive, repeatable trends associated with the beam quality of an RFL based a multimode graded-index fiber. First, the beam quality of the

146
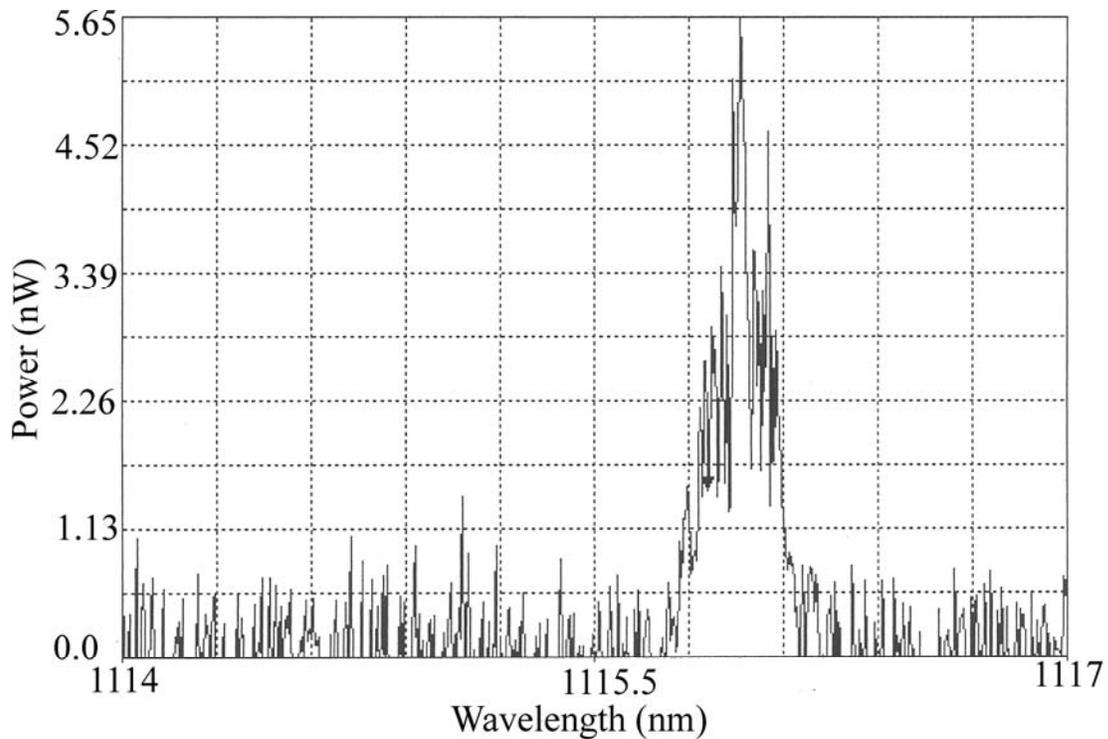
Figure 63. Stokes spectra produced by an RFL configuration which used an output coupler with a singlemode reflectivity of R=99%; the Stokes power was 30 mW.
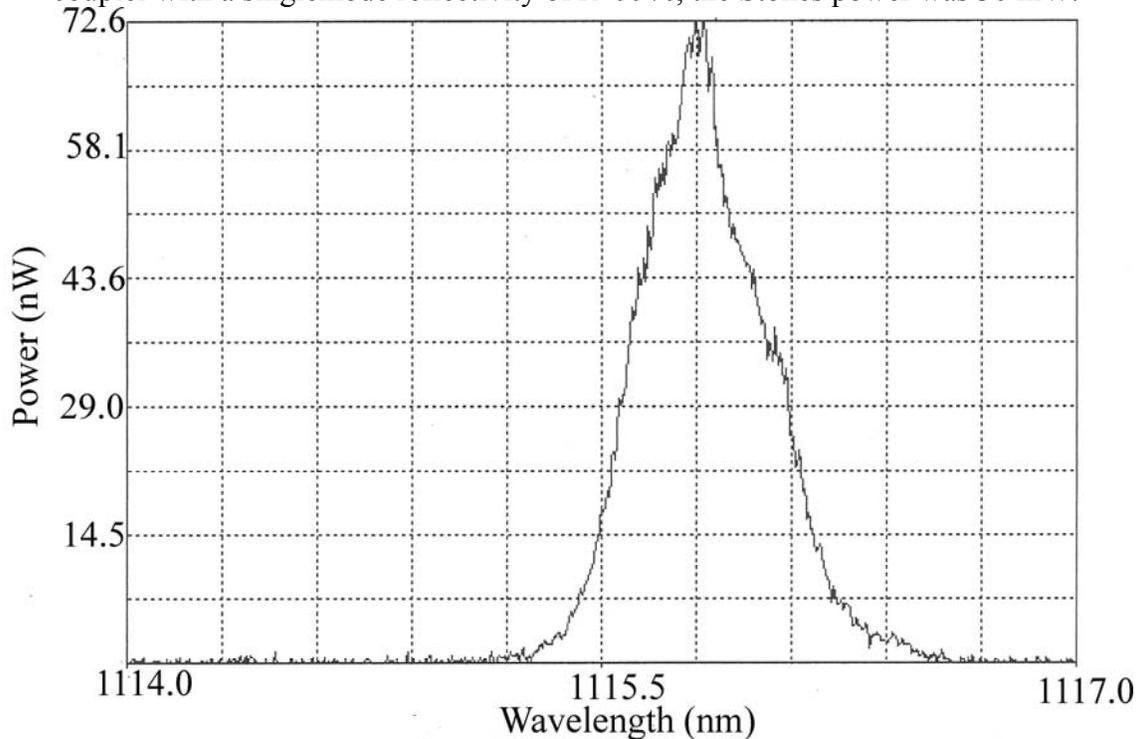
Figure 64. Stokes spectra produced by an RFL configuration which used an output coupler with a singlemode reflectivity of R=99%; the Stokes power was 500 mW.

147
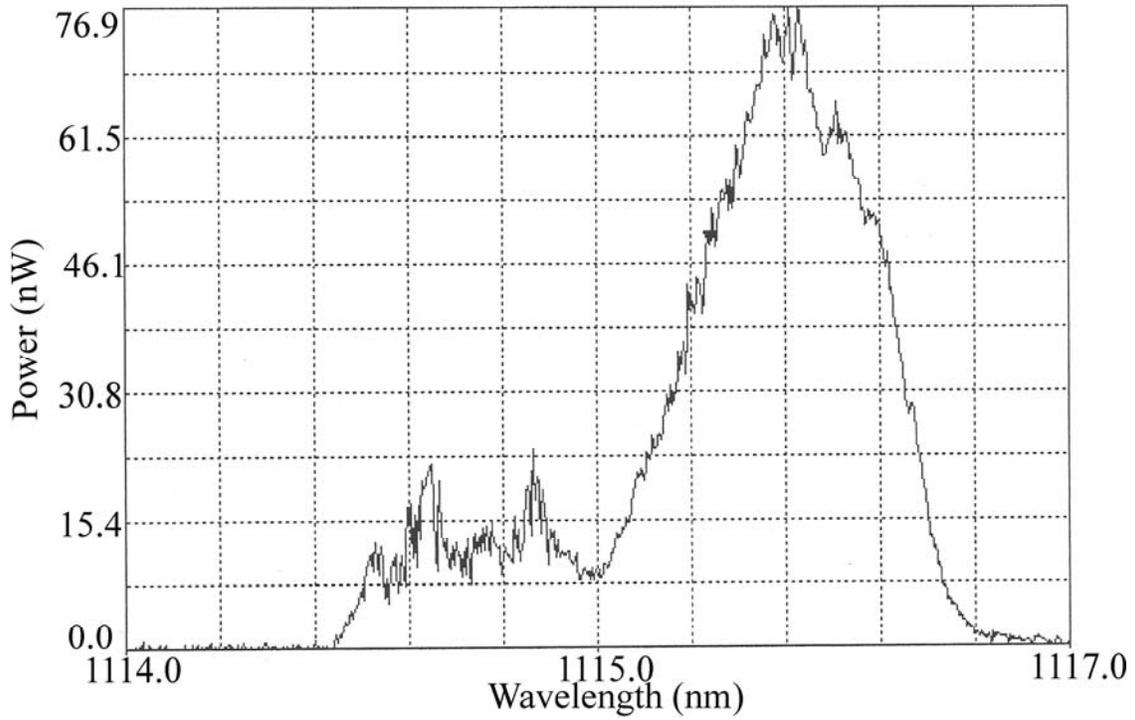
Figure 65. Sample Stokes spectra produced by an RFL configuration using an output coupler with a singlemode reflectivity of *R*=99%; the Stokes power was 1050 mW.
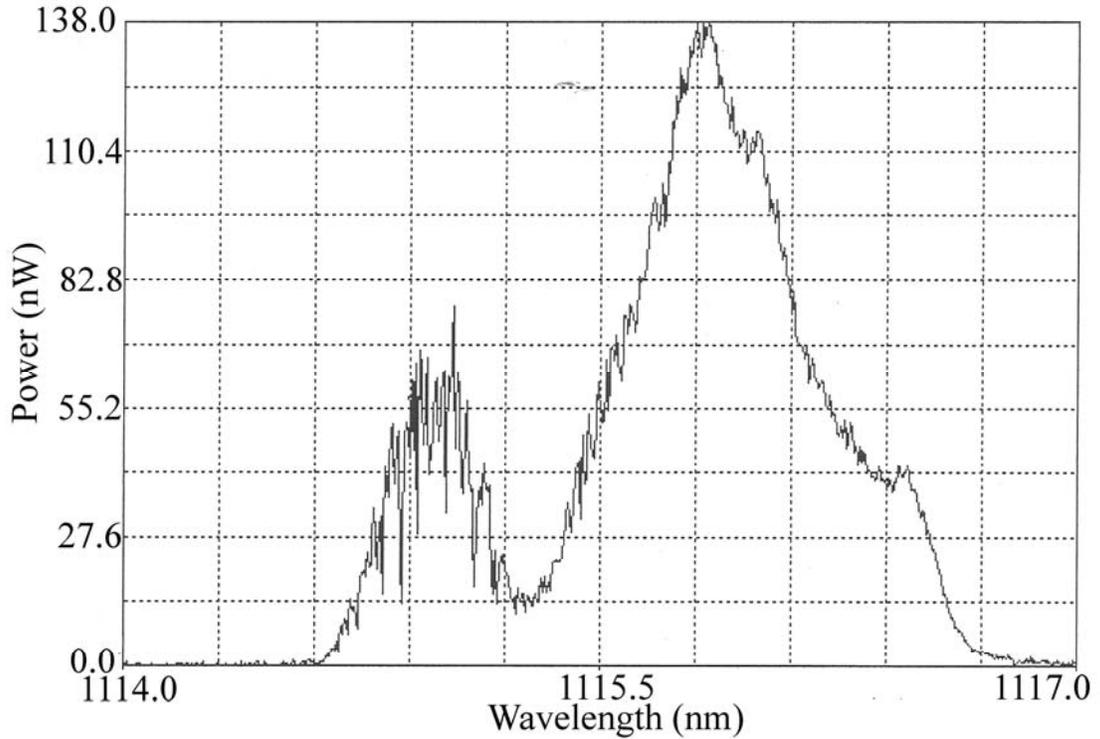
Figure 66. Stokes spectra produced by an RFL configuration which used an output coupler with a singlemode reflectivity of *R*=99%; the Stokes power was 1450 mW.

148
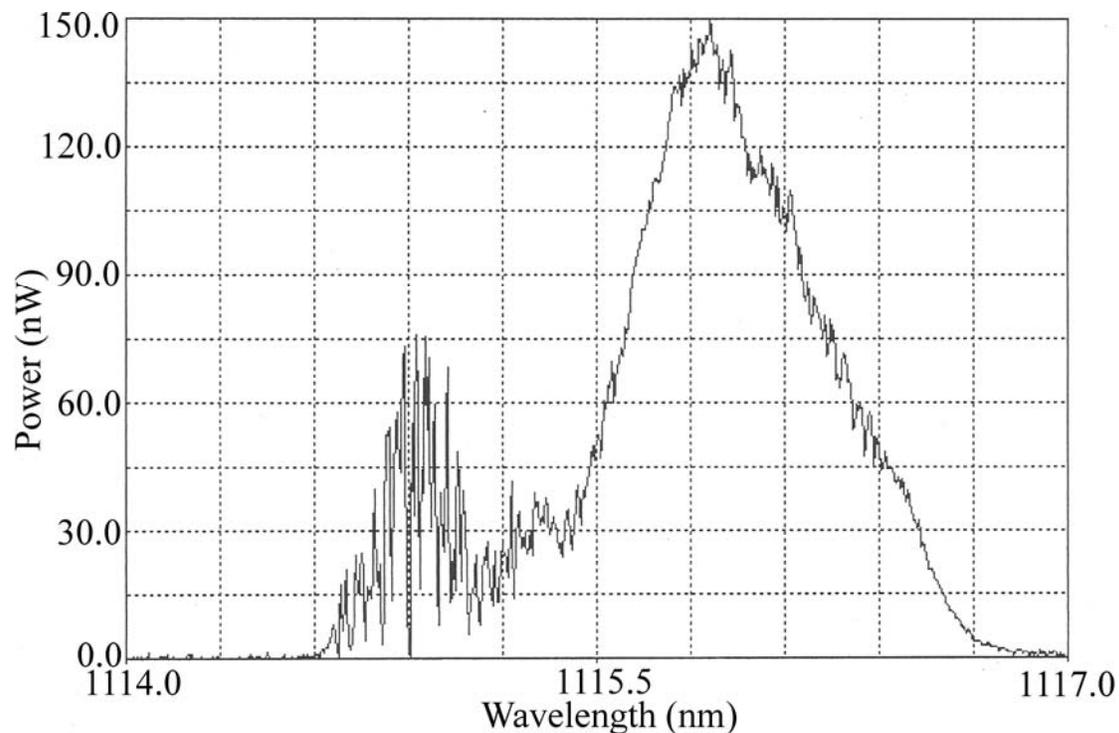
Figure 67. Stokes spectra produced by an RFL configuration which used an output coupler with a singlemode reflectivity of R=99%; the Stokes power was 1900 mW.

Stokes output decreased as the Stokes power increased. Second, degraded beam quality corresponded to RFL configurations which used high reflectivity MMFBGs as the output coupler. Unfortunately, a complete analysis of these two trends is not possible without high resolution measurements of the MMFBGs used to build the RFLs. Such high resolution measurements require a tunable laser which was not available in the MMFBG characterizations performed in Section 7.2. However, a qualitative explanation of these two trends can made by making an analogy to observations of peak splitting and spectral broadening in RFLs based on singlemode fibers [98,99,100].

Babin *et al*. showed that increased output Stokes power corresponded to spectral broadening of the Stokes output [100]. In the RFLs studied in this document, spectral broadening introduced additional wavelength components to the MMFBG. The

149

MMFBGs transformed these additional wavelengths into additional transverse Stokes modes of the fiber which degraded the beam quality of the Stokes beam.

Babin *et al.* also showed that RFL configurations that employed output coupler gratings with high reflectivity experienced gain saturation which lead to peak splitting [98,99]. Babin *et al.* showed that peak splitting was absent from the Stokes output of RFL configurations which used output coupler gratings with low reflectivity [98]. Peak splitting reinforced the shorter wavelength components of the Stokes beam at the expense of some of the longer wavelength components of the Stokes beam. Due to the MMFBG these shorter wavelength components of the beam were transformed into higher-order Stokes modes. Thus, RFL configurations which used output coupler MMFBGs with high reflectivity produced Stokes beams with worse beam quality than RFL configurations which used output coupler MMFBGs with low reflectivity.

7.4.4. Section Summary

This set of experiments showed that an RFL based on a multimode fiber can be a moderate power device (7 W) which operated with an optical-to-optical conversion efficiency of greater than 50% (relative to the coupled pump beam). If the 70% coupling efficiency of the pump into the RFL is considered, this efficiency is only 35%. This was nevertheless a significant improvement over the 10% efficiency reported by Codemard *et al.* or the 23% efficiency reported by Karpov *et al.* Clearly, RFLs based on multimode graded-index fibers are efficient and therefore a viable avenue for power scaling RFLs.

Higher Stokes powers however, resulted in degraded beam quality of the Stokes beam. It was also shown that RFL configurations which used output coupler MMFBGs

150

with high singlemode reflectivity produced Stokes beams with worse beam quality than RFL configurations which used an coupler MMFBG with low singlemode reflectivity.

7.5. Beam Combination Using Raman Fiber Lasers

7.5.1. Introduction

As discussed in Chapter 6, there is a great deal of interest in finding methods of combining semiconductor lasers, fiber lasers and solid state lasers to produce efficient high-average-power systems with bright output in a combined single beam. SRS as a beam combination and power scaling method remains largely undeveloped, owing in part to the difficulty of achieving a low Stokes threshold. Recent experiments by Flusche *et al.* involving SRS fiber beam combination have used high peak powers from temporally coherent pulsed pump laser beams in a multimode fiber to reach the Stokes threshold [20]. Chapter 6 of this document examined the possibility of using a Stokes seed to lower the effective SRS threshold. Another way to achieve a low Stokes threshold is to employ an RFL as an SRS fiber beam combiner.

This section describes the first ever demonstration of the SRS beam combination of two temporally incoherent CW pump sources using an RFL based on a multimode graded-index fiber. Employing an oscillator as the beam combiner avoids the high SRS thresholds of previous experiments and thus allows the combination of CW pump sources. Several different configurations of the RFL were examined in these experiments. One RFL configuration produced a Stokes beam which was 296% brighter than the input pump beams used to generate it. A different RFL configuration produced a 5.8 W Stokes beam with an optical conversion efficiency of 55%. The RFL beam

151

combiners described in this section had slope efficiencies which approached or even exceeded unity at the powers tested.

7.5.2. Experimental Setup

The setup of this experiment is shown in Figure 68. The multimode fiber used in the RFL was based on a 2500 m long graded-index Ge-doped fused silica fiber with 50 μm core (0.20 NA) and a 125 μm cladding. Two separate unpolarized Nd:YAG pump lasers (1064 nm) were polarized in orthogonal directions using two PBSs. Each polarized pump beam (channel) then traversed a $\lambda/2$ wave plate before being combined into a single beam by passing each channel through a common PBS. Rotating the respective wave plates changed the amount of pump power from each laser that was launched into the RFL; rotating the wave plates did not alter the launching conditions of either pump beam. The output from the RFL was collimated using a microscope objective. The residual pump beam was separated from the Stokes beam using a long wave pass edge filter at 1064 nm.

5 different RFL configurations were tested. Each configuration used the same input coupler MMFBG; only the output coupler MMFBG was varied. The input coupler MMFBG had a single-mode reflectivity of R=99%. The singlemode reflectivity of the 5 output coupler MMFBGs used in this experiment were given by the manufacturer to be respectively R=99%, R=90%, R=80%, R=60%, and R=30% (at 1117 nm). A 6th RFL configuration was tested which used the Fresnel reflection off of the bare fiber end as an output coupler with a reflectivity of R=4%. In each configuration, the input end of the fiber was aligned to maximize the generated output Stokes power. The RFL was

characterized in terms of the power, the beam quality and the spectral content of the Stokes beam.

7.5.3. Results and Discussion

The power in the Stokes beam was measured as a function of the pump power coupled into the RFL. Initially the RFL was pumped with only a single pump channel. Once the first pump channel reached its maximum coupled power of about 5 W, additional pump power was added via the second channel. The Stokes power generated by each RFL configuration is shown in Figure 69.
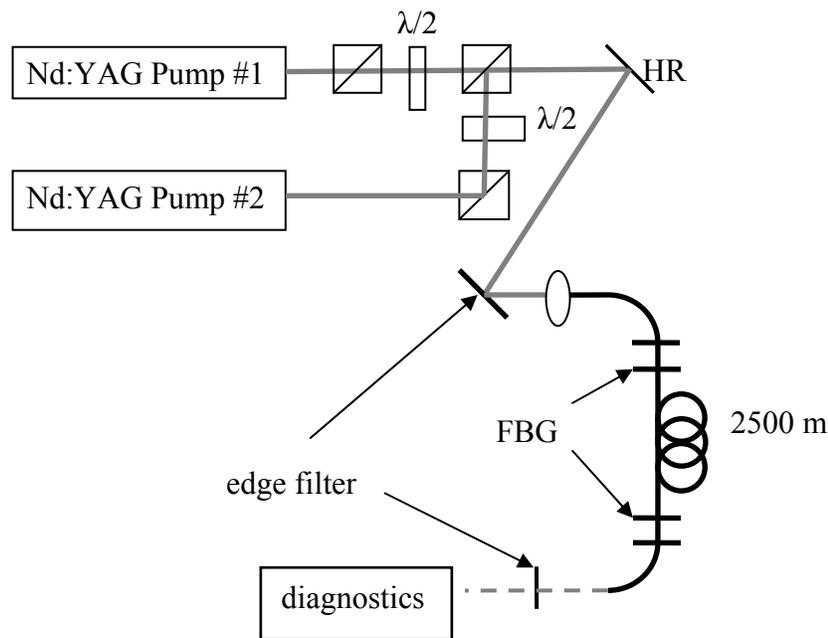
Figure 68. Experimental setup of an RFL beam combiner.

The RFL beam combiner configuration which used an MMFBG output coupler with a singlemode reflectivity of R=90% and the RFL beam combiner configuration which used an output coupler with a reflectivity of R=4% produced the greatest and the least amount of Stokes power respectively. The RFL configuration which used an

153

MMFBG output coupler with a singlemode reflectivity of R=90% had an optical

conversion efficiency of 56%, a Stokes threshold of ~4 W and a slope efficiency of 87%.
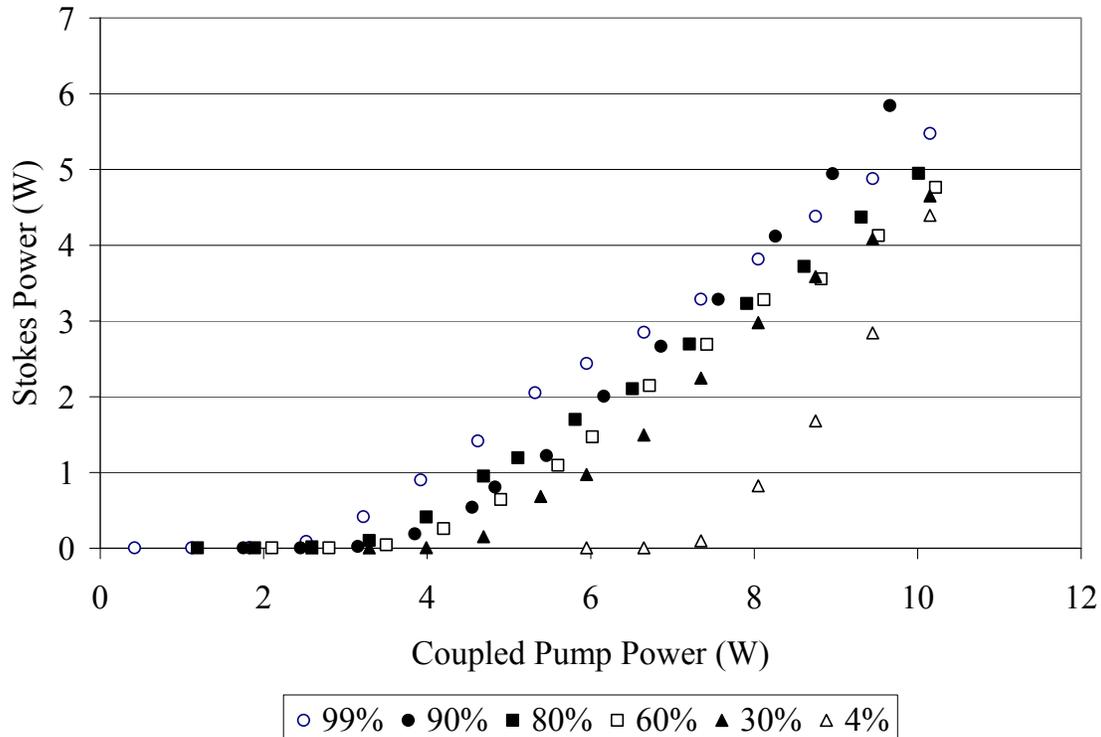
Figure 69. Coupled pump power versus output Stokes power of various configurations of
an RFL beam combiner.

The RFL configuration which used an output coupler with a reflectivity of R=4%

had an optical conversion efficiency of 41%, a Stokes threshold of ~7 W and a slope

efficiency of 126% (at the powers measured). At higher pump powers, the slope

efficiencies are expected to moderate and roll over due to pump depletion. The

maximum Stokes power, the efficiency, the Stokes threshold, the beam quality (at the

maximum Stokes power) and the brightness enhancement of each RFL configuration is

listed in Table 11.

In general, RFL beam combiner configurations which used output coupler

MMFBGs with high singlemode reflectivity produced more Stokes power than RFL

154

beam combiner configurations which used output coupler MMFBGs with low

singlemode reflectivity. However, RFL beam combiner configurations which used

output coupler MMFBGs with low singlemode reflectivity generated Stokes beams with

better beam quality than RFL beam combiner configurations which used output coupler

MMFBGs with high singlemode reflectivity. The only exception for these two trends

was the RFL beam combiner configuration which used the output coupler MMFBG with

a singlemode reflectivity of R=90%. In general, the Stokes threshold of the RFL beam

combiner configurations increased as the singlemode reflectivity of the output coupler

MMFBG increased; the only exception was RFL beam combiner configuration which

used an output coupler MMFBG with a singlemode reflectivity of R=90%.

Table 11. **Comparison of the performance characteristics of various RFL beam combiner configurations.**

Singlemode Reflectivity	Stokes Power	Slope Efficiency	Conversion Efficiency	Stokes Threshold	Pump M^2	Stokes M^2	Brightness Enhancement
99%	5.5 W	69%	51%	2.8 W		3.5	133%
90%	5.8 W	87%	56%	3.7 W		4.0	112%
80%	4.9 W	66%	46%	3.3 W	5.8	3.1	153%
60%	5.3 W	76%	48%	4.0 W		2.4	270%
30%	4.8 W	77%	44%	4.7 W		2.3	267%
4%	4.4 W	126%	41%	7.3 W		2.1	296%

Beam quality measurements of the Stokes beams generated by the various RFL

beam combiner configurations at different Stokes powers are shown in Figure 70. Beam

quality in the form of M^2 was calculated by characterizing the diameter of the beam at

about 20 different locations as it traversed the focus of a lens with a 300 mm focal length.

The beam diameter at each location was determined using the average of 50 images taken

with an Alpha NIR InGaAs camera. Neutral density filters were used to prevent

saturation of the camera. A least-squared fit was used to determine the value of M^2.

155
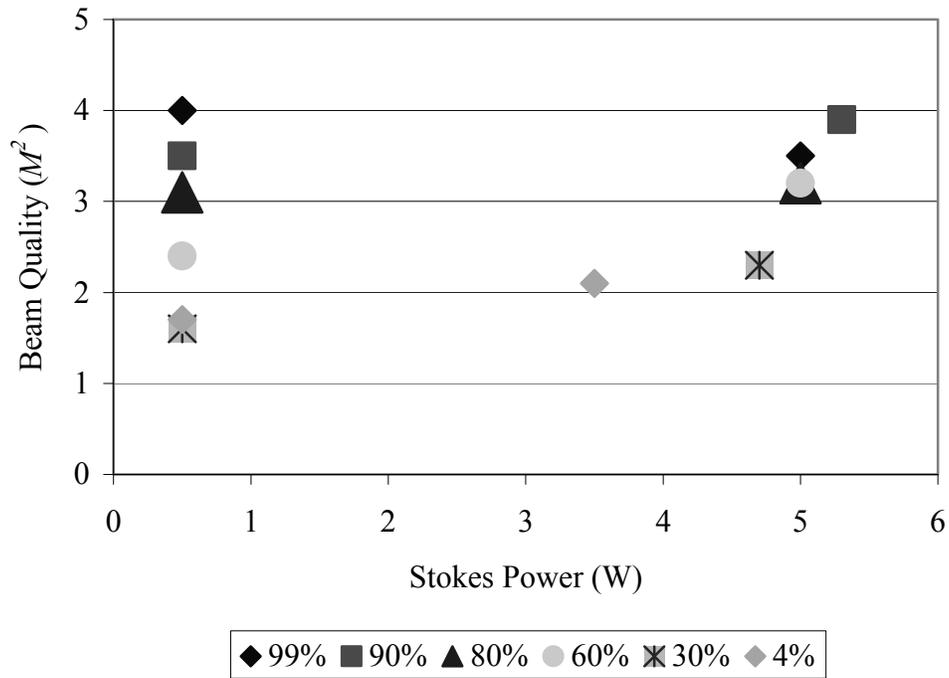
Figure 70. Beam quality of the Stokes output of various configurations of the RFL beam combiner.

As can be seen in Figure 70, there is a definite correlation between the beam quality of the Stokes beam produced by a given RFL beam combiner configuration and the singlemode reflectivity of the output coupler MMFBG used in that configuration. RFL beam combiner configurations which used an output coupler MMFBG with a low singlemode reflectivity produced Stokes output with better beam quality than RFL beam combiner configurations which used an output coupler MMFBG with a high singlemode reflectivity. As explained in Section 7.4.3, RFL beam combiner configurations which used an output coupler MMFBG with a high reflectivity experienced peak splitting which degraded the beam quality of the output Stokes beam.

There was also a correlation between the output Stokes power and the beam quality of the Stokes beam. For a given RFL configuration, higher output powers

156

corresponded to lower beam quality of the Stokes beam. One exception was the RFL configuration which used an MMFBG output coupler with a singlemode reflectivity of R=99%. This is similar to the power versus beam quality observations that were reported for the RFL configurations discussed in Section 7.4.

An examination of the spectra of the output Stokes beam produced by the RFL beam combiner is also revealing. At 2 W of pump power, the Stokes beam produced by an RFL beam combiner configuration which used an output coupler MMFBG with a singlemode reflectivity of R=90% contained only a single peak centered at 1117.2 nm, as can be seen in Figure 71. This relatively broad peak contained a wide range of wavelengths (FWHM=0.9 nm); the MMFBG transformed these wavelengths into additional transverse modes in the Stokes beam. As a result, this RFL beam combiner configuration had a Stokes beam with relatively poor beam quality (M^2=3.5).

At 5.8 W of Stokes power, the spectrum of the 1st Stokes order contained multiple peaks with the highest peak centered on 1115.5 nm; this spectrum is shown in Figure 72. The MMFBG translated these shorter wavelengths into higher-order transverse Stokes modes. This reduced the beam quality of the output Stokes beam (M^2=3.9) and offset the SRS beam cleanup effect.

The reflectivity of the output coupler MMFBG also affected the number of Stokes orders in the Stokes beam produced by an RFL beam combiner configuration. For example, at 2 W of Stokes power, the RFL beam combiner configuration which used an output coupler with a reflectivity of R=4% produced the Stokes spectrum shown in Figure 73 which contained only a single Stokes order. By contrast, at 2 W of Stokes power, the RFL beam combiner configuration which used an output coupler MMFBG

with a singlemode reflectivity of R=90% produced a Stokes beam which contained the two Stokes orders shown Figure 74. The 2nd Stokes order was generated by this configuration because of high intracavity intensity associated with using a high reflectivity MMFBG as an output coupler. The 2nd Stokes order was not resonant with the cavity. It was generated in a single-pass of the 2500 m fiber.
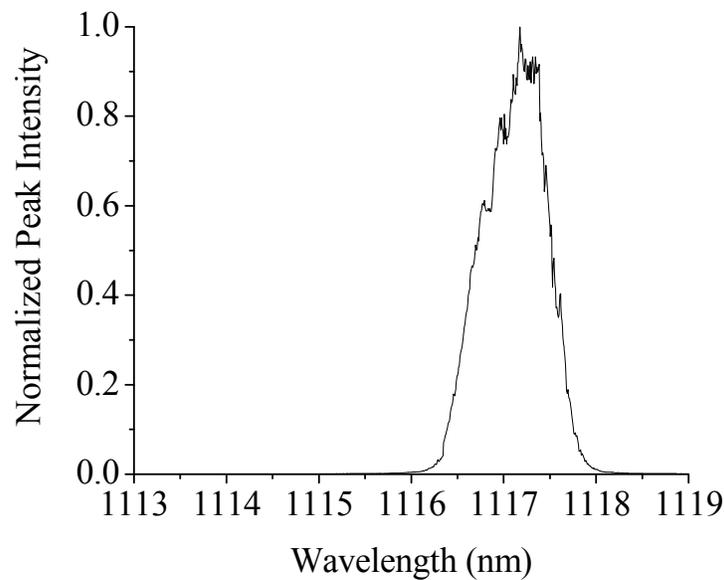
Figure 71. Spectrum produced by the RFL beam combiner configuration which used an output coupler MMFBG with a singlemode reflectivity of R=90% at 2.0 W of Stokes power.

The spectral output of all the tested RFL beam combiner configurations at their maximum output Stokes power is shown in Figure 75. The RFL beam confiner configuration which used the output coupler with a reflectivity of R=4% produced a Stokes beam with a spectrum which was peaked at about 1117 nm. This RFL beam combiner configuration produced the Stokes beam with the best beam quality.

158

By contrast, the main peak in the spectrum of the Stokes beam produced by the

RFL beam combiner configuration which used an MMFBG output coupler with a
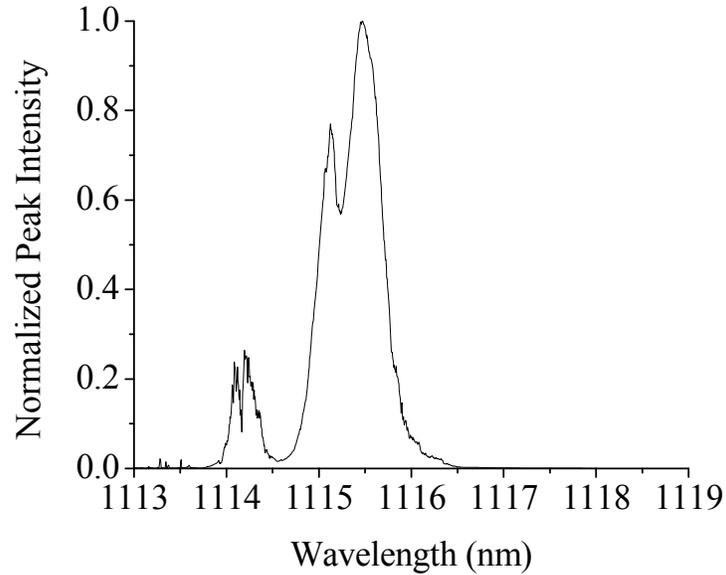
Figure 72. Spectrum produced by the RFL beam combiner configuration which used an output coupler MMFBG with a singlemode reflectivity of *R*=90%; the output Stokes power was 5.8 W.

center λ=1117 nm
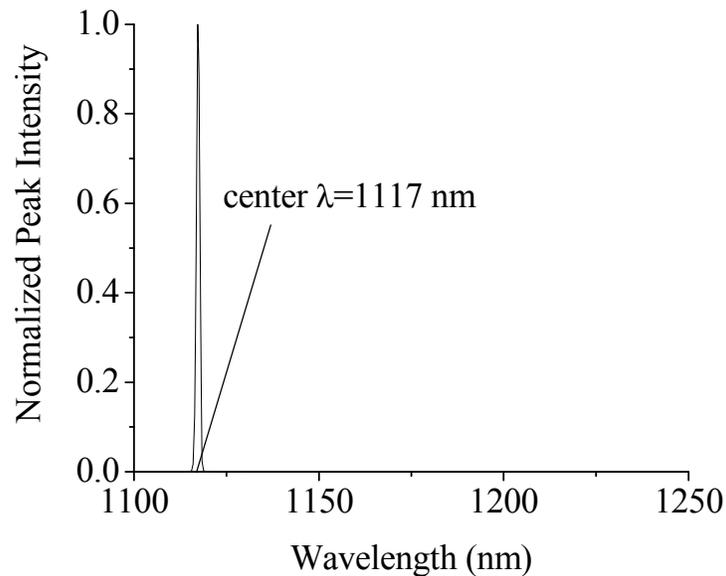
Figure 73. Spectrum produced by the RFL beam combiner configuration which used an output coupler with reflectivity of *R*=4%; the output Stokes power was 2 W.

singlemode reflectivity of R=30% was slightly downshifted in wavelength and was centered at 1116.8 nm. This spectrum also contained a small, additional lower-wavelength peak centered at 1115.6 nm. The Stokes beam generated by the RFL beam combiner configuration which used an MMFBG output coupler with a singlemode reflectivity of R=30% had slightly worse beam quality than the Stokes beam generated by the RFL beam combiner configuration which used the output coupler with a reflectivity of R=4%.
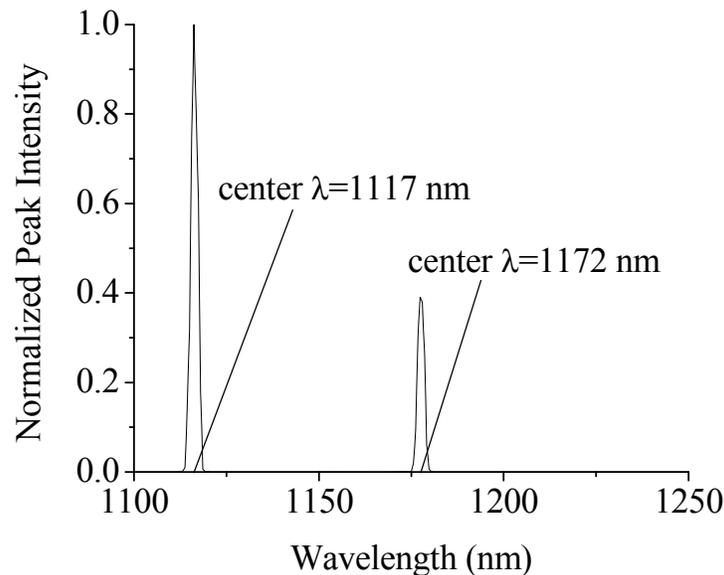
Figure 74. Spectrum produced by the RFL beam combiner configuration which used an MMFBG output coupler with a singlemode reflectivity of R=90%; the output Stokes power was 2 W.

The RFL beam combiner configuration which used an MMFBG output coupler with a singlemode reflectivity of R=90% produced the spectrum with the lowest wavelength components. The MMFBG translated these shorter wavelength components into higher-order transverse modes in the Stokes beam. The more lower-wavelength peaks contained in the Stokes spectrum, the worse the beam quality of the Stokes beam.

The 4.4 W of Stokes power (M^2=2.1) produced by the R=4% output coupler configuration was 296% brighter than the 10.8 W of the two overlapping pump beams (M^2=5.8) used to generate it. On the other hand, the 5.8 W of Stokes power (M^2=3.5) produced by the RFL beam combiner configuration which used an output coupler MMFBG with a singlemode reflectivity of R=90% was only 140% brighter than the coupled pump beams used to generate it. Clearly an RFL beam combiner can serve as a brightness converter.
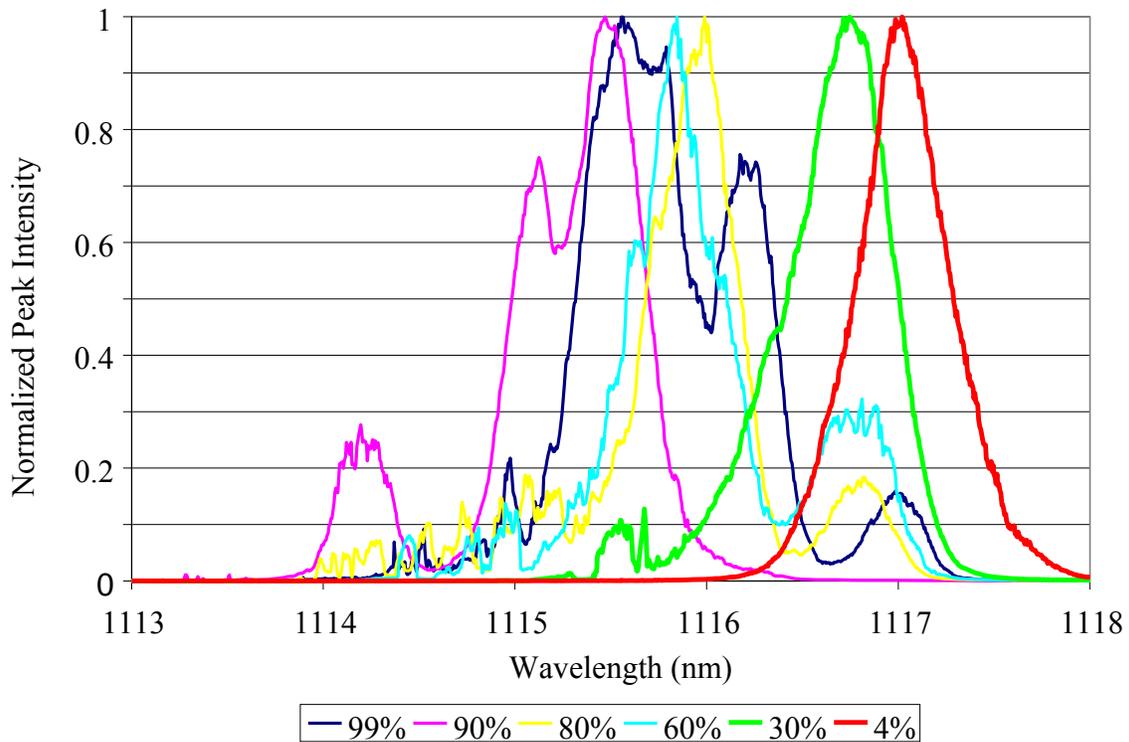
Figure 75. Spectra produced by the various configurations of the RFL beam combiner.

7.5.4. Section Summary

In summary, this section has demonstrated that an RFL based on a multimode graded-index fiber can be used as a practical method for SRS fiber beam combination. Multiple RFL beam combiner configurations were examined. One of these

configurations produced a 4.4 W Stokes beam which was 296% brighter than the pump beams used to generate it. A different RFL beam combiner configuration produced a 5.8 W Stokes beam which was 140% brighter than the pump beams used to generate it; the optical conversion efficiency of this configuration was 56%. Some of the RFL beam combiner configurations examined in this section had slope efficiencies which approached or even exceeded unity at the powers tested.

This section also demonstrated that at low Stokes powers, RFL beam combiner configurations which used an output coupler MMFBG with a low reflectivity could generate a near-singlemode Stokes beam. As the Stokes power and/or the singlemode reflectivity of the MMFBG output coupler increased, the beam quality of the Stokes beam decreased. While this work demonstrated the feasibility of combining 1064 nm pump beams to generate a single Stokes beam, the technique can be fully generalized to other wavelengths of interest which can be transmitted through an optical fiber.

7.6. Chapter Summary

This chapter discussed RFLs based on multimode graded-index fibers and their application to power scaling. First, it was demonstrated that RFLs based on multimode graded-index fibers can produce 7 W of Stokes power with efficiencies that are much greater than has been demonstrated for RFLs based on singlemode fibers. Second, this chapter showed that an RFL can be used as a highly efficient method of SRS fiber beam combination whereby multiple pump beams can be used to generate a single Stokes beam. Using multiple pump beams provides an innovative method of power scaling RFLs, provided a means can be found to launch greater numbers of pump beams into a multimode fiber.

Finally, it was shown that power scaling RFLs based on multimode fibers comes at a cost. Higher Stokes powers corresponded to decreased beam quality of the output Stokes beam. Furthermore, it was shown that RFL configurations which used output coupler MMFBGs with high singlemode reflectivity had worse beam quality than RFL configurations which used output coupler MMFBGs with low reflectivity.

163

8. Raman Fiber Lasers using Dichroic Mirrors

8.1. Motivation

Chapter 7 showed that an RFL based on a graded-index multimode fiber can produce over 7 W of Stokes power, with optical efficiencies greater than 50% and even greater slope efficiencies. Further power scaling of RFLs based on multimode fibers is possible through several routes. The possibility of using brighter pump lasers is discussed in Chapter 9. Chapter 9 also discusses the possibility of using novel kinds of MMFBGs which reinforce the SRS beam cleanup process rather than undermining it. It is also possible to replace MMFBGs with dichroic mirrors. This technique may prove useful in creating RFLs based on very large fibers because writing FBGs to large fibers presents significant challenges. For example, Avensys (the manufacturer of the MMFBGs used in this dissertation) reported that it is difficult to maintain a uniform transverse profile when writing MMFBGs to a fiber with a 50 μm core [109]. Presumably, writing uniform MMFBGs to larger fibers will present an even greater challenge.

Furthermore, as discussed in Chapter 5, the reflectivity of an FBG written to a multimode fiber has a modal dependence. As shown by Eq. (95), this modal dependence is a function of the radius of the fiber core. An FBG written to a larger fiber will have a smaller wavelength separation between reflected modes than an FBG written to a smaller fiber. Using an MMFBG with a small wavelength separation between reflected modes will result in a highly multimode Stokes beam even when the spectral output of the RFL is relatively narrow. RFLs based on very large multimode fibers would produce Stokes beams with lower beam quality than RFLs based on smaller multimode fibers. This

chapter examines the possibility of creating RFL configurations based on large gain fibers which do not require FBGs which are written directly to these large fibers.

One alternative configuration is to employ dichroic mirrors instead of MMFBGs, a technique that is reminiscent of the early designs of RFLs. This type of setup was abandoned in favor of all-fiber geometries in the early 1990s. However, in light of the potential limitations of writing FBGs to large multimode fibers, this chapter examines RFLs based on multimode graded-index fibers which use at least one dichroic mirror in place of an MMFBG.

This chapter discusses the performance of an RFL configuration which uses a dichroic mirror as the input coupler and an MMFBG as the output coupler and compares its performance to that of an RFL configuration that uses two MMFBGs. While the mirror-MMFBG RFL configuration and the two-MMFBG RFL configuration produced similar output Stokes powers, the two-MMFBG RFL configuration produced a Stokes beam with slightly better beam quality. The performance of an RFL configuration that used two dichroic mirrors is also discussed.

8.2. Experimental Setup

The baseline configuration of this experiment was an RFL configuration based on a 300 m long germanosilicate graded-index fiber with a 50 μm core (NA=0.2). A single MMFBG was spliced to each end of the gain fiber. Avensys reported the singlemode reflectivity of both gratings to be R=99% at the Stokes wavelength of 1117 nm. The output Stokes power was maximized by carefully aligning the fiber at the input end of the RFL. The performance of this setup was quantified in terms of the output Stokes power, the beam quality and the output spectrum of the output Stokes beam. These

measurements served as a standard against which to compare the performance of the other two RFL configurations.

The setup of the mirror-MMFBG configuration of the RFL is shown in Figure 76. This configuration used the same output coupler MMFBG as the configuration which employed two MMFBGs. However, the input coupler MMFBG was replaced with a dichroic mirror.   This dichroic mirror was actually a notch filter with a reflectivity of R=99% at the Stokes wavelength (1117 nm) and a transmissivity of T>95% at the pump wavelength (1064 nm). The position of the input fiber and the angle of the dichroic mirror were aligned to maximize the total output Stokes power. The performance of the mirror-MMFBG configuration of the RFL was characterized in terms of the power, the beam quality and the spectral characteristics of the generated Stokes beam. No effort was made to optimize the performance of the hybrid RFL configuration by using different MMFBG output couplers or by using dichroic mirrors with different reflectivity.
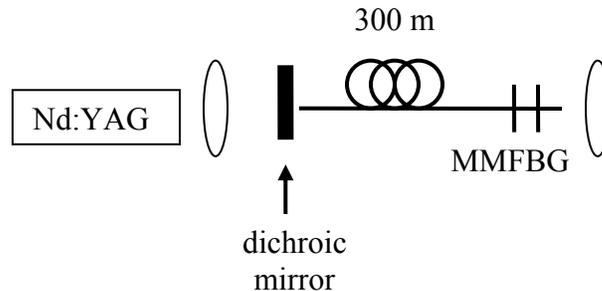
Figure 76. Diagram of the mirror-MMFBG configuration of an RFL based on multimode graded-index fiber.

The performance of an RFL configuration employing two dichroic mirrors was also characterized. In this setup, the output coupler MMFBG was replaced with a dichroic mirror which had a reflectivity of R=70% at 1117 nm. This dichroic mirror was used as the output coupler because its reflectivity of R=70% roughly matched the

166

reflectivity response of the output coupler MMFBGs to several higher-order transverse Stokes modes. On the other hand, the R=99% dichroic mirror was chosen as the input coupler to maximize the performance of the RFL. The position and orientation of the output end of the RFL fiber as well as the orientation of the output coupler mirror were adjusted to maximize the output Stokes power.

8.3. Results and Discussion

The output Stokes power as a function of the coupled pump power is shown in Figure 77 for both the baseline configuration of the RFL and the mirror-MMFBG configuration of the RFL. In terms of the generated Stokes power and the Stokes threshold, the two RFL configurations were very similar. The slope efficiency and the beam quality of the Stokes beams produced by the two configurations are shown in Table 12. The baseline configuration produced a Stokes beam with slightly better beam quality than the Stokes beam produced by the mirror-MMFBG configuration of the RFL.

The spectrum of the Stokes output produced by the baseline configuration of the RFL, shown in Figure 78, consisted of a single peak centered at 1116 nm. The spectrum of the Stokes output produced by the mirror-MMFBG configuration of the RFL, shown in Figure 79, contained three distinct peaks which were separated by 0.3 nm. The total range of these three subpeaks corresponded to the 1 nm bandwidth of the MMFBG output coupler (as measured by the manufacturer).

This three-peaked spectrum was a significant contrast to the near-single-peak spectrum produced by the baseline configuration of the RFL. These multiple peaks resulted from a Fabry-Perot cavity in the dichroic mirror. The MMFBG output coupler transformed these peaks into additional higher-order transverse principal modes in the

167

Stokes output and degraded the beam quality of the output Stokes beam. This explains why the beam quality of the Stokes beam created by the mirror-MMFBG configuration of the RFL was slightly worse than the beam quality of the Stokes beam created by the baseline configuration of the RFL.
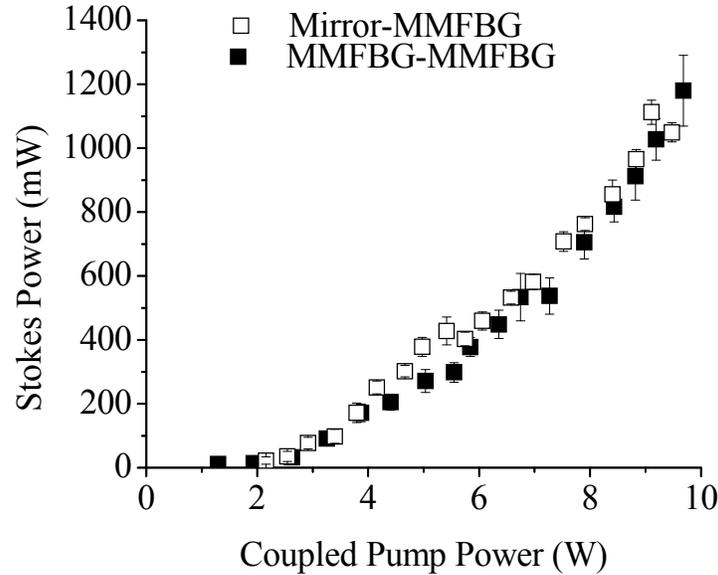
Figure 77. Stokes power produced by the baseline configuration of the RFL and the Stokes power produced by the mirror-MMFBG configuration of the RFL.

Table 12. Performance characteristics of RFL configurations employing MMFGBs and dichroic mirrors.

	MMFBG-MMFBG (baseline)	Mirror-MMFBG
Max Power	1.1 W	1.2 W
Slope Efficiency	19%	17%
Beam Quality (M^2)	2.7±0.3	3.1±0.3

The two-mirror RFL configuration produced slightly more output power (1.5 W) than the other two RFL configurations. While the spectral output of both the baseline configuration of the RFL and the mirror-MMFBG configuration of the RFL were relatively stable, the spectral output produced by the two-mirror configuration of the RFL was highly variable. Figure 80 provides an example of a typical spectral scan. Multiple

spectral scans were made, each of which contained multiple spectral peaks. This indicated that at any given time the two-mirror RFL configuration produced Stokes output which contained several different wavelength peaks. The number of peaks and their center wavelengths changed each time the spectrum was measured. This suggested that the spectral output produced by the two-mirror RFL configuration varied rapidly on a time scale of seconds.
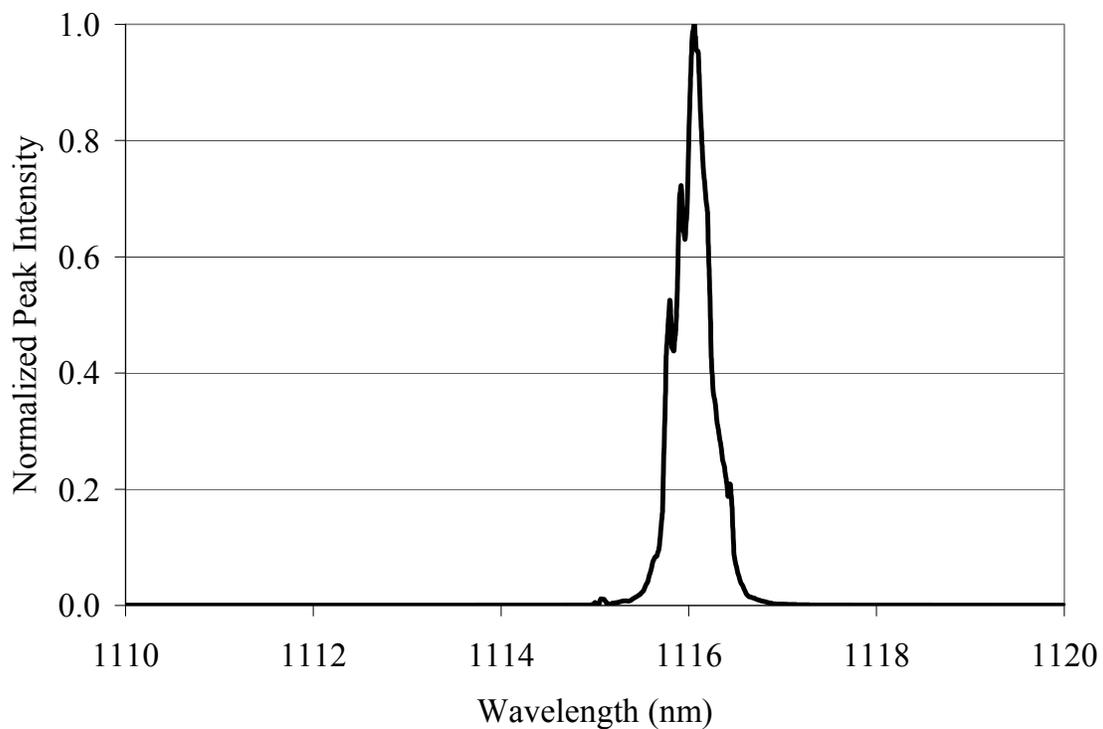
Figure 78. Spectrum produced by the baseline configuration of the RFL.

To understand the structure underlying the variations in the spectrum, nine separate spectral scans were taken sequentially; each scan lasted several minutes. The results of each of these scans were averaged together. This averaged spectrum, shown in Figure 81, contained a series of wavelength peaks. These wavelength peaks were separated by multiples of 0.3 nm. Incidentally, this 0.3 nm peak spacing was also present

169

in spectra produced by the mirror-MMFBG configuration of the RFL (shown in Figure 79). This peak spacing roughly corresponded to the free spectral range of a Fabry-Perot cavity of 1.4 mm; the thickness of the dichroic mirrors was measured to be ~1.3 mm. It should be noted that the mirror-mirror RFL configuration contained two different Fabry-Perot cavities (one for each mirror). Furthermore, it should be noted that only one side of each dichroic mirror was reflection coated. However, the rapidly varying Stokes spectrum was produced no matter which side of the dichroic mirror faced the fiber cavity.
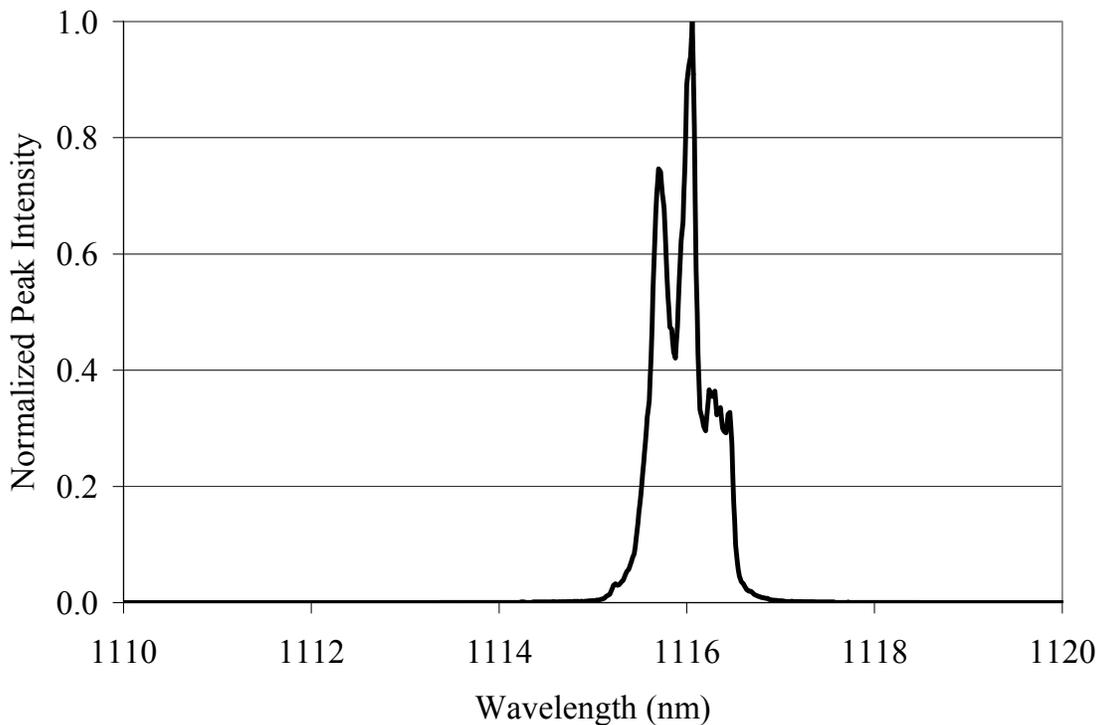
Figure 79. Spectrum produced by the mirror-MMFBG configuration of the RFL.

Unfortunately, it was not possible to force the RFL to generate Stokes output at only a single wavelength. Wavelength selection was attempted by adding different dispersive prisms to the RFL cavity in the hopes that only one wavelength would then be allowed to oscillate. Although several different prisms were tried, no significant changes

170

in the output spectra were observed; the dispersion of the prisms was simply not high

enough.
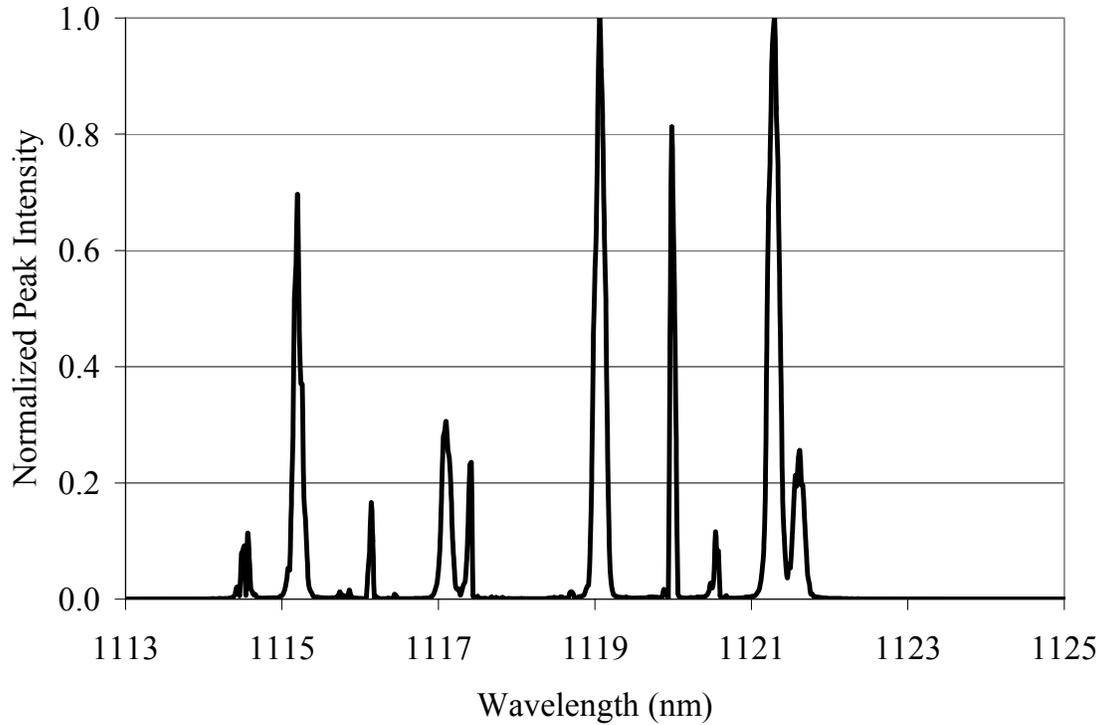
Figure 80. Typical output spectrum of an RFL configuration which used two dichroic
mirrors.

8.4. Chapter Summary

There was no appreciable difference between the output power of an RFL

configuration which used two MMFBGs and the output power of an RFL which used a

mirror-MMFBG configuration. However, the beam quality and the spectrum of the

Stokes beam generated by the mirror-MMFBG configuration of the RFL was slightly

worse than the beam quality and the spectrum of the Stokes beam generated by the

baseline configuration of the RFL. The dichroic mirror introduced a Fabry-Perot cavity

into the RFL which caused oscillation at multiple wavelengths. The number of spectral

peaks could be reduced by using thicker dichroic mirrors or by applying a reflective

171

coating directly to the ends of the fiber. Using a wedge-shaped dichroic mirror would also remove the Fabry-Perot cavity.
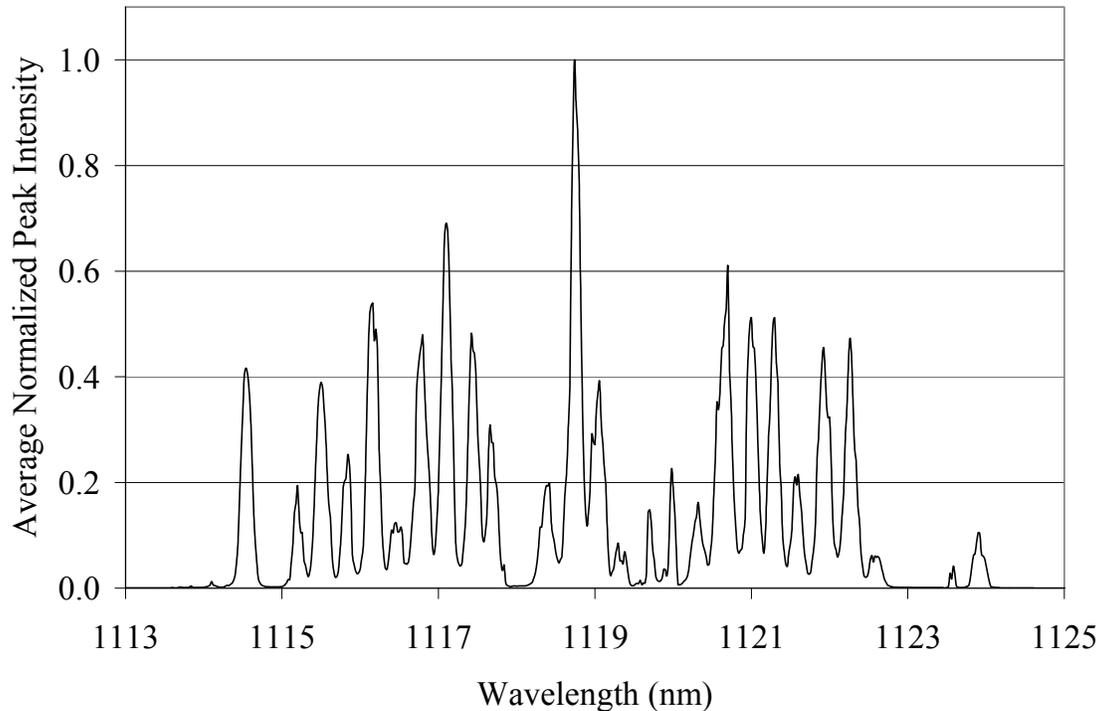
Figure 81. Averaged output spectra of an RFL configuration which used two dichroic mirrors.

A mirror-MMFBG configuration could be used to construct an RFL based on a fiber which is so large that a Bragg grating cannot be effectively written to it. A dichroic mirror could be used as the input coupler of the RFL. A Bragg grating written to a smaller multimode fiber could be fusion spliced onto the back end of an RFL and used as an output coupler. (Reversing the orientation of the MMFBG and mirror would prevent efficient coupling of the pump into the multimode fiber.) Care would need to be taken to minimize the losses inherent in propagation from the larger fiber to the smaller fiber containing the MMFBG. The experiments described in this chapter suggest that it should

172

be possible to create an RFL based on a fiber with a core size significantly greater than 50 μm even if it is difficult to write a Bragg grating to such a large fiber.

9. Conclusions

9.1. Summary

This dissertation explored the power scaling of Raman fiber devices based on multimode fibers, specifically RFAs and RFLs. A numerical model was developed which explained why SRS beam cleanup only occurs in graded-index fibers, but does not occur in step-index fibers. Numerical modeling also predicted that the beam quality of the Stokes output of an RFA depended on the beam quality of the input seed beam as well as the beam quality of the input pump beam. Experimental investigations of the RFA showed that the beam quality of the Stokes output was comparable to the beam quality of the Stokes input. Experimental investigations showed that the spectral properties of the output of the BSRS geometry of the RFA were superior to the spectral properties of the output of the FSRS geometry of the RFA.

The study of RFLs was primarily experimental. The results presented in this dissertation showed a nearly nine-fold increase in the demonstrated power of an RFL based on a multimode fiber relative to what was demonstrated by Baek and Roh [16] . It was also shown that an RFL based on a multimode graded-index fiber can have significantly better overall optical-to-optical (initial pump to final Stokes) efficiency than RFLs based on a fiber with a singlemode core [107,108]. It was further demonstrated that power scaling RFLs based on multimode graded-index fibers comes at the cost of lower beam quality of the output Stokes beam. This is primarily due to the multimode nature of the MMFBG used as the output coupler of the RFL because the MMFBG translated spectral broadening and peak splitting into additional modes in the Stokes output.

174

Finally, this dissertation effort developed two different methods of combining two CW pump beams to create a single Stokes beam, a process known as SRS beam combination. While both an RFA and an RFL were shown to be useful for SRS fiber beam combination, the latter was shown to be superior in terms of efficiency and power. The SRS beam combiner presented in this document demonstrated that SRS fiber beam combination via an RFL is a practical technology.

Section 9.2 of this chapter summarizes the research presented in this document. Section 9.3 lists the technical achievements described in this document, while Section 9.4 discusses several possible avenues for future research. These avenues for future research include direct diode pumping with high brightness fiber coupled diode lasers, using novel MMFBGs which reinforce the beam cleanup process and building Raman fiber devices based on different fiber materials. Cascaded RFLs based on graded-index multimode fibers are also presented as another promising area of future research.

9.2. Significant Contributions

9.2.1. SRS Beam Cleanup

Chapter 4 presented a model of SRS beam cleanup in multimode fibers. The overlap integrals of a multimode fiber, which represent the relative contribution of a given pump mode configuration to the gain of a given Stokes mode, were calculated. These overlap integrals showed that in a graded-index fiber, the LP_{01} Stokes mode tended to experience greater gain than any other transverse Stokes modes of the fiber. In the absence of an external seed, the uniform seeding conditions associated with spontaneous Raman scattering in a long fiber combined with the high gain of the LP_{01} Stokes mode to

produce a Stokes beam which was dominated by the LP_{01} mode. This was shown to be true for a variety of pump launching conditions.

The overlap integrals of a step-index fiber were computed and used to calculate the gain of the transverse Stokes modes of a step-index fiber given a variety of pump launching conditions. It was shown that in a step-index fiber, the LP_{01} mode does not experience preferential gain relative to the higher-order transverse Stokes modes of the fiber. This explains why beam cleanup only occurs in a graded-index fiber and not in a step-index fiber.

This is a significant improvement in the beam cleanup theory presented by Chiang, which evaluated the overlap integrals of a step-index fiber and used these results to describe the behavior of graded-index fibers [21]. It should also be noted that Chiang's model was restricted to examining the overlap of the intensity patterns of the modes rather than the overlap of the mode fields themselves. Finally, Chiang's model only considered the gain of the Stokes modes of a fiber for a single, carefully chosen launching condition of the pump beam.

9.2.2. Raman Fiber Amplifiers based on Graded-Index Fibers

As discussed in Chapter 4, previous experimental studies of SRS beam cleanup in graded-index fibers have only considered the generation of an unseeded Stokes beam in the absence of an external seed [17,20,21]. These studies reported very dramatic improvement in the beam quality of the output Stokes beam relative to the beam quality of the input pump beam used to generate it. Rice speculated that an RFA would provide similarly dramatic improvements in the beam quality of a seed beam as it was amplified;

Rice predicted that the amplified seed would be diffraction-limited even if the input seed was highly multimode [22].

Unlike the case of unseeded SRS, in the case of an RFA, the input seed power is not uniformly distributed amongst the Stokes modes of the fiber. This distinguishes unseeded SRS beam cleanup from the beam quality of the output Stokes beam produced by an RFA. The model presented in Chapter 4 examined the beam quality of the output of the FSRS geometry of an RFA by considering the interaction of the power in the pump and seed modes of the fiber. This interaction was governed by a set of coupled differential equations, the solution of which described the evolution of the pump and Stokes beams. A series of random input pump and input seed configurations were considered. The beam quality of the input mode distributions and the resulting output mode distributions were calculated in terms of M^2 to reveal that the beam quality of the input pump and the input seed beams determined the beam quality of the output Stokes beam.

This model predicted that given a pump beam with good beam quality, the beam quality of the amplified seed will be improved relative to the beam quality of the input Stokes beam. Furthermore, this model predicted that given a poor quality pump beam, the beam quality of the Stokes output will be similar to the beam quality of the input seed, a prediction which was validated by the experimental investigations of the RFAs described in Chapter 5.

Morgan demonstrated an RFA based on a multimode fiber. He noted that the beam quality of the amplified seed was similar to the beam quality of the input seed; studies of unseeded SRS have shown the beam quality of the Stokes beam to be much

177

greater than the beam quality of the pump beam [110]. However, Morgan's research only examined an RFA which used a BSRS geometry. Furthermore, the relationship between the beam quality of the seed and the amplified seed was not extensively studied.

The original research described in this document examined the performance of an RFA based on a multimode graded-index fiber using both the FSRS geometry and the BSRS geometry. The beam quality of the amplified seed was experimentally demonstrated to be similar to the beam quality of the input seed. This observation is consistent with the model described in Chapter 4.

The experiments included in this dissertation also examined the beam quality of the output of the RFA as a function of the input seed power. An unseeded Stokes beam was observed to have good beam quality. However, when even small amounts of power from a multimode seed beam were launched into the RFA, the beam quality of the amplified Stokes beam was immediately degraded relative to the beam quality of the Stokes beam which was generated in the absence of a seed.

This experiment validated another aspect of the model presented in Chapter 4. According to this model, in the absence of an external seed, spontaneous Raman scattering uniformly seeded the transverse Stokes modes of a long fiber. Since the LP_{01} Stokes mode in a graded-index fiber had the greatest gain of all Stokes modes, the model predicted that it would become the dominant component of the Stokes output. In the case of the RFA, the seed power was no longer uniformly distributed amongst the transverse Stokes modes of the fiber. When higher-order transverse modes of the fiber were seeded with a relatively high percentage of the input seed power, mode competition did not favor the lower-order transverse Stokes modes even though they had better overlap with the

178

pump beam. This explains the difference between the beam quality of the Stokes output of an RFA and the beam quality of the Stokes beam produced by unseeded SRS.

This work also examined the differences between the FSRS geometry of the RFA and the BSRS geometry of the RFA in terms of the spectral output of the amplifier. It was shown that in the FSRS geometry, an RFA produced multiple wavelengths corresponding to a cascade of Stokes orders. At the pump powers tested (3.5 W), the Stokes output of the BSRS geometry of the RFA was primarily confined to the 1st Stokes order.

The difference between the output spectra produced by the FSRS geometry and the output spectra produced by the BSRS geometry can be explained in terms of FWM which provided a seed for higher Stokes orders. The phase-matching condition for FWM cannot be satisfied in the BSRS geometry and so the onset of the Stokes cascade was delayed. It should be noted that at sufficiently high power levels, the higher Stokes orders will eventually reach the single-pass SRS threshold and a Stokes cascade will eventually form, even in the BSRS geometry. However, the amount of power in the higher Stokes orders will be less for the BSRS geometry than for the FSRS geometry. For this reason, when high spectral purity is important, the BSRS geometry of the RFA may prove to be the preferred configuration.

9.2.3. Development of RFLs based on Multimode Fibers

An RFL based on a multimode graded-index fiber was developed by Baek and Roh, but the Stokes power and slope efficiency of this device were limited to 800 mW and 7% respectively [16]. The work described in this document demonstrated that an RFL based on a multimode graded-index fiber can produce up to 7 W of Stokes power.

179

An optical-to-optical (initial pump to final Stokes) efficiency of almost 35% was demonstrated. This efficiency was significantly greater than the optical-to-optical efficiency which has been reported for RFLs based on singlemode fibers.

The higher Stokes power came at a price however, because higher output Stokes powers were shown to correspond to lower beam quality of the Stokes output. It was shown that RFL configurations which employed output coupler MMFBGs with low reflectivity produced Stokes beams with better beam quality than RFLs configurations which used output coupler MMFBGs with high reflectivity. These observations were explained in terms of gain saturation in RFL configurations employing high reflectivity MMFBGs. It has been shown in RFLs based on singlemode fibers that gain saturation leads to peak splitting in the Stokes output. It was also shown that power scaling in RFLs based on singlemode fibers spectrally broadened the output Stokes spectra. Due to the multimode nature of the MMFBGs, the additional wavelengths introduced through peak splitting and spectral broadening corresponded to additional transverse modes in the Stokes output which reduced the beam quality of the output Stokes beam.

9.2.4. SRS Beam Combination in Graded-Index Fibers

This work also investigated SRS fiber beam combination, which has been largely undeveloped due to the difficulty of reaching the SRS threshold. Flusche *et al*. demonstrated SRS fiber beam combination using four pulsed pump beams from a single laser to reach the Stokes threshold [20]. This dissertation described two other methods of SRS fiber beam combination which combined two separate CW pump beams to generate a single Stokes beam. The first method, described in Chapter 6, used an RFA based on a 50 μm graded-index fiber. This device had an optical-to-optical efficiency of about 10%.

Chapter 7 described a second method of SRS fiber beam combination which utilized an RFL to combine two separate CW pump lasers to produce a single Stokes beam with output powers of 5.5 W and an optical-to-optical (coupled pump to final Stokes) efficiency of 51%. The results of Chapter 7 show that an RFL can be utilized as a practical method of SRS fiber beam combination.

This document showed that an RFL based on a multimode graded-index fiber can operate with high efficiency and output power, either as an SRS beam combiner or as a stand-alone oscillator. There is, however, a trade-off between Stokes power and beam quality. This limitation was shown to be primarily a function of the MMFBGs used to construct the RFL; approaches for improving the suitability of MMFBGs are discussed in Section 9.4.2.

9.2.5. RFLs based on Graded-Index Fibers using Dichroic Mirrors

Chapter 8 examined the possibility of creating RFL configurations based on multimode fibers which used dichroic mirrors instead of using MMFBGs. It was shown that the output power and efficiency of an RFL which used two dichroic mirrors was similar to the output power of an RFL which used two MMFBGs. Unfortunately, each of the dichroic mirrors formed a Fabry-Perot cavity which degraded the spectral quality of the output Stokes beam.

The possibility of creating an RFL configuration that used a combination of a dichroic mirror and an MMFBG was also examined. In terms of the generated Stokes power, this configuration performed similarly to the two-MMFBG RFL configuration. The beam quality of the Stokes beam produced by the RFL configuration which used two MMFBGs was slightly better than the beam quality of the Stokes beam produced by the

181

mirror-MMFBG configuration of the RFL. Using a dichroic mirror in place of a single MMFBG was shown to be potentially useful for creating RFLs based on very large multimode fibers.

9.3. Technical Achievements

-Explained why SRS beam cleanup is confined to graded-index fibers

-Modeled unseeded SRS beam cleanup in graded-index fibers

-Showed that the lower-order transverse Stokes modes of a graded-index fiber experience greater gain than the higher-order transverse Stokes modes

-Modeled the beam quality of the Stokes output of an RFA

-Showed the beam quality of the input pump beam of an RFA determined the beam quality of the output Stokes beam

-Showed the beam quality of the input seed beam of an RFA determined the beam quality of the output Stokes beam

-Experimentally validated predictions of the model of the beam quality of the Stokes beam produced by an RFA

-Experimentally characterized an RFA based on multimode graded-index fiber

-Developed RFL based on graded-index fiber

-Demonstrated an efficient SRS beam combiner based on RFL

-Demonstrated an SRS beam combiner based on RFA

9.4. Future Work

9.4.1. Direct Diode Pumping of Raman Fiber Devices

The future development of RFLs based on graded-index fibers could include direct diode pumping of the RFL. Efficient direct diode laser pumping of an RFL based

182

on a 50 µm graded-index fiber is simply not feasible at this time—the technology necessary for efficiently coupling the diode pump laser output into a multimode fiber is still being developed. In the work described in this dissertation, the maximum available CW pump power coupled into a 50 µm fiber was 14 W. However, the Lissotschenko Mikrooptik (LIMO) corporation currently offers pump diodes with 25 W of output power coupled into a 100 µm fiber [111]. A diode laser with the output coupled into a 50 µm fiber is also available from LIMO, but the power is limited to 6 W. Further improvements in this technology are likely. As greater fiber coupled pump powers become available, the true power scaling potential of Raman fiber devices based on multimode graded-index fibers can be examined fully.

9.4.2. Novel MMFBGs

One drawback to the monolithic design of RFLs based on multimode fibers is that FBGs written to multimode fibers are inherently multimode devices because different transverse modes of the fiber are reflected at different wavelengths with different reflectivity. In Chapter 7, it was shown that high output Stokes powers and high reflectivity output coupler MMFBGs can lead to peak splitting and spectral broadening. Due to the multimode nature of the MMFBG, peak splitting and spectral broadening introduced additional transverse modes into the Stokes output. In future studies it may be possible to reduce this problem by using novel MMFBG designs.

Szkopek *et al*. designed an MMFBG architecture which consisted of a series of concentric shells of alternating high and low index regions [112]. This design was experimentally tested and shown to create a grating with reflectivity of 98% and a bandwidth of <0.5 nm. This MMFBG was still multimode, but the reflectivity of the

LP_{01} mode was reported to be significantly higher than the reflectivity of other transverse modes of the fiber. This may prove to be a significant advantage in future work involving RFLs based on multimode fibers.

Another possible MMFBG architecture is to use conventional MMFBGs which have been designed with a large wavelength separation between reflected modes. An MMFBG with an appropriately large wavelength spacing between modes (i.e., greater than the linewidth of the Stokes output) could be applied to RFLs based on multimode fibers. In such an MMFBG, the mode selection of the MMFBG would serve to reinforce the beam cleanup process and provide a different avenue for achieving high output Stokes power with good beam quality.

Another factor which may play a role in the beam quality of the Stokes output of an RFL is the radial profile of the output coupler MMFBG. According to the manufacturer (Avensys), it is difficult to maintain a uniform radial profile throughout an FBG written to a multimode fiber [109]. A radial component of the MMFBG reflectivity spectrum can alter the beam quality of the output Stokes beam. For example, multiplying the profile of the LP_{01} mode by a profile of say, R^3 (where R is the radius) changes the M^2 value from 1.0→2.0; multiplying the profile by R^2 changes the M^2 value from 1.0→1.7. On the other hand, a profile of $1-R^2$ does not alter the M^2 value significantly. In the case of the LP_{11} mode, a mode profile of R^2 changes the M^2 value from 3.0→3.8, a profile of R^3 changes the M^2 value from 3.0→3.5. This suggests that future studies of RFLs based on multimode fibers which use MMFBGs should consider the effect of the radial profile of the MMFBG.

9.4.3. Cascaded Raman Fiber Lasers based on Multimode Fibers

In Chapter 7, using a long fiber in an RFL cavity was shown to result in a highly efficient RFL. However, the long generated significant power in higher Stokes orders, a significant drawback for a laser designed to create high output power at the 1st Stokes order wavelength. On the other hand, generating higher Stokes orders would be useful in creating a cascaded RFL based on a multimode fiber. To date, cascaded RFLs have only been demonstrated in using singlemode fibers.

A cascaded RFL based on a multimode fiber could be constructed simply by splicing multiple pairs of MMFBGs onto a single, long length of graded-index fiber, as shown in Figure 57. As seen in Figure 74, the Stokes output of one RFL which used a 2500 m long graded-index fiber contained two Stokes orders. In a cascaded RFL, the 2nd Stokes order would be resonant with a cavity consisting of a 2nd pair of MMFBGs. Eventually the intensity of this Stokes order would be sufficient to create a 3rd Stokes order, which would be resonant with a possible 3rd cavity consisting of a 3rd pair of gratings, etc.

The advantage of beam cleanup should result in sequential improvement in the beam quality of each subsequent Stokes order. The 1st Stokes order would have better beam quality than the pump beam; likewise the 2nd Stokes order could have better beam quality than that of the 1st Stokes order. Each subsequent cavity could result in significant improvements in the beam quality of the output Stokes beam. This has been demonstrated for single-pass, unseeded Stokes generation in a long fiber [21]. It is possible that a cascaded RFL based on a multimode graded-index could produce a near-diffraction-limited output Stokes beam.

185

9.4.4. Applications to Graded-Index fibers made of Novel Materials

The original research presented in this document has been confined to Raman fiber devices based on multimode graded-index Ge-doped fibers. However, one of the main advantages of the SRS process is wavelength flexibility, meaning that different Stokes wavelengths can be created by using a given pump source with a fiber based on a different material. In short, fibers with unique Stokes shifts can be used to create novel wavelengths.

Furthermore, some Raman gain media such as chalcogenide fibers, possess Raman gain coefficients which are much greater than the gain coefficient of Ge-doped fused silica. Currently however, the attenuation of these novel fibers is very high. Chalcogenide fibers could be used to create RFLs with higher Stokes output and lower thresholds, provided this attenuation issue can be overcome. This section reviews some of the properties of these alternative multimode fibers including P-doped fibers and chalcogenide fibers.

9.4.4.1. P-Doped Fibers

P-doped fibers have a much larger Stokes shift than Ge-doped silica fibers (1330 cm^{-1} compared to 440 cm^{-1}). The larger Stokes shift of P-doped fibers means that eyesafe wavelengths could be produced with only 2 Stokes shifts of an Nd:YAG pump laser (1064nm $\rightarrow$ 1588 nm). This is a stark contrast to the 6 Stokes shifts required to produce a similar wavelength using a Ge-doped silica fiber pumped by an Nd:YAG laser (1064nm$\rightarrow$ 1583 nm). The Raman gain of P-doped silica fiber is similar to the Raman gain of Ge-doped fiber: g_R=0.80x10^{-13} m/W and g_R=0.88x10^{-13} m/W respectively. It

186

should be noted that the attenuation of P-doped fiber is somewhat higher than the attenuation of Ge-doped fiber: 1.7 dB/km compared to 1.0 dB/km [113].

It should be possible to build RFLs and RFAs based on multimode P-doped fiber. Currently, our laboratory possesses a 1 km spool of P-doped fiber. A vendor (Avensys) was contacted about manufacturing MMFBGs for this fiber but no phase masks were available. Given sufficient funding, a phase mask could be obtained and gratings could be fabricated, allowing the creation of RFLs based on multimode graded-index P-doped fiber. It should also be possible to create such an RFL using a set of dichroic mirrors as discussed in Chapter 8, although in the absence of gratings, alignment will be a significant challenge. Constructing an RFA based on a multimode graded-index P-doped fiber should be a fairly straightforward process.

9.4.4.2. AsSe Fiber

Raman amplification has been demonstrated in AsSe fiber [114]. The gain of this fiber was reported to be 300 times higher than that of Ge-doped silica fibers. The Stokes shift of AsSe fiber is about 230 cm^{-1}. One drawback to these new fibers is that they have very high attenuation levels (0.7 dB/m for AsSe fiber).   This high attenuation could offset the advantage of a higher Raman gain. According to Eq. (42), the threshold of an RFL based on a 300 m length of 50 μm AsSe fiber would be on the order of hundreds of watts. A 1 m long RFL would have a threshold on the order of tens of watts.

9.4.4.3. AsSe$_3$ Fiber

AsSe$_3$ fibers have also been studied by Asobe *et al*. [115]. The peak of the Raman gain curve occurs at 344 cm^{-1}. The Raman gain is ~4.4×10^{-12} m/W, which is 44 times higher than the Raman gain of conventional fused silica fibers. Asobe *et al*. created

187

a 140/230 μm DCF which had attenuation of 0.7 dB/m [115]. An RFL constructed out of a 1 m long 50 μm AsSe$_3$ fiber would, according to Eq. (42), have a threshold on the order of dozens of watts.

9.4.4.4. Te Fiber

Plotnicenko *et al.* surveyed doped telluride fibers [116]. They measured the spontaneous Raman cross section of a fiber given various doping conditions; these measurements are summarized in Table 13. The Raman gain can be calculated from the Raman cross section using Eq. (22). Oshishi and Jose also investigated Te fibers with various doping concentrations and found gain values 30-40 times greater than that of silica; the Stokes shifts ranged from 725-780 cm^{-1} [117].

Table 13. The maximum gain of telluride fiber with various dopants, normalized to the gain of fused silica at 440 cm^{-1}, is given for various Stokes shift ranges [116].

Dopant	460 cm^{-1}	650-750 cm^{-1}	900-920 cm^{-1}
WO$_3$	50	90	65
GeO$_2$	50	80	--
MoO$_3$-WO$_3$	38	75	96

It should also be noted that an RFL based on an As$_2$Se$_3$ fiber with a core size of 6 μm (NA=0.19) has been reported. The cavity was 0.5 m long. The pump was a double clad Tm^{3+} silica fiber laser which produced 10 W of power at 2051 nm [93]. As FBGs are not yet available for chalcogenide fibers, dichroic mirrors were used instead. The RFL had an output power of 0.64 W and a slope efficiency of 66% at 2062 nm. When the length of the fiber was extended to 4 m, the 2nd a 2nd Stokes order was observed at 2074 nm. The Stokes shift was 28 cm^{-1}. The Raman gain was reported to be about 2 orders of magnitude greater than the gain of silica fibers; the attenuation was 0.6 dB/m.

Appendix A. Fusion Splice Parameters for FSU 995
Recipe for Splicing 50/125 μm Ge-doped Fiber to Itself

This effectiveness of this recipe was determined using an Agilent 8163A Lightwave multimeter to measure the total transmission of a broadband source. The recipe was optimized by adjusting the fusion times, the fusion currents and overlap of the recipe with an eye to maximizing the transmission of the resulting splice. Splices created using the recipe had an average loss measured to be approximately 0.1 dB. The parameters used in this recipe are given in Table 14.

Table 14. Parameters of a recipe for fusion splicing 50 μm fiber to μm fiber using the FSU 995 fusion splicer.

Prefusion Time	0.3 seconds
Prefusion Current	11.5 mA
Gap	50 μm
Overlap	12.0 μm
Fusion Time 1	0.3 seconds
Fusion Current 1	8.0 mA
Fusion Time 2	2.0 seconds
Fusion Current 2	11.5 mA
Fusion Time 3	1.0 seconds
Fusion Current 3	10.5 mA
Left MFD	9.8 μm
Right MFD	9.8 μm
Set Center	255
AOA Current	0.0 mA
Early Prefuse	No
Alignment Accuracy	0.25 μm
Loss Shift	0 dB
Auto Arc Center	No

Bibliography

1. http://www.globalsecurity.org/military/ops/linebacker-1.htm, 9 Sept 2005.

2. http://www.de.afrl.af.mil/Factsheets/ABLHistory.swf, 18 Oct 2005.

3. B. A. Smith, R. Wall, "THEL Laser Kills Short-Range Missile", *Aviat Week Space Technol*, **152**, 33, 12 June 2000.

4. M. Selinger, "Navy Office Seeking More Money for Laser Weapons", *Aerosp Dly*, 10, 8 Jul 2003.

5. http://www.boeing.com/defense-space/military/abl/news/2004/010004_contact.html, 9 Sept 2005.

6. J. Hecht, "Solid-State High-Energy Laser Weapons", *Opt & Photonics News*, **14**, 42-47, Jan 2003.

7. E .L. Dereniak, G.D. Boreman, *Infrared Detectors and Systems*, New York, John Wiley & Sons, Inc., 1996.

8. K. F. Gibson and W.G. Kernohan, "Lasers in Medicine—a Review", *J Med Eng Technol*, **17**, 51-57, 1993.

9. http://www.fsona.com/technology.php?sec=laser_guide, 10 Aug 2004.

10. http://www.arl.army.mil/main/ResearchHighlights/DEVisitScholars05.htm, 12 Aug 2005.

11. J. F. Ruger**, "**Eyesafe Raman Lasers developed in West Germany**",** *Proc SPIE***, 1207,** 155-63**,** 1998**.**

12. J. Hecht, "Photonic Frontiers: High-Power Fiber Lasers: Pumping up the Power", *Laser Foc W*, **41**, n 8, 66-70, 2005.

13. J. Morris, "AFRL Working to Shrink Laser Systems for Use on Tactical Aircraft*", Aerosp Dly, 2*, 30 March 2002.

14. A. J. Stentz, "Applications of Raman lasers and Amplifiers in Fiber Communication Systems," *Proc SPIE, 3263*, 91, 1998.

15. S. K. Sim, H. C. Lim, L. W. Lee, L. C. Chia, R. F. Wu, I. Cristiani, M. Rini and V. Degiorgio, "High-Power Cascaded Raman Fiber Laser using Phosphosilicate Fiber", *Elecron Lett*, **40**, 738-9, 2004.

16. S. H. Baek and W. B. Roh, "Single-Mode Raman Fiber Laser Based on a Mulitmode Fiber", *Opt Lett*, **29**, 153-5, 2004.

17. T. H. Russell, S. M. Willis, M. B. Crookston and W. B. Roh, "Stimulated Raman Scattering in Multimode Fibers and its Application to Beam Cleanup and Combining", *J Nonlinear Opt Phys Mater*, **11**, 303-16, 2002.

18. T. H. Russell, B. W. Grime, T. G. Alley and W. B. Roh, "Stimulated Brillouin Scattering Beam Cleanup and Combining in Optical Fiber", to be published in *Nonlinear Optics and Recent Advances in Optics*, Research Signpost, 2007.

19. T. H. Russell, *Laser Intensity Scaling Through Stimulated Scattering in Optical Fibers,* PhD Dissertation, AFIT/DS/ENP/02-03, School of Engineering, Air Force Institute of Technology, Wright-Patterson AFB, 2002 (ADA398033).

20, B. M. Flusche, T. G. Alley, T. H. Russell, and Won B. Roh, "Multi-port Beam Combination and Cleanup in Large Multimode Fiber Using Stimulated Raman Scattering," *Opt Express*, **14**, 11748-55, 2006.

21. K. S. Chiang, "Stimulated Raman Scattering in a Multimode Optical Fiber: Evolution of Modes in Stokes Waves", *Opt Lett*, **17**, 352-4, 1992.

22. R. Rice, "Multimode Raman Fiber Amplifier and Method", U.S. patent 6,353,087, 2002.

23. G. Keiser, *Optical Communication Essentials*, New York, McGraw-Hill, 2003.

24. J. Toulouse, "Optical Nonlinearities in Fibers: Review, Recent Examples, and Systems Applications", *J Lightwave Tech,* **23**, 3625-41, 2005.

25. T. Y. Fan, "Laser Beam Combining for High-Power, High-Radiance Sources", *IEEE J Sel Top Quantum Electron*, **11**, 567-77, 2005.

26. D. J. Griffiths, *Introduction to Electrodynamics*, *3rd ed.*, New Jersey, Prentice Hall, 1999.

27. C. K. Madsen, J. H. Zhou, *Optical Filter Design and Analysis*, New York, John Wiley and Sons, 1999.

28. P. N. Butcher and D. Cotter, *The Elements of Nonlinear Optics*, Cambridge, Cambridge University Press, 1990.

29. C. V. Raman, K. Krishnan, "A New Type of Secondary Radiation", *Nature*, **121**, 501-2, 1928.

30. C. V. Raman, "A Change in the Wavelength in Light Scattering", *Nature*, **121**, 619, 1928.

31. R. W. Boyd, *Nonlinear Optics*, New York, Academic Press, 2003.

32. R. G. Smith, "Optical Power Handing Capacity of Low Loss Optical Fibers as Determined by Stimulated Raman and Brillouin Scattering", *Appl Opt*, **11**, 2490-4, 1972.

33. E. Garmire, F. Pandarese and C. H. Townes, "Coherently Driven Molecular Vibrations and Light Modulation", *Phys Rev L*, **11**, 160-3, 1963.

34. P. N. Butcher and D. Cotter, *The Elements of Nonlinear Optics*, Cambridge, Cambridge University Press, 1990.

35. J. Ferraro, K. Nakamoto, Introductory Raman Spectroscopy, Boston, Academic Press, 2004.

36. G. P. Agrawal, Nonlinear Fiber Optics, 3rd ed., San Diego, Academic Press, 2001.

37.   C. Fukai, K. Nakajima, J. Zhou, K. Tajima, K. Kurokawa, and I. Sankawa, "Effective Raman Gain Characterstics in Germanium- and Fluorine-Doped Optical Fibers", *Opt Lett*, **29**, 545-7, 2004.

38.   S. K. Sharma, D. W. Matson, J. A. Philpotts, T. L. Roush, "Raman Study of the Structure of Glasses along SiO_2-GeO_2", *J Non-Cryst Solids*, **68**, 99-114, 1984.

39.   G. E. Walrafen and J. Stone, "Raman Spectral Characterization of Pure and Doped Fused Silica Optical Fibers", *Appl Spec*, **29**, 337-44, 1975.

40.   D. Marcuse, "Loss Analysis of Singlemode Fiber Splices", *The Bell Sys Tech J* **56**, 703-18, 1977.

41.   J. B. Spring, T. H. Russell, T. M. Shay, R. W. Berdine, A. D. Sanchez, B. G. Ward, W. B. Roh, "Comparison of Stimulated Brillouin Scattering Thresholds and Spectra in Non-Polarization-Maintaining and Polarization-Maintaining Passive Fibers", *Proc SPIE*, **5709**, 147-56, 2005.

42.   B. E. A. Saleh, M.C. Teich, *Fundamentals of Photonics*, New York, John Wiley and Sons, 1991.

43.   J. A. Buck, *Fundamentals of Optical Fibers*, New York, Wiley, 1995.

44.   A. W. Synder, J. D. Love, *Optical Waveguide Theory*, New York, Chapman and Hall, 1983.

45.   F. Di Teodoro, J. Koplow, S. W. Moore, D. A. V. Kliner, "Diffraction-limited, 300-kW Peak Power Pulses from a Coiled Multimode Fiber Amplifier", *Opt Lett*, **27**, 518-20, 2002.

46.   M. E. Fermann, "Singemode Excitation of Multimode Fibers with Ultrashort Pulses", *Opt Lett*, **23**, 52-4, 1998.

47.   J. P. Koplow, Dahv A.V. Kliner, L. Goldberg, "Singemode Operation of a Coiled Multimode Fiber Amplifier", *Opt Lett*, **25**, 442-4, 2000.

48.   A. Polynkin, P. Polynkin, A. Schűlzgen, M. Mansuripur, N. Peyghambarian, "Watts-Level, Short All-Fiber Laser at 1.5 μm with a Large Core and Diffraction-Limited Output via Intracavity Spatial-Mode Filtering", *Opt Lett*, **30**, 403-5, 2005.

49.   J. Limpert, L. Lieni, H. Zellmer, A. Tunnerman, "500 W Continuous-Wave Fiber Laser with Excellent Beam Quality", *Electon Lett*, **39**, 645-7, 2003.

50.   U. Griebner, H. Schönnagel, "Laser Operation with Nearly Diffraction-Limited Output from a Yb:YAG Multimode Channel Waveguide", *Opt Lett*, **24**, 750-2, 1999.

51.   H. Komine, W. H. Long, Jr., E. A. Stappaerts, and S. J. Brosnan, "Beam Cleanup and Low-distortion Amplification in Efficient High-Gain Hydrogen Raman Amplifiers", *J Optical Soc America B*, **3**, 1428-46, 1986.

52.   J. Goldhar, M. W. Taylor and J.R. Murray, "An Efficient Double-Pass Amplifier with Pump Intensity Averaging in a Light Guide", *IEEE J Quantum Electron*, **20**, 772-85, 1984.

53. D. C. Hanna, M.T.T. Pacheco, K.H. Wong, "High Efficiency and High Brightness Raman Conversion of Dye Laser Radiation," *Opt Commun*, **55**, 188-92, 1985.

54. J. Reintjes, R. H. Lehmberg, R. S. F. Chang, M. T. Duiganan, and G. Calame, "Beam Cleanup with Stimulated Raman Scattering in the Intensity-Averaging Regime", *J Optical Soc America B*, **3**, 1408-26, 1986.

55. J. C. van den Heuvel, "Numerical Study of Beam Cleanup by Stimulated Raman Scatttering", *J Optical Soc America B*, **4**, 650-7, 1995.

56. N. R. Islam and K. Sakuda, "Wave-front Reconstruction by Backward-Stimulated Raman Scattering in a Multimode Graded-Index Optical Fiber", *J Optical Soc America B, 14*, 3238-41, 1997.

57. A. Sharma, M. Dokhanian, Z.Q. Wu, R. Posey, A. Williams, P. Venkateswarlu, "Stimulated Raman Scattering in a Multimode Optical Fiber with Bend-Induced Loss", *Opt Commun*, **111**, 127-31, 1994.

58. F. Capasso and P. Di Porto, "Coupled-Mode Theory of Raman Amplification in Lossless Optical Fibers", *J Appl Phys*, **47**, 1472-6, 1976.

59. E. M. Dianov, I. A. Bufetov, M. M. Bubnov, M. V. Grekov, S. A. Sasiliev, O. I. Medvedkov, A. V. Shubin, A. N. Guryanov, V. F. Khopin, M. V. Yashkov, E. M. Deliso, D. L. Butler, "1.3 µm Raman Fiber Amplifier", *Proc SPIE*, **4083**, 101-9, 2000.

60. R. H. Stolen, "Fiber Raman Lasers", *Fiber and Integrated Opt*, **3**, 21-51, 1980.

61. H. Yoda, P. Polynkin, M. Mansuipur, "Beam Quality Factor of Higher Order Modes in a Step-Index Fiber", *J Lightwave Techol*, **24**, 1350-5, 2006.

62. C. Lin and R. Stolen, "Backward Raman Amplification and Pulse Steepening in Silica Fibers", *Appl Phys Lett*, **29**, 428-31, 1976.

63. M. Ikeda, "Stimulated Raman Amplification Characteristics in Long Span Singlemode Silica Fibers", *Opt Commun*, **39**, 148-52, 1981.

64. M. Nakazawa, T. Nakashima and S. Seikai, "Raman Amplification in 1.4-1.5 µm Spectral Region in Polarization-Preserving Optical Fibers", *J Optical Soc America B*, **2**, 515-21, 1985.

65. K. Vilhelmsson, "Simultaneous Forward and Backward Raman Scattering in Low-Attenuation Singlemode Fibers", *J Lightwave Techol*, **4**, 400-4, 1986.

66. C. A. Codemard, J. K. Sahu and J. Nilsson, "Cladding-Pumped Raman Fiber Amplifier for High-Gain, High-Energy Single-Stage Amplification", *2005 Optical Fiber Communications Conference*, OTuF5, 2005.

67. G. A. Koepf, D. M. Kalen and K. H. Greene, "Raman Amplification at 1.118 µm in Singlemode Fiber and its Limitation by Brillouin Scattering"**,** *Electon Lett*, **18**, 942-3, 1982.

68. A. E. Siegman, "New Developments in Laser Resonators", *Proc SPIE*, **1224**, 2-14, 1990.

69. T. H. Russell and W. B. Roh, "Threshold of Second-Order Stimulated Brillouin Scattering in Optical Fiber", *J Optical Soc America B*, **19**, 2341-5, 2002.

70. T. Y. Fan, "Laser Beam Combining for High-Power, High-Radiance Sources," *IEEE J Sel Top Quantum Electron,* **11**, 567-77, 2005.

71. D. A. Rockwell and C. R. Giuliano, "Coherent Coupling of Laser Gain Media using Phase Conjugation", *Opt Lett*, **11**, 147-9, 1986.

72. R. H. Moyer, M. Valley and M. C. Cimolino, "Beam Combination through Stimulated Brillouin Scattering", *J Optical Soc America B*, **5**, 2473-88, 1988.

73. T. H Russell, W. B. Roh, J. R. Marciante, "Incoherent Beam Combining using Stimulated Brillouin Scattering in Multimode fibers", *Optics Exp*, **8**, 246-54, 2001.

74. B. G. Grime, W. B. Roh, T. G. Alley, "Phasing of a Two-Channel Continuous-Wave Master Oscillator-Power Amplifier by use of a Fiber Phase-Conjugate Mirror", *Opt Lett,* **30**, 2415-7, 2005.

75. B. C. Rodgers, T. H. Russell, and W. B. Roh, "Laser Beam Combining and Cleanup by Stimulated Brillouin Scattering in Multimode Optical fiber", *J Opt Soc America B,* **24**, 1124-26, 1999.

76. R. S. F. Chang, R. H. Lehmberg, M. T. Duignan and N. Djeu, "Raman Beam Cleanup of a Severely Aberrated Pump Laser", *IEEE J of Quantum Electronics*, **21**, 477-87, 1985.

77. N. G. Basov, *Lasers and Holographic Data Processing*, Mir Publishers, Moscow, 1984.

78. M. H. Smith, D. W. Trainor, and C. Duzy, "Shallow Angle Beam Combining Using a Broad-Band XeF laser", *IEEE . Quantum Electron*, **26**, 942-9, 1990.

79. R. H. Stolen, "Nonlinearity in Fiber Transmission", *Proc IEEE*, **68**, 1232-6, 1980.

80. J. Archabault, S. G. Grubb, "Fiber Gratings in Lasers and Amplifiers", *J Lightwave Technol*, **15**, 1378-90, 1997.

81. K. O. Hill, Y. Fujii, D. C. Johnson, B. S. Kawasaki, "Photosensitivity in Optical Fiber Waveguides: Application to Reflection Filter Fabrication", *Appl Phys Lett*, **32**, 647-9, 1978.

82. R. Kashyap, *Fiber Bragg Gratings*, San Diego, Academic Press, 1999.

83. G. Meltz, W. W. Morey and W. H. Glenn, "Formation of Bragg Gratings in Optical Fibers by a Transverse Holographic Method", *Opt Lett*, **14**, 823-825, 1989.

84. P. J. Lemaire, R. M. Atkins, V. Mizrahi, W. A. Reed, "High Pressure H_2 Loading as a Technique for Achieving Ultrahigh Photosensitivity and Thermal Sensitivity in GeO_2 Doped Optical Fibers", *Electon Lett*, **29**, 1191-93, 1993.

85. H. Yu, C. Yang, Y. Wang, J. Zhang, J. Yang, R. Farkas, C. Q. Xu, "Bragg Gratings in a Multimode Fiber", *Proc SPIE*, **5577**, 354-61, 2004.

86. W. Yunming, D. Jingcao, Z. Mingde, S. Xiaohan, "Theoretical and Experimental Study on Multimode Optical Fiber Grating", *Opt Commun*, **250**, 54-62, 2005.

87. J. Zhang, H. Yu, C. Xu, W. Huang, "Multimode Optical Fiber Bragg Gratings: Modeling, Simulation and Experiments", *Proc SPIE*, **5579**, 435-42, 2004.

88. T. Mizunami, T. V. Djambova, T. Niiho and S. Gupta, "Bragg Gratings in Multimode and Few-mode Optical Fiber", *J Lightwave Technol*, **18**, 230-5, 2000.

89. L. Su and C. Lu, "Wavelength-Switching Fiber Laser Based on Multimode Fiber Bragg Gratings", *Electron Lett*, **41**, 11-3, 2005.

90. H. Yu, Y. Wang, C. Xu, A. D. Vandermeer, "Oscillation Wavelength Selection of Semiconductor Lasers using a Multimode Fiber Bragg Grating", *Opt Express*, **13**, 1660-5, 2005.

91. X. Feng, Y. Liu, S. Yuan, G. Kai, W. Zhang and X. Dong, "L-Band Switchable Dual Wavelength Erbiium-Doped Fiber Laser based on a Multimode Fiber*", Opt Express*, **12**, 3834-9, 2004.

92. C. Zhao, Z. Li, M. S. Demokan, X. Yang, W. Jin, "Switchable Multiwavelength SOA-Fiber Ring Laser based on a Slanted Multimode Fiber Bragg Grating", *Opt Commun*, **252**, 52-7, 2004.

93. S. D. Jackson and G. A. Sanchez, "Chalcogenide Glass Raman Fiber Laser", *Appl Phys Lett*, **88**, 221106-8, 2006.

94. J. C. Travers, S. V. Popov, J. R. Taylor, "Efficient Continuous-Wave Holey Fiber Raman Laser", *Appl Phys Lett*, **87**, 31106, 2005.

95. E. P. Ippen, "Low-Power Quasi-CW Raman Oscillator", *Appl Phys Lett*, **16**, 303-5, 1970.

96. R. H. Stolen, E. P. Ippen, A. R. Tynes, "Raman Oscillation in a Glass Optical Waveguide", *Appl Phys Lett*, **20**, 62-4, 1972.

97. K. O. Hill, B. S. Kawasaki and D. C. Johnson, "Low Threshold CW Raman Laser", *Appl Phys Lett*, **29**, 181-3, 1976.

98. S. A. Babin, D. V. Churkin and S. I. Kablukov, "Longitudinal Mode Structure of the Two-Stage Raman Fiber Laser", *Laser Physics*, **15**, 300-5, 2005.

99. S. A. Babin, A. S. Kurkov, V. V. Potapov, D. V. Churkin, "Dependence of the Spectral Properties of a Raman Fiber Laser on the Bragg Grating Temperature", *Quantum Electronics*, **33**, 1096-1100, 2006.

100. S. A. Babin, D. V. Churkin, A. E. Ismagulov, S. I. Kablukov and E. V. Podivilov, "Spectral Broadening in Raman Fiber Lasers", *Opt Lett*, **31**, 3007-9, 2006.

101. R. K. Jain, C. Lin, R. H. Stolen, W. Pleibel and P. Kaiser, "A High-Efficiency Tunable CW Rman Oscillator", *Appl Phys Lett*, **30**, 162-4, 1977.

102. I. K. Ilev, H. Kumagai and K. Toyoda, "Ultraviolet and Blue Discretely Tunable Double Pass Fiber Raman Laser", *Appl Phys Lett*, **70**, 3200-2, 1997.

103. E. O. Ammann, "Simulataneous Stimulated Raman Scattering and Optical Frequency Mixing in Lithium Iodate", *Appl Phys Lett*, **34**, 838-40, 1979.

104. R. P. Mildren, H. M. Pask and J. A. Piper, "Raman Lasers Offer Power and Wavelength Versatility", *Photon Spec*, **39**, 52-9, 2005.

105. E. M. Dianov and A. M. Prokhorov,"Medium-Power CW Raman Fiber Lasers", *IEEE J Sel Top Quantum Electron*, **6**, 1022-28, 2000.

106. S. K. Sim, H. C. Lim, L. W. Lee, L. C. Chia, R. F. Wu, I. Cristiani, M. Rini and V. Degiorgio, "High-Power Cascaded Raman Fiber Laser Using Phosphosilicate Fiber", *Electron Lett*, **40**, 738-9, 2004.

107. V. I. Karpov, E. M. Dianov, V. M. Paramonov, O. I. Medvedkov, M. M. Bubnov, S. L. Semyonov, S. A. Vasiliev, V. F. Hopin, A. N. Guriyanov, M. P. Bachynski, W. P. L. Clements, "Laser-diode pumped Phosphosilicate Raman Laser with an Output Power of 1 W", *Opt Lett*, **24**, 887-9, 1999.

108. C. A. Codemard, P. Dupriez, Y. Jeong, J. K. Sahu, M. Ibsen and J. Nilsson, "High-Power Continuous-Wave Cladding-Pumped Raman Fiber Laser", *Opt Lett*, **31**, 2290-2, 2006.

109. C. Zhou, Private Communiation

110. J. D. S. Morgan III, *Backward Amplification and Beam Cleanup of a Raman Fiber Oscillator using a Multimode Graded-Index Fiber Amplifier*, MS Thesis, AFIT/DS/ENP/06-11, School of Engineering, Air Force Institute of Technology, Wright-Patterson AFB, 2006 (ADA450053).

111. http://www.limo.de/en/laserpumpp.php, 30 Jan 2007.

112. T. Szkopek, V. Pasupathy, J. E. Sipe and P. W. E. Smith, "Novel Multimode Fiber for Narrow-Band Bragg Gratings", *IEEE J Quantum Electron*, **7**, 425-33, 2001.

113. E. M. Dianov, "Advances in Raman Fibers", *J Lightwave Techol*, **20,** 1457-62, 2002.

114. P. A. Thielen, L. B. Shaw, P. C. Pureza, V. Q. Nguyen, J. S. Sanghera, and I. D. Aggarwal, "Raman Amplification in AsSe Fiber", *Proc SPIE*, **4628**, 74-7, 2002.

115. M. S. Asobe, T. Kanamori, K. Naganuma, H. Itoh and T. Kaino, "Third-order Nonlinear Spectroscopy in As_2S_3 Chalcogenide Glass", *J of Appl Phys*, **77**, 5518-23, 1995.

116. V. G. Plotnichenko, V. O. Sokolov, V. V. Koltashev, G. M. Dianov, "Raman Band Intensities", *Opt Lett*, **30**, 1156-8, 2005.

117. Y. Ohishi and R. Jose, "Raman Characteristics of WO_3 and P_2O_5 doped TBSN glasses: A new Gain Medium for Broadband Fiber Raman Amplifiers", *Proc SPIE*, **6389**, 6, 2006.

196

REPORT DOCUMENTATION PAGE

The public reporting burden for this collection of information is estimated to average 1 hour per response, including the time for reviewing instructions, searching existing data sources, gathering and maintaining the data needed, and completing and reviewing the collection of information. Send comments regarding this burden estimate or any other aspect of the collection of information, including suggestions for reducing this burden to Department of Defense, Washington Headquarters Services, Directorate for Information Operations and Reports (0704-0188), 1215 Jefferson Davis Highway, Suite 1204, Arlington, VA 22202-4302. Respondents should be aware that notwithstanding any other provision of law, no person shall be subject to an penalty for failing to comply with a collection of information if it does not display a currently valid OMB control number.
PLEASE DO NOT RETURN YOUR FORM TO THE ABOVE ADDRESS.

1. REPORT DATE *(DD-MM-YYYY)*	2. REPORT TYPE		3. DATES COVERED *(From – To)*
30-06-2007	**Doctoral Dissertation**		Sept 2003 – Jun 2007

4. TITLE AND SUBTITLE	5a. CONTRACT NUMBER
	5b. GRANT NUMBER
Raman Fiber Lasers and Amplifiers based on Multimode Fibers and their Application to Beam Cleanup	5c. PROGRAM ELEMENT NUMBER
6. AUTHOR(S)	5d. PROJECT NUMBER
	2007-016
Terry, Nathan, B., Captain, USAF	5e. TASK NUMBER
	5f. WORK UNIT NUMBER

7. PERFORMING ORGANIZATION NAMES(S) AND ADDRESS(S)	8. PERFORMING ORGANIZATION REPORT NUMBER
Air Force Institute of Technology Graduate School of Engineering and Management (AFIT/EN) 2950 Hobson Way WPAFB OH 45433-7765	AFIT/DSP/ENP/07-2

9. SPONSORING/MONITORING AGENCY NAME(S) AND ADDRESS(ES)	10. SPONSOR/MONITOR'S ACRONYM(S)
AFRL/DELO Attn: Lt Col Leanne Henry 3550 Aberdeen Ave SE Kirtland, AFB 87117-5773 DSN: 505-246-9302	11. SPONSOR/MONITOR'S REPORT NUMBER(S)

12. DISTRIBUTION/AVAILABILITY STATEMENT
     APPROVED FOR PUBLIC RELEASE; DISTRIBUTION UNLIMITED.

13. SUPPLEMENTARY NOTES

14. ABSTRACT

  Raman fiber lasers (RFLs) and Raman fiber amplifiers (RFAs) in multimode fibers were explored. The RFL based on a graded-index fiber was shown to be very efficient relative to RFLs based on singlemode fibers. Several configurations of the RFL were examined; the beam quality of the Stokes beam depended on the reflectivity of the output coupler and the Stokes power. When used as a beam combiner, the RFL was a highly efficient brightness converter. RFL configurations which used dichroic mirrors were shown to be potentially useful for RFLs based on very large fibers.

The forward- and backward-seeded geometries of an RFA based on a graded-index fiber were examined. The beam quality of the output was observed to depend on the beam quality of the input. A numerical model explains this behavior in terms of mode competition and explains why beam cleanup occurs in graded-index fibers but not in step-index fibers. The spectrum of the forward-seeded geometry was superior to the spectrum of the backward-seeded geometry. The RFA was used as a beam combiner.

15. SUBJECT TERMS
     Beam Combination, Raman Fiber Amplifiers, Raman Fiber Lasers, Stimulated Raman Scattering, Beam Cleanup, Stokes Radiation, Lasers, Fiber Optics, Nonlinear Optcs

16. SECURITY CLASSIFICATION OF:			17. LIMITATION OF ABSTRACT	18. NUMBER OF PAGES	19a. NAME OF RESPONSIBLE PERSON
REPORT U	**ABSTRACT** U	**c. THIS PAGE** U	UU	197	Thomas G. Alley, LtCol , USAF (ENP)
					19b. TELEPHONE NUMBER *(Include area code)* (937) 255-6565, ext 4946; e-mail: Thomas.Alley@afit.edu